

Pharmaceutical Applications of Polymeric Nanomaterials

Guest Editors: Libo Wu and Lu Sun





Pharmaceutical Applications of Polymeric Nanomaterials

Journal of Nanomaterials

Pharmaceutical Applications of Polymeric Nanomaterials

Guest Editors: Libo Wu and Lu Sun



Copyright © 2011 Hindawi Publishing Corporation. All rights reserved.

This is a special issue published in volume 2011 of “Journal of Nanomaterials.” All articles are open access articles distributed under the Creative Commons Attribution License, which permits unrestricted use, distribution, and reproduction in any medium, provided the original work is properly cited.

Editor-in-Chief

Michael Z. Hu, Oak Ridge National Laboratory, USA

Advisory Board

James H. Adair, USA
C. Jeffrey Brinker, USA
T. Hyeon, Republic of Korea
Nathan Lewis, USA

Ed Ma, USA
Alon V McCormick, USA
Gary L. Messing, USA
Zhonglin Wang, USA

Enge Wang, China
Ching Ping Wong, USA
N. Xu, China
Jackie Y. Ying, Singapore

Associate Editors

Xuedong Bai, China
Theodorian Borca-Tasciuc, USA
Christian Brosseau, France
Sang-Hee Cho, Republic of Korea
Cui ChunXiang, China
Ali Eftekhari, USA
Claude Estournes, France
Alan Fuchs, USA
Lian Gao, China
Hongchen Chen Gu, China
Michael Harris, USA
Justin D. Holmes, Ireland
David Hui, USA
Wanqin Jin, China

Rakesh K. Joshi, USA
Do Kyung Kim, Republic of Korea
Kin Tak Lau, Hong Kong
Burtrand Lee, USA
Jun Li, Singapore
Shijun Liao, China
Gong Ru Lin, Taiwan
J. -Y. Liu, USA
Jun Liu, USA
Songwei Lu, USA
Daniel Lu, China
Gaurav Mago, USA
Sanjay R. Mathur, Germany
Nobuhiro Matsushita, Japan

Sherine Obare, USA
P. Panine, France
Edward Andrew Payzant, USA
Donglu Shi, USA
Bohua Sun, South Africa
Maryam Tabrizian, Canada
Theodore Tsotsis, USA
Xiaogong Wang, China
Yong Wang, China
Michael S. Wong, USA
Ping Xiao, UK
Zhi-Li Xiao, USA
Doron Yadlovker, Israel
Kui Yu, Canada

Contents

Pharmaceutical Applications of Polymeric Nanomaterials, LiboWu and Lu Sun

Volume 2011, Article ID 530874, 1 page

Emerging Technologies of Polymeric Nanoparticles in Cancer Drug Delivery, Erik Brewer, Jason Coleman, and Anthony Lowman

Volume 2011, Article ID 408675, 10 pages

Characterization of Plasmid DNA Location within Chitosan/PLGA/pDNA Nanoparticle Complexes Designed for Gene Delivery, Hali Bordelon, Alexandru S. Biris, Cristina M. Sabliov, and W. Todd Monroe

Volume 2011, Article ID 952060, 9 pages

Preparation of Nanoporous Polymer Films for Real-Time Viability Monitoring of Cells, Chia-Man Chou, Tong-You Wade Wei, Jou-May Maureen Chen, Wei-Ting Chang, Chang-Tze Ricky Yu, and Vincent K. S. Hsiao

Volume 2011, Article ID 436528, 6 pages

Dynamics of Spreading and Alignment of Cells Cultured *In Vitro* on a Grooved Polymer Surface, Thomas Peterbauer, Sergii Yakunin, Jakub Siegel, Steffen Hering, Marc Fahrner, Christoph Romanin, and Johannes Heitz

Volume 2011, Article ID 413079, 10 pages

Nanoparticles of Conjugated Methotrexate-Human Serum Albumin: Preparation and Cytotoxicity Evaluations, Azade Taheri, Fatemeh Atyabi, Faranak Salman Nouri, Fatemeh Ahadi, Mohammad Ali Derakhshan, Mohsen Amini, Mohammad Hossein Ghahremani, Seyed Nasser Ostad, Pooria Mansoori, and Rassoul Dinarvand

Volume 2011, Article ID 768201, 7 pages

Preparation and Characterization of Self-Emulsified Docetaxel, Gyeong Hae Kim, Ju Young Lee, Yun Mi Kang, Kkot Nim Kang, E. Sle Kim, Da Yeon Kim, Jae Ho Kim, and Moon Suk Kim

Volume 2011, Article ID 860376, 6 pages

Application of Flow Focusing to the Break-Up of a Magnetite Suspension Jet for the Production of Paramagnetic Microparticles, Lucía Martín-Banderas, Román González-Prieto, Alfonso Rodríguez-Gil, Mercedes Fernández-Arévalo, María Flores-Mosquera, Sebastián Chávez, and Alfonso M. Gañán-Calvo

Volume 2011, Article ID 527437, 10 pages

Biocompatible Metal-Oxide Nanoparticles: Nanotechnology Improvement of Conventional Prosthetic Acrylic Resins, Laura S. Acosta-Torres, Luz M. López-Marín, R. Elvira Núñez-Anita, Genoveva Hernández-Padrón, and Victor M. Castaño

Volume 2011, Article ID 941561, 8 pages

Water-Soluble Chitosan Nanoparticles Inhibit Hypercholesterolemia Induced by Feeding a High-Fat Diet in Male Sprague-Dawley Rats, Yi Tao, Hongliang Zhang, Bing Gao, Jiao Guo, Yinming Hu, and Zhengquan Su

Volume 2011, Article ID 814606, 5 pages

Preparation and Characterization of Zein and Zein-Chitosan Microspheres with Great Prospective of Application in Controlled Drug Release, Vinícius Mller, Juliana Francis Piai, André Ricardo Fajardo, Silvia Luciana Fávaro, Adley Forti Rubira, and Edvani Curti Muniz

Volume 2011, Article ID 928728, 6 pages



Dynamic Probing of Nanoparticle Stability In Vivo: A Liposomal Model Assessed Using In Situ Microdialysis and Optical Imaging, Chien-Chung Jeng, Shih-Hsun Cheng, Ja-an Annie Ho, Sam Hong-Yi Huang, Jerry C. Chang, Pi-Ju Tsai, Chung-Shi Yang, and Leu-Wei Lo
Volume 2011, Article ID 932719, 8 pages

Editorial

Pharmaceutical Applications of Polymeric Nanomaterials

Libo Wu¹ and Lu Sun²

¹ Pharmaceutical Development Department, MAP Pharmaceuticals, Inc., Mountain View, CA 94043, USA

² Department of Engineering and Technology, Indiana University-Purdue University Indianapolis, Indianapolis, IN 46202, USA

Correspondence should be addressed to Libo Wu, lwu@mappharma.com

Received 5 December 2010; Accepted 5 December 2010

Copyright © 2011 L. Wu and L. Sun. This is an open access article distributed under the Creative Commons Attribution License, which permits unrestricted use, distribution, and reproduction in any medium, provided the original work is properly cited.

With significant attention focused on nanoscience and nanotechnology in recent years, nanomaterials have been used in a wide variety of applications such as automotive, environmental, energy, catalysis, biomedical, drug delivery, and polymeric industries. Among those fields, the application of nanomaterials with pharmaceutical science is an emerging and rapidly growing field and has drawn increasing attention recently. Research and development in this field is mainly focused on several aspects such as the discoveries of novel functional nanomaterials, exploration on nanoparticles with controlled and targeted drug delivery characteristics, and investigation of biofunctionalized and diagnostic nanomaterials. In this special issue, we have invited a few papers related to recent advances in pharmaceutical application of polymeric nanomaterials.

The first article of this special issue provides a comprehensive literature review on the application of polymeric nanoparticles in cancer drug delivery especially on temperature and pH-responsive drug delivery systems. The second paper examines properties of the PLGA-chitosan nanoparticle/plasmid DNA complex after formation, determines the optimal ratio of plasmid DNA: nanoparticles for nucleic acid delivery purposes, and elucidates the location of the pDNA within the complexes. The third paper demonstrates an alternative way to monitor the viability of cells adhered on a nanoporous polymer film prepared by laser interference patterning in real time. The fourth paper uses mechanically embossed polyester films to analyze the dynamics of cell alignment and cell-specific factors modulating the response of chinese hamster ovary cells and of a rat myogenic cell line to the surface topography. The fifth article develops methotrexate-human serum albumin conjugates by a simple carbodiimide reaction and evaluates its cytotoxicity. The

sixth paper proposes to produce a self-microemulsifying docetaxel using PLGA, tetraglycol, labrasol, and cremophor ELP. The prepared Dtx-loaded self-microemulsifying system shows an inhibitory effect for proliferation of B16F10 melanoma cells. The seventh paper describes a straightforward production methodology of paramagnetic microparticles with homogeneous and selectable sizes using flow focusing technology and reports the development of an initial formulation of a stable iron oxide suspension compatible with the flow focusing requirements. The eighth paper proposes the use of nanostructured materials (TiO_2 and Fe_2O_3) for simultaneously coloring and/or improving the antimicrobial properties of PMMA resins. The ninth paper clarifies the effects of water-soluble chitosan and water-soluble chitosan nanoparticles on hypercholesterolemia induced by feeding a high-fat diet in male Sprague-Dawley rats. The tenth article presents the microspheres based on the protein Zein (ZN) and ZN associated to the natural polymer chitosan. The last paper of this special issue describes a novel methodology comprised of microdialysis and optical imaging to assess the liposome stability *in vivo*.

Libo Wu
Lu Sun

Review Article

Emerging Technologies of Polymeric Nanoparticles in Cancer Drug Delivery

Erik Brewer, Jason Coleman, and Anthony Lowman

Department of Chemical and Biological Engineering, Drexel University, 3141 Chestnut Street, Philadelphia, PA 19104, USA

Correspondence should be addressed to Erik Brewer, ecb34@drexel.edu

Received 2 June 2010; Accepted 2 August 2010

Academic Editor: Lu Sun

Copyright © 2011 Erik Brewer et al. This is an open access article distributed under the Creative Commons Attribution License, which permits unrestricted use, distribution, and reproduction in any medium, provided the original work is properly cited.

Polymeric nanomaterials have the potential to improve upon present chemotherapy delivery methods. They successfully reduce side effects while increasing dosage, increase residence time in the body, offer a sustained and tunable release, and have the ability to deliver multiple drugs in one carrier. However, traditional nanomaterial formulations have not produced highly therapeutic formulations to date due to their passive delivery methods and lack of rapid drug release at their intended site. In this paper, we have focused on a few “smart” technologies that further enhance the benefits of typical nanomaterials. Temperature and pH-responsive drug delivery devices were reviewed as methods for triggering release of encapsulating drugs, while aptamer and ligand conjugation were discussed as methods for targeted and intracellular delivery, with emphases on *in vitro* and *in vivo* works for each method.

1. Introduction

A major obstacle for chemotherapy is the inability to deliver adequate doses of drugs to the affected areas in the body. Systemic toxicity of these drugs limits their dose, while rapid clearance from circulation requires large doses in order to be effective. Doxorubicin, for instance, has a five to ten minute half life in the plasma [1].

Polymeric nanomaterials offer a promising solution by encapsulating chemotherapy drugs, and have been shown to reduce toxicity by providing a protective housing for the drug that limits its interaction with healthy cells [2–5]. As a result, the pharmacokinetic properties of the drug are based on the pharmacokinetic properties of the particle, as long as the drug can stay entrapped with the carrier until release is desired [6]. The potential benefits of such delivery devices also include controlled and long-term release rates, prolonged bioactivity, reduced side effects, increased patient compliance due to decreased administration frequency, and the ability to codeliver multiple drugs with synergistic effects to the same site [7–9].

Delivery devices made from erodible polymers are an attractive option over nonerodible ones because they degrade and gradually disappear after delivery [10]. Of these

polymers, poly(ϵ -caprolactone), poly(lactic acid) (PLA), poly(glycolic acid) (PGA), and their copolymers have been among the most extensively researched due to their biocompatibility, biodegradability, and regulatory approval [11–15]. For an anticancer drug carrier to prove effective, prolonged circulation times and controlled drug release at the tumor site are required [16, 17]. Various works have already been done to improve particle circulation time by limiting renal secretion and hindering uptake by the reticuloendothelial system (RES) [18–22]. This is often accomplished by pairing poly(ethylene glycol) (PEG) with the polymer of the nanoparticle. PEG has been shown to inhibit the binding of plasma proteins to the surface of polymeric drug carriers, preventing their recognition by the RES. This imparts “stealth” properties to the delivery device, increasing its systemic circulation time significantly [23].

Passive targeting is created because the size of the polymeric systems and their increased residence time make them suitable carriers to take advantage of the enhanced permeability and retention (EPR) effect in tumors [6, 24, 25]. The EPR effect is described as hyperpermeable tumor vessels that allow for the extravasation of circulating macromolecules, such as polymeric nanomaterials, that, combined with the lack of a lymphatic drainage system, results in their

gradual accumulation [26]. While this results in localized delivery gradually over time, there still remains the need for drugs that act intracellularly to release and permeate the cell walls. In addition, it has been shown that slow and passive drug release from drug-carrying particles reduces their effectiveness in cancer treatment [27]. Overall, passive polymer drug carriers have not demonstrated increased therapeutic efficacy due to lack of intercellular and localized, rapid drug delivery [28–30].

Current research has thus focused on advancing these polymer vehicles with “smart” technologies that are responsive to environmental stimuli. These can be separated into two categories: (1) site-targeting, where particles actively search for and attach themselves to specific and diseased cells by the use of molecules such as ligands, antibodies, and aptamers; (2) site-triggering, where chemical or physical changes in the environment trigger the rapid release of the drug payload. This review focuses on a few selected “smart” technologies in each category: ligand and aptamer site-targeting particles, and pH and temperature-responsive particles.

2. Smart Nanomaterials

2.1. Site-Targeted Nanomaterials

2.1.1. Ligands. Attaching targeting ligands to the particle surface can take advantage of the overexpression of various receptors on tumor cell surfaces [31, 32]. Coupled with the passive accumulation at tumor sites caused by the EPR effect, targeted particles can increase the interaction time between particles and the tumor cell and increase the likelihood of the particles being taken up by the tumor cells via endocytosis [33].

Targeted delivery takes advantage of differences in the expression of cell surface receptors between healthy and tumor cells. For example, folate receptors are known to be vastly overexpressed in several human tumors [34–36]. Attaching folate to the outer shell of particles can create a targeted drug delivery carrier. Folate conjugation has shown success at creating targeted anticancer agents that can avoid nonspecific attacks on normal tissue and increase cellular uptake within target cells [31–33, 37, 38].

PEG is commonly associated with the surfaces of micelle-like particles and liposomes to increase particle circulation. By coupling ligands to polyethylene glycol (PEG), a targeted particle can be created where the ligand is expressed on the particle surface. Combining the benefits of prolonged particle circulation with the benefits of delaying drug release, an ideal system exists for targeted delivery [33, 39–45]. The increased residence time increases the likelihood of interaction between receptor and target for targeted delivery.

Yoo et al. developed folate-conjugated PEG-co-poly (lactic-co-glycolic acid) (PEG-PLGA) micelles loaded with the anti-cancer drug doxorubicin that expressed folate on the micelle surface [33]. Studies indicated increased cytotoxicity and decreased tumor growth for folate conjugated micelles as opposed to nontargeted micelles and free DOX [33]. Targeted particles also showed increased cellular uptake [33].

2.1.2. Aptamers. Aptamers are DNA and RNA sequences that recognize specific target analytes [46]. Aptamers can be selected to bind with high specificity and affinity to a wide range of molecules such as organic dyes, amino acids, biological cofactors, antibiotics, peptides, proteins, and whole cells [47]. Aptamers are often compared to antibodies for their affinity to select molecules, but despite their similarities, offer several important advantages: aptamers can be easily synthesized *in vitro* without the need for an induced immune response from animals [48], which makes them able to target nonimmunogenic molecules; the aptamer synthesis process, SELEX, can be carried out in nonphysiological settings [49]; they are more stable and can be obtained at a lower cost [50].

Since the targeted molecule can be uniquely associated with a particular disease, early research into aptamers has concentrated on early-stage disease diagnosis, particularly in cancer. Common cancer diagnostic methods involve somatic or visual techniques, such as self-examinations and localized X-rays. A major disadvantage of these methods is that they do not lead to diagnoses until advanced stages in the disease, a factor in cancers high death rates [51, 52]. However, cancer is a genetic disease, and aptamers provide a way for screening at the molecular level using selective cell binding [53].

Cancer-detecting assays using fluorescent imaging that are currently being developed utilize aptamers conjugated with dye-doped silica nanoparticles. These fluorescent nanoparticles are favored over direct dye conjugation due to their signal amplification and ability to immobilize biomolecules [54–56]. These particles have often combined with magnetic particles, which allows for convenient separation of bound cells, to make two-part aptamer-based assays [53, 57, 58]. Gold nanoparticles, which are ideal contrasting agents, have been conjugated with cancer-targeting aptamers to successfully create assays for detecting prostate and breast cancer cells [59, 60].

The ability of aptamers to bind directly with diseased cells has gained them recognition in site-specific drug delivery research. In particular, systems utilizing polymeric nanovehicle and aptamer conjugates are believed to create devices that can deliver high drug doses to diseased cells in a controlled fashion with minimal toxicity to healthy cells.

In vitro studies involving these systems often utilize the A10 2'-fluoropyrimidine RNA aptamer, which targets the prostate-specific membrane antigen (PSMA) found on the LNCaP cell line. This allows for comparison with control groups tested against PC3 cells, another prostate-cancer cell line that does not display the PSMA antigen, to prove that the drug carriers only have affinity for cells expressing the targeted antigen [61–63]. Using fluorescent imaging, this comparison was able to establish that drug vehicles conjugated with the PSMA-targeting aptamer were internalized by cells via receptor-mediated endocytosis [64]. PEG-PLGA nanoparticles carrying the chemotherapy drug docetaxel and targeting PSMA cells *in vivo* have produced dramatic reduction in tumor sizes in mice compared to free docetaxel and non-targeted particles [61]. The increase in cancer cell toxicity was credited to a combination of the intracellular delivery of the drug, increased retention time,

and reduced circulation clearance at the tumor site due to high-affinity binding with the antigen.

Polymeric micelles have proven to increase the overall affinity of aptamers that exhibit ones considered too low for drug-aptamer delivery systems [65]. They do this by taking advantage of multivalent binding effects, where multiple aptamers on the micelle surface link with the cell-surface antigens to produce an overall stronger bond. This allows for the targeting of unique cellular antigens that would otherwise be considered unsuitable for drug-aptamer conjugates.

Polymeric nanocarriers provide the benefit of being able to carry multiple drugs in the same vehicle. This, combined with aptamer targeting, can be used to selectively deliver dual-drug payloads to cancerous cells. Due to their different mechanisms of action, the drugs may provide additive or synergistic effects that can allow for lower doses, and reduce side effects [66, 67]. More importantly, this is thought to combat drug resistance, a major problem associated with cancer drug treatment [68]. Packaging the drugs in a nanocarrier, as opposed to a simple mixture, allows for their simultaneous delivery on a cell-by-cell basis, which has been proven to be more effective [69–71].

This can even be used to combine drugs with different water solubility properties, as was accomplished by Zhang et al. using PEG-PLGA [9]. In systems where the aptamer binding initiates endocytosis, such as with A10 RNA aptamer, combinations of drugs and genes that require delivery to intracellular compartments to properly function experience greater benefits [72]. This approach has been used successfully in aptamer-gene conjugates [73, 74], and is beginning to see promise in aptamer-nanoparticle conjugates. Polyethyleneimine-grafted-PEG (PEI-PEG) nanoparticles carrying doxorubicin and the hairpin shRNA, which suppresses the antiapoptotic gene Bcl-xl, produced significantly lower cell viability and enhanced therapeutic efficacy compared to single drug-loaded nanoparticle aptamer systems and free drug mixtures [75].

2.2. Site-triggered Nanomaterials

2.2.1. pH-Responsive Nanomaterials. One method to promote drug release at the tumor site is by taking advantage of the lower pH of the tumor's microenvironment. Mildly acidic conditions exist in tumor and inflammatory tissues (pH 6.8) and in endosomes (pH 5–6) in comparison to the more neutral physiological condition (pH 7.4) [76, 77]. The ability of nanoparticles to accumulate in solid tumors has been shown by the enhanced permeation and retention (EPR) effect [6, 24, 25, 78]. In addition, it has also been demonstrated that nanoparticles can be taken up within cancer cells through a process called endocytosis [79, 80]. Many anticancer drugs, such as doxorubicin, work by inhibiting cell replication. Thus, for anticancer drugs to be effective, they must interact with intracellular components. If particles can gain access to the intracellular components through endocytosis, then it seems logical that the particle deliver its payload of anticancer drugs once inside the cell. Once the particle is taken up via endocytosis, the endocytic vesicles ultimately change to late endosomes and then to

lysosomes in which the proton concentration is 100 times higher (pH 5.0) than the physiological condition (pH 7.4) [76]. Micelle forming polymer-drug conjugates and drug loaded liposomes provide the potential for drug release within a lower pH environment. Drug release from micelles can be targeted to these acidic environments by conjugating the polymer to the drug with an acid-cleavable linkage. Release can be targeted to acidic conditions in liposomes by causing destabilization of the liposome shell under acidic conditions.

Nanomaterials such as liposomes and micelles are examples of particles that can accumulate in solid tumors as a result of the EPR effect [3, 9–11]. Micelles consist of a hydrophobic core and a hydrophilic corona or shell and are well suited to entrap and solubilize hydrophobic drugs within their core. Because some of the most commonly used cancer drugs are hydrophobic, micelles have gained widespread use for the delivery of cancer therapeutics [39, 41, 42, 45, 80–83]. Liposomes typically involve a bimolecular phospholipid membrane that encloses an aqueous compartment. Because liposomes contain a phospholipid membrane they can entrap hydrophobic drugs, but they can also encapsulate various hydrophilic drugs such as peptides, proteins, and nucleic acids within their aqueous compartment [84, 85]. Previous work has been done to increase liposome stability by increasing circulation time and by preventing drug leakage until the target is reached [86–88]. Micelle like particles and liposomes with pH sensitivity have shown great promise as delivery vehicles for anticancer drugs, DNA, RNA, proteins, and peptides [76, 82, 89–98].

In order for micelles to take on pH responsibilities, the drug is typically conjugated to the polymer that makes up the core of the micelle by an acid cleavable linkage. The creation of a polymer-drug conjugation is referred to as a polymeric prodrug and allows the drug to remain inactive until cleavage from the polymer carrier. When used in the formation of micelles, polymeric prodrugs can control release by chemically attaching the drug within the core of the micelle or by increasing the thermodynamic stability of the micelle in order to delay micelle degradation [39, 99]. In order to prolong drug release, an active substance can be linked to a polymeric molecule via a covalent bond which is naturally hydrolyzed *in vivo* [100–102]. For pH-responsiveness of polymeric prodrug micelles, the linkage between drug and polymer is more readily hydrolyzed at a lower pH.

If taken up via endocytosis, drug association with a polymer carrier can help avoid the multidrug resistance (MDR) effect (i.e. recycling of chemotherapy drugs). Drug association with a polymer carrier, either through conjugation or entrapment within the micelle core, can help limit free drug being outfluxed from the cancer cell through the *p*-glycoprotein pump.

Various works have been done involving the conjugation of the anti-cancer drug doxorubicin (DOX) to the hydrophobic core forming polymer of the micelle [82, 89, 93, 94]. The conjugation of drug to polymer was performed via a hydrazone linkage and ultimately resulted in enhanced DOX accumulation and cytotoxicity within tumor cells as opposed

to free DOX. One of the more promising aspects for this type of pH-responsive release is the ability of the DOX-conjugated micelles to circumvent the multi-drug resistant effect once taken up by endocytosis [82].

One of the main disadvantages of conjugating the drug to the polymer to get pH responsiveness is the need to maintain drug bioactivity throughout the conjugation scheme. Liposomes that are pH responsive overcome this barrier because the shell of the liposomes is what can be tailored to exhibit pH effects. Because of previous work to increase liposome stability and circulation, the liposome can circulate long enough to passively reach the target site (EPR effect), and the drug can stay associated with the liposome until the proper pH environment is reached [85–88, 91].

In order for liposomes to deliver their payload at the intracellular layer, the liposomes must first be taken up by endocytosis. Once taken up, the liposomes need to destabilize at the lower endosomal pH. This destabilization can allow the liposome to break down and deliver its contents into the cell cytoplasm. Modification by the inclusion of lipids with pH sensitivity can give the liposome “fusogenic” properties [91]. The term fusogenic refers to the ability of liposomes to destabilize at the lower endosomal pH and “fuse” with the endosomal bilayer to allow for access to the cell cytoplasm. This first became a desired intracellular release mechanism by the observation that certain viruses take advantage of the endosomal acidification to infect cells [91]. Acidic environments within the body also occur at tumors, inflamed or infected tissue, where pH sensitive delivery may also be desirable.

The most common pH-sensitive liposomes are composed of phosphatidylethanolamine (PE) as the primary bilayer component combined with compounds that are stable at a neutral pH, but unstable under acidic conditions [91]. Altering pH sensitivity is typically done by including pH-sensitive lipids, synthetic peptides/proteins, or pH-sensitive polymers within the lipid bilayer or the liposome aqueous compartment [91, 103–108]. With PE liposomes destabilization occurs by intercalation of amphiphilic molecules that contain a protonatable acidic group (i.e. a carboxylic group) that becomes protonated under acidic conditions and causes the PE molecule to revert to an inverted and unstable hexagonal phase [91, 109, 110]. Some of the most effective molecules included within the bilayer that induce pH sensitivity and ultimately, increase drug delivery to the cytoplasm, consist of combinations of dioleoylphosphatidylethanolamine (DOPE) and cholesteryl hemisuccinate (CHEMs) [91, 111, 112].

2.2.2. Thermoresponsive. Hyperthermia has been investigated as a method for triggered drug release to targeted areas in thermoresponsive liposomes. Here, *in vivo* temperatures are achieved through either older and more general methods, such as warmed baths or perfusates [113], or through more advances and localized methods, requiring ultrasonic and microwave units [114, 115]. Since most mammalian cells begin to show damage at 42°C [116], hyperthermia is defined as temperatures between this and physiological temperature (37°C). When the liposomes pass through the area with increased temperature, they release their encapsulated drugs.

In addition to localized drug release, hyperthermia offers other indirect benefits, such as increased microvessel permeability in tumors, which causes more liposomes to accumulate at the intended site [117, 118] while healthy microvessels are not significantly altered [119]; increased cell permeability, which allows the released drugs to diffuse through the cell walls more easily [120]; and increased sensitivity to thermal injury compared to healthy cells [121].

To take advantage of this triggering mechanism, liposomes must have a liquid-crystalline transition temperature (T_c) within the accepted temperature range. Upon reaching this temperature, they become highly permeable to their water-soluble contents, causing hydrophilic drugs to release in the intended location [122, 123]. T_c is a material property of the liposome polymer and is primarily determined by the length of its fatty acid chains [124]. This allows for the addition of other polymers to the liposome, notably polyethylene glycol (PEG), to increase the retention time and stability [125] and alter the release kinetics [126, 127], without significantly changing its transition temperature. To achieve a desirable T_c , it is possible to combine polymers with different transition temperatures in ratios that result in one in the hyperthermic range [128].

In order for a thermosensitive liposome to be considered for a drug-delivery device, it must be stable in plasma circulation, release minimal amount of drug at physiological temperatures, and then release its payload quickly in hyperthermia conditions. Common phospholipids include 1,2-dihexadecanoyl-sn-glycero-3-phosphocholine (DPPC), 1,2-distearoyl-sn-glycero-3-phosphocholine (DSPC), 1,2-distearoyl-sn-glycero-3-phosphoethanolamine (DSPE), and 1,2-dipalmitoyl-sn-glycero-3-phosphoglyceroglycerol (DPPGOG), often in combination and with varying amounts of PEG [113, 129–132].

In vivo experimentation has proven promising for these thermo-sensitive devices. The chemotherapy drug carboxyfluorescein (CF) produced a sixfold bioavailability increase in cancerous hamsters when packaged in a thermo-sensitive liposome under hyperthermia compared to free CF [132]. Similar nanovehicles carrying DOX successfully eliminated tumors in six out of nine cancerous mice after 60 days [133]. In a phase I clinical trial, temperature-sensitive liposomes carrying DOX were given to dogs with solid tumors in conjunction with localized hyperthermia. The study reported a 17-fold decrease in drug clearance rate when using the liposomes compared to the free drug, resulting in a higher bioavailability [134].

Alternatively, copolymers have been designed that have a different thermo-sensitive property, called the cloud point (CP), which changes over time, eliminating the need for hyperthermic conditions. Above the CP, the co-polymer precipitates out of solution and freely forms micelles that can encapsulate their drug; below the CP, the polymer dissolves into solution, causing the micelle to destabilize and release its payload [135]. Thus, these co-polymers are designed to begin with a CP that is below ambient conditions so that a drug vehicle can be made, and then end with a CP that is above physiological temperature after the micelles have been delivered to the target cells [136].

This has been achieved through the use of a novel class of hydrophobic lactate-containing polymers, notably poly(*N*-(2-hydroxypropyl) methacrylamide oligolactates) (pHPMAm-Lac_n) and poly(*N*-(2-hydroxyethyl) methacrylamide)-oligolactates (pHEMAm-Lac_n). The change in CP over time is caused by the hydrolysis of the lactate side group: as the polymer degrades and the lactate hydrolyzes, the polymer becomes more hydrophilic, causing an increase in the CP [135]. In both polymers, the initial CP is dependent on the length of the lactate chain, and can thus be tailored, though pHPMAm-Lac₂ and pHEMAm-Lac₂ provide the most convenient CPs of 10°C [137] and 22°C [138], respectively. To create an amphiphilic block copolymer, PEG is most commonly used as the hydrophilic segment to take advantage of its stealth properties and longer circulation times [139], as previously described.

These micelles have encountered obstacles in preliminary *in vitro* and *in vivo* experimentation, as release kinetics of encapsulated paclitaxel have been in large part due to diffusion rather than micelle destabilization [140]. In addition, fast degradation kinetics of the lactate chains, causing quick micelle destabilization, resulted in no measurable accumulation in mice 24 h after i.v. injection [141]. However, mPEG-*b*-p(HEMAm-Lac_n) polymers modified with methacryloxy-chloride in the micelle core have displayed prolonged circulation times *in vivo* and increased tumor accumulation compared to unmodified micelles [142]. This new class of thermosensitive polymers shows promise for future chemotherapy work.

2.3. Combined Smart Technologies. Because targeted particles can increase uptake by endocytosis, pH-sensitive release is desirable. Combining the benefits of a receptor-targeted micelle and a pH-responsive drug conjugate was performed by Bae et al. [92–95]. Targeting a surface receptor on cancer cells can cause increased cellular uptake, and a pH-responsive degradable bond between drug and polymer can cause release in the low pH environment of the lysosome. Folate was used as the targeting molecule and the pH-responsive hydrazone bond was used to conjugate DOX to the polymer. The self-assembling block copolymers required to prepare the targeted and pH-responsive micelles (approximately 60 nm), consisted of folate-PEG-poly(aspartate hydrazone doxorubicin) [FOL-PEG-P(Asp-Hyd-DOX)]. Delivery to tumor cells known to overexpress folate receptors has been shown with micelles using folate as the targeting moiety to cause increased endocytotic cellular uptake into the intracellular acidic compartments known as endosomes (pH 5–6) [33]. Drugs conjugated within a micelle by a hydrazone linkage show selective release within the low pH environment of endosomes [76, 82, 89].

In terms of effective dose (ED), the effective doses for free DOX and micelles without folate were similar, but the ED for folate conjugated micelles was lowered 2-fold compared to the free DOX micelles [93]. The overall findings by Bae et al. suggest that an intracellular, environment-targeting micelle drug carrier is one of the most effective approaches for cancer treatment [92]. Liposomes with pH-sensitivity

and targeting ligands have also been effectively used to increase residence time at the target cells, increase uptake, and increase intracellular delivery [37, 96, 98].

3. Conclusion

Smart technologies in polymer nanomaterials offer a unique way to deliver chemotherapy drugs to their intended target without affecting healthy cells. By utilizing the naturally low pH environment found in tumors and endosomes, these drug carriers are free to circulate in the body, only releasing their drugs at their intended location. Thermo-sensitive polymer vehicles, when combined with localized hyperthermia, can be triggered to release their payload at the desired site. Ligands and aptamers, on the other hand, provide a way for these vehicles to actively target cancerous cells and then induce receptor-mediated endocytosis for intracellular delivery. Compared to free drug and passive nanomaterial systems, these smart devices have proven to increase therapeutic effects and efficacy in a variety of cellular and animal models. Progression of these techniques will eventually lead to increased accuracy in delivering higher doses and more toxic drugs, which will require challenges like premature drug release and false cell targeting to be addressed. As these technologies are further developed and other methods of triggering and targeting emerge, smart polymer nanomaterials will be able to provide improved cancer treatment methods.

References

- [1] P. K. Working and A. D. Dayan, "Pharmacological-toxicological Expert Report. Caelyx. (Stealth liposomal doxorubicin HCl)," *Human and Experimental Toxicology*, vol. 15, no. 9, pp. 751–785, 1996.
- [2] T. L. ten Hagen, A. L. Seynhaeve, S. T. van Tiel, D. J. Ruiter, and A. M. Eggermont, "Pegylated liposomal tumor necrosis factor- α results in reduced toxicity and synergistic antitumor activity after systemic administration in combination with liposomal doxorubicin (Doxil) in soft tissue sarcoma-bearing rats," *International Journal of Cancer*, vol. 97, no. 1, pp. 115–120, 2002.
- [3] A. Gabizon, H. Shmeeda, and Y. Barenholz, "Pharmacokinetics of pegylated liposomal doxorubicin: review of animal and human studies," *Clinical Pharmacokinetics*, vol. 42, no. 5, pp. 419–436, 2003.
- [4] A. A. Gabizon, "Selective tumor localization and improved therapeutic index of anthracyclines encapsulated in long-circulating liposomes," *Cancer Research*, vol. 52, no. 4, pp. 891–896, 1992.
- [5] D. W. Northfelt, F. J. Martin, P. Working et al., "Doxorubicin encapsulated in liposomes containing surface-bound polyethylene glycol: pharmacokinetics, tumor localization, and safety in patients with AIDS-related Kaposi's sarcoma," *Journal of Clinical Pharmacology*, vol. 36, no. 1, pp. 55–63, 1996.
- [6] T. M. Allen and P. R. Cullis, "Drug delivery systems: entering the mainstream," *Science*, vol. 303, no. 5665, pp. 1818–1822, 2004.
- [7] M. Yokoyama, T. Okano, Y. Sakurai, H. Ekimoto, C. Shibasaki, and K. Kataoka, "Toxicity and antitumor activity

- against solid tumors of micelle-forming polymeric anticancer drug and its extremely long circulation in blood," *Cancer Research*, vol. 51, no. 12, pp. 3229–3236, 1991.
- [8] M. L. Hans and A. M. Lowman, "Biodegradable nanoparticles for drug delivery and targeting," *Current Opinion in Solid State and Materials Science*, vol. 6, no. 4, pp. 319–327, 2002.
 - [9] L. Zhang, A. F. Radovic-Moreno, F. Alexis et al., "Co-delivery of hydrophobic and hydrophilic drugs from nanoparticle-aptamer bioconjugates," *ChemMedChem*, vol. 2, no. 9, pp. 1268–1271, 2007.
 - [10] R. Herrero-Vanrell and M. F. Refojo, "Biodegradable microspheres for vitreoretinal drug delivery," *Advanced Drug Delivery Reviews*, vol. 52, no. 1, pp. 5–16, 2001.
 - [11] D. H. Lewis, "Controlled release of bioactive agents from lactide/glycolide polymers," in *Biodegradable Polymers as Drug Delivery Devices*, M. Chasin and R. Langer, Eds., pp. 1–41, Marcel Dekker, New York, NY, USA, 1990.
 - [12] R. Langer and J. P. Vacanti, "Tissue engineering," *Science*, vol. 260, no. 5110, pp. 920–926, 1993.
 - [13] E. Chiellini and R. Solaro, "Biodegradable polymeric materials," *Advanced Materials*, vol. 8, no. 4, pp. 305–313, 1996.
 - [14] B. Jeong, Y. H. Bae, D. S. Lee, and S. W. Kim, "Biodegradable block copolymers as injectable drug-delivery systems," *Nature*, vol. 388, no. 6645, pp. 860–862, 1997.
 - [15] K. Okada, H. Kawaide, T. Kuzuyama, H. Seto, I. S. Curtis, and Y. Kamiya, "Antisense and chemical suppression of the nonmevalonate pathway affects ent-kaurene biosynthesis in Arabidopsis," *Planta*, vol. 215, no. 2, pp. 339–344, 2002.
 - [16] A. Lavasanifar, J. Samuel, and G. S. Kwon, "Poly(ethylene oxide)-block-poly(L-amino acid) micelles for drug delivery," *Advanced Drug Delivery Reviews*, vol. 54, no. 2, pp. 169–190, 2002.
 - [17] M. Yokoyama, M. Miyauchi, N. Yamada et al., "Characterization and anticancer activity of the micelle-forming polymeric anticancer drug Adriamycin-conjugated poly(ethylene glycol)-poly(aspartic acid) block copolymer," *Cancer Research*, vol. 50, no. 6, pp. 1693–1700, 1990.
 - [18] D. D. Lasic, J. J. Vallner, and P. K. Working, "Sterically stabilized liposomes in cancer therapy and gene delivery," *Current Opinion in Molecular Therapeutics*, vol. 1, no. 2, pp. 177–185, 1999.
 - [19] T. M. Allen, M. S. Newman, M. C. Woodle, E. Mayhew, and P. S. Uster, "Pharmacokinetics and anti-tumor activity of vincristine encapsulated in sterically stabilized liposomes," *International Journal of Cancer*, vol. 62, no. 2, pp. 199–204, 1995.
 - [20] R. Gref, M. Lück, P. Quellec et al., "'Stealth' corona-core nanoparticles surface modified by polyethylene glycol (PEG): influences of the corona (PEG chain length and surface density) and of the core composition on phagocytic uptake and plasma protein adsorption," *Colloids and Surfaces B*, vol. 18, no. 3–4, pp. 301–313, 2000.
 - [21] R. Gref, Y. Minamitake, M. T. Peracchia, V. Trubetskoy, V. Torchilin, and R. Langer, "Biodegradable long-circulating polymeric nanospheres," *Science*, vol. 263, no. 5153, pp. 1600–1603, 1994.
 - [22] M. Tobio, R. Gref, A. Sánchez, R. Langer, and M. J. Alonso, "Stealth PLA-PEG nanoparticles as protein carriers for nasal administration," *Pharmaceutical Research*, vol. 15, no. 2, pp. 270–275, 1998.
 - [23] D. E. Owens III and N. A. Peppas, "Opsonization, biodistribution, and pharmacokinetics of polymeric nanoparticles," *International Journal of Pharmaceutics*, vol. 307, no. 1, pp. 93–102, 2006.
 - [24] X. Zhang, Y. Li, X. Chen et al., "Synthesis and characterization of the paclitaxel/MPEG-PLA block copolymer conjugate," *Biomaterials*, vol. 26, no. 14, pp. 2121–2128, 2005.
 - [25] H. Maeda, J. Wu, T. Sawa, Y. Matsumura, and K. Hori, "Tumor vascular permeability and the EPR effect in macromolecular therapeutics: a review," *Journal of Controlled Release*, vol. 65, no. 1–2, pp. 271–284, 2000.
 - [26] R. Duncan, M. J. Vicent, F. Greco, and R. I. Nicholson, "Polymer-drug conjugates: towards a novel approach for the treatment of endocrine-related cancer," *Endocrine-Related Cancer*, vol. 12, supplement 1, pp. S189–S199, 2005.
 - [27] L. Li, T. L. M. ten Hagen, D. Schipper et al., "Triggered content release from optimized stealth thermosensitive liposomes using mild hyperthermia," *Journal of Controlled Release*, vol. 143, no. 2, pp. 274–279, 2010.
 - [28] P. J. Cagnoni, "Liposomal amphotericin B versus conventional amphotericin B in the empirical treatment of persistently febrile neutropenic patients," *Journal of Antimicrobial Chemotherapy*, vol. 49, supplement 1, pp. 81–86, 2002.
 - [29] I. Judson, J. A. Radford, M. Harris et al., "Randomised phase II trial of pegylated liposomal doxorubicin (DOXIL/CAELYX) versus doxorubicin in the treatment of advanced or metastatic soft tissue sarcoma: a study by the EORTC Soft Tissue and Bone Sarcoma Group," *European Journal of Cancer*, vol. 37, no. 7, pp. 870–877, 2001.
 - [30] T. J. Walsh, R. W. Finberg, C. Arndt et al., "Liposomal amphotericin b for empirical therapy in patients with persistent fever and neutropenia. National Institute of Allergy and Infectious Diseases Mycoses Study Group," *New England Journal of Medicine*, vol. 340, no. 10, pp. 764–771, 1999.
 - [31] J. Y. Lu, D. A. Lowe, M. D. Kennedy, and P. S. Low, "Folate-targeted enzyme prodrug cancer therapy utilizing penicillin-V amidase and a doxorubicin prodrug," *Journal of Drug Targeting*, vol. 7, no. 1, pp. 43–53, 1999.
 - [32] Y. Lu and P. S. Low, "Folate targeting of haptens to cancer cell surfaces mediates immunotherapy of syngeneic murine tumors," *Cancer Immunology, Immunotherapy*, vol. 51, no. 3, pp. 153–162, 2002.
 - [33] H. S. Yoo and T. G. Park, "Folate receptor targeted biodegradable polymeric doxorubicin micelles," *Journal of Controlled Release*, vol. 96, no. 2, pp. 273–283, 2004.
 - [34] J. Cummings and C. S. McArdle, "Studies on the in vivo disposition of adriamycin in human tumours which exhibit different responses to the drug," *British Journal of Cancer*, vol. 53, no. 6, pp. 835–838, 1986.
 - [35] D. Goren, A. T. Horowitz, D. Tzemach, M. Tarshish, S. Zalipsky, and A. Gabizon, "Nuclear delivery of doxorubicin via folate-targeted liposomes with bypass of multidrug-resistance efflux pump," *Clinical Cancer Research*, vol. 6, no. 5, pp. 1949–1957, 2000.
 - [36] S. D. Weitman, A. G. Weinberg, L. R. Coney, V. R. Zurawski, D. S. Jennings, and B. A. Kamen, "Cellular localization of the folate receptor: potential role in drug toxicity and folate homeostasis," *Cancer Research*, vol. 52, no. 23, pp. 6708–6711, 1992.
 - [37] J. A. Reddy and P. S. Low, "Enhanced folate receptor mediated gene therapy using a novel pH-sensitive lipid formulation," *Journal of Controlled Release*, vol. 64, no. 1–3, pp. 27–37, 2000.
 - [38] S. Wang, R. J. Lee, G. Cauchon, D. G. Gorenstein, and P. S. Low, "Delivery of antisense oligodeoxynucleotides against the human epidermal growth factor receptor into cultured KB cells with liposomes conjugated to folate via

- polyethylene glycol," *Proceedings of the National Academy of Sciences of the United States of America*, vol. 92, no. 8, pp. 3318–3322, 1995.
- [39] H. S. Yoo, J. E. Oh, K. H. Lee, and T. G. Park, "Biodegradable nanoparticles containing doxorubicin-PLGA conjugate for sustained release," *Pharmaceutical Research*, vol. 16, no. 7, pp. 1114–1118, 1999.
- [40] H. S. Yoo and T. G. Park, "Biodegradable polymeric micelles composed of doxorubicin conjugated PLGA-PEG block copolymer," *Journal of Controlled Release*, vol. 70, no. 1-2, pp. 63–70, 2001.
- [41] G. S. Kwon and K. Kataoka, "Block copolymer micelles as long-circulating drug vehicles," *Advanced Drug Delivery Reviews*, vol. 16, no. 2-3, pp. 295–309, 1995.
- [42] G. Kwon, M. Naito, M. Yokoyama, T. Okano, Y. Sakurai, and K. Kataoka, "Block copolymer micelles for drug delivery: loading and release of doxorubicin," *Journal of Controlled Release*, vol. 48, no. 2-3, pp. 195–201, 1997.
- [43] G. Kwon, S. Suwa, M. Yokoyama, T. Okano, Y. Sakurai, and K. Kataoka, "Enhanced tumor accumulation and prolonged circulation times of micelle-forming poly(ethylene oxide-aspartate) block copolymer-adriamycin conjugates," *Journal of Controlled Release*, vol. 29, no. 1-2, pp. 17–23, 1994.
- [44] G. S. Kwon, M. Yokoyama, T. Okano, Y. Sakurai, and K. Kataoka, "Biodistribution of micelle-forming polymer-drug conjugates," *Pharmaceutical Research*, vol. 10, no. 7, pp. 970–974, 1993.
- [45] Y.-P. Li, Y.-Y. Pei, X.-Y. Zhang et al., "PEGylated PLGA nanoparticles as protein carriers: synthesis, preparation and biodistribution in rats," *Journal of Controlled Release*, vol. 71, no. 2, pp. 203–211, 2001.
- [46] G. F. Joyce, "Amplification, mutation and selection of catalytic RNA," *Gene*, vol. 82, no. 1, pp. 83–87, 1989.
- [47] S. D. Jayasena, "Aptamers: an emerging class of molecules that rival antibodies in diagnostics," *Clinical Chemistry*, vol. 45, no. 9, pp. 1628–1650, 1999.
- [48] S. Tombelli, M. Minunni, E. Luzi, and M. Mascini, "Aptamer-based biosensors for the detection of HIV-1 Tat protein," *Bioelectrochemistry*, vol. 67, no. 2, pp. 135–141, 2005.
- [49] T. Mairal, V. C. Özalp, P. Lozano Sánchez, M. Mir, I. Katakis, and C. K. O'Sullivan, "Aptamers: molecular tools for analytical applications," *Analytical and Bioanalytical Chemistry*, vol. 390, no. 4, pp. 989–1007, 2008.
- [50] R. Nutiu and Y. Li, "Structure-switching signaling aptamers: transducing molecular recognition into fluorescence signaling," *Chemistry*, vol. 10, no. 8, pp. 1868–1876, 2004.
- [51] P. C. Hoffman, A. M. Mauer, and E. E. Vokes, "Lung cancer," *Lancet*, vol. 355, no. 9202, pp. 479–485, 2000.
- [52] J. L. Mulshine and D. C. Sullivan, "Lung cancer screening," *New England Journal of Medicine*, vol. 352, no. 26, pp. 2714–2720, 2005.
- [53] J. E. Smith, C. D. Medley, Z. Tang, D. Shangguan, C. Lofton, and W. Tan, "Aptamer-conjugated nanoparticles for the collection and detection of multiple cancer cells," *Analytical Chemistry*, vol. 79, no. 8, pp. 3075–3082, 2007.
- [54] X. Zhao, L. R. Hilliard, S. J. Mechery et al., "A rapid bioassay for single bacterial cell quantitation using bioconjugated nanoparticles," *Proceedings of the National Academy of Sciences of the United States of America*, vol. 101, no. 42, pp. 15027–15032, 2004.
- [55] X. Zhao, R. Tapeç-Dytioco, and W. Tan, "Ultrasensitive DNA detection using highly fluorescent bioconjugated nanoparticles," *Journal of the American Chemical Society*, vol. 125, no. 38, pp. 11474–11475, 2003.
- [56] X. Zhao, R. P. Bagwe, and W. Tan, "Development of organic-dye-doped silica nanoparticles in a reverse microemulsion," *Advanced Materials*, vol. 16, no. 2, pp. 173–176, 2004.
- [57] J. K. Herr, J. E. Smith, C. D. Medley, D. Shangguan, and W. Tan, "Aptamer-conjugated nanoparticles for selective collection and detection of cancer cells," *Analytical Chemistry*, vol. 78, no. 9, pp. 2918–2924, 2006.
- [58] H. W. Chen, C. D. Medley, K. Sefah et al., "Molecular recognition of small-cell lung cancer cells using aptamers," *ChemMedChem*, vol. 3, no. 6, pp. 991–1001, 2008.
- [59] D. J. Javier, N. Nitin, M. Levy, A. Ellington, and R. Richards-Kortum, "Aptamer-targeted gold nanoparticles as molecular-specific contrast agents for reflectance imaging," *Bioconjugate Chemistry*, vol. 19, no. 6, pp. 1309–1312, 2008.
- [60] C.-C. Huang, S.-H. Chiu, Y.-F. Huang, and H.-T. Chang, "Aptamer-functionalized gold nanoparticles for turn-on light switch detection of platelet-derived growth factor," *Analytical Chemistry*, vol. 79, no. 13, pp. 4798–4804, 2007.
- [61] O. C. Farokhzad, J. Cheng, B. A. Tepley et al., "Targeted nanoparticle-aptamer bioconjugates for cancer chemotherapy in vivo," *Proceedings of the National Academy of Sciences of the United States of America*, vol. 103, no. 16, pp. 6315–6320, 2006.
- [62] O. C. Farokhzad, S. Jon, A. Khademhosseini, T.-N. T. Tran, D. A. LaVan, and R. Langer, "Nanoparticle-aptamer bioconjugates: a new approach for targeting prostate cancer cells," *Cancer Research*, vol. 64, no. 21, pp. 7668–7672, 2004.
- [63] O. C. Farokhzad, A. Khademhosseini, S. Jon et al., "Microfluidic system for studying the interaction of nanoparticles and microparticles with cells," *Analytical Chemistry*, vol. 77, no. 17, pp. 5453–5459, 2005.
- [64] S. Dhar, F. X. Gu, R. Langer, O. C. Farokhza, and S. J. Lippard, "Targeted delivery of cisplatin to prostate cancer cells by aptamer functionalized Pt(IV) prodrug-PLGA-PEG nanoparticles," *Proceedings of the National Academy of Sciences of the United States of America*, vol. 105, no. 45, pp. 17356–17361, 2008.
- [65] Y. Wu, K. Sefah, H. Liu, R. Wang, and W. Tan, "DNA aptamer-micelle as an efficient detection/delivery vehicle toward cancer cells," *Proceedings of the National Academy of Sciences of the United States of America*, vol. 107, no. 1, pp. 5–10, 2010.
- [66] C. Walsh, "Molecular mechanisms that confer antibacterial drug resistance," *Nature*, vol. 406, no. 6797, pp. 775–781, 2000.
- [67] D. Hanahan, G. Bergers, and E. Bergsland, "Less is, more, regularly: metronomic dosing of cytotoxic drugs can target tumor angiogenesis in mice," *Journal of Clinical Investigation*, vol. 105, no. 8, pp. 1045–1047, 2000.
- [68] H. Joensuu, K. Holli, M. Heikkinen et al., "Combination chemotherapy versus single-agent therapy as first- and second-line treatment in metastatic breast cancer: a prospective randomized trial," *Journal of Clinical Oncology*, vol. 16, no. 12, pp. 3720–3730, 1998.
- [69] Y. Wang, S. Gao, W.-H. Ye, H. S. Yoon, and Y.-Y. Yang, "Co-delivery of drugs and DNA from cationic core-shell nanoparticles self-assembled from a biodegradable copolymer," *Nature Materials*, vol. 5, no. 10, pp. 791–796, 2006.
- [70] Y. Wang, L.-S. Wang, S.-H. Goh, and Y.-Y. Yang, "Synthesis and characterization of cationic micelles self-assembled from a biodegradable copolymer for gene delivery," *Biomacromolecules*, vol. 8, no. 3, pp. 1028–1037, 2007.
- [71] N. Wiradharma, Y. W. Tong, and Y.-Y. Yang, "Self-assembled oligopeptide nanostructures for co-delivery of drug and gene

- with synergistic therapeutic effect," *Biomaterials*, vol. 30, no. 17, pp. 3100–3109, 2009.
- [72] L. Cerchia, P. H. Giangrande, J. O. McNamara, and V. de Franciscis, "Cell-specific aptamers for targeted therapies," *Methods in Molecular Biology*, vol. 535, pp. 59–78, 2009.
- [73] T. C. Chu, K. Y. Twu, A. D. Ellington, and M. Levy, "Aptamer mediated siRNA delivery," *Nucleic Acids Research*, vol. 34, no. 10, article e73, 2006.
- [74] J. O. McNamara II, E. R. Andrechek, Y. Wang et al., "Cell type-specific delivery of siRNAs with aptamer-siRNA chimeras," *Nature Biotechnology*, vol. 24, no. 8, pp. 1005–1015, 2006.
- [75] E. Kim, Y. Jung, H. Choi et al., "Prostate cancer cell death produced by the co-delivery of Bcl-xL shRNA and doxorubicin using an aptamer-conjugated polyplex," *Biomaterials*, vol. 31, no. 16, pp. 4592–4599, 2010.
- [76] Y. Bae, S. Fukushima, A. Harada, and K. Kataoka, "Design of environment-sensitive supramolecular assemblies for intracellular drug delivery: polymeric micelles that are responsive to intracellular pH change," *Angewandte Chemie. International Edition*, vol. 42, no. 38, pp. 4640–4643, 2003.
- [77] G. Helmlinger, A. Sckell, M. Dellian, N. S. Forbes, and R. K. Jain, "Acid production in glycolysis-impaired tumors provides new insights into tumor metabolism," *Clinical Cancer Research*, vol. 8, no. 4, pp. 1284–1291, 2002.
- [78] Y. Matsumura and H. Maeda, "A new concept for macromolecular therapeutics in cancer chemotherapy: mechanism of tumorotropic accumulation of proteins and the antitumor agent smancs," *Cancer Research*, vol. 46, no. 12, part 1, pp. 6387–6392, 1986.
- [79] K. Kataoka, G. S. Kwon, M. Yokoyama, T. Okano, and Y. Sakurai, "Block copolymer micelles as vehicles for drug delivery," *Journal of Controlled Release*, vol. 24, no. 1–3, pp. 119–132, 1993.
- [80] G. S. Kwon and T. Okano, "Polymeric micelles as new drug carriers," *Advanced Drug Delivery Reviews*, vol. 21, no. 2, pp. 107–116, 1996.
- [81] G. S. Kwon, M. Naito, M. Yokoyama, T. Okano, Y. Sakurai, and K. Kataoka, "Physical entrapment of adriamycin in AB block copolymer micelles," *Pharmaceutical Research*, vol. 12, no. 2, pp. 192–195, 1995.
- [82] H. S. Yoo, E. A. Lee, and T. G. Park, "Doxorubicin-conjugated biodegradable polymeric micelles having acid-cleavable linkages," *Journal of Controlled Release*, vol. 82, no. 1, pp. 17–27, 2002.
- [83] H. S. Yoo, K. H. Lee, J. E. Oh, and T. G. Park, "In vitro and in vivo anti-tumor activities of nanoparticles based on doxorubicin-PLGA conjugates," *Journal of Controlled Release*, vol. 68, no. 3, pp. 419–431, 2000.
- [84] T. M. Allen, "Liposomal drug formulations: rationale for development and what we can expect for the future," *Drugs*, vol. 56, no. 5, pp. 747–756, 1998.
- [85] D. Momekova, S. Rangelov, S. Yanev et al., "Long-circulating, pH-sensitive liposomes sterically stabilized by copolymers bearing short blocks of lipid-mimetic units," *European Journal of Pharmaceutical Sciences*, vol. 32, no. 4–5, pp. 308–317, 2007.
- [86] M. C. Woodle, "Sterically stabilized liposome therapeutics," *Advanced Drug Delivery Reviews*, vol. 16, no. 2–3, pp. 249–265, 1995.
- [87] S. Zalipsky, "Chemistry of polyethylene glycol conjugates with biologically," *Advanced Drug Delivery Reviews*, vol. 16, no. 2–3, pp. 157–182, 1995.
- [88] A. Gabizon and D. Papahadjopoulos, "Liposome formulations with prolonged circulation time in blood and enhanced uptake by tumors," *Proceedings of the National Academy of Sciences of the United States of America*, vol. 85, no. 18, pp. 6949–6953, 1988.
- [89] M. Hrubý, C. Koňák, and K. Ulbrich, "Polymeric micellar pH-sensitive drug delivery system for doxorubicin," *Journal of Controlled Release*, vol. 103, no. 1, pp. 137–148, 2005.
- [90] M.-S. Hong, S.-J. Lim, Y.-K. Oh, and C.-K. Kim, "pH-sensitive, serum-stable and long-circulating liposomes as a new drug delivery system," *Journal of Pharmacy and Pharmacology*, vol. 54, no. 1, pp. 51–58, 2002.
- [91] S. Simões, J. N. Moreira, C. Fonseca, N. Düzgüneş, and M. C. P. de Lima, "On the formulation of pH-sensitive liposomes with long circulation times," *Advanced Drug Delivery Reviews*, vol. 56, no. 7, pp. 947–965, 2004.
- [92] Y. Bae, W.-D. Jang, N. Nishiyama, S. Fukushima, and K. Kataoka, "Multifunctional polymeric micelles with folate-mediated cancer cell targeting and pH-triggered drug releasing properties for active intracellular drug delivery," *Molecular BioSystems*, vol. 1, no. 3, pp. 242–250, 2005.
- [93] Y. Bae and K. Kataoka, "Significant enhancement of antitumor activity and bioavailability of intracellular pH-sensitive polymeric micelles by folate conjugation," *Journal of Controlled Release*, vol. 116, no. 2, pp. e49–e50, 2006.
- [94] Y. Bae, N. Nishiyama, S. Fukushima, H. Koyama, M. Yasuhiro, and K. Kataoka, "Preparation and biological characterization of polymeric micelle drug carriers with intracellular pH-triggered drug release property: tumor permeability, controlled subcellular drug distribution, and enhanced in vivo antitumor efficacy," *Bioconjugate Chemistry*, vol. 16, no. 1, pp. 122–130, 2005.
- [95] Y. Bae, N. Nishiyama, and K. Kataoka, "In vivo antitumor activity of the folate-conjugated pH-sensitive polymeric micelle selectively releasing adriamycin in the intracellular acidic compartments," *Bioconjugate Chemistry*, vol. 18, no. 4, pp. 1131–1139, 2007.
- [96] G. Shi, W. Guo, S. M. Stephenson, and R. J. Lee, "Efficient intracellular drug and gene delivery using folate receptor-targeted pH-sensitive liposomes composed of cationic/anionic lipid combinations," *Journal of Controlled Release*, vol. 80, no. 1–3, pp. 309–319, 2002.
- [97] J. J. Sudimack, W. Guo, W. Tjarks, and R. J. Lee, "A novel pH-sensitive liposome formulation containing oleyl alcohol," *Biochimica et Biophysica Acta*, vol. 1564, no. 1, pp. 31–37, 2002.
- [98] T. Ishida, M. J. Kirchmeier, E. H. Moase, S. Zalipsky, and T. M. Allen, "Targeted delivery and triggered release of liposomal doxorubicin enhances cytotoxicity against human B lymphoma cells," *Biochimica et Biophysica Acta*, vol. 1515, no. 2, pp. 144–158, 2001.
- [99] Y. Li and G. S. Kwon, "Methotrexate esters of poly(ethylene oxide)-block-poly(2-hydroxyethyl-L- aspartamide). Part I: effects of the level of methotrexate conjugation on the stability of micelles and on drug release," *Pharmaceutical Research*, vol. 17, no. 5, pp. 607–611, 2000.
- [100] M. G. Rimoli, L. Avallone, P. de Caprariis, A. Galeone, F. Forni, and M. A. Vandelli, "Synthesis and characterisation of poly(D,L-lactic acid)-idoxuridine conjugate," *Journal of Controlled Release*, vol. 58, no. 1, pp. 61–68, 1999.
- [101] M. Zaccagna, G. Di Luca, F. Cateni, S. Zorzet, and V. Maurich, "Improvement of physicochemical and biopharmaceutical properties of theophylline by poly(ethylene glycol) conjugates," *Farmaco*, vol. 58, no. 12, pp. 1307–1312, 2003.

- [102] K. Hoste, K. de Winne, and E. Schacht, "Polymeric prodrugs," *International Journal of Pharmaceutics*, vol. 277, no. 1-2, pp. 119-131, 2004.
- [103] E. Mastrobattista, G. A. Koning, L. van Bloois, A. C. S. Filipe, W. Jiskoot, and G. Storm, "Functional characterization of an endosome-disruptive peptide and its application in cytosolic delivery of immunoliposome-entrapped proteins," *Journal of Biological Chemistry*, vol. 277, no. 30, pp. 27135-27143, 2002.
- [104] C. J. Provoda, E. M. Stier, and K.-D. Lee, "Tumor cell killing enabled by listeriolysin O-liposome-mediated delivery of the protein toxin gelonin," *Journal of Biological Chemistry*, vol. 278, no. 37, pp. 35102-35108, 2003.
- [105] R. Ishiguro, M. Matsumoto, and S. Takahashi, "Interaction of fusogenic synthetic peptide with phospholipid bilayers: orientation of the peptide α -helix and binding isotherm," *Biochemistry*, vol. 35, no. 15, pp. 4976-4983, 1996.
- [106] S. Nir, F. Nicol, and F. C. Szoka Jr., "Surface aggregation and membrane penetration by peptides: relation to pore formation and fusion," *Molecular Membrane Biology*, vol. 16, no. 1, pp. 95-101, 1999.
- [107] J.-C. Leroux, E. Roux, D. Le Garrec, K. Hong, and D. C. Drummond, "N-isopropylacrylamide copolymers for the preparation of pH-sensitive liposomes and polymeric micelles," *Journal of Controlled Release*, vol. 72, no. 1-3, pp. 71-84, 2001.
- [108] T. Mizoue, T. Horibe, K. Maruyama et al., "Targetability and intracellular delivery of anti-BCG antibody-modified, pH-sensitive fusogenic immunoliposomes to tumor cells," *International Journal of Pharmaceutics*, vol. 237, no. 1-2, pp. 129-137, 2002.
- [109] V. P. Torchilin, F. Zhou, and L. Huang, "pH-Sensitive liposomes," *Journal of Liposome Research*, vol. 3, no. 2, pp. 201-255, 1993.
- [110] D. D. Lasic, "Novel applications of liposomes," *Trends in Biotechnology*, vol. 16, no. 7, pp. 307-321, 1998.
- [111] C.-J. Chu, J. Dijkstra, M.-Z. Lai, K. Hong, and F. C. Szoka, "Efficiency of cytoplasmic delivery by pH-sensitive liposomes to cells in culture," *Pharmaceutical Research*, vol. 7, no. 8, pp. 824-834, 1990.
- [112] V. A. Slepishkin, S. Simões, P. Dazin et al., "Sterically stabilized pH-sensitive liposomes. Intracellular delivery of aqueous contents and prolonged circulation in vivo," *Journal of Biological Chemistry*, vol. 272, no. 4, pp. 2382-2388, 1997.
- [113] M. B. Yatvin, J. N. Weinstein, W. H. Dennis, and R. Blumenthal, "Design of liposomes for enhanced local release of drugs by hyperthermia," *Science*, vol. 202, no. 4374, pp. 1290-1293, 1978.
- [114] J. van der Zee, D. González González, G. C. Van Rhoon, J. D. P. Van Dijk, W. L. J. Van Putten, and A. A. M. Hart, "Comparison of radiotherapy alone with radiotherapy plus hyperthermia in locally advanced pelvic tumours: a prospective, randomised, multicentre trial," *Lancet*, vol. 355, no. 9210, pp. 1119-1125, 2000.
- [115] R. D. Issels, L. H. Lindner, P. Wust et al., "Regional hyperthermia (RHT) improves response and survival when combined with systemic chemotherapy in the management of locally advanced, high grade soft tissue sarcomas (STS) of the extremities, the body wall and the abdomen: a phase III randomised prospective trial (EORTC-ESHO intergroup trial)," in *Proceedings of the 43rd Annual Meeting of ASCO*, Chicago, Ill, USA, 2007.
- [116] G. Crile Jr., "Selective destruction of cancers after exposure to heat," *Annals of surgery*, vol. 156, pp. 404-407, 1962.
- [117] G. Kong, R. D. Braun, and M. W. Dewhirst, "Characterization of the effect of hyperthermia on nanoparticle extravasation from tumor vasculature," *Cancer Research*, vol. 61, no. 7, pp. 3027-3032, 2001.
- [118] M. H. Gaber, N. Z. Wu, K. Hong, S. K. Huang, M. W. Dewhirst, and D. Papahadjopoulos, "Thermosensitive liposomes: extravasation and release of contents in tumor microvascular networks," *International Journal of Radiation Oncology Biology Physics*, vol. 36, no. 5, pp. 1177-1187, 1996.
- [119] G. Kong, R. D. Braun, and M. W. Dewhirst, "Hyperthermia enables tumor-specific nanoparticle delivery: effect of particle size," *Cancer Research*, vol. 60, no. 16, pp. 4440-4445, 2000.
- [120] L. Huang, K. Ozato, and R. E. Pagano, "Interactions of phospholipid vesicles with murine lymphocytes. I. Vesicle-cell adsorption and fusion as alternate pathways of uptake," *Membrane Biochemistry*, vol. 1, no. 1-2, pp. 1-25, 1978.
- [121] L. F. Fajardo and S. D. Prionas, "Endothelial cells and hyperthermia," *International Journal of Hyperthermia*, vol. 10, no. 3, pp. 347-353, 1994.
- [122] D. Papahadjopoulos, K. Jacobson, S. Nir, and T. Isac, "Phase transitions in phospholipid vesicles. Fluorescence polarization and permeability measurements concerning the effect of temperature and cholesterol," *Biochimica et Biophysica Acta*, vol. 311, no. 3, pp. 330-348, 1973.
- [123] T. Y. Tsong, "Kinetics of the crystalline liquid crystalline phase transition of dimyristoyl α lecithin bilayers," *Proceedings of the National Academy of Sciences of the United States of America*, vol. 71, no. 7, pp. 2684-2688, 1974.
- [124] T. M. Allen, C. Hansen, F. Martin, C. Redemann, and A. F. Yau-Young, "Liposomes containing synthetic lipid derivatives of poly(ethylene glycol) show prolonged circulation half-lives in vivo," *Biochimica et Biophysica Acta*, vol. 1066, no. 1, pp. 29-36, 1991.
- [125] H. Yoshioka, "Surface modification of haemoglobin-containing liposomes with polyethylene glycol prevents liposome aggregation in blood plasma," *Biomaterials*, vol. 12, no. 9, pp. 861-864, 1991.
- [126] A. R. Nicholas, M. J. Scott, N. I. Kennedy, and M. N. Jones, "Effect of grafted polyethylene glycol (PEG) on the size, encapsulation efficiency and permeability of vesicles," *Biochimica et Biophysica Acta*, vol. 1463, no. 1, pp. 167-178, 2000.
- [127] A. K. Kenworthy, K. Hristova, D. Needham, and T. J. McIntosh, "Range and magnitude of the steric pressure between bilayers containing phospholipids with covalently attached poly(ethylene glycol)," *Biophysical Journal*, vol. 68, no. 5, pp. 1921-1936, 1995.
- [128] S. Mabrey and J. M. Sturtevant, "Investigation of phase transitions of lipids and lipid mixtures by high sensitivity differential scanning calorimetry," *Proceedings of the National Academy of Sciences of the United States of America*, vol. 73, no. 11, pp. 3862-3866, 1976.
- [129] M. Hossann, M. Wiggerhorn, A. Schwerdt et al., "In vitro stability and content release properties of phosphatidylglycerol containing thermosensitive liposomes," *Biochimica et Biophysica Acta*, vol. 1768, no. 10, pp. 2491-2499, 2007.
- [130] D. Needham, D. G. Anyarambhatla, G. Kong, and M. W. Dewhirst, "A new temperature-sensitive liposome for use with mild hyperthermia: characterization and testing in a human tumor xenograft model," *Cancer Research*, vol. 60, no. 5, pp. 1197-1201, 2000.

- [131] D. Needham, G. Anyarambhatla, G. Kong, and M. W. Dewhirst, "A new temperature-sensitive liposome for use with mild hyperthermia: characterization and testing in a human tumor xenograft model," *Cancer Research*, vol. 60, no. 5, pp. 1197–1201, 2000.
- [132] L. H. Lindner, M. E. Eichhorn, H. Eibl et al., "Novel temperature-sensitive liposomes with prolonged circulation time," *Clinical Cancer Research*, vol. 10, no. 6, pp. 2168–2178, 2004.
- [133] G. Kong, G. Anyarambhatla, W. P. Petros et al., "Efficacy of liposomes and hyperthermia in a human tumor xenograft model: importance of triggered drug release," *Cancer Research*, vol. 60, no. 24, pp. 6950–6957, 2000.
- [134] M. L. Hauck, S. M. La Rue, W. P. Petros et al., "Phase I trial of doxorubicin-containing low temperature sensitive liposomes in spontaneous canine tumors," *Clinical Cancer Research*, vol. 12, no. 13, pp. 4004–4010, 2006.
- [135] O. Soga, C. F. van Nostrum, A. Ramzi et al., "Physicochemical characterization of degradable thermosensitive polymeric micelles," *Langmuir*, vol. 20, no. 21, pp. 9388–9395, 2004.
- [136] D. Neradovic, C. F. van Nostrum, and W. E. Hennink, "Thermoresponsive polymeric micelles with controlled instability based on hydrolytically sensitive N-isopropylacrylamide copolymers," *Macromolecules*, vol. 34, no. 22, pp. 7589–7591, 2001.
- [137] O. Soga, C. F. van Nostrum, and W. E. Hennink, "Poly(N-(2-hydroxypropyl) methacrylamide mono/di lactate): a new class of biodegradable polymers with tuneable thermosensitivity," *Biomacromolecules*, vol. 5, no. 3, pp. 818–821, 2004.
- [138] C. J. F. Rijcken, T. F. J. Veldhuis, A. Ramzi, J. D. Meeldijk, C. van Nostrum, and W. E. Hennink, "Novel fast degradable thermosensitive polymeric micelles based on PEG-block-poly(N-(2-hydroxyethyl)methacrylamide-oligolactates)," *Biomacromolecules*, vol. 6, no. 4, pp. 2343–2351, 2005.
- [139] G. Molineux, "Pegylation: engineering improved pharmaceuticals for enhanced therapy," *Cancer Treatment Reviews*, vol. 28, supplement A, pp. 13–16, 2002.
- [140] O. Soga, C. F. van Nostrum, M. Fens et al., "Thermosensitive and biodegradable polymeric micelles for paclitaxel delivery," *Journal of Controlled Release*, vol. 103, no. 2, pp. 341–353, 2005.
- [141] O. Soga, *In vivo efficacy of paclitaxel-loaded thermosensitive biodegradable polymeric micelles*, M.S. thesis, Department of Pharmaceutics, Utrecht Institute for Pharmaceutical Sciences, Utrecht, The Netherlands, 2006.
- [142] C. J. Rijcken, C. J. Snel, R. M. Schiffelers, C. F. van Nostrum, and W. E. Hennink, "Hydrolysable core-crosslinked thermosensitive polymeric micelles: synthesis, characterisation and in vivo studies," *Biomaterials*, vol. 28, no. 36, pp. 5581–5593, 2007.

Research Article

Characterization of Plasmid DNA Location within Chitosan/PLGA/pDNA Nanoparticle Complexes Designed for Gene Delivery

Hali Bordelon,¹ Alexandru S. Biris,² Cristina M. Sabliov,¹ and W. Todd Monroe¹

¹ Biological and Agricultural Engineering Department, Louisiana State University Agricultural Center,
Rm. 149 E.B. Doran Bldg., Baton Rouge, LA 70803, USA

² Nanotechnology Center, Applied Science Department, University of Arkansas at Little Rock, Little Rock, AR 72211, USA

Correspondence should be addressed to W. Todd Monroe, tmonroe@lsu.edu

Received 2 June 2010; Accepted 25 July 2010

Academic Editor: Lu Sun

Copyright © 2011 Hali Bordelon et al. This is an open access article distributed under the Creative Commons Attribution License, which permits unrestricted use, distribution, and reproduction in any medium, provided the original work is properly cited.

Poly(D,L-lactide-co-glycolide-) (PLGA-)chitosan nanoparticles are becoming an increasingly common choice for the delivery of nucleic acids to cells for various genetic manipulation techniques. These particles are biocompatible, with tunable size and surface properties, possessing an overall positive charge that promotes complex formation with negatively charged nucleic acids. This study examines properties of the PLGA-chitosan nanoparticle/plasmid DNA complex after formation. Specifically, the study aims to determine the optimal ratio of plasmid DNA:nanoparticles for nucleic acid delivery purposes and to elucidate the location of the pDNA within these complexes. Such characterization will be necessary for the adoption of these formulations in a clinical setting. The ability of PLGA-chitosan nanoparticles to form complexes with pDNA was evaluated by using the fluorescent intercalating dye OliGreen to label free plasmid DNA. By monitoring the fluorescence at different plasmid: nanoparticle ratios, the ideal plasmid:nanoparticle ration for complete complexation of plasmid was determined to be 1:50. Surface-Enhanced Raman Spectroscopy and gel digest studies suggested that even at these optimal complexation ratios, a portion of the plasmid DNA was located on the outer complex surface. This knowledge will facilitate future investigations into the functionality of the system *in vitro* and *in vivo*.

1. Introduction

Successful gene delivery and expression remains a significant hurdle that must be overcome before genetic therapies gain clinical acceptance. As such, there is currently much emphasis on further developing nucleic acid delivery systems, which can be classified into three categories: physical injection, viral vectors, and nonviral vectors [1]. Direct injection of genetic material is locally effective in tissues such as skin and muscle, but it can be invasive for more interior tissues, and it requires significant involvement of medical personnel during clinical administration [2]. Viral vectors have been effective in gene delivery, but significant immunological effects in patients have severely hampered their use [1–3]. Nonviral vectors include liposomes, lipid reagents, and polymeric nanoparticles (NPs). Because of their biocompatibility and ability to reach more interior

target tissues, these delivery systems have the potential to circumvent the issues surrounding both direct injection and viral vectors [1, 2, 4–6]. Polymeric NPs have an advantage over both liposomes and lipid reagents because of their ease of manipulation, control over DNA release profiles, and biological stability *in vivo* [7]. In addition, the properties of these NPs can be easily modified, for example, by addition of functional polymer groups to increase uptake or improve release of cargo genetic material [4, 5, 8].

One of the major drawbacks to gene encapsulation in synthetic polymers for delivery using bottom-up techniques is the incorporation of plasmid DNA (pDNA) into the particles during the synthesis phase. The encapsulation method requires the pDNA to be in contact with organic solvents, decreasing the chance for successful cellular delivery [9]. Of the polymeric NPs, delivery systems based on chemically modified cationic polymers have proven to be most effective

[7, 10–12]. Kumar et al. developed cationically modified PLGA NPs which were designed to bind to pDNA post-synthesis in an attempt to reduce its degradation prior to delivery. In their study, a PVA-chitosan blend was used to stabilize PLGA NPs and to provide a positively charged surface for pDNA association [13, 14]. Many reports have emphasized the use of the cationic polysaccharide chitosan to readily complex with negatively charged pDNA [10, 15–17]. Kasturi et al. found that pDNA encapsulated within PLGA leads to significant confinement of the complexes within endolysosomes, yet the application of chitosan to the surface of the NPs was projected to improve pDNA-NP release from the endolysosomes and offer a more protected path through the cytoplasm to the nucleus [18].

There are several reports on various aspects of chitosan-PLGA NPs for pDNA delivery, focusing on preparation methods, the final characteristics of synthesized NPs, and their behavior *in vivo* (i.e., cytotoxicity and transfection efficiency) [15–17, 19–21]. The ability of NPs to limit nuclease degradation of encapsulated pDNA has also been well documented [4, 21–23]. There is a gap in information regarding particle characteristics and their effect on DNA binding which has been addressed only recently [24–26]. Surface images have been captured by scanning probe microscopy, a newer technique applied to this topic, yet are only capable of verifying morphology of the occurring particle-DNA complexes and not the degree of DNA encapsulation [24]. Studies have demonstrated that modification of particle characteristics such as particle size and overall surface charge can directly affect the amount and avidity of nucleic acid binding [27]. Variations in chitosan type and content, PLGA type, and particle preparation methods (i.e., centrifugation, freeze-drying) have been used to change these NP characteristics and have been shown to directly affect the binding efficiencies of the particles to nucleic acids such as antisense DNA oligonucleotides [24, 25] and small interfering RNAs [26]. Good manufacturing practices in pharmaceutical development require a thorough characterization of polymeric nanoparticles both before and after drug loading. The biological and chemical characteristics of nanoparticles can be altered by nucleic acid binding and must be completely understood before these delivery systems can be useful clinically [28]. Despite recent advancements in the synthesis and characterization of polymeric nanoparticles as improved drug delivery systems, the location of DNA in the particle-DNA complexes remains unknown.

It is the intent of this study to synthesize cationic chitosan-PLGA NPs designed for pDNA delivery, to verify the physiochemical properties of the particles while exploring their effect on pDNA binding at varied ratios, and ultimately to identify the location of DNA relative to the particles in the pDNA-NP complex. Methods used to characterize the complex include dynamic light scattering (DLS), scanning electron microscopy (SEM), and gel electrophoresis complexation and digestion assays. A newer technique, Surface-Enhanced Raman Spectroscopy (SERS), was utilized to detect pDNA location within the complexes. The final aim of this study is to provide further insight

into an NP delivery system designed for plasmid DNA delivery that is completely characterized with respect to DNA location in the polymer-DNA complex. This knowledge will be necessary for development of NP-based genetic therapy formulations.

2. Materials

PLGA (Poly(DL-lactide-co-glycolide)) (50 : 50 (LA : GA), MW (40,000–75,000)) was purchased from Sigma Aldrich. PVA (Polyvinyl Alcohol) (Sigma, MW 9000–10,000) was obtained from Polysciences, Inc. Protasan chitosan chloride (>75–90 deactylate, 150–400kDa) was purchased from NovaMatrix Inc. (Norway). Ethyl Acetate HPLC/ACS grade was acquired from Fisher Scientific (Pittsburg, PA). The nanopure water (ddH₂O) used in dialysis was prepared using a Nanopure Diamond (Barnstead) water purification system. Nylon closures were purchased from Fisher Scientific (Pittsburg, PA). pAcGFP1-N1 plasmid was obtained from Clontech Corporation (Mountain View, CA). Quant-IT OliGreen ssDNA Reagent and SYBR Gold nucleic acid stain were purchased from Invitrogen Corporation (Grand Island, NY). Fluorescence measurements were performed using Plastibrand PMMA cuvettes (1.5 ml) purchased from Sigma Aldrich (St. Louis, MO) and measured using the Perkin Elmer LS 55 Luminescence Spectrometer (Waltham, MA). ReadyAgarose Mini Gels (1% Agarose, 8 wells) were purchased from Bio-Rad Laboratories (Hercules, CA). Chitosanase (*Streptomyces*) and lysozyme (chicken egg white) were purchased from EMD Biosciences (San Diego, CA), and DNase I was purchased from New England Biolabs (Ipswich, MA).

3. Methods

3.1. PLGA Nanoparticle Synthesis. An organic phase was made by dissolving 200 mg PLGA in 10 ml of ethyl acetate at room temperature, stirring for 2 hours at 400 rpm using a C25KC shaking incubator (New Brunswick Scientific, Edison, NJ). An aqueous phase was made by dissolving 100 mg PVA in 10 ml of 0.1 mM ethyl acetate water solution at 75°C for 5 min, under stirring. Following cooling, 30 mg chitosan chloride was added to the PVA solution, and the mixture was stirred for 15–30 min at 1000 rpm on the vortex mixer. The solution was allowed to degas at room temperature until clear. Following this step, 2.5 ml of organic phase was added dropwise to 10 ml aqueous phase under stirring at 14,000 rpm with the Ultra-Turrax T25 homogenizer T18 basic (Ika Works Inc., Wilmington, NC). Then, the emulsion was homogenized for extra 10 minutes and sonicated while in an ice bath for 10 min at 40% amplitude, 2 seconds on and 2 seconds off using a sonicator model CV33 (Vibracell, Sonic & Materials Inc., Denbury CT). The solvent was evaporated with a Buchi rotovap R-124 (Buchi Analytical Inc., New Castle DE) set at 30°C, under 40 psi vacuum and a nitrogen flow at 100 kpa for 10 min. A 40 μ l sample was removed and used for DLS analysis. The rest of the sample underwent purification by dialysis, followed by freeze-drying.

3.2. Purification. The sample was purified by dialysis, using 100,000 MWCO, 1.8 ml/cm dialysis tubing (Fischer Scientific, Pittsburgh, PA), against distilled water. Dialysis was run for 8 hours, changing water every 2 hours. The particle solution was removed from inside the tube and placed into borosilicate vials with trehalose (2 : 1 w/w trehalose:particles) added prior to freeze-drying.

3.3. Freeze-Drying. While freeze-dryer temperature was allowed to drop to $\sim -35^{\circ}\text{C}$, the sample was prepared by approximate particle weight volume as 4.7 mg/ml. Enough trehalose was added to empty, clean borosilicate vials to achieve a 1 : 1 or 1 : 2 trehalose-to-particle ratio. The appropriate volume of purified particle solution was added to the vial and mixed gently until trehalose was dissolved. The vials containing 1 : 2 w/w particles:trehalose mixtures were frozen at -80°C in an angled rack for 2 hours. Next, the sample vials were connected to the Labconco freeze dryer (FreeZone 2.5 Plus) and allowed to freeze-dry at -35°C for 48 hours. The obtained powder was stored under refrigerated conditions until further use.

3.4. Chi/PLGA- pDNA Complex Formation. 0.5 mg of dried NP was weighed out and combined with 0.5 ml of water. The solution was vortexed for 15 minutes at 1000 rpm. NPs and pDNA were combined in Millipore water, vortexed for 30 seconds, and allowed to complex at pDNA/NP ratios of 1 : 1, 1 : 10, 1 : 20, 1 : 50, and 1 : 100 by weight at room temperature undisturbed for 1 hour.

3.5. DNA Entrapment. To each sample, 25 μl of OliGreen (OG) fluorescent nucleic acid stain (1X concentration in water per manufacturer's recommendations) was added to complexes containing a total of 4 ng of pDNA and incubated at room temperature in a dark space for 5 minutes in a 1.5 ml cuvette. After incubation, the total volume in the cuvette was raised to 500 μl using Millipore water. The relative fluorescence was determined using 490 nm excitation and 520 nm emission wavelengths in an LS55B Luminescence Spectrophotometer. Complexes were analyzed in pDNA/NP ratios of 1 : 1, 1 : 10, 1 : 20, 1 : 50, and 1 : 100 (w/w).

3.6. Electrophoretic Mobility. Electrophoretic mobility of pDNA-NP complexes was determined by gel electrophoresis. 100 ng of pDNA (10 ng/ μl) in similar pDNA/NP ratios described previously was mixed with 4 μl of loading buffer, loaded into agarose gels (1% w/v) and run in TAE buffer at 6 V/cm for 60 minutes, followed by staining with SYBR Gold for 15 minutes and visualization on a transilluminator.

3.7. Particle Size, Size Distribution, and Zeta Potential. NPs and pDNA-NP complexes were characterized in terms of size, size distribution, and zeta potential by dynamic light scattering (DLS) using the Malvern Zetasizer Nano ZS (Malvern Instruments Inc., Southborough, MA). In all cases, a volume of 1.3 ml of each sample at a concentration of 0.3 mg/ml was placed in a polystyrene cuvette and the measurements were performed at 25°C . The viscosity and

refraction index were set equal to those specific to water. Zeta potential was measured with a disposable capillary cell with a volume of 1 ml after purification. The mean values of size and PDI were determined using a monomodal distribution.

3.8. Enzymatic Digestion Assays. DNase I was used to digest pDNA not internalized within the NP complex whereas chitosanase and lysozyme were used to digest the NP polymers. DNase I (1U) was added to free pDNA and pDNA-NP complexes (1 : 50 pDNA/NP) in the supplied DNase buffer, followed by incubation for 10 minutes at 37°C . Plasmid digestion was analyzed via electrophoresis as described above. A chitosanase/lysozyme solution was prepared by combining 80 μl chitosanase (0.25 U/mL) with 20 μl of lysozyme (100 U/mL in 50 mM sodium acetate buffer) similar to that used to degrade chitosan NPs reported by Mao et al. [22]. 5 μl of the enzyme cocktail was added to pDNA and complexes (1 : 50 pDNA/NP) and incubated at 37°C for 18 hours. Samples were analyzed for enzymatic digestion via electrophoresis as described above.

3.9. pDNA Localization Using Surface-Enhanced Raman Spectroscopy. For the SERS experiments, silver NPs of 10 to 20 nm diameter were prepared first by citrate or borohydride mediated reduction of chloroauric acid or silver nitrate, respectively, based on the following protocol. Sodium borohydride was added gradually to water followed by sodium citrate and by AgNO_3 (dropwise) under slow stirring. Polyvinyl pyrrolidone (PVP) was added to the solution, and the mixture was stirred for 30 minutes. The resulting product was a goldish yellowish solution in color. The high magnification TEM image of the silver nanoparticles (SNPs) is shown in Figure 1(a).

The pDNA-NP complex suspension was mixed in equal parts with the SNP colloidal suspension under stirring for 2 hours over ice. A few droplets of the final mixture were deposited on a glass slide for Raman analysis. The overall analysis schematic is shown in Figure 1(b). Raman scattering studies were done at room temperature with a 633 nm (1.96 eV) laser excitation with a Horiba Jobin Yvon LabRam HR800 spectrometer equipped with a charge-coupled detector and two grating systems: 600 and 1800 lines/mm. The laser beam intensity measured at the sample was kept at 10 mW, and the acquisition time was 5 seconds per sample. An Olympus microscope focused the incident beam to a spot size of $<1\ \mu\text{m}^2$, and the backscattered light was collected 180° from the direction of incidence. Raman shifts were calibrated on a silicon wafer at the $520\ \text{cm}^{-1}$ peak.

4. Results

4.1. Particle Size, Size Distribution, and Zeta Potential. Particle size analysis by DLS was completed for a range of pDNA-NP complex ratios. As shown in Figure 2(a), the size of the complexes was compared as a function of pDNA/NP ratios ranging from 0 (no DNA) to 1 (w/w). The effect of complexing NPs with pDNA binding at varied ratios produced particle sizes that increased with increasing

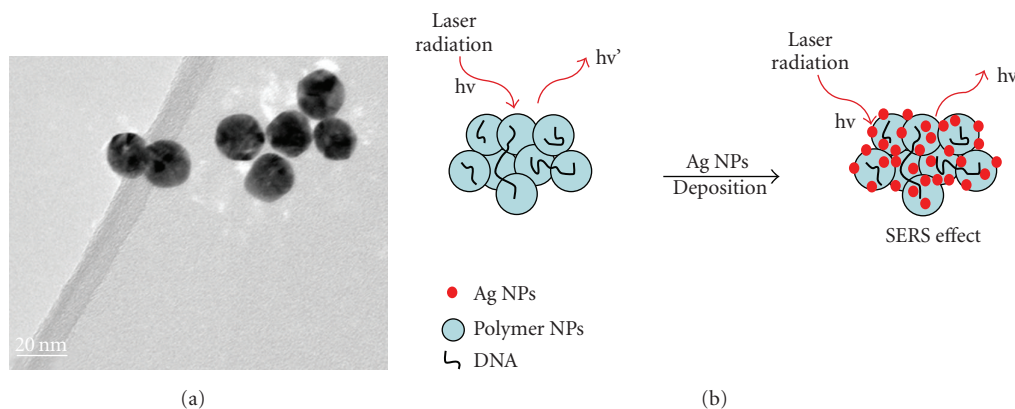


FIGURE 1: (a) High resolution TEM images of the Ag nanoparticles used for the SERS experiments. (b) The schematic of the Raman and SERS analysis of the DNA-Polymer NP mixtures.

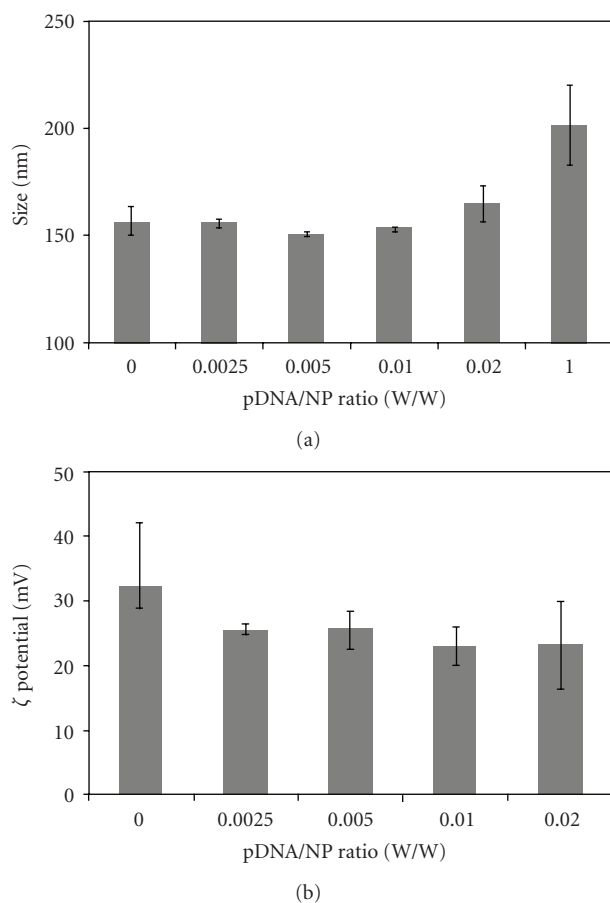


FIGURE 2: Size (a) and zeta potential (b) of pDNA-NP complexes, as a function of pDNA/NP ratios ($n = 3$; mean \pm standard error).

pDNA/NP ratio. All pDNA-NP complexes remained less than 200 nm in size for 1 : 400, 1 : 200, 1 : 100, 1 : 50, 1 : 10, and 1 : 1 w/w pDNA/NP.

Zeta potential analysis, shown in Figure 2(b), performed on the same pDNA-NP complexes indicates that the complexes were positively charged with a zeta potential higher

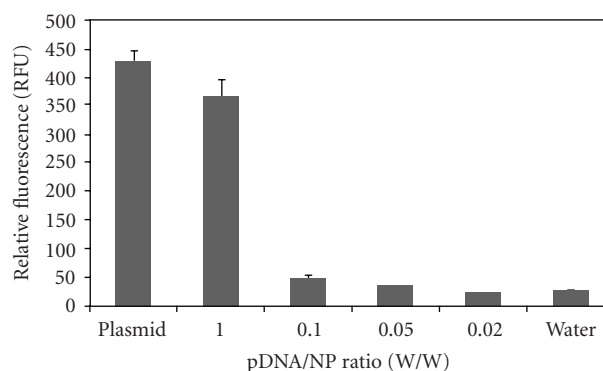


FIGURE 3: The relative fluorescence of pDNA in each sample is dependent on the quantity of NPs in each complex. Maximum fluorescence is exhibited by free pDNA. Decreasing pDNA/NP ratios yield decreasing fluorescence intensities ($n = 5$; mean \pm standard error).

than 20 mV at all ratios studied. The pDNA-NP complexes at 1 : 1 ratio were not further analyzed because their larger diameter is not practical for cell delivery and a much larger amount of material would be required for accurate zeta potential analysis. As expected, adding more negatively charged pDNA decreased the zeta potential of the DNA-NP complexes.

4.2. DNA Entrapment and Electrophoretic Mobility Studies.

The complex formation of pDNA and NPs was confirmed by fluorescence and gel electrophoresis. The relative fluorescence from the OliGreen nucleic acid stain is an indication of free, or incompletely complexed, DNA within the sample. Maximum fluorescence is exhibited by the sample that contained only free plasmid in water. As seen in Figure 3, a decrease in the pDNA/NP ratio corresponds to a decrease in fluorescence intensity. Such a decrease in fluorescence indicates that the pDNA is complexed to the point that DNA dye association and fluorescence are prevented. At a pDNA/NP ratio of 0.02, a 94% decrease in fluorescence intensity is observed compared to that of the free pDNA.

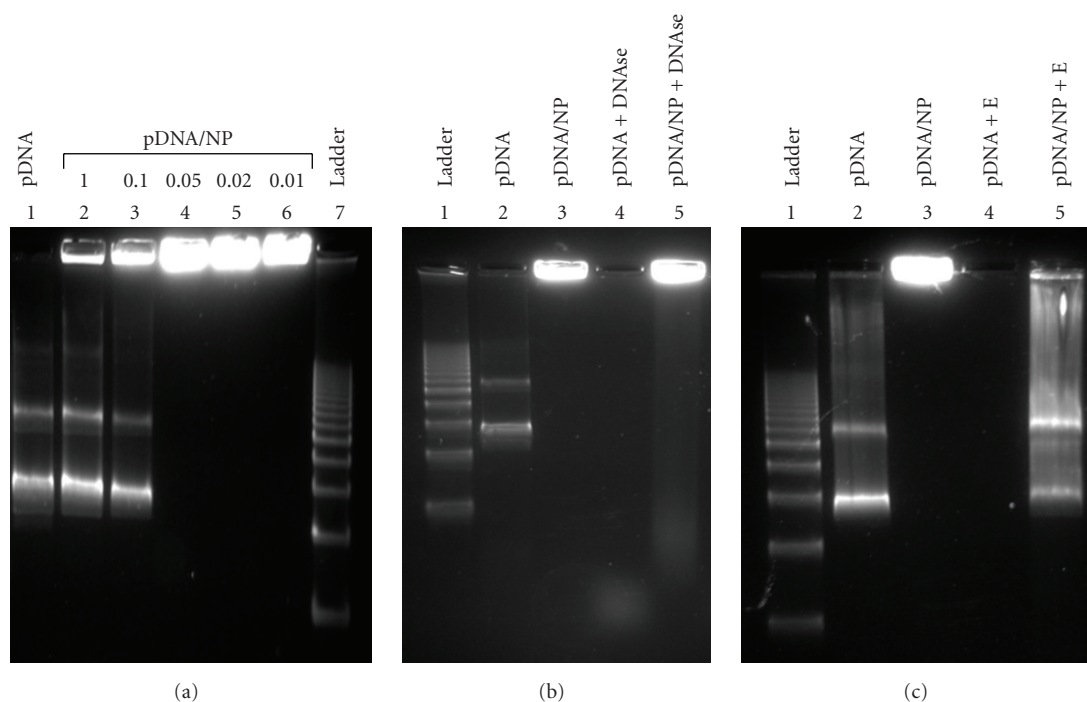


FIGURE 4: Gel analysis of complex formation and degradation. (a) Complexes formed at various ratios: lane 1: 100 ng plasmid DNA; lane 2: 1 : 1 plasmid:particle complex; lane 3: 0.1; lane 4: 0.05; lane 5: 0.02; lane 6: 0.01; lane 7: 1 kb ladder. (b) Plasmid and pDNA/NP complexes after nuclease digestion using DNase I: lane 1: 1 kb ladder; lane 2: 100 ng plasmid; lane 3: 0.02 complex; lane 4: 100 ng plasmid with DNase I; lane 5: 0.02 complex with DNase I. (c) Plasmid and pDNA/NP complexes treated with chitosanase and lysozyme: lane 1: 1 kb ladder; lane 2: 100 ng plasmid; lane 3: 0.02 plasmid:particle complex; lane 4: 100 ng plasmid with chitosanase/lysozyme; lane 5: 0.02 complex with chitosanase/lysozyme.

Comparison of this value to a negative control containing only water indicates complete complexation of all free pDNA using these synthesis and complexing methods. The complete uptake of all of the pDNA indicates the ideal ratio for protection and delivery of the entire DNA load.

Electrophoretic mobility studies further support the Oligreen fluorescence assay data, where the mobility of free plasmids is compared to that of complexes. Plasmid bands are visible in complexes in lanes 2-3 of the gel (Figure 4(a)), indicating the presence of free pDNA in the corresponding samples of 1 and 0.1 pDNA/NP ratios, similar to the bands seen in lane 1, that contain only free plasmid. No free plasmid bands are visible in subsequent lanes of pDNA/NP complexes of ratios 0.05, 0.02 and 0.01, indicating complete complexation of all free plasmid. In these samples, the only staining is visible in the gel wells, where the increased NP content retards electrophoretic mobility of the complex.

4.3. Enzymatic Degradation of pDNA and Complexes. After incubation with DNase I, gel electrophoresis confirms the degradation of free pDNA, with no bands visible except a faint band of high mobility at the bottom of the gel image (Figure 4(b), lane 4). The smeared pattern in lane 5 is an indication that some of the pDNA in the complex was available for digestion, as fragments of various sizes with higher mobility than those of undigested plasmid are visible. A lesser degree of digestion occurs for complexes, as the

smeared band does not contain fragments as small as those in lane 4. In the pDNA-NP sample exposed to DNase, there is still a large amount of remaining complexes that exhibit no electrophoretic mobility and are thus seen as bands in the gel well, suggesting protection from endonuclease digestion.

As a means to determine if the PLGA and chitosan nanoparticles could be digested to free plasmid DNA for further analysis, a mixture of chitosanase and lysozyme was used to digest these NPs as previously described in [22]. Gel electrophoresis of digestion of free pDNA with this enzyme mixture in this system reveals no visible pDNA bands, indicating plasmid degradation (Figure 4(c), lane 4). Comparison of lanes 3 and 5 indicates release of pDNA from complexes upon incubation with the enzyme mixture and suggests the ability of the complex to protect the DNA from enzymatic degradation. The combination of DNase and chitosanase/lysozyme digestions was used sequentially to digest free plasmid on the exterior of complexes, followed by digestion of the NP complexes to free encapsulated pDNA. The chitosanase/lysozyme was chosen to partially degrade the NP complexes so that entrapped pDNA could be released and analyzed. Because chitosanase is not an enzyme that these NPs would likely encounter in human tissue, it is obviously less relevant for modeling stability of these formulations *in vivo*; however this enzyme has utility in characterization studies of therapeutic formulations. In this test to treat complexes with DNase, followed by its

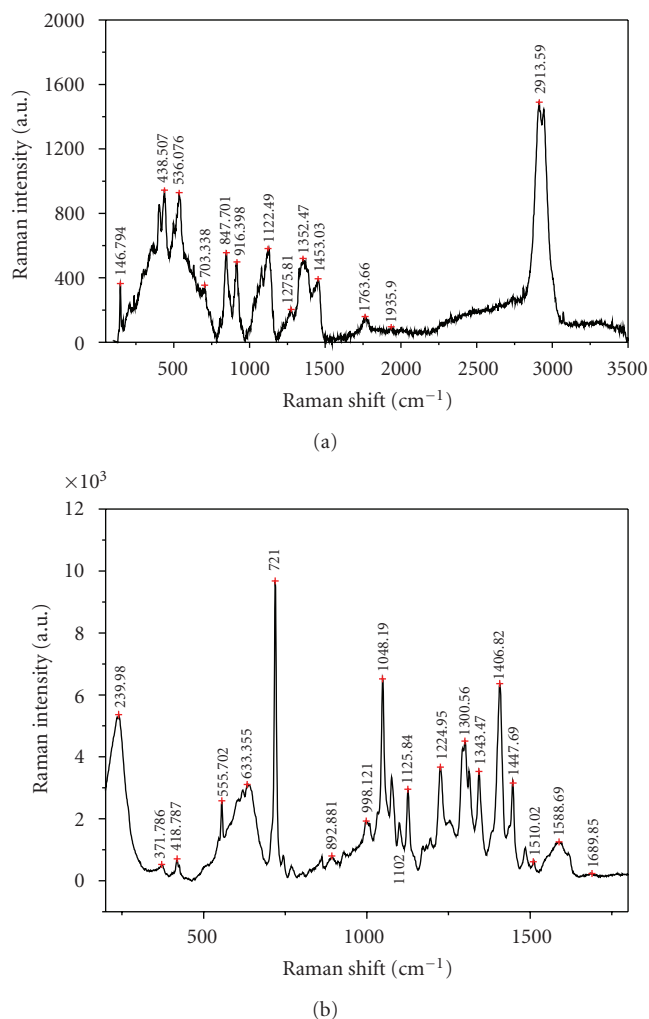


FIGURE 5: (a) Typical Raman spectrum of the pDNA/NP complexes. (b): Representative SERS spectrum of the pDNA/NP complexes conjugated PLGA NPs and decorated with silver nanoparticles (SNPs). It can be observed that the strong scattering peaks corresponding to pDNA and since the signal was mostly collected due to the SERS effect generated by the SNPs, it can be concluded that the DNA is present mostly on the surface of the PLGA NPs.

inactivation, then digestion with the chitosanase/lysozyme mixture, the result was complete digestion of the plasmid (data not shown,) suggesting either incomplete DNase inactivation or, similar to the lane 4 result, digestion of the plasmid by the chitosanase and lysozyme mixture.

4.4. Raman Spectroscopy Analysis. Raman spectroscopy is a powerful tool for the identification of various organic and biologic molecules with high specificity. One major drawback is its inability of detecting the interactions of small clusters of molecules, down to single molecule level. Organic systems, such as polymers, have strong Raman characteristic scattering features, which can overlap onto the peaks corresponding to biological molecules, like DNA, making the spectral identification and distinction between

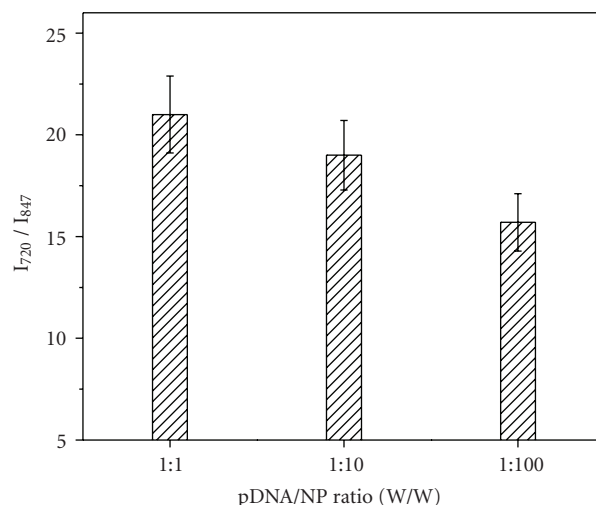


FIGURE 6: The variation of the ratio between the 720 cm^{-1} (DNA-Adenine) and 847 cm^{-1} PLGA (rCH2) peaks intensity values with the relative concentration of DNA to polymer NPs based on the SERS analysis of the complexes.

such systems difficult. A characteristic Raman spectrum of the pDNA-NP complexes is shown in Figure 5(a) and is typical to the polymeric structures (with the strongest peak features corresponding to the CH stretching modes $2900\text{--}3000\text{ cm}^{-1}$). The 847 cm^{-1} peak (rCH2) was considered as a reference band for the concentration analysis of the polymer NP relative to pDNA. Very weak peaks overimposed onto the polymer spectrum can be attributed to pDNA. Given the depth of penetration of the 633 nm laser beam into the polymeric samples, the presence of the pDNA strands onto the surface of the polymeric nanostructures is difficult to prove and quantify, since their corresponding peaks are significantly weaker as compared to those of the polymer NPs. As a result, a novel SERS-based approach was used to only acquire Raman signal from the top surface of the polymer surfaces. For this, silver nanoparticles (SNPs) were deposited onto the surfaces of the pDNA-PLGA complexes, which enabled a strong enhancement of the pDNA signal, as shown in Figure 5(b). The presence of the SNPs on the surfaces of the polymer NPs was found to be responsible for a strong SERS effect, which preferentially allowed the collection of Raman scattering signal from the surface of the pDNA-coated polymer nanostructures (the peaks corresponding to the polymer nanomaterials were highly reduced or disappeared, including the strong C-H stretching modes; not shown here). The characteristic 721 cm^{-1} peaks assigned to Adenine are easily visible, similar to that of both Raman and silver-based SERS studies on DNA [29, 30]. This approach allowed the understanding, with clear identification and probing, of the surface morphology and chemistry of the polymer NPs by indicating that while much of the pDNA is entrapped within the complexes, some of the DNA molecules are present on the outer surface. Further morphological studies will be necessary to determine the exact conformation of the exterior pDNA on outer complex

surfaces, yet it is presumed that it is not completely sterically shrouded by polymer, as some enzymatic degradation of the plasmid does still occur.

The strong SERS effect generated by the SNPs deposited onto the surface of the pDNA-NP complexes was also used to obtain relative pDNA concentration information relative to the polymer NPs as their relative concentration was varied in the following pDNA/NP ratios: 1, 0.1 and 0.01. The results are presented in Figure 6. It can be clearly observed that as the ratio pDNA/polymer decreases, the ratios between the 721 cm^{-1} (pDNA) and 847 cm^{-1} (PLGA) peaks follow a similar decreasing trend. Therefore, it can be concluded that the pDNA coverage of the NP complexes surface varied according to their relative concentrations.

5. Discussion

Complex formation between chitosan-PLGA NPs and pDNA was confirmed using both fluorescence and gel electrophoresis techniques. Significant complex formation was seen beginning in pDNA/NP ratios of 0.1 and lower. Using the fluorescent intercalating dye OliGreen, free pDNA within the complexes could be labeled and quantified relative to samples containing only free pDNA. The complexation of all pDNA was confirmed by comparison of the relative fluorescence of samples containing pDNA-NP complexes (0.02 ratio) to a pure water sample and indicates that no free pDNA is present. The lack of electrophoretic mobility of the pDNA in the complexed form further confirms complete encapsulation, as no free plasmid bands were visible in complexes with pDNA/NP ratios lesser than 0.1. These data suggest good correlation between the fluorescence staining method and the gel mobility method, both of which are relatively easy to carry out.

The protection from enzymatic digestion that NP complexes afford to pDNA was confirmed by gel electrophoresis after treatment with DNase and chitosanase/lysozyme mixtures. A standard pDNA/NP complex ratio of 0.02 was subjected to enzyme digestion and gel analysis. Partial complex dissociation was seen with treatment of chitosanase and lysozyme, where gel electrophoresis confirms that no free pDNA is present after initial complex formation. Chitosanase/lysozyme digestion degrades the nanoparticle portion of the complexes, freeing the pDNA. Gel digest studies also confirm that free pDNA is unable to sustain exposure to the concentrated chitosanase/lysozyme solution and is completely degraded. The presence of intact pDNA in the 0.02 complex sample suggests the ability of the NPs to provide protection from enzymatic degradation, an aspect important for efficient gene delivery *in vivo*.

The addition of DNase I to free pDNA was used as a control to measure the extent of free plasmid degradation. Complexes treated with the nuclease exhibit limited electrophoretic mobility, indicating that within the complex, some of the pDNA must be exposed to the introduced enzyme. Because the complex offers protection from enzymatic degradation to the pDNA within it, this data suggests that the degraded DNA is located on the outside of the complex. These results are in excellent correlation with

the SERS analysis afforded by SNPs deposited on surface of pDNA/NP complexes. Standard Raman analysis of the complexes did not enable elucidation of DNA peaks within the NP complex, yet silver-based SERS showed greatly enhanced DNA peaks and clearly indicated the presence of pDNA strands on the surface of the complexes. Such a dual approach for the surface analysis of polymeric nanoparticles complexed with various biological systems could represent a technique not limited for the study of their chemical and morphological properties but useful also for following them *in vitro* and *in vivo* as they interact with various cells and tissues. Such approaches could also prove useful in studying the delivery of the biological agents into cells via nanoparticle platforms and the release of the active therapeutics from polymeric nanosurfaces.

6. Conclusions

PLGA-chitosan NPs 150 nm in size, with a zeta potential of +34 mV, were synthesized by the proposed, optimized method. Complexing of NPs with pDNA was successful, with pDNA-NP complexes less than 200 nm in size for 0.025, 0.05, 0.01, 0.02, 0.1, and 1.0 pDNA/NP w/w ratios. All complexes were positively charged for the ratios studied ($>20\text{ mV}$). Complexes with pDNA/NP ratios of 0.02 and greater showed no electrophoretic mobility, indicating the successful uptake of all pDNA into the complex. Electrophoresis studies of the complexes after incubation with chitosanase/lysozyme indicate their ability to offer protection of the pDNA from enzymatic degradation. This characteristic is of importance for clinical adoption of these formulations, where protection of nucleic acids from enzymatic degradation in both the extracellular and intracellular spaces is critical for *in vivo* efficacy. The electrophoretic mobility of the complexes after treatment with DNase I suggests that some of the pDNA is located on the outside of the complex, and SERS data supports these findings. The decoration of the pDNA-NP complexes with SNPs allowed the use of Raman spectroscopy for the analysis of the surface-only micro environments of the samples and indicates the presence of exposed pDNA strands at the surface of the polymer NP structures. This novel nondestructive approach can be developed in highly sensitive platforms for understanding and studying the interactions between biologic and organic systems. Clarification of the location of DNA within polymeric nanoparticulate delivery systems will aid in optimizing formulations that can achieve targeted delivery with minimal degradation. These aspects will be critical for good manufacturing practices in pharmaceutical development, validation, and clinical administration of these therapeutics. Further studies are needed to evaluate the *in vitro* and *in vivo* delivery and expression of plasmids in this form of the PLGA-chitosan NP complex and whether these results correlate with the variety of physicochemical characterizations made in this study.

Acknowledgments

The authors would like to thank Anna Charron Dugas and Meocha Whaley at Louisiana State University for technical

expertise in particle synthesis. Funding was provided by the National Science Foundation (CBET-0748195) and the State of Louisiana Board of Regents Support Fund. This material is based upon work supported by an Honors College TAF grant to H. Bordelon. This paper was approved for publication by the Director of the Louisiana Agricultural Experiment Station as no. 2010-232-5138. C. M. Sabliov and W. T. Monroe contributed equally to this work.

References

- [1] S. S. Davis, "Biomedical applications of nanotechnology—implications for drug targeting and gene therapy," *Trends in Biotechnology*, vol. 15, no. 6, pp. 217–224, 1997.
- [2] T. Niidome and L. Huang, "Gene therapy progress and prospects: nonviral vectors," *Gene Therapy*, vol. 9, no. 24, pp. 1647–1652, 2002.
- [3] E. J. Simon, "Human gene therapy: genes without frontiers?" *American Biology Teacher*, vol. 64, no. 4, pp. 264–270, 2002.
- [4] J. Zhu, A. Tang, L. P. Law et al., "Amphiphilic core-shell nanoparticles with poly(ethylenimine) shells as potential gene delivery carriers," *Bioconjugate Chemistry*, vol. 16, no. 1, pp. 139–146, 2005.
- [5] J. Panyam and V. Labhasetwar, "Biodegradable nanoparticles for drug and gene delivery to cells and tissue," *Advanced Drug Delivery Reviews*, vol. 55, no. 3, pp. 329–347, 2003.
- [6] S. M. Moghimi, A. C. Hunter, and J. C. Murray, "Nanomedicine: current status and future prospects," *FASEB Journal*, vol. 19, no. 3, pp. 311–330, 2005.
- [7] A. Bragonzi, A. Boletta, A. Biffi et al., "Comparison between cationic polymers and lipids in mediating systemic gene delivery to the lungs," *Gene Therapy*, vol. 6, no. 12, pp. 1995–2004, 1999.
- [8] W. R. Gombotz and D. K. Pettit, "Biodegradable polymers for protein and peptide drug delivery," *Bioconjugate Chemistry*, vol. 6, no. 4, pp. 332–351, 1995.
- [9] I. Bala, S. Hariharan, and M. N. V. R. Kumar, "PLGA nanoparticles in drug delivery: the state of the art," *Critical Reviews in Therapeutic Drug Carrier Systems*, vol. 21, no. 5, pp. 387–422, 2004.
- [10] M. Koping-Hoggard, I. Tubulekas, H. Guan et al., "Chitosan as a nonviral gene delivery system. Structure-property relationships and characteristics compared with polyethylenimine in vitro and after lung administration in vivo," *Gene Therapy*, vol. 8, no. 14, pp. 1108–1121, 2001.
- [11] M. X. Tang and F. C. Szoka, "The influence of polymer structure on the interactions of cationic polymers with DNA and morphology of the resulting complexes," *Gene Therapy*, vol. 4, no. 8, pp. 823–832, 1997.
- [12] D. Goula, C. Benoist, S. Mantero, G. Merlo, G. Levi, and B. A. Demeneix, "Polyethylenimine-based intravenous delivery of transgenes to mouse lung," *Gene Therapy*, vol. 5, no. 9, pp. 1291–1295, 1998.
- [13] M. N. V. R. Kumar, U. Bakowsky, and C. M. Lehr, "Preparation and characterization of cationic PLGA nanospheres as DNA carriers," *Biomaterials*, vol. 25, no. 10, pp. 1771–1777, 2004.
- [14] M. N. V. R. Kumar, S. S. Mohapatra, X. Kong, P. K. Jena, U. Bakowsky, and C.-M. Lehr, "Cationic poly(lactide-co-glycolide) nanoparticles as efficient in vivo gene transfection agents," *Journal of Nanoscience and Nanotechnology*, vol. 4, no. 8, article no. 005, pp. 990–994, 2004.
- [15] A. Bozkir and O. M. Saka, "Chitosan nanoparticles for plasmid DNA delivery: effect of chitosan molecular structure on formulation and release characteristics," *Drug Delivery*, vol. 11, no. 2, pp. 107–112, 2004.
- [16] Y. Zhang, J. Chen, Y. Zhang et al., "A novel PEGylation of chitosan nanoparticles for gene delivery," *Biotechnology and Applied Biochemistry*, vol. 46, no. 3–4, pp. 197–204, 2007.
- [17] T. Dastan and K. Turan, "In vitro characterization and delivery of chitosan-DNA microparticles into mammalian cells," *Journal of Pharmacy and Pharmaceutical Sciences*, vol. 7, no. 2, pp. 205–214, 2004.
- [18] S. P. Kasturi, K. Sachaphibulkij, and K. Roy, "Covalent conjugation of polyethyleneimine on biodegradable microparticles for delivery of plasmid DNA vaccines," *Biomaterials*, vol. 26, no. 32, pp. 6375–6385, 2005.
- [19] K. Tahara, T. Sakai, H. Yamamoto, H. Takeuchi, and Y. Kawashima, "Establishing chitosan coated PLGA nanosphere platform loaded with wide variety of nucleic acid by complexation with cationic compound for gene delivery," *International Journal of Pharmaceutics*, vol. 354, no. 1–2, pp. 210–216, 2008.
- [20] X.-P. Guan, D.-P. Quan, K.-R. Liao, W. Tao, X. Peng, and K.-C. Mai, "Preparation and characterization of cationic chitosan-modified poly(D,L-lactide-co-glycolide) copolymer nanospheres as DNA carriers," *Journal of Biomaterials Applications*, vol. 22, no. 4, pp. 353–371, 2008.
- [21] J. Chen, B. Tian, X. Yin et al., "Preparation, characterization and transfection efficiency of cationic PEGylated PLA nanoparticles as gene delivery systems," *Journal of Biotechnology*, vol. 130, no. 2, pp. 107–113, 2007.
- [22] H.-Q. Mao, K. Roy, V. L. Troung-Le et al., "Chitosan-DNA nanoparticles as gene carriers: synthesis, characterization and transfection efficiency," *Journal of Controlled Release*, vol. 70, no. 3, pp. 399–421, 2001.
- [23] K. Khatir, A. K. Goyal, P. N. Gupta, N. Mishra, and S. P. Vyas, "Plasmid DNA loaded chitosan nanoparticles for nasal mucosal immunization against hepatitis B," *International Journal of Pharmaceutics*, vol. 354, no. 1–2, pp. 235–241, 2008.
- [24] N. Nafee, S. Taetz, M. Schneider, U. F. Schaefer, and C.-M. Lehr, "Chitosan-coated PLGA nanoparticles for DNA/RNA delivery: effect of the formulation parameters on complexation and transfection of antisense oligonucleotides," *Nanomedicine*, vol. 3, no. 3, pp. 173–183, 2007.
- [25] S. Taetz, N. Nafee, J. Beisner et al., "The influence of chitosan content in cationic chitosan/PLGA nanoparticles on the delivery efficiency of antisense 2'-O-methyl-RNA directed against telomerase in lung cancer cells," *European Journal of Pharmaceutics and Biopharmaceutics*, vol. 72, no. 2, pp. 358–369, 2008.
- [26] H. Katas, S. Chen, A. A. Osamuyimen, E. Cevher, and H. O. Alpar, "Effect of preparative variables on small interfering RNA loaded Poly(D,L-lactide-co-glycolide)-chitosan submicron particles prepared by emulsification diffusion method," *Journal of Microencapsulation*, vol. 25, no. 8, pp. 541–548, 2008.
- [27] S. Mao, W. Sun, and T. Kissel, "Chitosan-based formulations for delivery of DNA and siRNA," *Advanced Drug Delivery Reviews*, vol. 62, no. 1, pp. 12–27, 2009.
- [28] R. B. Gupta, "Nanoparticle technology for drug delivery," in *Drugs and the Pharmaceutical Sciences: Nanoparticle Technology for Drug Delivery*, vol. 159, p. 403, Informa Health Care, 2006.
- [29] T. O'Connor, S. Mansy, M. Bina, D. R. McMillin, M. A. Bruck, and R. S. Tobias, "The pH-dependent structure of calf thymus DNA studied by Raman spectroscopy," *Biophysical Chemistry*, vol. 15, no. 1, pp. 53–64, 1982.

- [30] F. Feng, G. Zhi, H. S. Jia, L. Cheng, Y. T. Tian, and X. J. Li, "SERS detection of low-concentration adenine by a patterned silver structure immersion plated on a silicon nanoporous pillar array," *Nanotechnology*, vol. 20, no. 29, Article ID 295501, 2009.

Research Article

Preparation of Nanoporous Polymer Films for Real-Time Viability Monitoring of Cells

Chia-Man Chou,¹ Tong-You Wade Wei,² Jou-May Maureen Chen,² Wei-Ting Chang,³ Chang-Tze Ricky Yu,² and Vincent K. S. Hsiao^{2,4}

¹ Division of Pediatric Surgery, Department of Surgery, Taichung Veterans General Hospital, 160 Section 3 Chung-Kang Road, Taichung 40705, Taiwan

² Graduate Institute of Biomedicine and Biomedical Technology, National Chi Nan University, 1 University Road Puli, Nantou 54561, Taiwan

³ Department of Applied Chemistry, National Chi Nan University, 1 University Road Puli, Nantou 54561, Taiwan

⁴ Department of Applied Materials and Optoelectronic Engineering, National Chi Nan University, 1 University Road, Puli, Nantou 54561, Taiwan

Correspondence should be addressed to Vincent K. S. Hsiao, kshsiao@ncnu.edu.tw

Received 19 May 2010; Accepted 1 July 2010

Academic Editor: Lu Sun

Copyright © 2011 Chia-Man Chou et al. This is an open access article distributed under the Creative Commons Attribution License, which permits unrestricted use, distribution, and reproduction in any medium, provided the original work is properly cited.

We have demonstrated an alternative way to monitor the viability of cells adhered on a nanoporous polymer film in real time. The nanoporous polymer films were prepared by laser interference patterning. During exposure of holographic patterning, the dissolved solvents were phase separated with photocured polymer and the nanopores were created as the solvents evaporated. The diffracted spectra from the nanoporous polymer film responded to each activity of the cell cycle, from initial cell seeding, through growth, and eventual cell death. This cell-based biosensor uses a nanoporous polymer film to noninvasively monitor cell viability and may prove useful for biotechnological applications.

1. Introduction

Nanoporous materials with a pore size ranging from 1 nm to 100 nm have demonstrated applications in a number of multidisciplinary fields [1]. The large internal surface area of nanoporous materials optimizes their use as a functional structure which absorbs or interacts with atoms, ions, and molecules. In biosensing applications [2–7], the porosity yields a large surface-to-volume ratio that enables the immobilization and hybridization of a higher percentage of analyte, such as protein or DNA. The selectivity and sensitivity of nanopore-based biological sensors are dramatically increased by designing nanopores with different surface modification techniques [8–13]. Polymeric materials are widely used in biological applications [14–17] because of the ease of synthesis and intrinsic functional properties, such as biodegradability and biocompatibility, which are key characteristics for cell and tissue engineering. Polymeric

materials have also attained much attention in nanoscience and nanotechnology as they can be designed for advanced, smart applications. Several techniques, such as soft lithography, template-directed emulsion, and polymerization-induced phase separation, have been demonstrated as practical means to fabricate nanoporous polymers with different functionalities [18–23]. We have developed a system to fabricate nanoporous polymers by holographic interference patterning using a photo-curable monomer containing a polar solvent (formamide) or solvent/liquid crystal (LC) mixture [24, 25]. The nanoporous structure is determined by the interference pattern generated by one or more laser beams. We have also demonstrated that such polymeric, nanoporous photonic structures could be used as sensitive and selective sensors that detect solvent vapor, relative humidity, and protein [26–31].

In this paper, we demonstrate a cell-based biosensor using nanoporous polymeric film. The transmitted spectrum

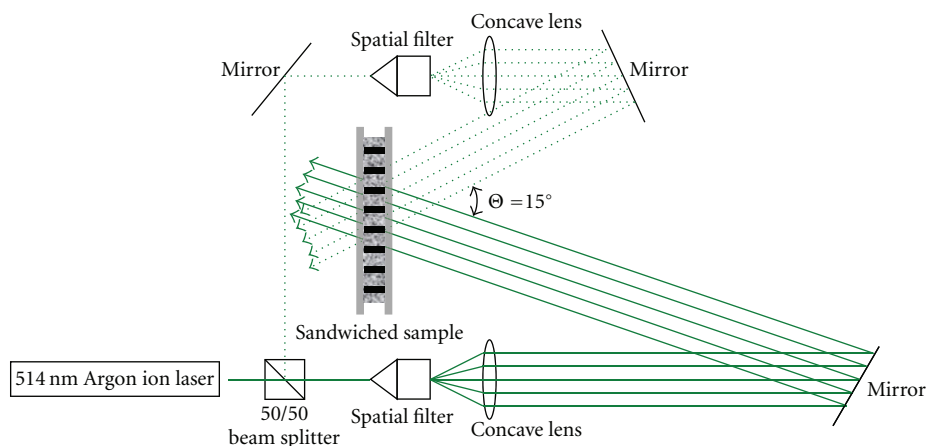


FIGURE 1: The schema of optical setup for fabricating the nanoporous polymer film.

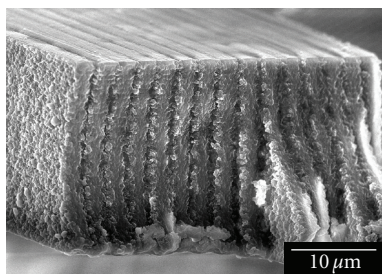


FIGURE 2: SEM cross-sectional micrograph of the nanoporous polymer film.

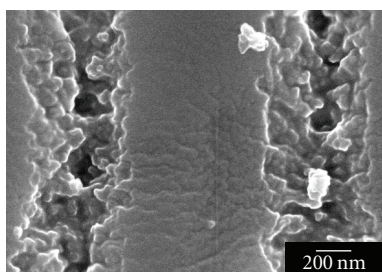


FIGURE 3: SEM surface morphology of nanopores.

from an ordered, nanoporous polymer substrate varies from initial cell seeding, during cell growth, and cell death. This spectral-based analysis provides an alternative way to monitor cell culture viability using optical transducer scheme, which has advantage of label-free detection, in contrast to fluorescence detection. HeLa, a common cervical cancer cell line, served as the cell model for the studies.

2. Experimental Section

A photo-curable monomer containing 10 wt% 3-amino-propyltriethoxysilane (APTES, Aldrich), 20 wt% acetone

solution (Aldrich), 20 wt% liquid crystal (MDA3061, Merck Taiwan), 40 wt% dipentaerythritol hydroxypenta acrylate (Aldrich), 1 wt% Rose Bengal (Spectra Group Limited), 2 wt% n-phenylglycine (Aldrich), and 7 wt% n-vinylpyrrolidinone (Aldrich) was used to fabricate the nanoporous polymer structures. We first mixed the monomer syrup homogeneously with a mixer and sonicator. Second, we sandwiched 20 μL of the monomer onto one glass slide and covered the syrup with another ITO-coated glass slide. The thickness of the sandwiched sample was controlled by a 15 μm plastic spacer. Third, we used a 514 nm Argon ion laser as the exposure source to conduct the holographic interference patterning process. During the holographic interference patterning, the sandwiched sample was exposed under two laser beams of 100 mW at a writing angle of 15 degrees for one minute. Figure 1 shows the schematic of the optical setup for fabricating the nanoporous polymer film by holographic interference patterning. Fourth, immediately following the interference patterning, we postcured the sandwiched sample under a white light source for 24 hours. After the postcuring process, the sandwiched sample was separated for cell seeding. The nanoporous polymer remained upon the non-ITO-coated glass slide. The surface and cross-sectional morphologies of the fabricated nanoporous polymer film were characterized by a low voltage scanning electron microscope (LVSEM). The cervical cancer cell line HeLa was cultured with DMEM medium with 5% fetal bovine serum, 2 mM L-glutamine, and sodium pyruvate. The nanoporous polymeric sample was sterilized with 70% ethanol, exposed to UV light for 30 minutes, and subsequently placed in a 6-cm petridish. 3×10^5 HeLa cells were seeded onto the petridish for 8 hours and the cells attached to the nanoporous polymer were photographed with a microscope (Olympus CKX41) bound CCD camera (Olympus DP71). The transmission spectra from the cell-seeded samples were characterized using an Ocean Optics HR4000 spectrometer.

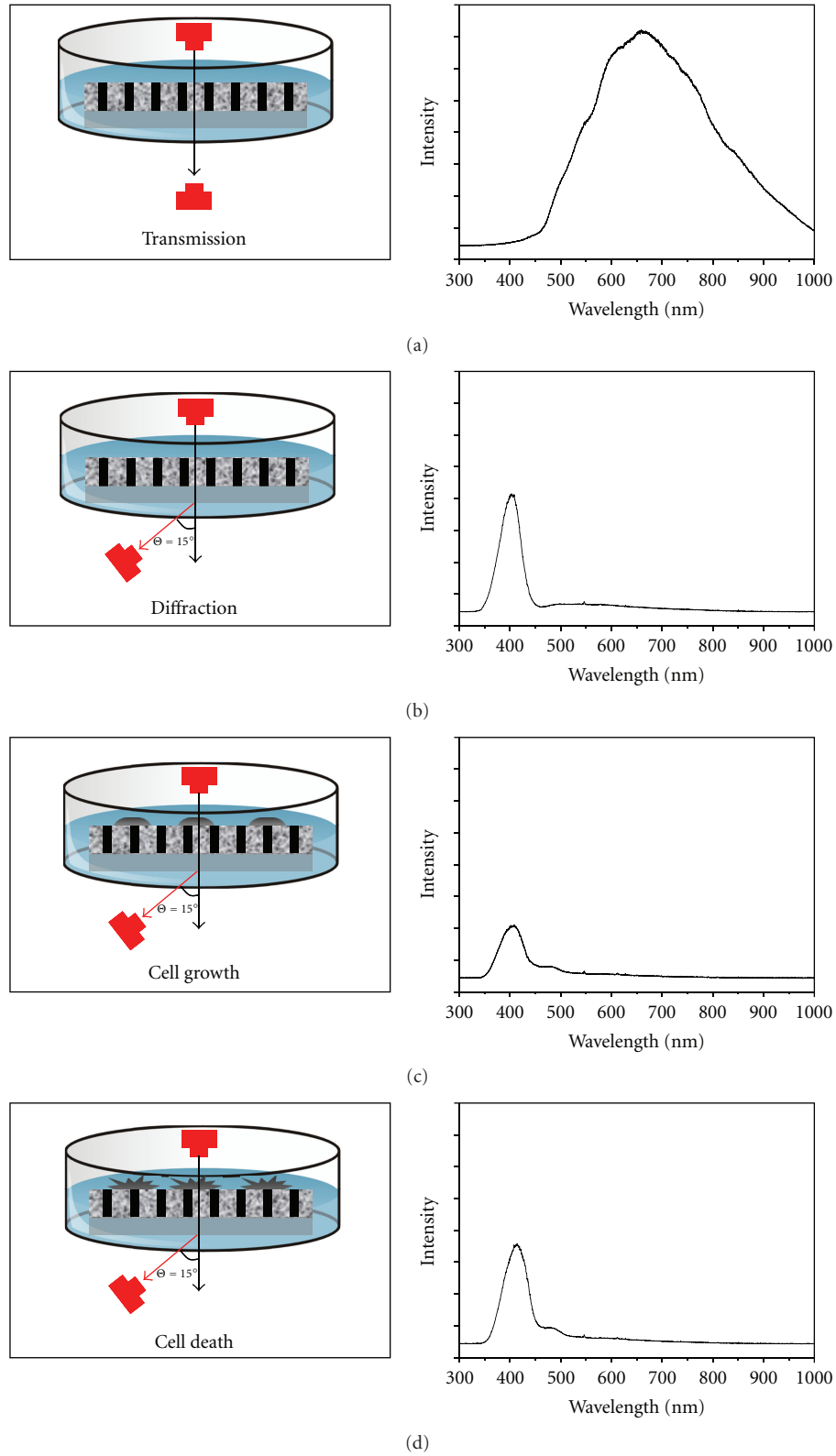


FIGURE 4: Optical design used to monitor the biological viability of the cells using the nanoporous polymer film. On the right are the representative spectra corresponding to the each process. (a) To measure the transmitted light from the sample, illumination (light source) and observation (detector) are aligned on the same optical path and the corresponded spectra shows a broad shape which is not suitable for biological observation. (b) To measure the diffracted light, the observation (detector) is placed in the position of the diffracted light path, 15° from the sample normal, leading to a sharp spectrum signal. (c) Seeding the cells on the sample surface introduces a scattering effect as the cells scatter some light out of the diffracted light path and the intensity of spectrum decreases. (d) Cell death causes the cells to detach from the sample surface and the intensity of spectrum increases.

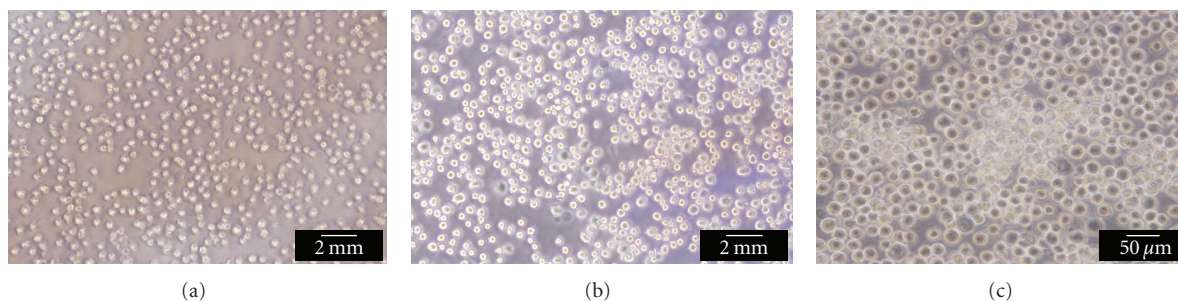


FIGURE 5: Observation of phase-contrast microscopic images of cervical cancer cells on the surface of nanoporous polymer film (a) before cell seeding; (b) after 8 hrs cell seeding and incubation and (c) after 8 hrs of cell seeding and incubation, and the inducing cell death for 8 hrs at room temperature.

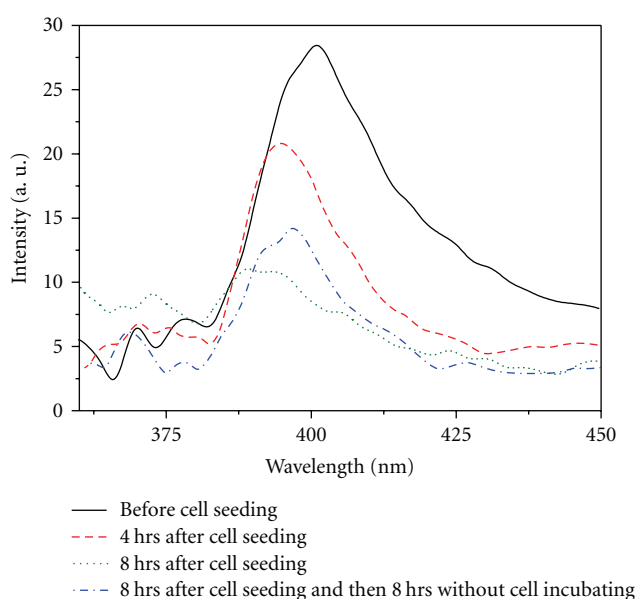


FIGURE 6: The diffraction spectra characterized from the nanoporous polymer film at different time of cell incubation.

3. Results and Discussion

In a typical process of holographic interference patterning using photopolymer and LC/solvent mixture, the photopolymer is polymerized in the bright region (constructive interference) while the LC/solvent tends to be trapped in the dark region (destructive interference) by the photochemical potential force during the photopolymerization process. Under the photochemically induced phase-separation state, the LC/solvent phase separates from the polymer and generates an ordered structure defined by the holographic interference pattern. After opening the sandwiched sample, the solvent evaporates and a well-defined nanoporous photonic polymer structure is obtained. Figure 2 shows the SEM cross-sectional micrograph of nanoporous polymer film fabricated by two-beam interference patterning. A one-dimensional lamella structure consisting of layered polymers and patterned nanopores was successfully prepared by the

holographic technique. Figure 3 depicts the surface morphology of the nanopores separated by the polymer. The pore size observed within the polymer lamella ranges between 50–200 μm .

Figure 4 shows a schematic illustration of the optical design and corresponding spectra of the cell-based biosensor using the nanoporous polymer film. Since the cell culturing process was conducted in media, the nanoporous polymer film situated on one side of the glass slide has to be stable in the aqueous environment. We have observed that by adding the APTES compound, the nanoporous polymer film's water-stability is strongly enhanced [26]. Moreover, it should be noted that APTES is commonly used for preparing amino functional groups on glass and silica. The APTES-modified materials are biocompatible and suitable for biosensing applications. The addition of APTES in the photopolymer not only enhances the stability, but also the biocompatibility of nanoporous polymer film. When both light source and detector are positioned normal to the sample, the nanoporous polymer film presents a relative spectrum containing a broad peak ranging from 450 nm to 1000 nm, as shown in Figure 4(a). If the detector is placed at the position of diffracted light, the obtained spectrum shows a sharp peak is observed at the wavelength of ~ 400 nm, as shown in Figure 4(b). The introduction of adhered cells on the surface of the nanoporous polymer film generates scattering and the intensity of diffraction decreases, as shown in Figure 4(c). Figure 4(d) depicts the reverse, as the detachment of the cells due to cell death increases the intensity of the light scatter. Herein, lies the sensing mechanism of this biosensor. The light scatter from viable, adhered cells is transduced via the intensity and peakshift properties of the diffraction spectrum.

To verify the cell attachment on the sample surface, optical microscopy was performed on nanoporous polymer during the cell viability. Figures 5(a) and 5(b) show the phase-contrast microscope images for cervical cells seeded on the surface of nanoporous polymer film after 0–8 hr cell incubation, respectively. Cervical cancer cells appear with a small round shape on the surface of nanoporous polymer film. Figure 5(c) shows the image for cervical cells after 8 hr cell seeding and kept in the room temperature without cell incubation. The clear image of cells indicates the cell

attaching on the surface of nanoporous polymer film while the unclear image (out of focusing) indicates the unattached cells. We speculate that some of the unattached cells are from the dead cells that could be proved from the optical spectroscopy.

The change of light scattering from the biological activity on the nanoporous polymer film was monitored using fiber optical spectroscopy. Figure 6 shows the relative intensity of diffracted light dependent on the time of cell seeding upon the nanoporous polymer film. After 4 hr cell incubating, the diffracted light decreases. Light scattering generated by cell adhesion onto the sample causes a decrease of diffracted light. We also observed that the peak wavelength (~ 400 nm) diffracted from the sample blue-shifts 5 nm after 4 hrs cell growth. According to the Bragg condition, $\lambda = 2n_{\text{ave}}\Lambda$, where λ is the peak wavelength of spectrum, n_{ave} is the average refractive index of sample, and Λ is period of the periodic structure, we speculate that the attachment of the cells might induce a change in the refractive index and further change the peak wavelength of the diffracted spectrum. 8 hr cell incubating make the intensity of peak wavelength of spectrum decrease and the wavelength blue-shift 8 nm. We removed the sample from the incubator and recorded the diffraction spectrum after 8 hrs and found that the intensity of the spectrum increased and redshifted 8 nm. The cells should become nonviable upon prolonged periods of time removed from the incubator. The cells detached from the sample and the sample has become more transparent. Such biological activities were recorded by the optical spectrum from the nanoporous polymer film.

4. Conclusion

We have successfully prepared a nanoporous polymer film which has served as a platform to observe cell activity. The ordered nanopores were created by a holographic interference patterning technique. The diffracted spectra observed from the nanoporous polymer film responded to the attached cell activity of cell seeding, growth, and death. The cell-based biosensor fabricated by the nanoporous polymer film offers a label-free, noninvasive method to continuously monitor cell activity and may prove useful for biotechnological applications.

Acknowledgments

This work was supported by Taichung Veterans General Hospital/National Chi Nan University Joint Research Program (TCVGH-NCNU-987907, TCVGH-NCNU-997902). The authors thank John R. Waldeisen for technical discussion and preparation of the paper.

References

- [1] G. Q. Lu and X. S. Zhao, *Nanoporous Materials: Science and Engineering*, Imperial College Press, London, UK, 2004.
- [2] O. A. Saleh and L. L. Sohn, "An artificial nanopore for molecular sensing," *Nano Letters*, vol. 3, no. 1, pp. 37–38, 2003.
- [3] H. Liu, P. He, Z. Li, and J. Li, "High surface area nanoporous platinum: facile fabrication and electrocatalytic activity," *Nanotechnology*, vol. 17, no. 9, pp. 2167–2173, 2006.
- [4] C. R. Martin and Z. S. Siwy, "Learning nature's way: biosensing with synthetic nanopores," *Science*, vol. 317, no. 5836, pp. 331–332, 2007.
- [5] S. Benner, R. J. A. Chen, N. A. Wilson et al., "Sequence-specific detection of individual DNA polymerase complexes in real time using a nanopore," *Nature Nanotechnology*, vol. 2, no. 11, pp. 718–724, 2007.
- [6] S. G. Lemay, "Nanopore-based biosensors: the interface between ionics and electronics," *ACS Nano*, vol. 3, no. 4, pp. 775–779, 2009.
- [7] B. M. Venkatesan, B. Dorvel, S. Yemenicioglu, N. Watkins, I. Petrov, and R. Bashir, "Highly sensitive, mechanically stable nanopore sensors for DNA analysis," *Advanced Materials*, vol. 21, no. 27, pp. 2771–2776, 2009.
- [8] H. Chang, F. Kosari, G. Andreadakis, M. A. Alam, G. Vasmatazis, and R. Bashir, "DNA-mediated fluctuations in ionic current through silicon oxide nanopore channels," *Nano Letters*, vol. 4, no. 8, pp. 1551–1556, 2004.
- [9] K. A. Kilian, T. Böcking, K. Gaus, M. Gal, and J. J. Gooding, "Peptide-modified optical filters for detecting protease activity," *ACS Nano*, vol. 1, no. 4, pp. 355–361, 2007.
- [10] Z. Yang, Z. Xie, H. Liu, F. Yan, and H. Ju, "Streptavidin-functionalized three-dimensional ordered nanoporous silica film for highly efficient chemiluminescent immunosensing," *Advanced Functional Materials*, vol. 18, no. 24, pp. 3991–3998, 2008.
- [11] D. Losic, M. A. Cole, B. Dollmann, K. Vasilev, and H. J. Griesser, "Surface modification of nanoporous alumina membranes by plasma polymerization," *Nanotechnology*, vol. 19, no. 24, Article ID 245704, 7 pages, 2008.
- [12] M. Wanunu, J. Sutin, and A. Meller, "DNA profiling using solid-state nanopores: detection of DNA-binding molecules," *Nano Letters*, vol. 9, no. 10, pp. 3498–3502, 2009.
- [13] V. Mussi, P. Fanzio, L. Repetto et al., "DNA-functionalized solid state nanopore for biosensing," *Nanotechnology*, vol. 21, no. 14, Article ID 145102, 5 pages, 2010.
- [14] T. Cassagneau and F. Caruso, "Conjugated polymer inverse opals for potentiometric biosensing," *Advanced Materials*, vol. 14, no. 24, pp. 1837–1841, 2002.
- [15] J. T. Borenstein, E. Barnard, B. Orrick, W. Cheung, C. Sundback, and J. P. Vacanti, "Microfabricated biodegradable scaffolds for tissue engineering of vital organs," in *Proceedings of Materials Research Society Symposium*, pp. 9–11, 2004.
- [16] X. Wang, Y.-G. Kim, C. Drew, B.-C. Ku, J. Kumar, and L. A. Samuelson, "Electrostatic assembly of conjugated polymer thin layers on electrospun nanofibrous membranes for biosensors," *Nano Letters*, vol. 4, no. 2, pp. 331–334, 2004.
- [17] A. Monge, N. Snecko, E. Gutiérrez-Puebla et al., "One teflon®-like channelled nanoporous polymer with a chiral and new uninodal 4-connected net: sorption and catalytic properties," *Chemical Communications*, no. 10, pp. 1291–1293, 2005.
- [18] W. Qian, Z.-Z. Gu, A. Fujishima, and O. Sato, "Three-dimensionally ordered macroporous polymer materials: an approach for biosensor applications," *Langmuir*, vol. 18, no. 11, pp. 4526–4529, 2002.
- [19] V. Lehmann, "Biosensors: barcoded molecules," *Nature Materials*, vol. 1, no. 1, pp. 12–13, 2002.
- [20] A. Valsesia, P. Colpo, M. M. Silvan, T. Mezziani, G. Ceccone, and F. Rossi, "Fabrication of nanostructured polymeric

- surfaces for biosensing devices,” *Nano Letters*, vol. 4, no. 6, pp. 1047–1050, 2004.
- [21] S. Sotiropoulou, V. Vamvakaki, and N. A. Chaniotakis, “Stabilization of enzymes in nanoporous materials for biosensor applications,” *Biosensors and Bioelectronics*, vol. 20, no. 8, pp. 1674–1679, 2005.
 - [22] Q. Li, J. F. Quinn, Y. Wang, and F. Caruso, “Preparation of nanoporous polyelectrolyte multilayer films via nanoparticle templating,” *Chemistry of Materials*, vol. 18, no. 23, pp. 5480–5485, 2006.
 - [23] S. Wu, S. R. Park, and X. S. Ling, “Lithography-free formation of nanopores in plastic membranes using laser heating,” *Nano Letters*, vol. 6, no. 11, pp. 2571–2576, 2006.
 - [24] V. K. S. Hsiao, T.-C. Lin, G. S. He et al., “Optical microfabrication of highly reflective volume Bragg gratings,” *Applied Physics Letters*, vol. 86, no. 13, Article ID 131113, 3 pages, 2005.
 - [25] V. K. S. Hsiao, K.-T. Yong, A. N. Cartwright et al., “Nanoporous polymeric photonic crystals by emulsion holography,” *Journal of Materials Chemistry*, vol. 19, no. 23, pp. 3998–4003, 2009.
 - [26] V. K. S. Hsiao, W. D. Kirkey, F. Chen, A. N. Cartwright, P. N. Prasad, and T. J. Bunning, “Organic solvent vapor detection using holographic photopolymer reflection gratings,” *Advanced Materials*, vol. 17, no. 18, pp. 2211–2214, 2005.
 - [27] X. Fang, V. K. S. Hsiao, V. P. Chodavarapu, A. H. Titus, and A. N. Cartwright, “Colorimetric porous photonic bandgap sensors with integrated CMOS color detectors,” *IEEE Sensors Journal*, vol. 6, no. 3, pp. 661–666, 2006.
 - [28] V. K. S. Hsiao, J. R. Waldeisen, Y. Zheng, P. F. Lloyd, T. J. Bunning, and T. J. Huang, “Aminopropyltriethoxysilane (APTES)-functionalized nanoporous polymeric gratings: fabrication and application in biosensing,” *Journal of Materials Chemistry*, vol. 17, no. 46, pp. 4896–4901, 2007.
 - [29] J. Shi, V. K. S. Hsiao, and T. J. Huang, “Nanoporous polymeric transmission gratings for high-speed humidity sensing,” *Nanotechnology*, vol. 18, no. 46, Article ID 465501, 6 pages, 2007.
 - [30] J. Shi, V. K. S. Hsiao, T. R. Walker, and T. J. Huang, “Humidity sensing based on nanoporous polymeric photonic crystals,” *Sensors and Actuators B*, vol. 129, no. 1, pp. 391–396, 2008.
 - [31] W. Yan, V. K. S. Hsiao, Y. B. Zheng, Y. M. Shariff, T. Gao, and T. J. Huang, “Towards nanoporous polymer thin film-based drug delivery systems,” *Thin Solid Films*, vol. 517, no. 5, pp. 1794–1798, 2009.

Research Article

Dynamics of Spreading and Alignment of Cells Cultured *In Vitro* on a Grooved Polymer Surface

Thomas Peterbauer,^{1,2} Sergii Yakunin,¹ Jakub Siegel,¹ Steffen Hering,¹ Marc Fahrner,³ Christoph Romanin,³ and Johannes Heitz¹

¹Institute of Applied Physics, Johannes Kepler University Linz, 4040 Linz, Austria

²Department of Pharmacology and Toxicology, University of Vienna, 1090 Vienna, Austria

³Institute of Biophysics, Johannes Kepler University Linz, 4040 Linz, Austria

Correspondence should be addressed to Johannes Heitz, Johannes.heizt@jku.at

Received 21 April 2010; Revised 28 June 2010; Accepted 7 July 2010

Academic Editor: Lu Sun

Copyright © 2011 Thomas Peterbauer et al. This is an open access article distributed under the Creative Commons Attribution License, which permits unrestricted use, distribution, and reproduction in any medium, provided the original work is properly cited.

We used mechanically embossed polyester films to analyze the dynamics of cell alignment and cell-specific factors modulating the response of Chinese hamster ovary (CHO) cells and of a rat myogenic cell line to the surface topography. The films used had grooves with a periodicity of approximately 750 nm and a depth of 150 nm. Both cell lines responded to the topographical feature. On unpatterned control areas, cells of both lines showed a random distribution with orientation angles close to 45°. Both cell types exhibited an elongated morphology on the patterned surface. CHO cells typically showed bipolar spreading. Their contact area increased almost exclusively along the groove direction. Likewise, freshly seeded rat myoblasts displayed protrusions emerging in parallel with the grooves. However, myoblasts frequently had more than two sites with plasma protrusions pulling the cells along different grooves. They could also develop lamellipodia expanding without a preferred direction and long filopodia.

1. Introduction

For mammalian cells, adhesion to the extracellular matrix or to the cell culture substratum when grown *in vitro* plays an essential role for many processes such as proliferation and differentiation. Cells attach to the surface *via* focal adhesions, connecting the surface to the cytoskeleton. Formation of these interfaces is not only affected by surface chemistry (including the presence of ligands), electrostatic charge, wettability, and elastic modulus [1, 2]. Surfaces can provide micro- and nanosized topographical clues to guide alignment, migration of cells or outgrowth of neurites along a specific orientation [3, 4]. To probe the ability of cells to respond to surface topography, grooved substrata are often used, usually resulting in physical guidance along the direction of the grooves and reorganization of the cytoskeleton. Alignment occurs on grooves with periods <20 μm [4] and depths down to a threshold around 30–90 nm [5–8]. Despite a large body of literature, however, fundamental questions remain open. The basic mechanism

by which cells recognize surface geometry remains obscure. It may be a more or less passive process, whereby adhesion molecules best fitting the local topography simply draw cells or cellular components into the observed shape, or it may involve more elaborate regulatory mechanisms. It is also not clear if there is one uniform mechanism active over the entire range of scales which evoke a response, or if different processes accomplish guidance on the micro- and nanoscale, respectively. The extent of contact guidance depends on cell type used, plating density, and, most import, feature geometry and feature aspect ratio [6, 9–13]. In some instances, growth perpendicular to the groove direction has been observed [14, 15], and the response of cells may depend on soluble factors [15].

We have recently employed laser processing to generate polystyrene films with periodic surface ripple structures with a periodicity of 200 nm–800 nm and a depth of 40 nm–150 nm [16]. We probed a range of cell lines for proliferation and contact guidance. Although the aspect

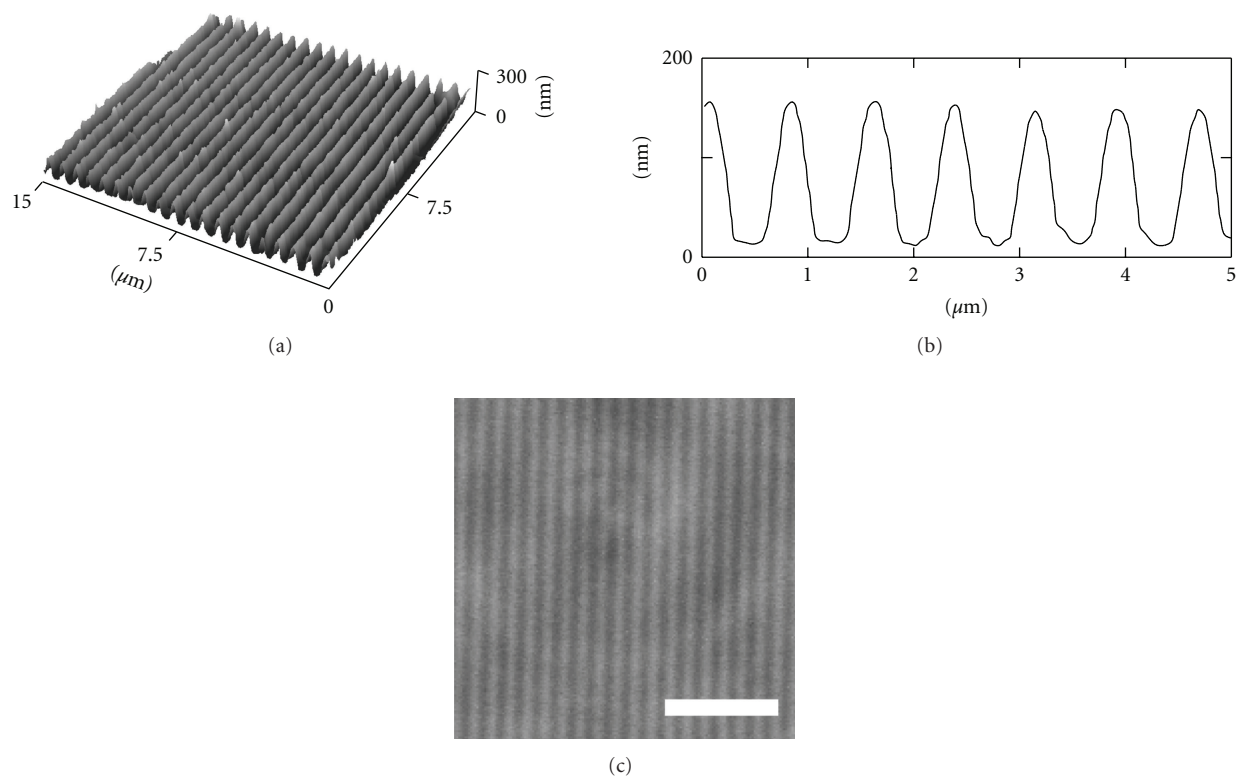


FIGURE 1: (a) Surface plot of a mechanically embossed polyester film characterized by AFM. (b) Schematic cross-section of an AFM image. (c) Phase-contrast light microscopic image of a patterned film obtained with a 25x oil immersion objective. Scale bar, 5 μm .

ratios of the surfaces were lower than those employed in most other studies (e.g., [6] or [17]), parallel alignment of cells occurred above a cell-specific critical periodicity of 200 nm–400 nm. Here, we focus on the dynamics of cell spreading and alignment, and we attempt to gain some insight in the cell-specific factors responsible for the variability of cell alignment. We employed mechanically embossed polyester films. This replication method, which is frequently used to fabricate diffractive surfaces (e.g., holograms), offers the advantage of low-cost mass production. We selected CHO cells, which are quite sensitive with respect to surface topography [18] and a rat myoblast cell line displaying less pronounced contact guidance [16].

2. Materials and Methods

2.1. Preparation of Patterned Surfaces. The surfaces were fabricated by mechanical embossing of polyester carrier films [19]. The films were coated with an UV-curable polyester resin, imprinted with an embossing machine containing the pattern, and photopolymerized. In some initial experiments, the films were additionally irradiated with far UV light with a wavelength of 172 nm as previously described [20]. The latter treatment, which introduces polar oxidic groups on the surface, enhanced biocompatibility for cell lines weakly attaching to the substratum such as human embryonic kidney (HEK 293) cells, but was found to be unnecessary

for other cell types. The surface topography of the films was analysed using a diCP II (Veeco Instruments, Mannheim, Germany) atomic force microscope (AFM). Before use in cell culture, samples were sterilized for 20 minutes with 70% ethanol and washed with phosphate-buffered saline (PBS). The films were placed in 35 mm Petri dishes with a 0.18 mm synthetic bottom permitting oil immersion microscopy (μ -Dishes, ibidi, Martinsried, Germany). Appropriately shaped Teflon rings were inserted to prevent floating of the films.

2.2. Cell Culture and Labelling. CHO-K1 cells and a cell line derived from rat skeletal myoblasts [19] were cultured at 37°C and 5% CO_2 in Dulbecco's Modified Eagle Medium (DMEM; EuroClone, Pero, Italy) supplemented with 10% fetal bovine serum (FBS, EuroClone) and 5 $\mu\text{g mL}^{-1}$ gentamycin (EuroClone) in a humidified atmosphere. Cells were harvested with PBS containing 0.05% trypsin containing 0.02% EDTA and seeded onto the patterned surfaces. Typically, the cells were used in cell passage number between 10 and 30 and seeded onto the substrates at a density of about 1000 cells mm^{-2} . In some experiments, cells were stained after harvesting with the lipophilic fluorescent dye PKH26 (Sigma Aldrich, Vienna, Austria) according to the manufacturer's recommendations. For time-lapse video microscopy (performed at ambient CO_2 concentration), media were supplemented with 50 mM Hepes·NaOH (pH 7.2, Sigma).

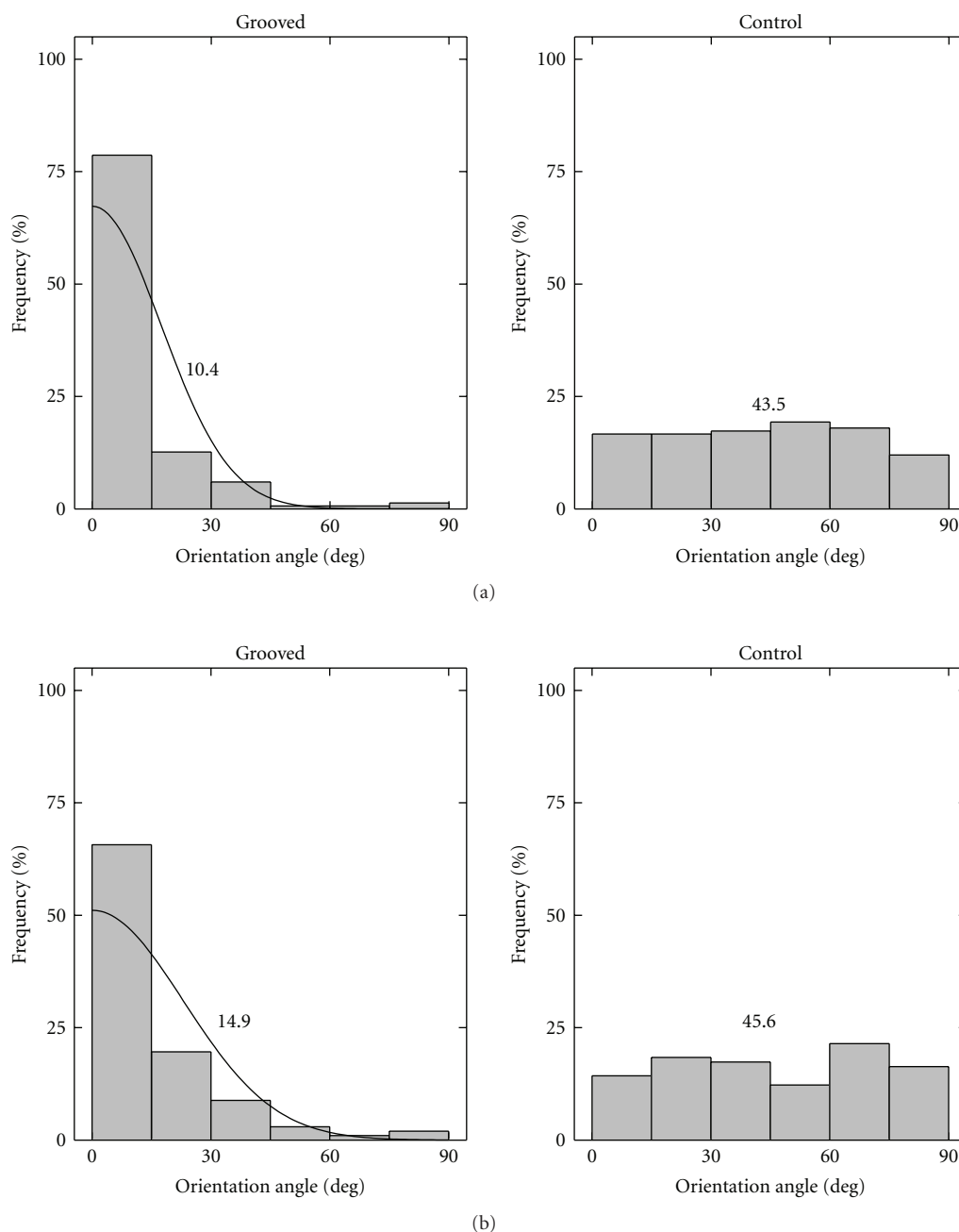


FIGURE 2: (a) Histograms of orientation angles of CHO cells ($n = 150$) on grooved polyester films (left panel) or on adjacent unpatterned control areas (right panel) one day post seeding. (b) Orientation angles of rat myoblasts ($n = 100$). Curves represent probability density functions of half-normal distributions fitted to the data sets. Inlet values represent average orientation angles.

2.3. Microscopy and Image Analysis. Brightfield, phase contrast and fluorescence microscopic images were captured with an inverted microscope (Axiovert 200, Zeiss, Oberkochen, Germany) equipped with a Zeiss LSM 510 laser scanning module and a transmitted light detector. Image analysis was performed with ImageJ 1.43 (available at <http://rsb.info.nih.gov/ij>). The outlines of cells were traced using the NeuronJ plugin [21]. After conversion into closed polygons, ellipses were fitted to the outlines. The orientation angle of a cell was defined as the absolute value (in degrees)

of the smallest angle between the major axis of the best-fitting ellipse and the direction of the grooves. This approach ignores the sign of the deviation and, thus, gives values which vary between 0° (perfect alignment) and 90° (exactly perpendicular orientation). Cell populations with random orientation should have an average orientation angle of 45° .

The shape of the cells was quantified by measurement of their minimum and maximum Feret's diameter (minimum and maximum caliper length, resp.) and by the dimension-

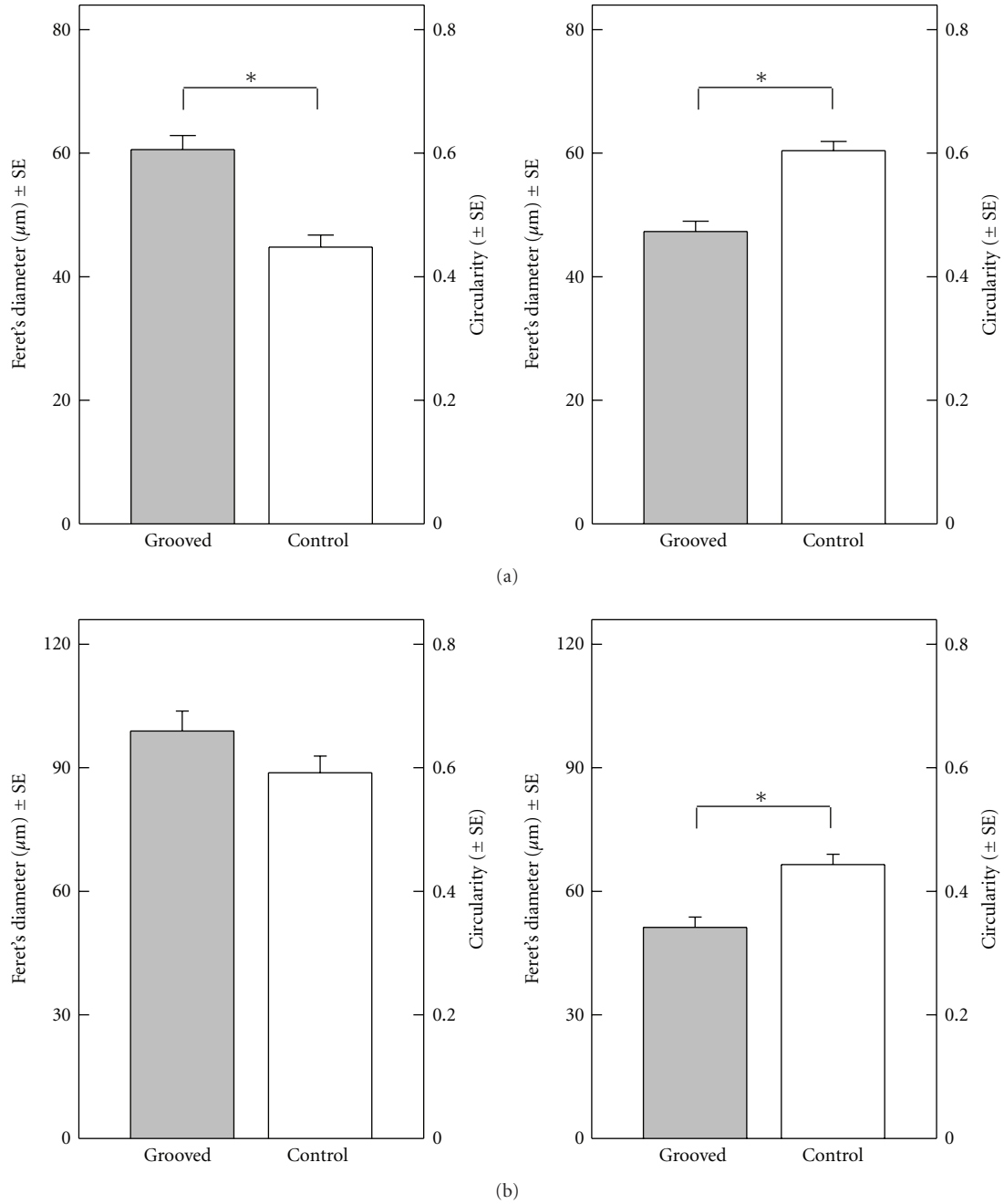


FIGURE 3: (a) Maximum Feret's diameter and circularity of CHO cells on a grooved substratum (grey bars) or on an adjacent unpatterned control area (open bars) one day post seeding ($n = 150$). (b) Morphology of rat myoblasts. Asterisks denote statistically significant differences ($P < .05$).

less shape index circularity

$$M = \frac{4\pi A}{P^2}, \quad (1)$$

where A is the area of a cell and P is its perimeter. A perfect circle has a circularity of 1, while the values for deformed objects approach zero. The solidity of cells was estimated by the ratio of the area of a cell to the area of its convex hull. Pairwise comparisons for statistical significance were made

by Student's t -test. Results were considered as statistically different at $P < .05$.

3. Results

3.1. Characterization of Grooves. The topology of the surfaces generated by mechanical embossing was evaluated by AFM (Figure 1). The average depth of the grooves was 154 ± 11 nm with a periodicity of 758 ± 22 nm. The surface structures were visible by conventional light microscopy,

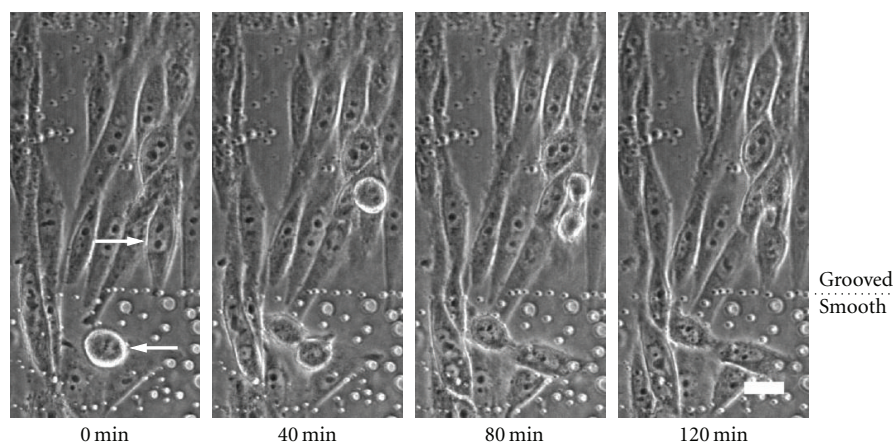


FIGURE 4: Time-lapse phase contrast images of a near-confluent CHO cell culture growing on a mechanically embossed polyester film. The dashed line denotes the border between an area with grooves (upper part of the images) and smooth control area (lower part of the images). Arrows denote cells which underwent mitosis. Scale bar, 20 μm .

allowing to determine their direction and the orientation angle of cells growing on the surface. Due to refractive properties of the material, however, peak maxima of the line pattern changed with the focus plane. Thus, it was not possible to determine directly whether the lines visible in the light microscopic images correspond to grooves or ridges, respectively. However, we saw in some microscope images features in bright color which were obviously elevated above or on top of the groove structure. From this we conclude that probably the bright lines in the microscope images correspond to the groove ridges, while the valleys between them are more dark.

3.2. Cell Alignment. The two cell lines studied responded to the patterned surface by alignment along the direction of the grooves. The degree of alignment was somewhat variable, depending on the cell culture conditions, passage number and seeding density. When cultured under identical conditions and low to moderate cell densities, CHO cells showed more pronounced alignment than rat myoblasts (Figure 2). This observation is in line with our previous report on the sensitivity of the two cell lines to surface structure periodicity [16]. Cell populations growing on adjacent unpatterned control areas consistently displayed random orientation with average orientation angles close to 45° . The substrate topography not only affected orientation, but also cell morphology (Figure 3). Cell populations growing on grooves were more elongated than control cells and tended to have a higher average maximum Feret's diameters (a statistically significant difference was only found for CHO cells). Both cell lines showed little motility, neither on grooved nor on smooth films (data not shown). Nonetheless, the general alignment on grooved films was maintained even in fairly dense cell layers, in which neighbouring cells can act as physical barriers (Figure 4). Mitotic cells detached from the surface, rounded up, and divided. The daughter cells occupied the space freed by the mother cell by spreading

along the direction of grooves. Upon reaching confluency, however, the alignment of rat myoblasts degraded quickly, owing to their tendency to overgrow other cells rather than maintaining a strict monolayer.

3.3. Time-Lapse Microscopy. To study attachment and spreading in more detail, freshly harvested cells were seeded onto patterned films and analyzed by time-lapse microscopy. Under our cell culture conditions, the time required to complete attachment varied considerably. Rat myoblasts could complete attachment within 1–2 hours, while CHO cells required 5 hours or more. No differences between cells seeded onto a grooved surface and control cells on adjacent smooth areas were apparent (data not shown). When seeded onto a grooved surface, many CHO cells displayed strictly bipolar spreading (Figure 5). Short cytoplasmic processes, 3–6 μm in diameter, and bleb-like structures protruded preferentially from two opposing sites of the cells in parallel with the groove direction. The cells elongated along the groove direction with little lateral spreading. The final width of the cells (estimated as the minimum Feret's diameter) as measured one day after seeding was not much above that of freshly trypsinized, round cells (Figure 5(c)).

3.4. Cytoplasmic Protrusions. A more complex picture emerged when rat myoblasts were used. Three or more major cytoplasmic protrusions were frequently visible on freshly seeded cells, which emerged not necessarily on opposing poles (Figure 6). Again, initial protrusion of these structures closely followed the direction of the grooves. With increasing diameter during later stages of spreading, the cytoplasmic processes could trespass individual grooves. The cells displaying these features did not necessarily elongate exactly along the groove direction. Being pulled along distinct grooves, they could adopt a triangular or otherwise deformed shape and a skewed alignment with respect to the groove direction. Rat myoblasts could also develop large

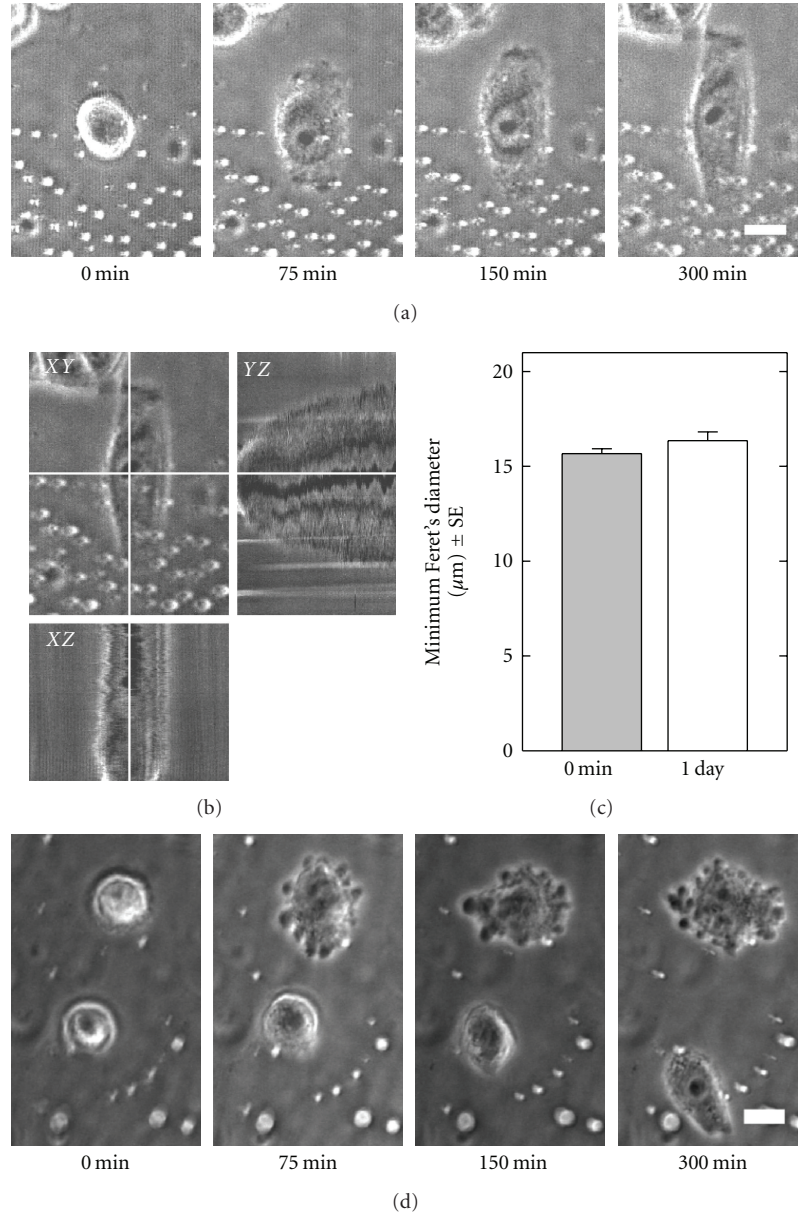


FIGURE 5: Attachment of CHO cells. (a) Time-lapse phase contrast microscopy of a freshly harvested CHO cell on a grooved substrate. Scale bar, 10 μm . (b) Orthogonal stack slices with time as the z-axis (300 minutes, 150 slices). The cell elongates along the vertically oriented grooves and displays little lateral spreading. (c) Average minimum Feret's diameter of freshly harvested, floating CHO cells (grey bar) and CHO cells cultured for one day on a grooved substratum (open bar). Both evaluations were performed for $n = 100$ cells. (d) Time-lapse phase contrast microscopy of a freshly harvested CHO cells on a unpatterned smooth substrate.

lamellipodia, which extended not only along the grooves, but also perpendicular to them, resulting in lateral spreading. In addition, freshly harvested rat myoblasts frequently had long filopodia, which could be visualized with the lipophilic membrane dye PKH26 (Figure 7(a)). Most filopodia showed highly dynamic expansion, motions and retractions, but some remained motionless and aligned with the groove direction. We never found CHO cells carrying comparable structures when stained with the dye. Only short cytoplasmic protrusions were observed. A fraction of these structures was aligned with the groove direction (Figure 7(b)).

Overall, our observations indicate that the rat myoblasts developed more complex morphological features (including multiple cytoplasmic protrusions, lamellipodia, and filopodia) than CHO cells. In order to have a simple quantitative measure for these observations, we reasoned that the solidity index of a simple oval or rod-shaped cell is equal to one, while more complex shapes will most likely have convex deficiencies along their boundaries. We therefore compared the solidities of rat myoblasts, attached either to the grooved surface or to control areas, with those of CHO cells. Significantly lower values were obtained for rat

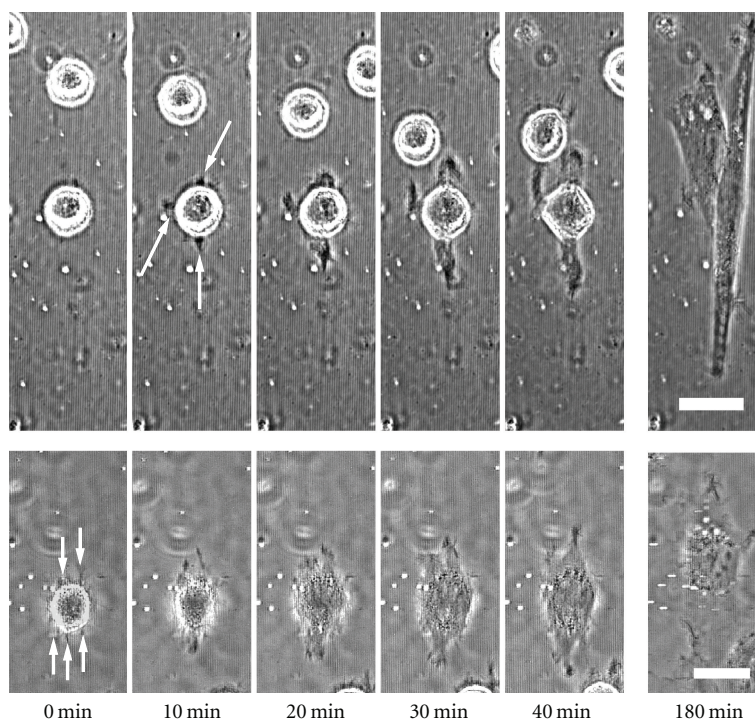


FIGURE 6: Time-lapse phase contrast images of rat myoblasts freshly seeded onto a grooved polyester film. The grooves were oriented vertically. Arrows indicate the location of cytoplasmic protrusions. The cell in the upper panel shows 3 major initial cytoplasmic protrusions, while multiple protrusions are visible on the cell in the lower panel. Scale bars, 20 μm .

myoblasts (Figure 8). There were no significant differences between cells of one type growing on grooves and control cells on unpatterned areas.

4. Discussion

Mechanical embossing of polyester films provided a convenient method to fabricate a grooved surface to study contact guidance of murine cells. Fairly smooth grooves (with an aspect ratio close to 0.2) were chosen to permit detectable, but not perfect alignment. The two cell lines employed reacted to the surface topology by aligning parallel to the direction of the grooves and by adopting an elongated morphology (Figures 2 and 3). Thus, they followed the general trend observed for a wide range of different cells on comparable surface topologies [4, 22]. The cells aligned primarily during attachment and spreading, regardless of whether they originated from mitosis of cells detaching from surface during culture (Figures 4 and 5). While both cell lines displayed orientation angles deviating little from the direction of the grooves, differences became apparent when analyzing the dynamics of cell attachment and spreading. One may distinguish several degrees of complexity of these processes. In the simple case, a cell follows bipolar dilation with little lateral expansion (apart from a prototypical CHO cell, melanocytes would be a good example). In this case, it may be feasible to describe the response to various surface geometries in a dose-response fashion as successfully done

by several authors [10, 23]. One has to postulate that these cells possess a kind of “quorum sensing” mechanism which allows the existence of not more than two poles and suppresses expansion in other directions. The integrin adhesion network [24] may be a candidate for this task. It must be a dynamic mechanism, since cells can adjust their alignment within a few hours, as indicated by recent work with surfaces with reconfigurable microtopography [25].

Rat myoblasts represented more complex cases. These cells frequently developed protrusions from more sites and/or protrusions with different morphologies (filopodia, lamellipodia), displayed lateral spreading and a deformed shape (Figure 6). These more elaborate morphologies appear to be cell-specific rather than the consequence of the surface topology, at least when quantified with the very basic shape descriptor solidity. However, a common observation was that many of the initial cellular processes emerging from a cell (except lamellipodia) protruded along the groove direction even if the cell as a whole displayed poor alignment with the surface feature after completing attachment. In other words, the protruding organelles of a cell may sense surface geometries at thresholds lower than those determined by measurement of the orientation of entire cells or cell populations. Consequently, it is not clear whether the cell-specific threshold values for contact guidance reported in the literature (which are usually estimated by measuring whole-cell orientations) truly reflect the ability of the cells to sense these geometries. It is quite possible that all mammalian cells share a very similar threshold, which is blurred by cell-specific morphological features affecting the overall cell orientation.

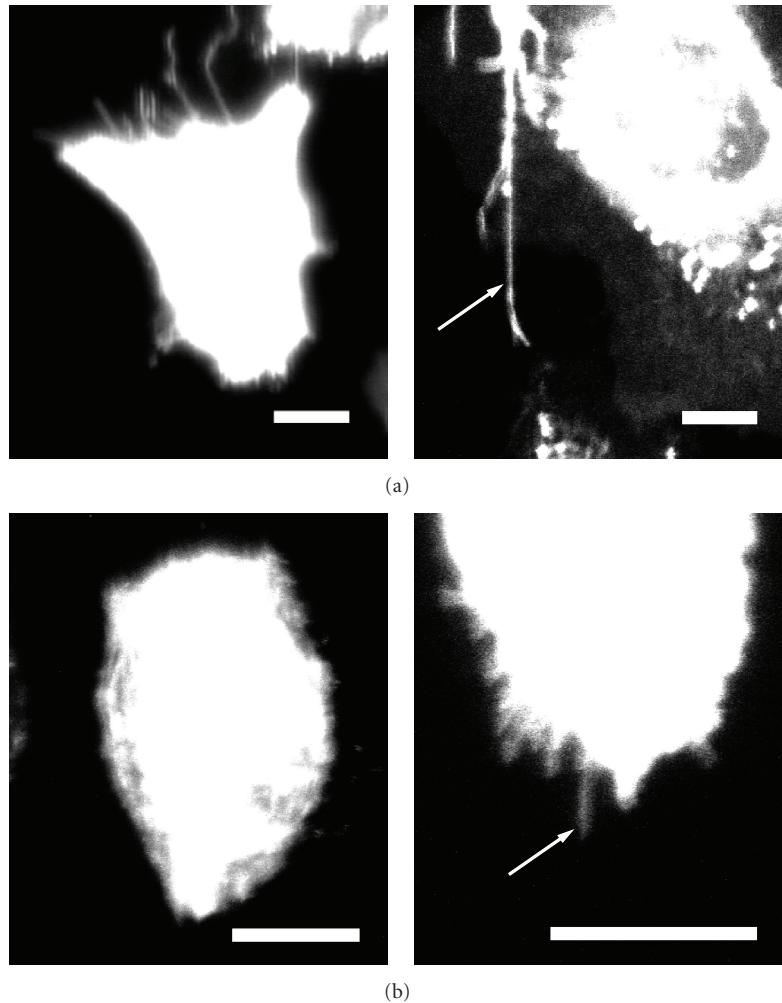


FIGURE 7: Fluorescence images of rat myoblasts (a) and CHO cells (b) growing for one day on grooved substrata. The cells were stained with the membrane dye PKH26 before seeding. The grooves were oriented vertically. Arrows indicate filopodia or cell protrusions aligned with the grooves. The myoblast cell shown in the upper right panel has partially internalized the dye. Scale bars, $10\ \mu\text{m}$.

Fujita et al. analyzed the dynamics of alignment of mesenchymal stem cells on a surface with similar topographical features as ours [26]. They found that cell protrusions expanded and retracted as if they were probing the surrounding area. Since protrusions perpendicular to the grooves tended to retract more rapidly than those with a parallel orientation, these authors suggested that the retraction phase is an important factor for cell alignment. The cogent idea behind their model is that cell protrusions extending perpendicular to the topographical feature can form focal adhesions only on the ridges, while protrusions extending in parallel can form stable complexes along their entire length. Thus, the latter could be less prone to retraction. The movements of the cell protrusions observed with our cell lines did not allow to distinguish clear cycles of extension and retraction (when viewed at low magnification, they appeared as almost continuous forward movements), but this concept is certainly worth to be further explored.

The role of filopodia in establishing alignment also remains a controversial issue. It is generally believed that

filopodia act as sensory organelles probing the environment [27]. They may determine the spatial localization of focal adhesions [28] and they respond to topographical features down to a threshold distance of approximately 35 nm [29]. In addition, filopodia aligned parallel to nanoscaled grooves were found after fixation of the cells (e.g., [15]). However, analysis of the movements of filopodia of mesenchymal stem cells on a grooved substratum did not reveal a specific direction [26]. Our observations also indicate that distinct filopodia are not a prerequisite for contact guidance. Under our cell culture conditions, we only observed short protrusions on CHO cells, although the response of this cell line to the patterned substratum generally outperformed that of rat myoblasts which frequently displayed long filopodia (Figure 7). Our observations do by no means argue against a general sensory role of filopodia. However, long filopodia can easily span the distance of several groove periodicities. During their movements, they often touch the substratum only with their tips. Hence, filopodia may be able to sense topographical features on a very restricted scale, but not

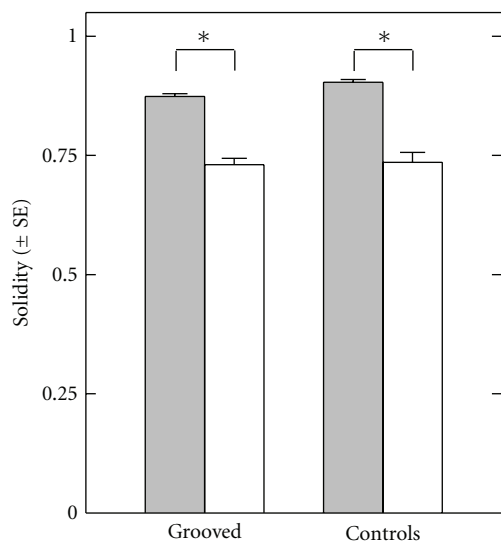


FIGURE 8: Average solidity of CHO cells (grey bar) and rat myoblasts (open bar) after one day of culture on a grooved polyester film or on adjacent unpatterned control areas ($n > 100$). Asterisks denote a statistically significant difference ($P < .05$).

the direction of grooves which are broader than the average diameter of filopodia. Alternatively, if they can sense the direction, multiple filopodia emerging from one cell with all probing different grooves may still be unable to pull a cell into a specific direction. Clearly, more detailed analyses of the movements of filopodia and the other cellular protrusions and quantification of traction forces applied to the substrate would be helpful to resolve their role in sensing surface topography.

5. Conclusion

We have here demonstrated that mechanical embossing of polymer foils can successfully be utilized to generate large quantities of patterned substrates to study the responses of cells to nanotopographical features. Our results suggest that the oriented spreading of the cell types studied is largely determined by the very first protrusions emerging from a cell, with their location being affected by subtle topographical features. In general, the rat myoblasts developed more complex morphological features (including multiple cytoplasmic protrusions, lamellipodia, and filopodia) than CHO cells. Our studies are still in the stage of basic. However, the findings of this work may be relevant for future applications in cell therapies, tissue engineering, and cell tests for development of novel pharmaceuticals.

Acknowledgment

This work was supported by the Austrian NANO initiative (Project no.NSI-NBPF).

References

- [1] J. Y. Lim and H. J. Donahue, "Cell sensing and response to micro- and nanostructured surfaces produced by chemical and topographic patterning," *Tissue Engineering*, vol. 13, no. 8, pp. 1879–1891, 2007.
- [2] L. Marcotte and M. Tabrizian, "Sensing surfaces: challenges in studying the cell adhesion process and the cell adhesion forces on biomaterials," *ITBM-RBM*, vol. 29, no. 2-3, pp. 77–88, 2008.
- [3] R. G. Flemming, C. J. Murphy, G. A. Abrams, S. L. Goodman, and P. F. Nealey, "Effects of synthetic micro- and nanostructured surfaces on cell behavior," *Biomaterials*, vol. 20, no. 6, pp. 573–588, 1999.
- [4] E. Martínez, E. Engel, J. A. Planell, and J. Samitier, "Effects of artificial micro- and nano-structured surfaces on cell behaviour," *Annals of Anatomy—Anatomischer Anzeiger*, vol. 191, no. 1, pp. 126–135, 2009.
- [5] S. Fujita, M. Ohshima, and H. Iwata, "Time-lapse observation of cell alignment on nanogrooved patterns," *Journal of the Royal Society Interface*, vol. 6, supplement 3, pp. S269–S277, 2009.
- [6] F. C. M. J. M. van Delft, F. C. van den Heuvel, W. A. Loesberg et al., "Manufacturing substrate nano-grooves for studying cell alignment and adhesion," *Microelectronic Engineering*, vol. 85, no. 5-6, pp. 1362–1366, 2008.
- [7] B. Wójciak-Stothard, A. Curtis, W. Monaghan, K. Macdonald, and C. Wilkinson, "Guidance and activation of murine macrophages by nanometric scale topography," *Experimental Cell Research*, vol. 223, no. 2, pp. 426–435, 1996.
- [8] B. Zhu, Q. Zhang, Q. Lu et al., "Nanotopographical guidance of C6 glioma cell alignment and oriented growth," *Biomaterials*, vol. 25, no. 18, pp. 4215–4223, 2004.
- [9] S. A. Biela, Y. Su, J. P. Spatz, and R. Kemkemer, "Different sensitivity of human endothelial cells, smooth muscle cells and fibroblasts to topography in the nano-micro range," *Acta Biomaterialia*, vol. 5, no. 7, pp. 2460–2466, 2009.
- [10] R. Kemkemer, S. Jungbauer, D. Kaufmann, and H. Gruler, "Cell orientation by a microgrooved substrate can be predicted by automatic control theory," *Biophysical Journal*, vol. 90, no. 12, pp. 4701–4711, 2006.
- [11] M. T. Lam, S. Sim, X. Zhu, and S. Takayama, "The effect of continuous wavy micropatterns on silicone substrates on the alignment of skeletal muscle myoblasts and myotubes," *Biomaterials*, vol. 27, no. 24, pp. 4340–4347, 2006.
- [12] A. I. Teixeira, P. F. Nealey, and C. J. Murphy, "Responses of human keratocytes to micro- and nanostructured substrates," *Journal of Biomedical Materials Research A*, vol. 71A, no. 3, pp. 369–376, 2004.
- [13] W.-B. Tsai and J.-H. Lin, "Modulation of morphology and functions of human hepatoblastoma cells by nano-grooved substrata," *Acta Biomaterialia*, vol. 5, no. 5, pp. 1442–1454, 2009.
- [14] A. M. Rajnicek, S. Britland, and C. D. McCaig, "Contact guidance of CNS neurites on grooved quartz: influence of groove dimensions, neuronal age and cell type," *Journal of Cell Science*, vol. 110, no. 23, pp. 2905–2913, 1997.
- [15] A. I. Teixeira, G. A. McKie, J. D. Foley, P. J. Bertics, P. F. Nealey, and C. J. Murphy, "The effect of environmental factors on the response of human corneal epithelial cells to nanoscale substrate topography," *Biomaterials*, vol. 27, no. 21, pp. 3945–3954, 2006.

- [16] E. Rebollar, I. Frischauf, M. Olbrich et al., "Proliferation of aligned mammalian cells on laser-nanostructured polystyrene," *Biomaterials*, vol. 29, no. 12, pp. 1796–1806, 2008.
- [17] W. A. Loesberg, J. te Riet, F. C. M. J. M. van Delft et al., "The threshold at which substrate nanogroove dimensions may influence fibroblast alignment and adhesion," *Biomaterials*, vol. 28, no. 27, pp. 3944–3951, 2007.
- [18] B. Zhu, Q. Lu, J. Yin, J. Hu, and Z. Wang, "Effects of laser-modified polystyrene substrate on CHO cell growth and alignment," *Journal of Biomedical Materials Research B*, vol. 70B, no. 1, pp. 43–48, 2004.
- [19] A. del Campo and E. Arzt, "Fabrication approaches for generating complex micro- and nanopatterns on polymeric surfaces," *Chemical Reviews*, vol. 108, no. 3, pp. 911–945, 2008.
- [20] T. Peterbauer, J. Heitz, M. Olbrich, and S. Hering, "Simple and versatile methods for the fabrication of arrays of live mammalian cells," *Lab on a Chip*, vol. 6, no. 7, pp. 857–863, 2006.
- [21] E. Meijering, M. Jacob, J.-C. F. Sarria, P. Steiner, H. Hirling, and M. Unser, "Design and validation of a tool for neurite tracing and analysis in fluorescence microscopy images," *Cytometry Part A*, vol. 58, no. 2, pp. 167–176, 2004.
- [22] C. J. Bettinger, R. Langer, and J. T. Borenstein, "Engineering substrate topography at the Micro- and nanoscale to control cell function," *Angewandte Chemie*, vol. 48, no. 30, pp. 5406–5415, 2009.
- [23] P. Clark, P. Connolly, A. S. G. Curtis, J. A. T. Dow, and C. D. W. Wilkinson, "Topographical control of cell behaviour: II. multiple grooved substrata," *Development*, vol. 108, no. 4, pp. 635–644, 1990.
- [24] B. Geiger, J. P. Spatz, and A. D. Bershadsky, "Environmental sensing through focal adhesions," *Nature Reviews Molecular Cell Biology*, vol. 10, no. 1, pp. 21–33, 2009.
- [25] M. T. Lam, W. C. Clem, and S. Takayama, "Reversible on-demand cell alignment using reconfigurable microtopography," *Biomaterials*, vol. 29, no. 11, pp. 1705–1712, 2008.
- [26] S. Fujita, D. Ono, M. Ohshima, and H. Iwata, "Supercritical CO₂-assisted embossing for studying cell behaviour on micro-textured surfaces," *Biomaterials*, vol. 29, no. 34, pp. 4494–4500, 2008.
- [27] P. K. Mattila and P. Lappalainen, "Filopodia: molecular architecture and cellular functions," *Nature Reviews Molecular Cell Biology*, vol. 9, no. 6, pp. 446–454, 2008.
- [28] C. Schäfer, B. Borm, S. Born, C. Möhl, E.-M. Eibl, and B. Hoffmann, "One step ahead: role of filopodia in adhesion formation during cell migration of keratinocytes," *Experimental Cell Research*, vol. 315, no. 7, pp. 1212–1224, 2009.
- [29] M. J. Dalby, N. Gadegaard, M. O. Riehle, C. D. Wilkinson, and A. S. Curtis, "Investigating filopodia sensing using arrays of defined nano-pits down to 35 nm diameter in size," *The International Journal of Biochemistry & Cell Biology*, vol. 36, no. 10, pp. 2005–2015, 2004.

Research Article

Nanoparticles of Conjugated Methotrexate-Human Serum Albumin: Preparation and Cytotoxicity Evaluations

**Azade Taheri,¹ Fatemeh Atyabi,^{1,2} Faranak Salman Nouri,¹ Fatemeh Ahadi,¹
Mohammad Ali Derakhshan,¹ Mohsen Amini,³ Mohammad Hossein Ghahremani,^{2,4}
Seyed Nasser Ostad,^{2,4} Pooria Mansoori,⁵ and Rassoul Dinarvand^{1,2}**

¹ Department of Pharmaceutics, Faculty of Pharmacy, Tehran University of Medical Sciences, P.O. Box 14155-6451, Tehran, Iran

² Nanotechnology Research Centre, Faculty of Pharmacy, Tehran University of Medical Sciences, Tehran, Iran

³ Department of Pharmacology, Faculty of Pharmacy, Tehran University of Medical Sciences, Tehran, Iran

⁴ Drug Design and Development Research Centre, Faculty of Pharmacy, Tehran University of Medical Sciences, Tehran, Iran

⁵ Faculty of Medicine, Ahvaz Jundishapur University of Medical Science, P.O. Box 12244-9876, Ahvaz, Iran

Correspondence should be addressed to Rassoul Dinarvand, dinarvand@tums.ac.ir

Received 1 June 2010; Revised 5 July 2010; Accepted 1 August 2010

Academic Editor: Libo Wu

Copyright © 2011 Azade Taheri et al. This is an open access article distributed under the Creative Commons Attribution License, which permits unrestricted use, distribution, and reproduction in any medium, provided the original work is properly cited.

Methotrexate-human serum albumin conjugates were developed by a simple carbodiimide reaction. Methotrexate-human serum albumin conjugates were then crosslinked with 1-ethyl-3-(3-dimethylaminopropyl) carbodiimide HCl (EDC) to form nanoparticles. The size of nanoparticles determined by laser light scattering and TEM was between 90–150 nm. Nanoparticles were very stable at physiologic conditions (PBS pH 7.4, 37°C) and after incubation with serum. The effect of amount of EDC used for crosslinking on the particle size and free amino groups of nanoparticles was examined. The amount of crosslinker showed no significant effect on the size of nanoparticles but free amino groups of nanoparticles were decreased by increasing the crosslinker. The physicochemical interactions between methotrexate and human serum albumin were investigated by differential scanning calorimetry (DSC). Nanoparticles were more cytotoxic on T47D cells compared to free methotrexate. Moreover, methotrexate-human serum albumin nanoparticles decreased the IC₅₀ value of methotrexate on T47D cells in comparison with free methotrexate.

1. Introduction

HSA as a drug carrier represents a new strategy for controlled drug delivery. Its use as a polymeric particulate system [1, 2] or conjugates with drug molecules [3] has been reported. HSA conjugates can localize drugs in special site and control the release of drugs. Therefore, HSA is considered as good candidate for drug delivery in cancer therapy [4]. MTX is a folate antagonist and is used widely in the treatment of human cancer. MTX induces cancer cure in women suffering from metastatic choriocarcinoma [5, 6]. Moreover this antimetabolite has several defects. After I.V. administration, MTX is rapidly cleared from circulation through the kidneys. Mean distribution half-life of MTX is 1.5–3.5 hrs [7]. Consequently, tumor exposure time of MTX is short. Several efforts have been made to

reduce MTX defects. In a study, MTX has been physically incorporated into bovine serum albumin nanoparticles to target and control the release of MTX in tumor environment [8]. A disadvantage of this system may be the increased chance of tumor resistance due to the sustained release of methotrexate. Moreover, non-targeted release of drugs may induce side effects [9]. Conjugation of cytotoxic drugs to carriers decreases the systemic toxicity and increases their therapeutic benefits [10]. HSA plays an important role as a nutrient for proliferating tumors; consequently HSA is a very good candidate for conjugating cytotoxic drugs [11]. Preparation of MTX-HSA conjugates have been reported before. Endo et al. studied the cytotoxicity of conjugated MTX on MM46 cells [12]. They showed that free MTX was more cytotoxic than MTX-HSA conjugates on the tumor cell line. In this study we have prepared MTX-HSA nanoparticles

using MTX-HSA conjugates. MTX-HSA nanoparticles with a size of less than 150 nm have a good chance to reach tumor cells through the porous membranes of vascular system as a result of enhanced penetration and retention (EPR) effect. Previous studies have shown the benefit of nanoparticles for the delivery of cytotoxic agents [13]. Moreover, the release of free MTX from nanoparticles in serum would be low thus fewer side effects would be expected [10]. The physicochemical characterizations of nanoparticles, the effect of the amount of crosslinker on particle size and free amino groups of nanoparticles, and stability properties of the MTX-HSA nanoparticles were evaluated.

2. Materials and Methods

2.1. Materials. Methotrexate USP was kindly donated by Cipla Pharmaceutical Co., India. 1-ethyl-3-(3-dimethylaminopropyl) carbodiimide HCl and human serum albumin (HSA) were purchased from Sigma (Steinheim, Germany). Total protein kit (Micro Lowry) was from Sigma (Saint Louis, USA). PMRI-1640 modified medium and penicillin/streptomycin solution were obtained from Gibco Invitrogen (Carlsbad, CA). MTT was obtained from Sigma (St. Louis, USA). Methanol and acetonitrile used as mobile phase in HPLC and DMSO were purchased from Merck (Darmstadt, Germany). Deionized water was used throughout the experiment. All other chemicals used were of reagent grade.

2.2. Preparation of MTX-HSA Conjugates. MTX (20 mg) with EDC (15 mg) was dissolved in DMSO (1.25 ml). The solution was placed in water bath at 50°C for 15 min. Then the solution was cooled to room temperature and was added to HSA solution (250 mg HSA in 2 ml PBS pH 7.4). After reaction time, unreacted MTX, EDC, and DMSO were removed using Amicon Ultra-4 Centrifugal Filter Devices (Millipore, USA).

2.3. Gel Permeation Chromatography (GPC). Gel permeation chromatography was carried out using a GPC system (Agilent 1100 Liquid Chromatographer, Agilent technologies, USA) with a refractive index detector (Agilent technologies, USA) and PL Aquagel-OH mixed gel-filtration column (300×7.5 mm internal diameter, pore size 8 µm; Agilent technologies, USA). Water at a flow rate of 1.2 ml/min was used as mobile phase. All experiments were performed at 23°C. HSA (50 mg/ml) and MTX-HSA conjugates (20 mg/ml) were dissolved in water separately and were injected to GPC system. Figure 1 shows the GPC chromatogram of MTX-HSA conjugate and HSA. The GPC chromatogram of MTX-HSA conjugate showed a peak at 19.8 min whereas a single peak was found for HSA. No additional peak was detected for free MTX and HSA in the GPC chromatogram of MTX-HSA conjugate. These results indicated that MTX was coupled to HSA successfully and no polymerization of HSA took place.

After analysis of MTX-HSA conjugate by GPC analysis, HPLC analysis was used for identifying the MTX-HSA conjugate and quantitative analysis of free MTX.

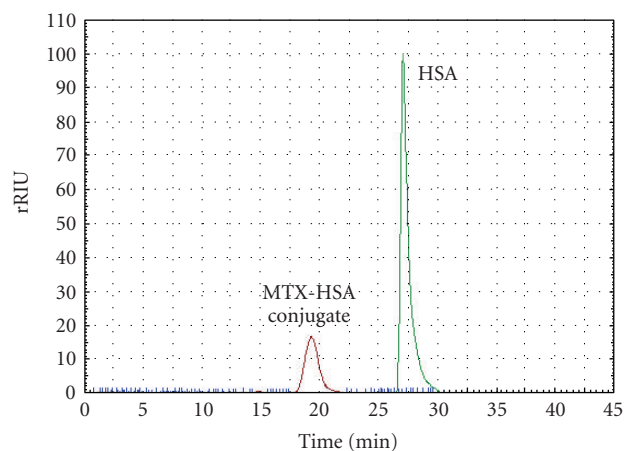


FIGURE 1: The GPC chromatogram of MTX-HSA conjugate and HSA.

2.4. High-Performance Liquid Chromatography Analysis of MTX and MTX-HSA Conjugate. MTX-HSA conjugates were characterized and tested for the content of free MTX using HPLC. The amount of free drug in the conjugates was determined by reverse-phase HPLC after precipitation of MTX-HSA conjugate and extraction of free MTX in an organic solvent. After addition of 2 mL of methanol containing ZnSO₄ (1% w/v) to the conjugates (2 mg) dissolved in water (0.5 mL), the samples were mixed and centrifuged for 10 minutes at 5000 rpm. The supernatant was analyzed using a C18 column (4.6 × 250 mm, pore size 5 µm; Teknokroma, Barcelona, Spain). The mobile phase (phosphate buffer pH 7.2: acetonitrile, 88:12 v/v) was delivered at a flow rate of 1.20 ml/min with a pump (WellChrom, K-1001, Knauer, Berlin, Germany). The free MTX was detected at 305 nm with an ultraviolet detector (WellChrom, K-2600, Knauer). Then a solution of methotrexate and a mixture solution of MTX and MTX-HSA conjugate were injected to the above system separately. In addition, 2 mg of MTX-HSA conjugate and 0.5 mg of MTX were dissolved in 0.5 ml 0.01 N NaOH and mixed; after addition of 1 mL of ethyl acetate, the samples were mixed and centrifuged for 10 minutes at 15000 rpm. The aqueous phase was discarded, and the organic solvent evaporated under nitrogen flow. The residues redissolved in methanol (100 µL) and were injected to the above HPLC system.

2.5. Preparation of MTX-HSA Nanoparticles. MTX (20 mg) with EDC (15 mg) was dissolved in DMSO (1.25 ml). The solution was placed in water bath at 50°C for 15 min. Then the solution was cooled to room temperature and was added to HSA solution (250 mg HSA in 2 ml PBS pH 7.4) at the rate of 1 ml/min under constant stirring (600 rpm). The MTX-HSA conjugates so formed were cross-linked by adding 5 mg EDC under constant stirring at room temperature for 4 h to produce MTX-HSA nanoparticles. Dialysis against PBS was performed (cellulose membrane, cutoff 12000 kDa from Merck, Germany) for removing unbound MTX, EDC, and DMSO. Nanoparticles were then lyophilized at -40°C for 48 h (Lyotrap Plus, LTE, scientific ltd, Oldham, UK).

2.6. Determination of MTX/HSA Molar Ratio in Nanoparticles. 12.5 mg of MTX-HSA nanoparticles was accurately weighed and dissolved in 4 ml of 0.1 N NaOH. MTX content was determined by using UV absorbance of the solution in 372 nm. The calibration plot of dissolved MTX in 0.1 N NaOH was linear in the range of 0.005–0.2 mg/ml. It was assumed that the molar absorptivity of MTX did not change by conjugation [14]. HSA absorbance was negligible at this wavelength. HSA content of nanoparticles was determined using Total Protein Kit, Micro Lowry, Peterson's Modification from Sigma-Aldrich.

2.7. Measurement of Size and Size Distribution of Nanoparticles. Lyophilized nanoparticles were suspended in PBS to make a 1% solution. Then the size, polydispersity and zeta potential of MTX-HSA nanoparticles were determined by Zetasizer Nano ZS (Malvern Instruments, Worcestershire, UK).

2.8. Transmission Electron Microscopy (TEM). Lyophilized nanoparticles were characterized by Transmission Electron Microscope (Zeiss EM 900, Jena, Germany).

2.9. Differential Scanning Calorimetry (DSC). The thermal behavior of MTX, HSA, physical mixture of MTX and HSA, and MTX-HSA nanoparticles was studied by Differential Scanning Calorimetry (DSC-60, Shimadzu, Japan) over a range of 20 to 200°C, at a scan rate of 10°C per min.

2.10. In Vitro Release of MTX. The release of MTX was evaluated by measuring the release of free MTX in phosphate buffer (pH 7.4) and serum as follows.

An exact amount of MTX-HSA conjugate nanoparticles, MTX-HSA conjugate, and MTX (20 mg) was dissolved in 2 ml of PBS (pH 7.4) separately. The solutions were introduced in dialysis tube (cellulose membrane, cutoff 12000 kDa, Merck, Germany). The tubes were placed into capped, wide mouth jars containing 10 ml of PBS (pH 7.4) as release medium. These jars were placed in a shaker water bath (37°C) for 72 hours. Every 24 hours, 0.1 ml of release mediums was removed and replaced with 0.1 ml of the same buffer solution. Samples were analyzed by high-performance liquid chromatography (HPLC) on a Teknokroma C18, 4.6 × 250 mm column at 305 nm to determine the free MTX [15]. 30 mg of MTX-HSA conjugate nanoparticles, MTX-HSA conjugate, and MTX were incubated with 3 ml of foetal calf serum (FCS) and then were placed in 37°C. Every 24 h free MTX was determined in FCS [15].

2.11. Determination of Amino Groups in Conjugates. The free amino groups of nanoparticles were determined using 2, 4, 6-trinitrobenzene-sulfonic acid (TNBS) [16]. After the reaction of nanoparticles with TNBS, nanoparticles were separated using Amicon Ultra-4 Centrifugal Filter Devices (Millipore, USA). The filtrate was analyzed for remaining free TNBS at 349 nm.

2.12. In Vitro Cytotoxicity of Nanoparticles. Human breast cancer cells (T47D) were cultivated in RPMI-1640 medium

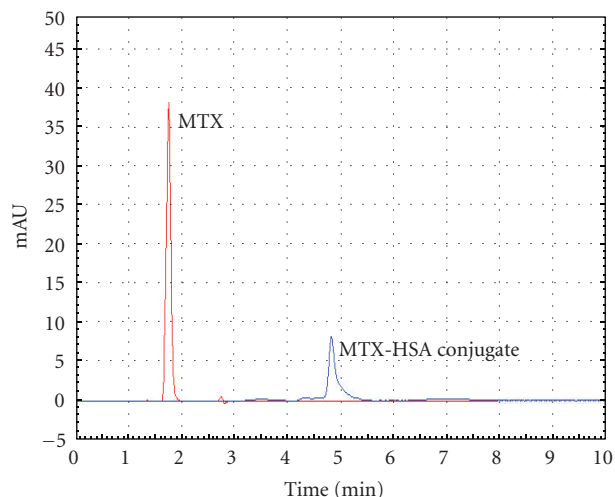


FIGURE 2: HPLC chromatogram of free MTX and MTX-HSA conjugate.

supplemented with 10% fetal bovine serum and 1% penicillin-streptomycin at 37°C in a humidified incubator with 5% CO₂. Cells were maintained in an exponential growth phase by periodic subcultivation.

T47D breast cancer cells were seeded in 96-well plates (Costar, IL, USA) at the density of 10000 viable cells/well and incubated 24 h to allow cell attachment. The medium was replenished every other day. The cells were incubated with the MTX and MTX-HSA nanoparticles at concentrations of 6.25 to 100 nM for 96 h. At appropriate time intervals, 20 µl of MTT (5 mg/ml in PBS) was added to each well, and the culture medium containing MTT solution was removed after 3–4 hrs. The formazan crystals were dissolved in 100 µl DMSO and read at 570 nm. Cell viability was calculated by the following equation:

$$\text{Cell viability (\%)} = \left(\frac{\text{Int}_s}{\text{Int}_c} \right) n \times 100, \quad (1)$$

where Int_s is the colorimetric intensity of the cells incubated with the samples and Int_c is the colorimetric intensity of the cells incubated with the phosphate buffer (pH 7.4) only as positive control. IC₅₀, the drug concentration at which 50% cell growth inhibited, was calculated by the curve fitting of the cell viability data using Prism 4.0 (Graphpad, San Diego, USA).

3. Results and Discussion

3.1. Characterization of MTX-HSA Conjugates. Figure 1 shows the GPC chromatogram of MTX-HSA conjugate and HSA. The GPC chromatogram of MTX-HSA conjugate showed a peak at 19.8 min whereas a single peak was found for HSA. There were not any additional peaks for free MTX and HSA in the GPC chromatogram of MTX-HSA conjugate. These results indicated that MTX was coupled to HSA successfully, and no polymerization of HSA took place.

Figure 2 shows the HPLC chromatogram of free MTX and MTX-HSA conjugate. Free MTX showed a single peak at

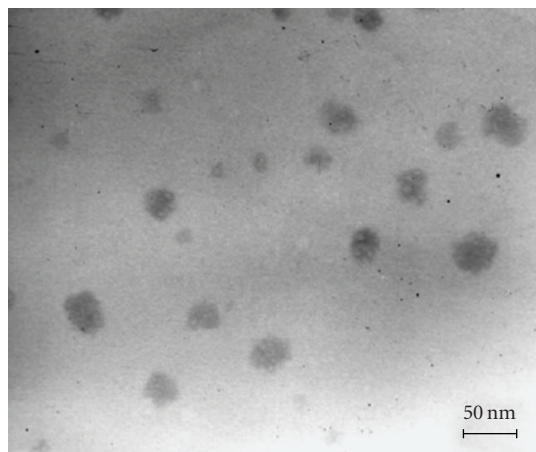


FIGURE 3: Transmission electron micrograph of MTX-HSA nanoparticles (MTX-HSA molar ratio: 2).

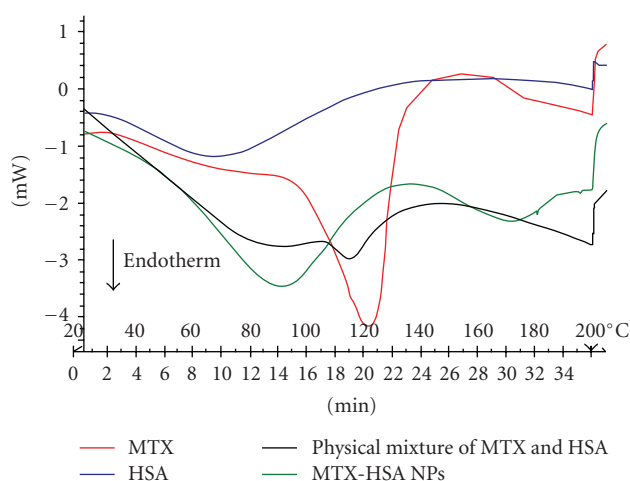


FIGURE 4: DSC thermogram of MTX, HSA, physical mixture of MTX and HAS and MTX-HSA nanoparticles.

1.9 min while the mixture solution of MTX-HSA conjugate and free MTX showed two separate peaks at 1.9 and 4.9 min. After injection of residues of liquid-liquid extraction with ethyl acetate, only one peak was detected at 1.9 min. Because in the process of liquid-liquid extraction with an organic solvent such as ethyl acetate, MTX-HSA conjugate remained in aqueous phase and only free MTX could have moved to the organic phase. This result confirms that the peak seen at 4.9 min is related to MTX-HSA conjugate.

3.2. Characterization of MTX-HSA Conjugated Nanoparticles.

Three types of nanoparticles were prepared with MTX-to-HSA molar ratios of approximately 2, 8, and 12. The size, drug content, zeta potential, and polydispersity of various samples are reported in Table 1. Nanoparticles were analyzed with TEM. Figure 3 shows the transmission electron micrographs of nanoparticles. The diameter of nanoparticles determined by laser light scattering was in the range of 90–150 nm. As can be seen in Figure 3 the size of nanoparticles

determined by TEM was approximately 50 nm. Laser light scattering measurements were aimed at providing average values for the hydrodynamic diameter while TEM is a direct, model independent technique depicting the internal structure of the individual nanoparticles. Smaller sizes of nanoparticles determined by TEM compared with laser light scattering have been previously reported [2].

Figure 4 shows the DSC thermograms of MTX, HSA, physical mixture of MTX and HSA, and MTX-HSA conjugate nanoparticles. Differential scanning calorimetry (DSC) technique was used to confirm successful conjugation of methotrexate to human serum albumin [17, 18]. The control experiments were carried out each using pure methotrexate, human serum albumin, and physical mixture of methotrexate and human serum albumin. The two endothermic peaks of physical mixture of methotrexate and human serum albumin (78°C and 120°C) are similar to endothermic peaks of pure methotrexate (122°C) and pure human serum albumin (70°C) whereas an endothermic peak (90°C) was observed for MTX-HSA conjugate. The analysis of calorimetric data suggested that conjugation of methotrexate to human serum albumin led to a shifting of the T_m to lower temperatures. Compared to MTX, HSA and physical mixture of methotrexate and human serum albumin, apparent difference observed in the thermal behaviors and physicochemical properties of MTX-HSA conjugates supports the possibility of conjugation of methotrexate to human serum albumin.

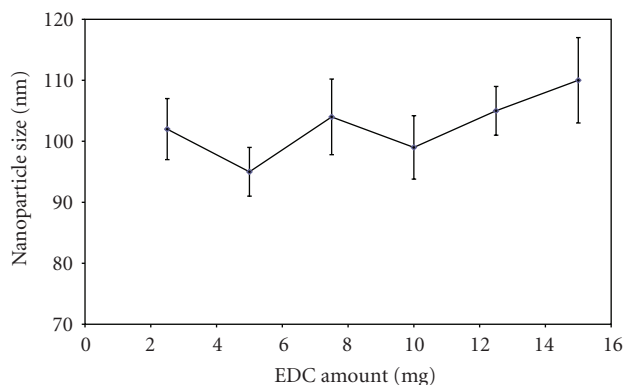
Figure 5(a) shows the particle size of MTX-HSA nanoparticles cross-linked with different amount of EDC (2.5, 5, 7.5, 10, 12.5, and 15 mg). The results indicate that the amounts of EDC used for cross-linking did not have significant effect on the size of nanoparticles. Figure 5(b) shows that by increasing the amount of cross-linker the free amino groups per HSA molecule are decreased.

3.3. In Vitro Release of MTX. MTX-HSA nanoparticles were stable in both phosphate buffer (pH 7.4) and fetal calf serum (FCS) at 37°C. After 72 hours, only 5% and 9% of MTX were released from MTX-HSA nanoparticles in phosphate buffer and FCS media, respectively. Nanoparticles with different MTX/HSA molar ratios released similar amount of MTX at physiologic condition (PBS pH 7.4 and 37°C) and after incubation with FCS. 6% and 10.2% of MTX were released from MTX-HSA conjugates in PBS pH 7.4 and FCS, respectively. It is obvious that 100% of free MTX were released in PBS pH 7.4 and 37°C and after incubation with FCS.

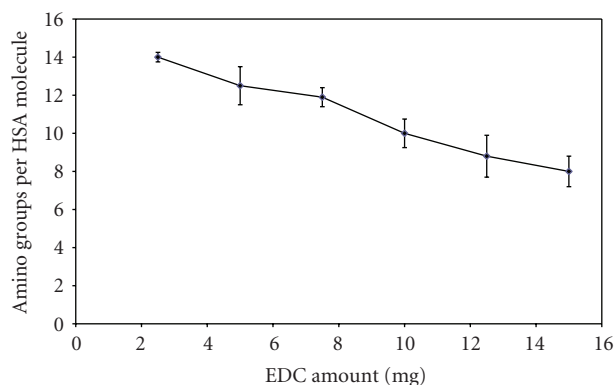
3.4. In Vitro Cytotoxicity of Nanoparticles. Figure 6 shows the in vitro cytotoxicity of free MTX drug and MTX-HSA nanoparticles with different molar ratios of MTX to HSA on T47D breast cancer cells. As can be seen the cytotoxicity of MTX-HSA nanoparticles on T47D cells was significantly higher than that of free MTX. It can also be seen that MTX-HSA conjugates inhibited the cell proliferation even in lower concentration at 96 h. The IC₅₀ (the dose which produces

TABLE 1: Preparation and characterization variables and parameters of MTX-HSA conjugate nanoparticles.

Sample	MTX (mg)	HSA (mg)	EDC used for MTX conjugation (mg)	MTX/HSA molar ratio	Particle diameter (nm)	Zeta Potential (mV)	Polydispersity
1	20	250	15	12 ± 0.12	150.3 ± 5.1	-16 ± 0.2	0.20 ± 0.01
2	20	350	15	8 ± 0.18	111.7 ± 4.6	-12 ± 0.5	0.10 ± 0.01
3	20	700	15	2 ± 0.09	95.5 ± 3.2	-9 ± 0.2	0.12 ± 0.01



(a)



(b)

FIGURE 5: The effect of the amount of EDC on the size of MTX-HSA nanoparticles (a) and the number of free amino groups on the surface of nanoparticles (b).

50% inhibition of growth) of free MTX drug and MTX-HSA nanoparticles on T47D cells with incubation time of 96 h is shown in Table 2. These data show that MTX-HSA nanoparticles decreased the IC₅₀ value of MTX on T47D breast cancer cells in comparison with free MTX.

Drug-carrier conjugated systems may be internalized by different cell types, suggesting that they may be a suitable carrier system for the transport of drugs into cells [19]. Nanoparticles formulations might improve drug deposition and activity while reducing systemic toxicity and adverse events [20]. The conjugation of cytotoxic drugs to carriers can decrease the adverse reaction of these drugs. There are different strategies for using albumin as a drug delivery

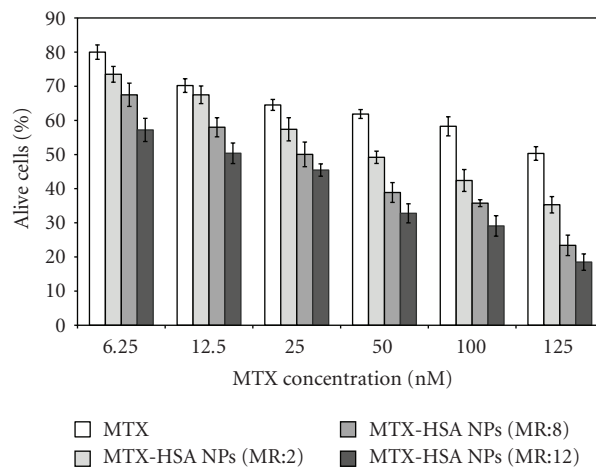


FIGURE 6: Cytotoxicity effect of free methotrexate and MTX-HSA NPs on T47D breast cancer cells after 96 h.

system for cancer therapy [21]. One strategy may be the preparation of albumin particles loaded with cytotoxic agent [8]. The disadvantage of this method is that release of the cytotoxic agent in blood circulation induces side effects. Another strategy is the conjugation of cytotoxic agents to HSA [3, 22]. The disadvantage of this system is the lower toxicity of the conjugated system in comparison to the free drug [22]. However, there are other reports showing higher cytotoxicity for the conjugated systems including the current study [3]. In this study we tried to prepare nanoparticles from MTX-HSA conjugates to increase the cytotoxicity of the system on one hand and to reduce the presumed side effects of the system on another hand. Three types of nanoparticles with different molar ratios of MTX to HSA were produced by variation of the amount of HSA used in synthesis. Carboxylic acid groups of MTX were activated by EDC coupling agent. These activated groups react with primary amino groups of albumin. We used DMSO as a solvent for both MTX and EDC. DMSO plays the role of desolvating agent for HSA molecules. Nanoparticles were prepared by desolvation process and then were stabilized by addition of different amounts of EDC as cross-linker. EDC acts as the crosslinking agent between carboxylic acid groups of HSA and free amino groups of HSA. Figure 5(a) demonstrates that the concentration of cross-linker above 2% (5 mg EDC for 250 mg albumin) has no significant effect on the size of nanoparticles. Increasing

TABLE 2: IC₅₀ of MTX and MTX-HSA nanoparticles on T47D breast cancer cells after 96 h.

	MTX	MTX-HSA NPs (MR:2)*	MTX-HSA NPs (MR:8)	MTX-HSA NPs (MR:12)
IC ₅₀ (nM)	123.4 ± 4.2	45.6 ± 2.5	24.6 ± 3.4	14.3 ± 2.9

*MR: molar ratio of MTX/HAS.

the amount of cross-linker decreased the free amino groups of nanoparticles (Figure 5(b)). Low drug release from the system both in phosphate buffer (pH 7.4) and in serum indicates the stability of the nanoparticles. Consequently, after I.V. administration of nanoparticles, the concentration of free MTX in plasma will be very low, hence less side effects are expected. The results of cytotoxicity test indicated the higher cytotoxicity of MTX-HSA nanoparticles compared to that of free MTX free drug. The cell viability measured at 125 nM drug concentration was decreased from 50.3% for MTX free drug to 35.3%, 23.4%, and 18.5% for the MTX-HSA nanoparticles with MTX-to-HSA molar ratio of 2, 8, and 12, respectively, after 96 h of incubation. As can be seen in Figure 6, MTX-HSA nanoparticles prepared using higher molar ratio of MTX to HSA showed better inhibition of cell proliferation even at low drug concentration (6.25 nM) ($P < .05$). The IC₅₀ of MTX in the MTX-HSA nanoparticles with molar ratio of 2, 8, and 12 is 2.5-, 5-, and 10-fold lower than that of free MTX on T47D cells, respectively.

The increased antitumor activity of MTX-HSA nanoparticles may be related to enhanced transendothelial cell transport of albumin which is mediated by the gp60 (albumin) receptor and caveolar transport [23, 24]. Albumin binding to gp60 activates caveolin-1 resulting in the formation of caveoli, which transport albumin and other plasma constituents across the endothelial cell to the interstitial space. The increased antitumor activity of MTX-HSA nanoparticles may also be related to the enhanced intratumor delivery of MTX. The gp60 receptors are specific for albumin and, once activated, allow for transport of albumin complexes across blood vessel wall barriers into underlying tumor tissue [25]. Moreover, MTX has similar structure to folate. It is possible that the molecules of methotrexate on the surface of nanoparticles play the role of targeting moieties and increase the transendothelial transport and cytotoxic effect of MTX-HSA nanoparticles.

4. Conclusion

MTX was successfully conjugated to HSA using EDC. The conjugates were then crosslinked using EDC to prepare nanoparticles with a size range of 90 to 150 nm. The nanoparticles prepared in this study were shown to be more soluble in aqueous and PBS media. It was also shown that the MTX-HSA conjugated nanoparticles were of more cytotoxic effect on T47D cell line than MTX free drug. In conclusion it can be said that the MTX-HSA nanoparticles were showed to be superior in vitro antitumor activity when compared to MTX free drug. These nanoparticles appear to be a good candidate for further antitumor tests in animal models.

Abbreviations

HSA: Human serum albumin
 MTX: Methotrexate
 MTX-HSA: Methotrexate-Human serum albumin
 EDC: 1-ethyl-3-(3-dimethylaminopropyl) carbodiimide HCl

References

- [1] W. Chen, B. Gu, H. Wang, J. Pan, W. Lu, and H. Hou, "Development and evaluation of novel itraconazole-loaded intravenous nanoparticles," *International Journal of Pharmaceutics*, vol. 362, no. 1-2, pp. 133-140, 2008.
- [2] S. Das, R. Banerjee, and J. Bellare, "Aspirin loaded albumin nanoparticles by coacervation: implications in drug delivery," *Trends in Biomaterials and Artificial Organs*, vol. 18, no. 2, pp. 203-212, 2005.
- [3] F. Esmaeili, R. Dinarvand, M. H. Ghahremani et al., "Docetaxel-albumin conjugates: preparation, in vitro evaluation and biodistribution studies," *Journal of Pharmaceutical Sciences*, vol. 98, no. 8, pp. 2718-2730, 2009.
- [4] T. Tanaka, P. Decuzzi, M. Cristofanilli et al., "Nanotechnology for breast cancer therapy," *Biomedical Microdevices*, vol. 11, no. 1, pp. 49-63, 2009.
- [5] R. Hertz, J. Lewis Jr., and M. B. Lipsett, "Five years' experience with the chemotherapy of metastatic choriocarcinoma and related trophoblastic tumors in women," *American Journal of Obstetrics and Gynecology*, vol. 82, no. 3, pp. 631-640, 1961.
- [6] J. R. Bertino, "Ode to methotrexate," *Journal of Clinical Oncology*, vol. 11, no. 1, pp. 5-14, 1993.
- [7] S. Friberg and S. Mattson, "On the growth rates of human malignant tumors: implications for medical decision making," *Journal of Surgical Oncology*, vol. 65, no. 4, pp. 284-297, 1997.
- [8] K. Santhi, S. A. Dhanaraj, M. Koshy, S. Ponnusankar, and B. Suresh, "Study of biodistribution of methotrexate-loaded bovine serum albumin nanospheres in mice," *Drug Development and Industrial Pharmacy*, vol. 26, no. 12, pp. 1293-1296, 2000.
- [9] S. Jayaprakash, S. Mohamed Halith, P. U. Mohamed Firthouse, K. Kulaturanpillai, Abhijith, and M. Nagarajan, "Preparation and evaluation of biodegradable microspheres of methotrexate," *Asian Journal of Pharmaceutics*, vol. 3, no. 1, pp. 26-29, 2009.
- [10] L. W. Seymour, "Passive tumor targeting of soluble macromolecules and drug conjugates," *Critical Reviews in Therapeutic Drug Carrier Systems*, vol. 9, no. 2, pp. 135-187, 1992.
- [11] G. Stehle, H. Sinn, A. Wunder et al., "Plasma protein (albumin) catabolism by the tumor itself—implications for tumor metabolism and the genesis of cachexia," *Critical Reviews in Oncology/Hematology*, vol. 26, no. 2, pp. 77-100, 1997.
- [12] N. Endo, Y. Kato, and Y. Takeda, "In vitro cytotoxicity of a human serum albumin-mediated conjugate of methotrexate with anti-MM46 monoclonal antibody," *Cancer Research*, vol. 47, no. 4, pp. 1076-1080, 1987.

- [13] F. Esmaeili, R. Dinarvand, M. H. Ghahremani, S. N. Ostad, H. Esmaily, and F. Atyabi, "Cellular cytotoxicity and in-vivo biodistribution of docetaxel poly(lactide-co-glycolide) nanoparticles," *Anti-Cancer Drugs*, vol. 21, no. 1, pp. 43–52, 2010.
- [14] A. Kosasih, B. J. Bowman, R. J. Wigent, and C. M. Ofner III, "Characterization and in vitro release of methotrexate from gelatin/methotrexate conjugates formed using different preparation variables," *International Journal of Pharmaceutics*, vol. 204, no. 1-2, pp. 81–89, 2000.
- [15] B. Nuernberg, M. Kohlbrenner, R. Faulkner, and D. Furst, "Rapid quantitation of methotrexate and its metabolites in human serum, urine and bile, using solid-phase extraction and high-performance liquid chromatography," *Journal of Chromatography*, vol. 487, no. 2, pp. 476–482, 1989.
- [16] A. F. S. A. Habeeb, "Determination of free amino groups in proteins by trinitrobenzenesulfonic acid," *Analytical Biochemistry*, vol. 14, no. 3, pp. 328–336, 1966.
- [17] N. M. Anande, S. K. Jain, and N. K. Jain, "Con-A conjugated mucoadhesive microspheres for the colonic delivery of diloxanide furoate," *International Journal of Pharmaceutics*, vol. 359, no. 1-2, pp. 182–189, 2008.
- [18] G. Yousefi, S. M. Foroutan, A. Zarghi, and A. Shafaati, "Synthesis and characterization of methotrexate polyethylene glycol esters as a drug delivery system," *Chemical and Pharmaceutical Bulletin*, vol. 58, no. 2, pp. 147–153, 2010.
- [19] B. Wang, W. Qiao, Y. Wang, L. Yang, Y. Zhang, and P. Shao, "Cancer therapy based on nanomaterials and nanocarrier systems," *Journal of Nanomaterials*, vol. 2010, Article ID 796303, 9 pages, 2010.
- [20] M. Brzoska, K. Langer, C. Coester, S. Loitsch, T. O. F. Wagner, and C. V. Mallinckrodt, "Incorporation of biodegradable nanoparticles into human airway epithelium cells—in vitro study of the suitability as a vehicle for drug or gene delivery in pulmonary diseases," *Biochemical and Biophysical Research Communications*, vol. 318, no. 2, pp. 562–570, 2004.
- [21] F. Kratz, "Albumin as a drug carrier: design of prodrugs, drug conjugates and nanoparticles," *Journal of Controlled Release*, vol. 132, no. 3, pp. 171–183, 2008.
- [22] M. C. Garnett and R. W. Baldwin, "An improved synthesis of a methotrexate-albumin-791T/36 monoclonal antibody conjugate cytotoxic to human osteogenic sarcoma cell lines," *Cancer Research*, vol. 46, no. 5, pp. 2407–2412, 1986.
- [23] T. A. John, S. M. Vogel, C. Tiruppathi, A. B. Malik, and R. D. Minshall, "Quantitative analysis of albumin uptake and transport in the rat microvessel endothelial monolayer," *American Journal of Physiology*, vol. 284, no. 1, pp. L187–L196, 2003.
- [24] W. Schubert, P. G. Frank, B. Razani, D. S. Park, C.-W. Chow, and M. P. Lisanti, "Caveolae-deficient endothelial cells show defects in the uptake and transport of albumin in vivo," *Journal of Biological Chemistry*, vol. 276, no. 52, pp. 48619–48622, 2001.
- [25] N. Desai, V. Trieu, Z. Yao et al., "Increased antitumor activity, intratumor paclitaxel concentrations, and endothelial cell transport of cremophor-free, albumin-bound paclitaxel, ABI-007, compared with cremophor-based paclitaxel," *Clinical Cancer Research*, vol. 12, no. 4, pp. 1317–1324, 2006.

Research Article

Preparation and Characterization of Self-Emulsified Docetaxel

Gyeong Hae Kim, Ju Young Lee, Yun Mi Kang, Kkot Nim Kang, E. Sle Kim, Da Yeon Kim, Jae Ho Kim, and Moon Suk Kim

Department of Molecular Science and Technology, Ajou University, Suwon 443-749, Republic of Korea

Correspondence should be addressed to Moon Suk Kim, moonskim@ajou.ac.kr

Received 3 June 2010; Revised 2 August 2010; Accepted 11 August 2010

Academic Editor: Lu Sun

Copyright © 2011 Gyeong Hae Kim et al. This is an open access article distributed under the Creative Commons Attribution License, which permits unrestricted use, distribution, and reproduction in any medium, provided the original work is properly cited.

The aim of this paper was to prepare a self-microemulsifying docetaxel (Dtx) using PLGA, Tetraglycol, Labrasol, and Cremophor ELP. The prepared Dtx-loaded self-microemulsifying system (SMES) showed the initial size of the range of 80–100 nm with narrow size distribution and the negative zeta-potential values. Its morphology was a spherical shape by atomic force microscopy. In experiment of stability, Dtx-loaded SMES prepared in DW and BSA condition showed good stability at 37°C for 7 days. The viability of the B16F10 cells incubated with Dtx-loaded SMES, Dtx-solution, and Taxol were decreased as a function of incubation time. In conclusion, we confirmed that Dtx-loaded SMES showed an inhibitory effect for proliferation of B16F10 melanoma cells.

1. Introduction

The first-line treatment of various cancers includes surgery, radiotherapy, or a combined treatment regimen [1–4]. As second-line treatment for cancer, the chemotherapy using anticancer drugs may be treated to remove completely cancers [1–6]. Many highly potent anticancer drugs are clinically treated as available commercial products. However, the utility of these cancer chemotherapeutic drugs in clinical applications is limited by very low solubility in aqueous [7, 8].

Paclitaxel (Ptx), isolated from the bark of *Taxus brevifolia*, has significant activity against a variety of tumors such as breast cancer, advanced ovarian carcinoma, lung cancer, and head and neck carcinoma [9]. Docetaxel (Dtx) is also an anticancer drug belonging to the second generation of the taxoid family [10]. Ptx and Dtx are hydrophobic drugs with poor aqueous solubility [11, 12]. To enhance solubility of Ptx, it is currently formulated for clinical application as Taxol by Cremophor EL-based solvent system containing dehydrated ethanol [13].

Recently, various formulations such as liposomes, emulsions, micelles, microspheres, and polymeric nanoparticles have been employed for the encapsulating Ptx and Dtx including several anticancer drugs [14–20]. The selection of

a proper Ptx and Dtx encapsulating formulation is important to improve the instability problems such as subsequent precipitation of the solubilised hydrophobic Ptx and Dtx for in vivo treatment.

The poor water solubility of Ptx and Dtx can be improved by the formulation with oil, low molecular weight surfactants, and so forth. The self-microemulsifying system (SMES) are isotropic mixtures of oil, a surfactant, and cosurfactants, which form fine oil-in-water emulsions when exposed to aqueous media [21–23]. Thus, the SMES was found to be highly suitable for the incorporation of hydrophobic Ptx and Dtx. Because SMES may be a promising way to load hydrophobic Dtx in delivery system, here, we report on the preparation of Dtx-loaded SMES which could result in an improvement of stability of the solubilised hydrophobic Dtx in aqueous media.

2. Materials and Methods

2.1. Materials. Poly (D,L-lactide-co-glycolide) (PLGA, molecular weight, 8,000, 20,000 and 90,000 g/mole) was purchased from Boehringer Ingelheim (Ingelheim, Germany). Docetaxel was purchased from Naprod Life Science Pvt, Ltd (India). Paclitaxel (Genexol) was purchased from Samyang

TABLE 1: Formulation for the preparation of Dtx-loaded SMES.

Composition (g, w/w)	Formulation		
	F1	F2	F3
Drug (Docetaxel)		0.003	
Solubilizer (Tetraglycol)		0.5	
PLGA 8k g/mol	0.005		
PLGA 20k g/mol		0.005	
PLGA 90k g/mol			0.005
Cosurfactant (Labrasol)		0.14	
Surfactant (Cremophor ELP)		0.16	
Zeta-potential (mV)	-7.7 ± 0.4	-2.8 ± 1.3	-4.3 ± 0.6

Genex Co. (Seoul, Korea). Caprylocaproyl macrogol-8 glyceride (Labrasol) was obtained from Gattefosse (Westwood, NJ, USA). Cremophor ELP was purchased from BASF (Germany). Tetraglycol was purchased from Sigma Chemical Co. (St. Louis, MO, USA). All other chemicals were of reagent grade. The deionized water (DW) was prepared by a Milli-Q purification system from Millipore (Molsheim, France).

2.2. Preparation of Dtx-Loaded SMES, Dtx-Solution, and Taxol. A series of SMES was prepared in each of the various formulas with PLGA, docetaxel, solubilizer, surfactant, and cosurfactant. Briefly, PLGA, Dtx, Tetraglycol, Labrasol, and Cremophor ELP in the various ratios (Table 1) were added into the vial, followed by heating on a hot plate to 60–70°C with stirring and vortex mixing until Dtx had perfectly dissolved. A solution of 3 mg of SMES was carefully weighed in 10 mL tube. It was then emulsified by contacting to 7 mL DW and vortexed, followed by keeping at room temperature for about 30 minutes to use in subsequent studies. The prepared Dtx-loaded SMES used without any purification. A 6 mg of Dtx and Ptx was added into 10 mL mixture of Cremophor EL and ethanol (v/v = 1/1) to prepare Dtx-solution and Taxol, respectively [19–21].

2.3. Dtx Encapsulation Efficiency. The Dtx-loaded SMES and Dtx-solution prepared as final concentration of 0.43 mg/mL of Dtx in 7 mL DW. The flask was allowed to equilibrate for 30 minutes at RT. The solution was thereafter filtered through a filter paper. The Dtx encapsulation efficiency in the solution was analyzed using a high-performance liquid chromatography (HPLC), Agilent 1200 series LC system equipped with detection at 220 nm using a diode array detector (Agilent Technologies, Inc., Santa Clara, USA). A Sunfire C18 column (4.6 × 150 mm, 5 μm) was used. The mobile phase consisted of a distilled water:acetonitrile:methanol (41:48:11 v/v) mixture, and the column was eluted at a flow rate of 1.0 mL/min. The Dtx encapsulation efficiency was calculated by comparison with the standard calibration curves prepared with known concentrations of Dtx. Three

independent Dtx-loaded SMES experiments were performed for each Dtx encapsulation efficiency and then averaged.

2.4. Size Analysis of Dtx-Loaded SMES, Dtx-Solution and Taxol. For analysis, formulation (50 μL) of Dtx-loaded SMES, Dtx-solution and Taxol were diluted with 50 mL DW in volumetric flask, followed by vortex mixing gently mixed. The particle size, size distribution, and surface charge of resultant formulation were determined by dynamic light scattering (DLS, ELS-8000, Photol, Japan) at room temperature. The analysis was individually measured for three samples of Dtx-loaded SMES, Dtx-solution, and Taxol, and then calculated as average value using three individual sizes.

2.5. Morphology of Dtx-Loaded SMES. The shape and surface morphology were investigated by atomic force microscopy (AFM). A 10 μL of Dtx-loaded SMES was transferred onto silicon wafer which was washed with MeOH. The wafer was quickly placed in liquid nitrogen, followed by the freeze-drying for 2 days. AFM measurements were carried out in the tapping mode with a nanoscope IV instrument (Digital Instruments Inc.).

2.6. Stability of Dtx-Loaded SMES, Dtx-Solution, and Taxol. Dtx-loaded SMES, Dtx-solution, and Taxol were prepared with 7 mL DW or a solution of 0.9% NaCl and 5% bovine serum albumin (Bovogen, Australia) and individually placed in 10 mL tube. The tube was constantly shaken at 100 rpm and 37°C for 7 days. At the set time, the droplet size was individually measured for three samples of Dtx-loaded SMES, Dtx-solution, and Taxol, and then calculated as average value.

2.7. Cell Culture. B16F10 melanoma cell line was obtained by Korea Cell Line Bank and cultured in culture media (MEM (Minimum Essential Medium, Gibco BRL, USA) supplemented with 10% fetal bovine serum (Gibco BRL, USA) and 1% PS (Penicillin streptomycin, Gibco BRL, USA)), and maintained at 37°C in 5% CO₂ humidified atmosphere. The cells were seeded into 75-cm² flasks, cultured, and changed medium every 2 days.

2.8. Cell Cytotoxicity Tests. B16F10 cell suspension (2 × 10⁴ cells/well) was seeded in a 48-well plate. The cells were incubated overnight to allow for cell attachment under culture media. The cells were incubated without and with Dtx-loaded SMES, Dtx-solution, and Taxol for 7 days without changing of culture media [19–21]. The final concentration of the Dtx and Ptx in the cell culture medium was adjusted to 1 μg/mL. Cell viability was determined by using water-soluble enzyme substrate MTT which was converted to purple water-insoluble product formazan accumulated in the cytoplasm of viable cells. Cell viability of each well performed individually and then calculated as average value. In brief, 100 μL of PBS solution of the MTT tetrazolium substrate (5 mg/mL) was added after 1, 4, and 7 days. After incubation for 4 h at 37°C, the resulting purple formazan precipitate was solubilized by the addition of 1 mL of DMSO and shaken

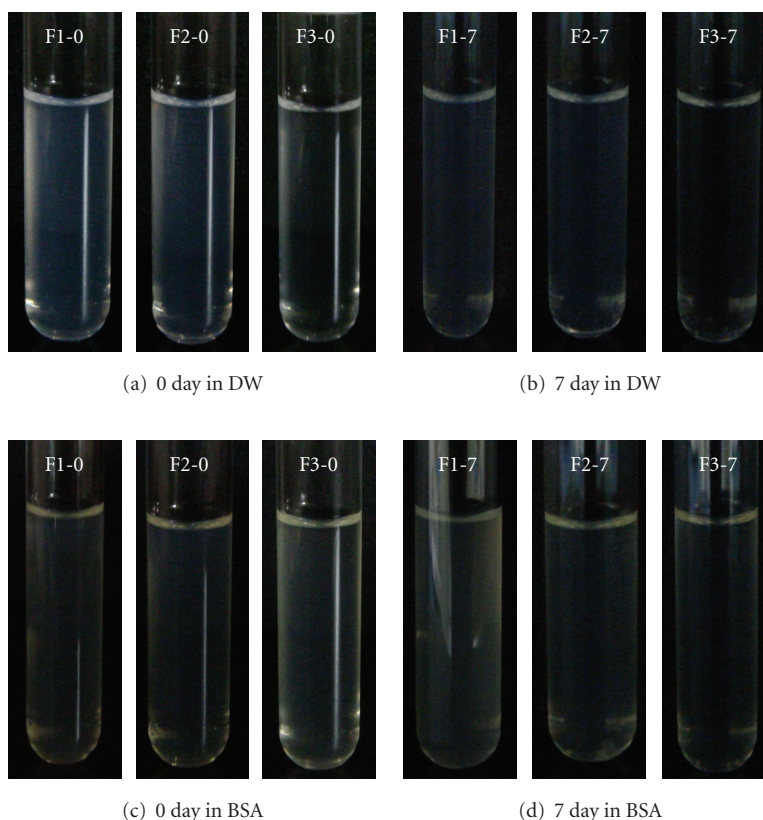


FIGURE 1: Pictures (a, c) before and (b, d) after incubation at 37°C for 7 days of Dtx-loaded SMES prepared in (a, b) DW and (c, d) BSA with different formulations F1–F3.

for 30 minutes. An aliquot from each well (100 μ L) was transferred to 96-well plates and then read using a plate reader of an ELISA (E-max, Molecular Device, USA). The optical density of each well was determined at 590 nm.

2.9. Statistical Analysis. Cytotoxicity data were obtained from independent experiments in which each of the five treatment conditions were tested in triplicate. All data are presented as means \pm standard deviations (SD). The results were analyzed by one-way ANOVAs using the Prism 3.0 software package (GraphPad Software Inc., San Diego, CA, USA).

3. Results and Discussion

3.1. Preparation of Dtx-Loaded SMES. The Dtx-loaded SMES were prepared by using Dtx, tetraglycol, Cremophor ELP, Labrasol, and PLGA; the formulation is summarized in Table 1. The prepared Dtx-loaded SMES were observed visually. As shown in Figure 1(a) Dtx-loaded SMES (F1–F3) showed the transparent emulsion solution for all formulations, indicating that Dtx was successfully incorporated into the SMES. The Dtx encapsulation efficiency is above 70%. Dtx-solution and Taxol showed the transparent solution.

The size and size distribution of Dtx-loaded SMES measured by DLS were shown in Table 2. The average size

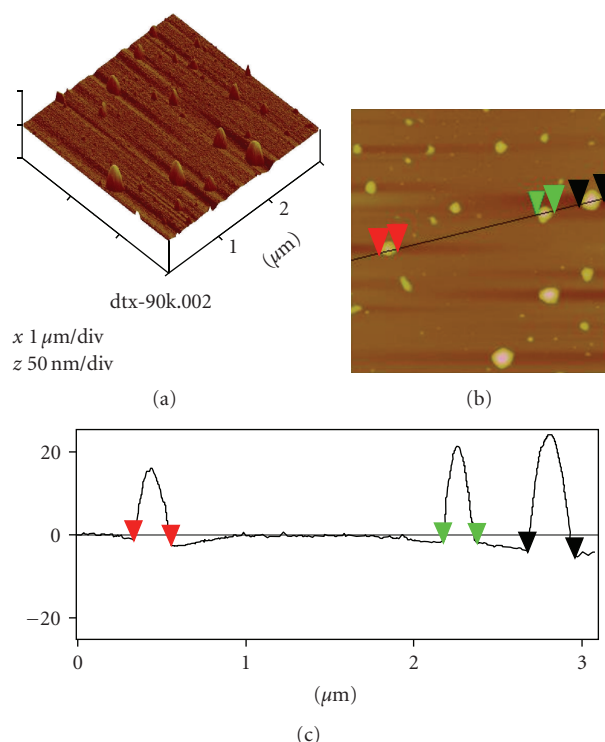


FIGURE 2: AFM image of Dtx-loaded SMES (F3).

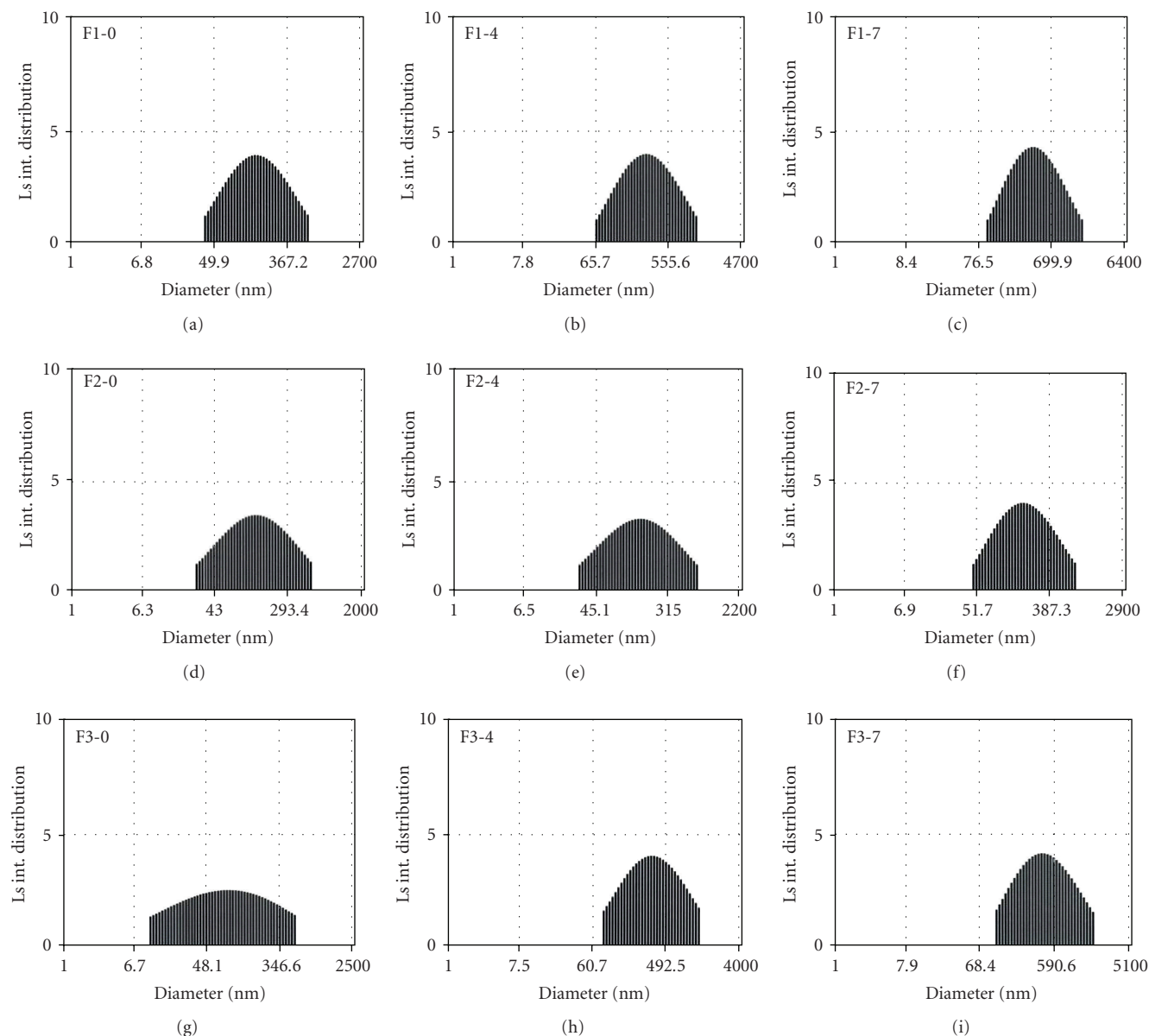


FIGURE 3: DLS images measured after incubation at 37°C at 0, 4, and 7 days of Dtx-loaded SMES prepared in BSA with different formulations F1–F3 (0, 4 and 7 represent the incubation time).

of the Dtx-loaded SMES determined from the DLS was in the range of 80–100 nm. It seemed that the changes of PLGA molecular weight did not significantly affect the size of the resultant Dtx-loaded SMES. Even though the droplet size distribution was slightly broader for increasing PLGA molecular weight, F1–F3 is formulation with appropriate size. Meanwhile, Dtx-solution and Taxol showed the average size in the range of 200–300 nm.

The AFM morphology of Dtx-loaded SMES showed the spherical shape with smooth surface as shown in Figure 2. A comparatively uniform droplet size of Dtx-loaded SMES was also observed at AFM, indicating no aggregation or adhesion among SMES.

3.2. Stability of Dtx-Loaded SMES. The stability of Dtx-loaded SMES is important to maintain the in vivo therapeutic concentration of Dtx. Surface charge may be an important indication for the stability of Dtx-loaded SMES in medium. The zeta potential of the Dtx-loaded SMES indicates the negative surface charges (Table 1). This implies that the repulsion among the Dtx-loaded SMES with the same type of surface charge can provide stability.

To examine stability of the solubilised Dtx in DW and BSA condition, Dtx-loaded SMES, Dtx-solution, and Taxol were prepared with DW or a solution of 0.9% NaCl and 5% BSA (Figures 1 and 4). The prepared Dtx-loaded SMES, Dtx-solution, and Taxol were constantly shaken at 100 rpm and

TABLE 2: The changes of average particle size by incubation for 0–7 days at 37°C of Dtx-loaded SMES prepared in DW and BSA condition with different formulations F1–F3.

Condition		In DW			In BSA condition ^a		
Formulation		F1	F2	F3	F1	F2	F3
Particle size (nm) ^b	Initial	85 ± 1	92 ± 3	93 ± 13	116 ± 4	87 ± 2	113 ± 8
	4 days	93 ± 5	88 ± 4	77 ± 20	218 ± 15	93 ± 6	167 ± 11
	7 days	115 ± 5	99 ± 4	93 ± 15	234 ± 3	126 ± 9	226 ± 3

^aA solution of 0.9% NaCl and 5% bovine serum albumin.

^bThe mean and standard deviation of particle size for each formulation was calculated by individual measurement of three formulations.

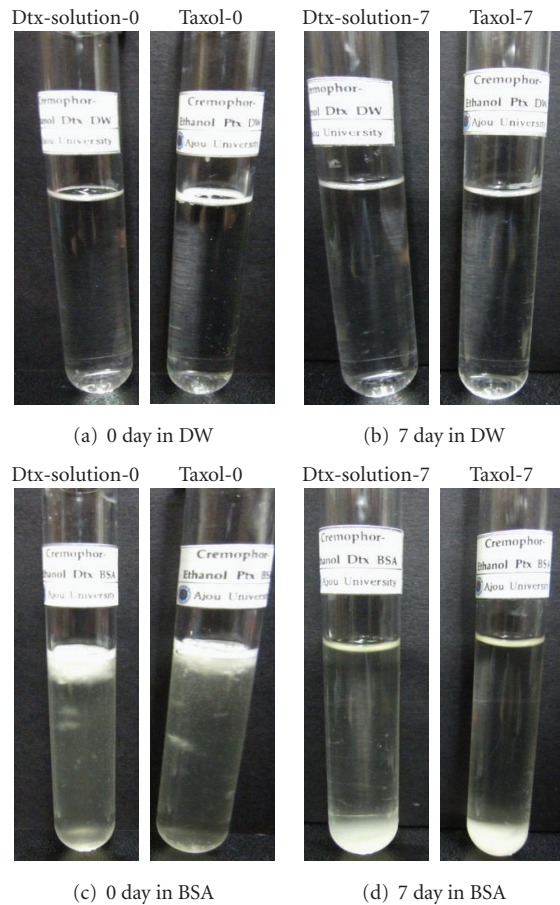


FIGURE 4: Pictures (a, c) before and (b, d) after incubation at 37°C for 7 days of Dtx-solution and Taxol prepared in (a, b) DW and (c, d) BSA.

37°C for 7 days. There is a little change of particle size for F1–F3, Dtx-solution, and Taxol prepared in DW as shown in Figures 1(b) and 1(d), indicating the stability of Dtx-loaded SMES, Dtx-solution, and Taxol in DW.

For Dtx-loaded SMES, Dtx-solution, and Taxol prepared in BSA, the size of Dtx-loaded SMES steadily increased as a function of time (Table 2). The sizes of F1 and F3 at 7 days were approximately two times larger than those at 0 day. Meanwhile, F2 was maintained the original size for at least 4 days and only increased from 87 to 126 nm (Figure 3). It can be noted that proper Dtx encapsulating formulation can lead to stability of solubilised Dtx. Meanwhile Dtx-solution and

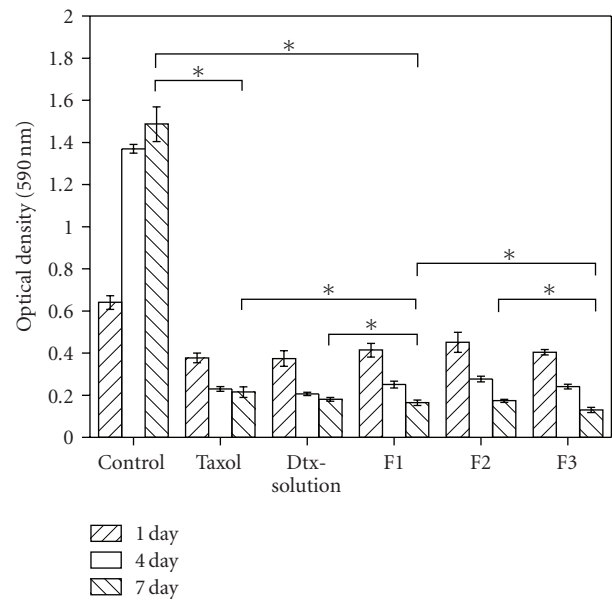


FIGURE 5: In vitro cytotoxicity of B16F10 melanoma cell against Dtx-loaded SMES of formulations F1, F2, and F3 for 1, 4, and 7 days. The cells grown on a culture plate without Dtx-loaded SMES were used as the control and the cells with Taxol and Dtx-solution were used for comparison (* $P < .001$).

Taxol precipitated immediately in BSA condition, indicating nonstability of Dtx-solution and Taxol (Figure 4).

3.3. Antitumor Activity of Dtx-Loaded SMES. The cytotoxicity for Dtx-loaded SMES (F1–F3), Dtx-solution, and Taxol for comparison was evaluated using B16F10 melanoma cell line (Figure 5). The B16F10 cells in the control experiment proliferated as a function of culture time. However, the viability of the B16F10 cells incubated with Dtx-loaded SMES (F1–F3) was approximately 50%–60% and 30%–40% at 4 days and 7 days, indicating that increasing the incubation time from 24 to 48 h led to more cell death. A similar viability of the B16F10 cells was observed when Dtx-solution and Taxol were used for 4 days. However, the viability of the B16F10 cells for Dtx-solution and Taxol was maintained when the incubation time was extended to 7 days. This indicates that the Dtx-loaded SMES was somewhat more effective in inhibition of B16F10 cell proliferation than Dtx-solution and Taxol. Thus, it appeared that the slightly

improved inhibition of B16F10 cell proliferation may be due to the Dtx-loaded SMES's stability.

4. Conclusion

The authors prepared the Dtx-loaded SMES to improve their stability. The prepared Dtx-loaded SMES showed a spherical shape in the range of 80–90 nm. The authors found that the formulation of the Dtx-loaded SMES prepared in DW and BSA showed a little change in the particle size for 7 days. Dtx-loaded SMES showed an inhibitory effect on B16F10 melanoma proliferation. Thus, further research on the animal model using Dtx-loaded SMES prepared in this work is now in progress.

Acknowledgments

This paper was supported by a grant from the new faculty research fund of Ajou University, KMOHW (Grant no. A050082) and Priority Research Centers Program through NRF funded by the Ministry of Education, Science and Technology (2009-0093826).

References

- [1] L. M. Gommersall, M. Arya, I. Mushtaq, and P. Duffy, "Current challenges in Wilms' tumor management," *Nature Clinical Practice Oncology*, vol. 2, no. 6, pp. 298–304, 2005.
- [2] M. Reni, E. Mazza, A. Tosoni, and A. A. Brandes, "Novel therapeutics in adult malignant brain gliomas," *Expert Opinion on Investigational Drugs*, vol. 14, no. 6, pp. 643–657, 2005.
- [3] C. E. Saadeh, "Chemotherapy- and radiotherapy-induced oral mucositis: review of preventive strategies and treatment," *Pharmacotherapy*, vol. 25, no. 4, pp. 540–554, 2005.
- [4] R. Garcia-Carbonero and J. G. Supko, "Current perspectives on the clinical experience, pharmacology, and continued development of the camptothecins," *Clinical Cancer Research*, vol. 8, no. 3, pp. 641–661, 2002.
- [5] A. Margaritis and B. Manocha, "Controlled release of doxorubicin from doxorubicin/ γ -polyglutamic acid ionic complex," *Journal of Nanomaterials*, vol. 2010, Article ID 780171, 9 pages, 2010.
- [6] S. U. Choi and S. Y. Han, "Targeting cancer stem cells," *Tissue Engineering and Regenerative Medicine*, vol. 6, pp. 100–103, 2009.
- [7] K. Cho, X. Wang, S. Nie, Z. Chen, and D. M. Shin, "Therapeutic nanoparticles for drug delivery in cancer," *Clinical Cancer Research*, vol. 14, no. 5, pp. 1310–1316, 2008.
- [8] P. Li and L. Zhao, "Developing early formulations: practice and perspective," *International Journal of Pharmaceutics*, vol. 341, no. 1–2, pp. 1–19, 2007.
- [9] J. P. Jain, M. Sokolsky, N. Kumar, and A. J. Domb, "Fatty acid based biodegradable polymer," *Polymer Reviews*, vol. 48, no. 1, pp. 156–191, 2008.
- [10] Z. Xu, L. Chen, W. Gu et al., "The performance of docetaxel-loaded solid lipid nanoparticles targeted to hepatocellular carcinoma," *Biomaterials*, vol. 30, no. 2, pp. 226–232, 2009.
- [11] J. Y. Lee, K. S. Kim, Y. M. Kang et al., "In vivo efficacy of paclitaxel-loaded injectable in situ-forming gel against subcutaneous tumor growth," *International Journal of Pharmaceutics*, vol. 392, no. 1–2, pp. 51–56, 2010.
- [12] A. Sparreboom, O. van Tellingen, W. J. Nooijen, and J. H. Beijnen, "Preclinical pharmacokinetics of paclitaxel and docetaxel," *Anti-Cancer Drugs*, vol. 9, no. 1, pp. 1–17, 1998.
- [13] R. M. Straubinger, A. Sharma, M. Murray, and E. Mayhew, "Novel Taxol formulations: Taxol-containing liposomes," *Journal of the National Cancer Institute. Monographs*, no. 15, pp. 69–78, 1993.
- [14] J. H. Park, S. Lee, J.-H. Kim, K. Park, K. Kim, and I. C. Kwon, "Polymeric nanomedicine for cancer therapy," *Progress in Polymer Science*, vol. 33, no. 1, pp. 113–137, 2008.
- [15] S.-S. Feng, L. Mei, P. Anitha, C. W. Gan, and W. Zhou, "Poly(lactide)-vitamin E derivative/montmorillonite nanoparticle formulations for the oral delivery of Docetaxel," *Biomaterials*, vol. 30, no. 19, pp. 3297–3306, 2009.
- [16] N. T. Huynh, C. Passirani, P. Saulnier, and J. P. Benoit, "Lipid nanocapsules: a new platform for nanomedicine," *International Journal of Pharmaceutics*, vol. 379, no. 2, pp. 201–209, 2009.
- [17] J. Portilla-Arias, R. Patil, J. Hu et al., "Nanoconjugate platforms development based in poly(β ,L-malic acid) methyl esters for tumor drug delivery," *Journal of Nanomaterials*, vol. 2010, Article ID 825363, 8 pages, 2010.
- [18] T. Hekmatara, S. Gelperina, V. Vogel, S.-R. Yang, and J. Kreuter, "Encapsulation of water-insoluble drugs in poly(butyl cyanoacrylate) nanoparticles," *Journal of Nanoscience and Nanotechnology*, vol. 9, no. 8, pp. 5091–5098, 2009.
- [19] W. Qiao, B. Wang, Y. Wang, L. Yang, Y. Zhang, and P. Shao, "Cancer therapy based on nanomaterials and nanocarrier systems," *Journal of Nanomaterials*, vol. 2010, Article ID 796303, 9 pages, 2010.
- [20] R. Tong and J. Cheng, "Anticancer polymeric nanomedicines," *Polymer Reviews*, vol. 47, no. 3, pp. 345–381, 2007.
- [21] P. Gao, B. D. Rush, W. P. Pfund et al., "Development of a supersaturable SEDDS (S-SEDDS) formulation of paclitaxel with improved oral bioavailability," *Journal of Pharmaceutical Sciences*, vol. 92, no. 12, pp. 2386–2398, 2003.
- [22] S. Y. Lee, H. Hyun, J. Y. Youn et al., "Preparation of nano-emulsified paclitaxel using MPEG-PLGA diblock copolymers," *Colloids and Surfaces A*, vol. 313–314, pp. 126–130, 2008.
- [23] Y. Liu, P. Zhang, N. Feng, X. Zhang, S. Wu, and J. Zhao, "Optimization and in situ intestinal absorption of self-microemulsifying drug delivery system of oridonin," *International Journal of Pharmaceutics*, vol. 365, no. 1–2, pp. 136–142, 2009.

Research Article

Application of Flow Focusing to the Break-Up of a Magnetite Suspension Jet for the Production of Paramagnetic Microparticles

Lucía Martín-Banderas,^{1,2} Román González-Prieto,³ Alfonso Rodríguez-Gil,⁴ Mercedes Fernández-Arévalo,¹ María Flores-Mosquera,² Sebastián Chávez,⁴ and Alfonso M. Gañán-Calvo^{2,5}

¹ Department of Pharmacy and Pharmaceutical Technology, Faculty of Pharmacy, University of Seville, 41012 Seville, Spain

² R&D Department, Ingeniatics Tecnologías S.L., 41900 Camas (Seville), Spain

³ Centro Andaluz de Biología Molecular y Medicina Regenerativa, CABIMER-CSIC, 41092 Seville, Spain

⁴ Department of Genetics, Faculty of Biology, University of Seville, 41012 Seville, Spain

⁵ Department of Aerospace Engineering and Fluids Mechanics, ESI, University of Seville, 41092 Seville, Spain

Correspondence should be addressed to Alfonso M. Gañán-Calvo, amgc@us.es

Received 31 May 2010; Accepted 25 July 2010

Academic Editor: Lu Sun

Copyright © 2011 Lucía Martín-Banderas et al. This is an open access article distributed under the Creative Commons Attribution License, which permits unrestricted use, distribution, and reproduction in any medium, provided the original work is properly cited.

Paramagnetic particles offer an extensive improvement in the magnetic separation or purification of a wide variety of protein molecules. Most commercial paramagnetic particles are synthesized by laborious and costly procedures. A straightforward production of paramagnetic microparticles with homogeneous and selectable sizes using flow focusing (FF) technology is described in this work. The development of an initial formulation of a stable iron oxide suspension compatible with the FF requirements is also reported. The obtained particles, below 10 microns in diameter and presenting smooth and reactive surface, were codified with an organic fluorophore and showed excellent properties for covalent attachment of biomolecules such as proteins and its subsequent recognition by flow cytometry. Furthermore, particles with suitable magnetite content resulted as well-suited for commercial magnet separators for these purposes.

1. Introduction

Magnetic polymer particles usually consist of a core of silica or polystyrene covered by paramagnetic nanoparticles, typically iron oxide. In other cases iron oxide is entrapped within a polymer matrix that can be engineered to exhibit the desired physical and chemical properties, providing a reactive surface to which proteins and polynucleotides can be conjugated. The conventional methods for preparing paramagnetic microparticles include (a) swelling [1], (b) dispersion polymerization [2], (c) emulsion polymerization [3], (d) emulsion-solvent extraction-evaporation [4], (e) porous membranes [5], (f) layer-by-layer [6], (g) conventional sol-gel method [7].

Commercial particles for these purposes are produced by a multiple-step procedure resulting in a laborious and costly production process.

Magnetic particles offer high potential benefits in multiple fields, particularly in biotechnology and biomedicine. According to their use in these later fields, they can be simply classified into two wide groups: particles for *in vivo* or *in vitro* [8–10] applications. In biochemical applications, the use of these particles for multiplexed assays constituted a particularly useful tool, allowing homogeneous results, facilitating the sample manipulation, and avoiding the risk of sample loss.

In these uses, paramagnetic microparticles need to satisfy the following prerequisites: they should be stable in water, uniform in size, and responsive to magnetic field gradients. In addition, they must be identifiable by a suitable system (usually by an optical codification system) [10–16].

Here we report a very versatile and controlled procedure for the production of dye-labelled solid paramagnetic polymeric microparticles, yielding remarkable size accuracy with

negligible size dispersion and allowing surface engineering or design. We demonstrate some crucial advantages over alternative methods for the size ranges considered in this work (from about 1 to 10 microns):

- (i) high production rate from a single nozzle (some orders of magnitude by multiplexing can be scaled up though this is out of the scope of present work),
- (ii) one-step production,
- (iii) selectable size using the same device,
- (iv) strict control on the particle size distribution (zero-rejection production).

The first stage of the synthesis procedure implies the elaboration of a stable magnetite suspension. We have evaluated several stabilizing agents to obtain a suitable magnetite suspension compatible with a standard Flow Focusing (FF) nozzle. Then, we directly utilize the magnetite suspension to produce nearly monodisperse drops without any external excitation source or additional purification steps [17] inside a continuous phase. Those drops yield solid microspheres through solvent extraction by the continuous phase. This approach allows the production of magnetic fluorescent-encoded beads with a uniform morphology, narrow diameter distribution, and controlled and suitable fluorescent and magnetic properties in a one-step easy way. Magnetic properties were evaluated by a simple magnetic separation test and by measuring magnetite content. The effectiveness of the microbead array for covalent attachment of biomolecules was tested in a quantitative way. Finally, the ability of the fluorescently labeled microspheres for the detection of biomolecule interactions using flow cytometry was also tested, extending the study of previously synthesized “barcoded” particles produced by the FF technology [18].

1.1. Flow Focusing Technology. In short, FF is a simple and low-cost atomization technique based on the combination of a specific geometry and hydrodynamic forces providing a remarkable accuracy in size, narrow size dispersion, and feasibility. The appropriate fluid combinations allow not only particles to be obtained but also monodisperse bubbles, sprays, or emulsions at micro- and nanoscales. The phenomenon is characterized by the presence of a steady microjet which is “sucked” through a small orifice and eventually breaks up into droplets of well-defined size under very gentle operation conditions and reliability [19].

One of its most important innovative applications is the possibility of obtaining solid microparticles by means of solidifying the controlled-size microdrops generated. Depending on the nature of the fluids employed, different solidifying processes can be used: thermal solvent evaporation/extraction, cooling of melted materials, chemical hardening, UV-curable monomers, and so forth. As the drops are generated with a precise, narrow size distribution, the solid particles maintain the same geometrical features. In addition, this technology is suitable for particle engineering through the manipulation of its internal morphology, all in one-step: depending on the use of single, multiple or

coaxial feeding capillaries, homogeneous particles, or single/multivesicle microcapsules with one or multiple shells of controllable thickness can be achieved. Some nice examples of particle production by FF technology are controlled multicore microcapsules [20], poly(lactic-co-glycolic acid) (PLGA) particles for drug encapsulation of hydrophilic (gentamicin sulphate) [21] and lipophilic (lidocaine) drugs and also for proteins such as green fluorescent protein [22, 23], solid lipid particles obtained by spray cooling using a special thermostated FF nozzle [21], or encoded fluorescent microparticles for biomolecules detection [17, 18].

One of the main advantages of FF technology is the predictability of the final microparticle diameter with a remarkable accuracy. In the present work, the FF technology was adapted to the solvent extraction encapsulation method using a simple FF liquid-liquid configuration. In this case, the drop diameter (d_g) could be calculated from the expression of the jet diameter (d_j) as

$$d_g = \left(\frac{3\pi}{2k} \right)^{1/3} d_j, \quad (1)$$

where k is the wavenumber of the fastest growing perturbation on the jet (approximately $k \approx 0.5$ for most liquid-liquid combinations) which depends on the viscosities and densities ratios between the inner and outer liquids [20, 24]. The jet diameter depends on geometry of the nozzle (mainly D , orifice diameter) and the operating conditions (mainly the liquid flow rates; see references [18, 25, 26]) only. Hence, the final droplet diameter can be written as

$$d_g = \left(\frac{3\pi}{2k} \right)^{1/3} \left(\frac{Q_d}{Q_t} \right)^{1/2} D, \quad (2)$$

where Q_d and Q_t are the inner and outer fluid flow rates, respectively.

The particle diameter (d_p) is calculated by taking into account the drop diameter, the polymer density (ρ_p), and the polymer concentration (C , mass of polymer per volume of solution):

$$d_p = \left(\frac{3\pi C}{2k\rho_p} \right)^{1/3} \left(\frac{Q_d}{Q_t} \right)^{1/2} D. \quad (3)$$

Thus, given a desired final particle diameter, it is possible to set up the experimental conditions so as to drastically reduce the numbers of trials, or, conversely, for a specific flow rate combination and properties of the liquids, the final particle diameter can be predicted.

Several technological approaches have been previously used to synthesize magnetic particles for these purposes. However, important limitations were found related to

- (i) the nozzle geometry, where even the nozzle orientation affected the particle morphology due to the effect of gravity forces [27],
- (ii) the nozzle fabrication: nozzles fabricated in PMDS (poly(dimethylsiloxane)) by soft lithography needed to be pretreated to avoid wetting problems and presented leak problems [27–29],

- (iii) the method applied for drop solidification such as UV-curable monomers, which required the application of high temperatures for long times (60°C, overnight) [28] and to remove monomer in excess [29] or to employ toxic reactants such as glutaraldehyde as a cross-linker agent [30].

2. Materials and Methods

2.1. Materials. The following chemicals were purchased from Sigma-Aldrich (USA) and were used as received: polystyrene (PS) ($M_w = 4000\text{--}200000$); poly(styrene-co-maleic acid) partial isobutyl/methyl ester (PSMiso); poly(styrene-co-maleic acid) partial sec-butyl/methyl ester (PSM-sec); rhodamine B; magnetite Fe_3O_4 98%, dichloromethane (DCM) 99.9% grade HPLC; oleic acid; polyvinyl alcohol (PVA), MW 72000; protein G, protein A, and fluorescein-labelled rabbit antimouse antibody. Ethyl acetate (EA) PRS was obtained from Panreac Química S.A. (Barcelona, Spain), Ethocel from The Dow Chemical Company, and Aerosil 200 Pharma, Eudragit RS PO, and Eudragit S100 from Degussa AG, Barcelona, Spain.

2.2. Methods

2.2.1. Preparation of Magnetite Suspension. To elaborate the paramagnetic nanoparticle suspension, oleic acid, silicon oxide (Aerosil 200 Pharma), cellulose (Ethocel), and methacrylates (Eudragit RS PO, Eudragit S100) were assayed as stabilizing agents.

As a carrier, a 4% w/v polymer solution was prepared in ethyl acetate (EA). Then, the stabilizing agent was codissolved or dispersed in that solution at different concentrations (0.6–1.5% w/v). After this, an accurately weighed aliquot of the paramagnetic nanomaterial (40–160 mg), 20–30 nm in size, was added and dispersed by sonication for 5 minutes. The newly prepared suspension was left standstill for 60 minutes. To evaluate the degree of sedimentation, several images of the suspension in a 10 mL glass vial were taken at 0, 10, 30, and 60 minutes. Finally, the presumed stable suspension was filtered through a 15–20 μm filter (Albet LabScience, Spain).

2.2.2. Preparation of Paramagnetic Microparticles by FF. An axisymmetric FF device was employed to prepare the paramagnetic microparticles at $25 \pm 1^\circ\text{C}$ in a simple liquid-liquid configuration, adapting the technology to the traditional emulsion-evaporation/extraction microencapsulation method (see Figure 1(a)).

A simple FF nozzle, model Avant (with geometric dimensions $D = 100\ \mu\text{m}$, $D_0 = 150\ \mu\text{m}$, and $H = 100\ \mu\text{m}$; see Figure 1(a)) (Ingeniatrics Tecnolías S.L., Spain) was used to produce an o/w emulsion (see Figure 1(b)). The magnetite suspension, oil phase (focused fluid), was injected using a syringe pump (Harvard Apparatus, mod. “44” programmable, 55–1144) rated at 0.25–2 mL/h. The aqueous phase, distilled water (focusing fluid) was injected through

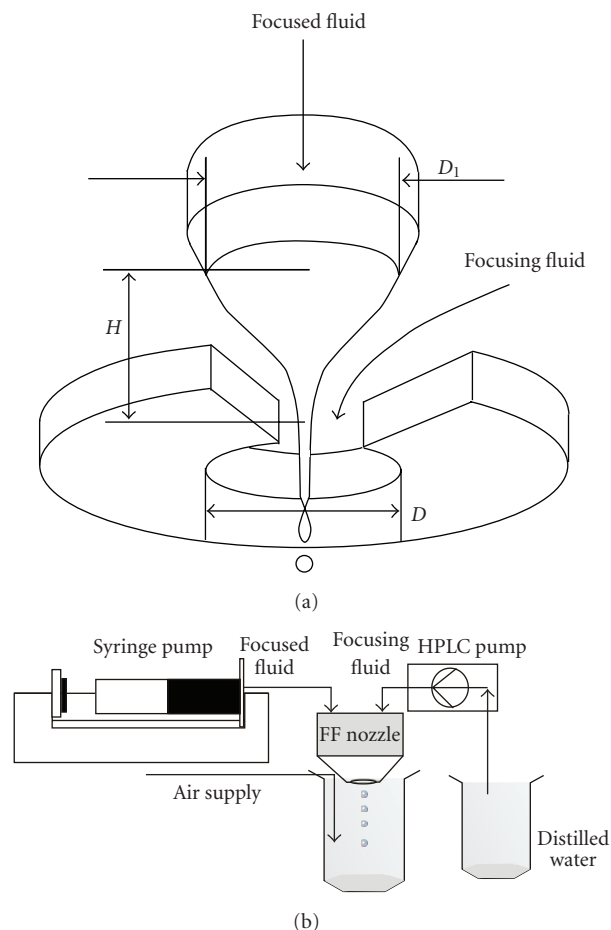


FIGURE 1: A simple FF nozzle (a) Scheme of functioning (D_1 inner diameter of capillary tube, H distance capillary tube and nozzle exit, D diameter of exit orifice); (b) Experimental setup for paramagnetic microparticle production adapting FF to the traditional microencapsulation method emulsion-evaporation of solvent.

an HPLC pump (Shimadzu Corp. mod. LC-10AD vp, Germany) at 2–4 mL/minute.

With a proper control of the relative flow rates of the two fluids employed, the oil phase steady microjet (magnetite suspension) issuing from the nozzle became unstable at a certain station and broke into uniform droplets [19, 25, 26]. To avoid microdrop coalescence or deformation, the emulsion was produced in a bath containing a PVA solution 1% w/v under agitation for 3 hours by continuous air bubbling. After this time, the solvent was evaporated and the microdrops formed solid microparticles which were collected by centrifugation (4500 rpm, 10 minutes, Orto Alresa, mod. Digicen, Spain) and washed three times with fresh distilled water. The microparticles were then stored either as dry powder after freeze-drying [frozen in liquid nitrogen and lyophilized at $-80.0 \pm 0.5^\circ\text{C}$ and 0.057 mbar; (Telstar, Cryodos, Spain)] or as a suspension, in distilled water containing sodium azide (0.2% w/v) to avoid microbial growth, and stored at $4.0 \pm 0.5^\circ\text{C}$, in order to increase

their physicochemical stability but without significantly modifying their characteristics.

To produce encoded paramagnetic microparticle with an optically identifiable code, rhodamine B was used as a model fluorophore. It was codissolved with the polymer in ethyl acetate at 0.2 mM concentration.

2.2.3. Characterisation of the Paramagnetic Microparticles (MPs). The shape and surface characteristics of the microspheres were determined by scanning electron microscopy (SEM) (Philips XL-30, USA) after coating lyophilised samples with a gold thin film. MP diameters of nonlyophilised samples were determined under conventional microscopy (Leica DM LS) using an image-processing program (Image J. 1.30 v). Diameters from 500–1000 microparticles randomly selected from various micrograph images were measured and statistically processed. Results obtained were confirmed by SEM.

The magnetite content was determined by measuring the content of Fe atoms in lyophilised samples by inductively coupled plasma mass spectrometry (ICP-MS) (Thermo Elemental X-7, Termo Scientific) at 259.940 nm. Samples were previously digested in a microwave digester (Anton Para, mod. 3000) by adding nitric acid and hydrogen peroxide.

The magnetite content was expressed as an encapsulation efficiency percentage (%EE):

$$\%EE = \left(\frac{Q}{Q_i} \right) * 100, \quad (4)$$

where Q is the amount of magnetite encapsulated and Q_i the initial magnetite amount employed.

The paramagnetic microparticle behaviour under covalent coupling protocol conditions was also studied. The effect of pH and temperature on microparticle aspect and morphology was evaluated for different periods of time.

2.2.4. Magnetic Separation Test. Magnetic particles 5 μ m in diameter, dispersed in 50 mL distilled water at a concentration of $\approx 10^7$ particles/mL were placed in a commercial magnetic separator (Merck ref. 69964). After prefixed intervals of time, an aliquot from supernatant was evaluated by counting the number of free particles in suspension using a Bürker camera.

2.2.5. Coupling of Protein G/A and Interaction Detection. In order to evaluate the affinity binding capacity of synthesized particles protein coupling assays were performed by the carbodiimide method as in previous work [18]. This is the most extensively used approach for coupling biomolecules to carboxylated surfaces. The method consists of activating carboxylic acid groups towards amide or ester formation.

Briefly, for protein conjugation, particles were activated with a freshly 1-ethyl-3-(3-dimethylaminopropyl)carbodiimide (EDC) solution in an activating medium, MES pH 5.4, for 20 minutes under stirring at room temperature. After several centrifugal washings microparticles were resuspended in coupling buffer, PBS pH 7.4, containing protein A or G. Then, particles were incubated for 2 hours

TABLE 1: Formulations tested to produce paramagnetic microparticles by using a FF simple nozzle (for F3 to F9. C_{polym} indicate polymer mixes of PS + PSM).

Formulation	C_{polym} (%w/v)	Stabilizing agent(%w/v)			Magnetite (%w/v)
		Aerosil	Ethocel	Eudragit RSPO	
F1	1	0.6	—	—	0.4
F2	1	—	—	0.6	0.4
F3	0.5 + 0.5	0.6	—	—	0.4
F4	1.4 + 0.6	0.6	—	—	0.4
F5	1.4 + 0.6	0.9	—	—	0.4
F7	2.8 + 1.2	0.6	—	—	0.4
F8	2.8 + 1.2	1.8	—	—	0.4
F9	2.8 + 1.2	0.9	—	—	0.4
F11	4	1.8	—	—	0.4
E2	4	—	1	—	0.6
E3	4	—	1.5	—	0.8
E5	4	0.6	1	—	0.6

under stirring agitation. After this, particles were collected by centrifugation (13000 rpm, 2 minutes; Eppendorf) and washed three times with washing buffer, MES 50 mM, NaCl 2 M and Tween 20 0.02%, pH 6. Finally, a blocking solution was added, PBS, NaN_3 0.1%, and BSA 1%, pH 7.4.

3. Results

3.1. Stability of Magnetite Suspension. As it was previously indicated, to produce the paramagnetic microparticles by a simple FF device, the formation of a paramagnetic nanomaterial suspension was required, constituting the focused fluid. This suspension had to be stable for the time necessary to guarantee the formation of particles with a minimal and homogeneous content in magnetite.

This was a crucial and difficult goal due to the density of magnetite, 4.8–5.1 g/L. The time required for a suspension to be considered stable was fixed at 60 minutes.

Different results were obtained depending on the material employed as stabilizing agent. The best results in terms of suspension stability were achieved with Aerosil 200 Pharma at concentrations over 12% w/w, which were capable of producing stable suspensions after 72 hours. The rest of the formulations were excluded for MP production due to suspension instability.

3.2. Microparticle Morphology and Aspect. The SEM images in Figure 2 are representative of the paramagnetic microparticle populations 5 μ m in diameter prepared by FF. A TEM image of commercial magnetite is also included (Figure 2(i)) (Philips CM-10). The surface features of the microparticles depended on the stabilizing agent employed and its concentration.

As it can be seen, spherical microparticles were obtained in all cases with the exception of the particles prepared with Eudragit RS PO (Figure 2(b)). In those cases where

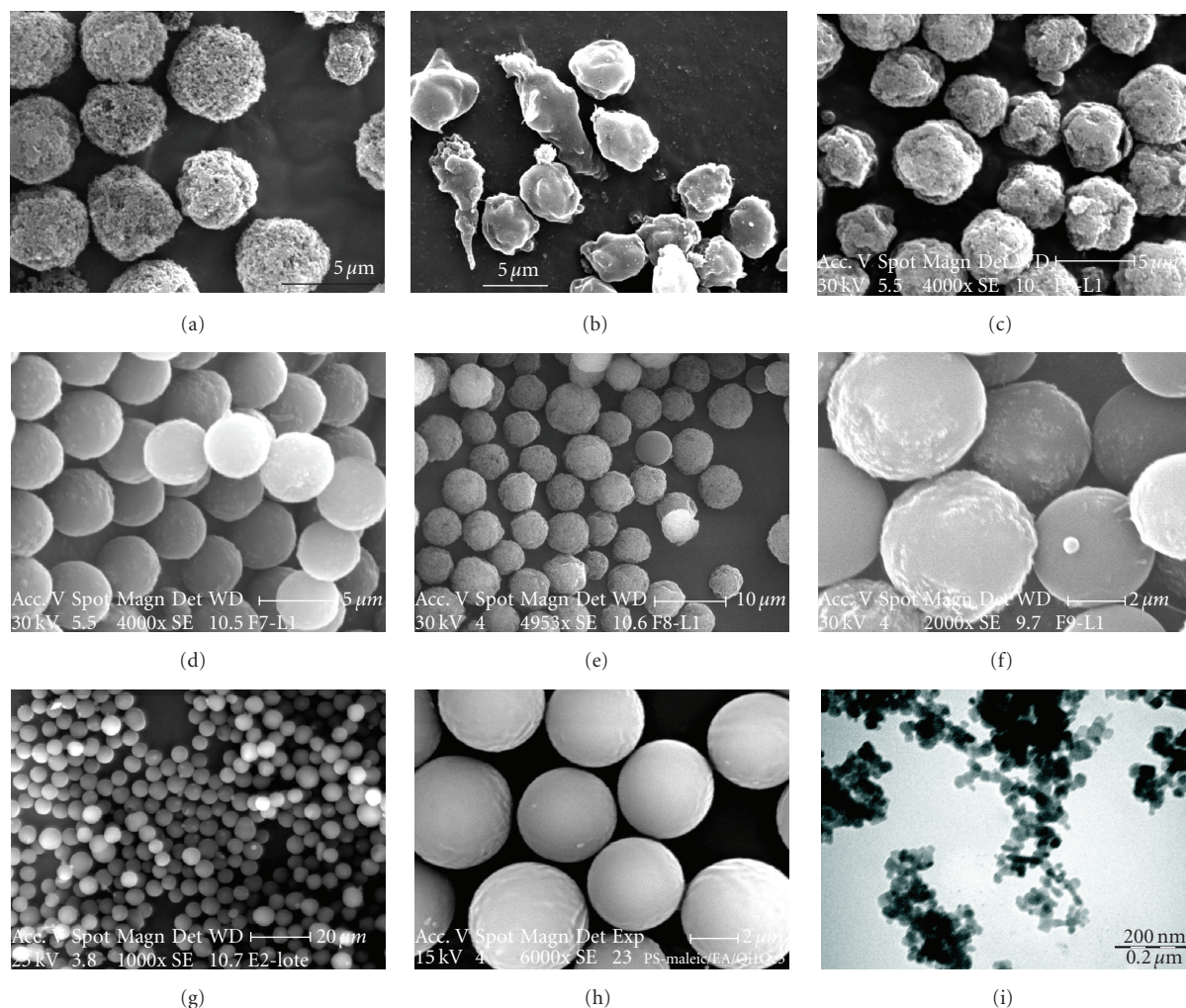


FIGURE 2: MPs aspect and morphology for formulations indicated: (a) F1; (b) F2, elaborated with Eudragit RSPO; (c) F5; (d) F7; (e) F8; (f) F9; (g) E3; (h) blank particles and, (i) TEM image of magnetite employed.

Aerosil or Ethocel was employed as stabilizing agents for the primary magnetite suspension, spherical particles were achieved although the particle surfaces depended on the magnetite/polymer/stabilizer ratio.

The effect of polymer concentration can be observed in Figures 2(a), 2(c), and 2(e). In these cases, the polymer concentration was 1, 2, and 4% w/v, respectively, and the stabilizing agent concentration was 30% w/w. Interestingly enough, as the polymer concentration increased, more regular spherically shaped particles were obtained. When the polymer concentration was kept at 4% w/w and the Aerosil concentration decreased from 30 to 12% w/w, it was possible to obtain particles with almost smooth surfaces (see Figures 2(d), 2(e), and 2(f)). This is an important aspect, because particles with highly porous surfaces promote unspecific unions that pose hindrances to the final application [31].

Ethocel, a water-insoluble ethyl cellulose used worldwide for many different functional purposes in pharmaceutical products, was also employed as a stabilizing agent in the range of 9 to 25% w/w. Figure 2(g) shows an example of

this type of particle. In all cases, spherical smooth particles were obtained (similar pictures not shown were obtained for the rest of the formulations tested). For illustrative purposes, Figure 2(h) shows “blank” particles, without magnetite.

3.3. Microparticle Size and Size Distribution. In the experiments here reported, particle size analysis showed nearly monosized particles with selectable size between 3 and 10 μm in diameter, almost five times smaller than some published examples of magnetic particles obtained using devices based on FF principle [27–30].

Table 2 summarizes the diameters obtained as a function of polymer and Aerosil concentration using a flow rate of 3 mL/minute for the focusing fluid and 1 mL/hour for the focused fluid (magnetite suspension).

In order to determine the versatility of the particular FF device designed for the particle production, the possibility of producing paramagnetic microparticles with programmable or selectable sizes using the same nozzle was studied. For this purpose, several combinations of fluid rates were tested to

TABLE 2: MPs size as a function of polymer and Aerosil concentration (Magnetite 4% w/v, Qt 3 mL/min, Qd 1 mL/h).

Formulation	D _{th} (μm)	D _{medium} (μm)	SD (μm)	VC (%)	GSD
F2	4.0	3.73	0.59	15.96	1.18
F3		3.80	0.39	10.34	1.10
F4		4.94	0.41	8.37	1.09
F5	4.7	4.95	0.49	9.86	1.09
F7		5.55	0.53	9.61	1.10
F8	6.2	6.03	0.67	11.06	1.12
F9	5.8	6.09	0.75	12.29	1.34
F11	5.8	5.78	0.25	4.39	1.05

obtain particles below 10 μm in diameter (some of them are shown in Figure 3). The formulation used for this study was F11. Figure 3 shows some of the results obtained.

For a given flow of focused fluid, an increase of the focusing liquid rate of flow leads to a decrease of the microparticle diameters. For a fixed focusing liquid rate of flow, an increase of the focused fluid flow rate leads to an increase in diameter(3). Thus, using a single nozzle with fixed geometrical parameters, it is possible to provide the required microparticle size by a simple adjustment of the liquid flow rates. The process setup also allowed the high-throughput synthesis of particles (10⁹ particles per hour and per nozzle) in a continuous manner superior to related procedures for the production of magnetic particles described in the literature [27–29, 32].

The reproducibility of the process was also confirmed. Using flow rates $Q_d = 1$ mL/hour and $Q_t = 3$ mL/minute, the intralot diameter was $5.78 \mu\text{m} \pm 0.25 \mu\text{m}$ with a VC equal to 4.39% ($n = 5$). The incorporation of rhodamine B into these polystyrene particles did not modify the final particle diameter.

In all cases, the experimental data were in accordance with the theoretical FF predictions (theoretical diameters are included in Figure 3). Successful results using the same mathematic model have been also reported for other loaded microparticles [21, 23].

3.4. Magnetite Content . The magnetite content was determined by ICP by measuring the Fe atom percentage. The theoretical Fe atom percentage in magnetite is 70.9%. Elemental analysis gave 69.2%. This experimental datum was used as the reference to calculate particle magnetite content.

Table 3 lists the results for the indicated formulations.

The best results were obtained using Aerosil as stabilizing agent, yielding an EE% of 74%. In the case of formulations with Ethocel, the maximum EE was about 28%. These results can be explained probably due to a more stable magnetite suspension obtained using Aerosil as stabilizing agent.

3.5. Microparticle Stability in Covalent Coupling Protocols. The aim of this brief study was to test the stability of microparticles under the pH, temperature, and time conditions involved in a covalent union process, following the usual protocols for *multiplex* assays.

TABLE 3: Magnetite content determined by ICP for formulations indicated (mean ± SD).

Sample	Fe _{th} (% w/w)	Fe _{exp.} (% w/w)	EE% (Fe)	EE% (magnetite)
Magnetite	70.91	69.784 ± 0.33	—	—
F8	4.48	3.09 ± 0.23	68.94 ± 0.30	74.01 ± 0.27
F9	4.48	0.605 ± 0.15	13.50 ± 0.53	14.49 ± 0.48
F11	4.48	2.382 ± 0.46	53.14 ± 0.45	57.05 ± 0.43
E2	6.84	1.22 ± 0.39	17.84 ± 0.49	19.15 ± 0.29
E3	7.53	1.80 ± 0.27	26.32 ± 0.38	28.26 ± 0.17
E5	6.73	1.22 ± 0.38	18.14 ± 0.60	19.47 ± 0.58

TABLE 4: Experimental conditions for paramagnetic microparticles stability study (particles were 5 μm in diameter).

Medium	pH	T (°C)	Time (h)	
PBS	7	37	2	4
MES	6	37	2	4
PBS-BSA	7.4	37	2	4
DENHART	8	90	10 minute	—
		55	2	4

Three types of polystyrene were employed as the polymer matrix formed to prepare the paramagnetic particles: PS, PSMiso, and PSMsec. Particles 5 μm in diameter were dispersed in different media and observed under optical microscopy at preset times (see Table 4).

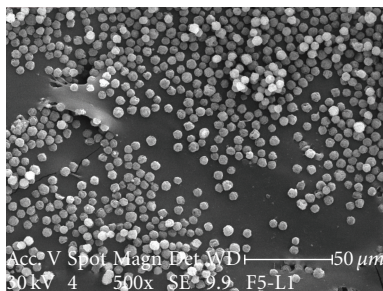
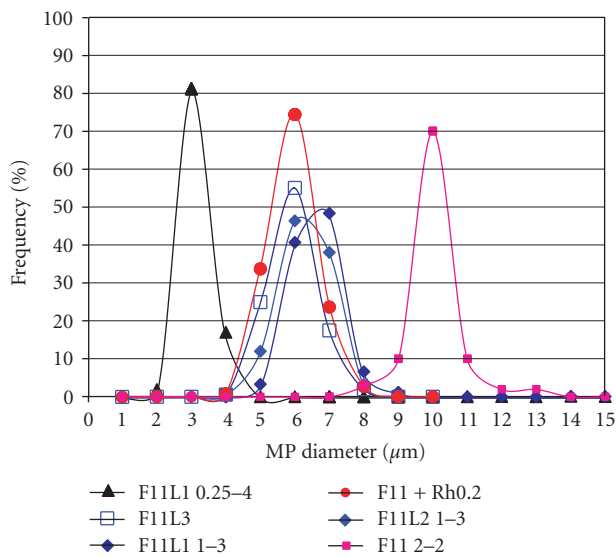
In PBS (pH 7), MES (pH 6), and PBS-BSA (pH 7.4) media, the microparticles maintained their morphology and size at 37°C for 4 hours, independently of the polymeric matrix composition.

The particles prepared with PSMsec also kept their properties at 90°C for 10 minutes and 55°C in Denhart medium (pH 8) for 4 hours, in contrast to those elaborated employing PSMiso. In this case, the particles showed a clear halo, began to dissolve and swelled, increasing their size in the first minutes of the assay (see Figure 4).

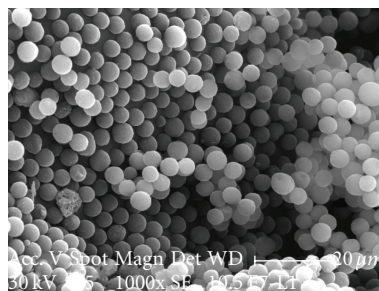
In view of these results, PSMsec was selected as the optimal polymer to prepare the MPs. Like the PSMiso, this polymer presents carboxyl groups at a high density (acid value ~ 180 mg KOH/g) which facilitates covalent unions. The improved stability of PSMsec could be due to the chemical structure of the sec-butyl residue that precludes any reagent to approach the carboxyl group.

3.6. Magnetic Separation Test. Highly magnetic particles are particularly useful in an immunoassay for their faster separations and thus faster assays becoming possible. Results obtained from this test are nicely shown in Figure 5, where the magnetic separation of F11 and E3 particles suspensions was very similar, confirming the higher magnetization of both formulations.

3.7. Immunoassays. Selected paramagnetic microparticles obtained were evaluated for immunoprecipitation assays.



(b)



(c)

FIGURE 3: (a) MPs size distribution as a function of focused and focusing fluid flow rates (\blacktriangle 0.25 mL/h–4 mL/min, \bullet \square 1 mL/h–3 mL/min, \blacksquare 2 mL/min–2 mL/min) (F11) (b) and (c) SEM images examples of particle size distribution.

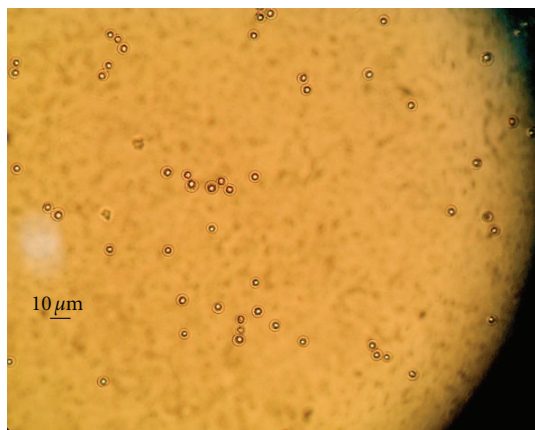


FIGURE 4: Presence of a dissolution halo for paramagnetic particles elaborated using PSMiso after 10 min incubating in Denhart medium at 90°C.

Proteins G and A were covalently coupled onto F11-codified microparticle surfaces.

Figure 6(a) shows a fluorescence microscopy image from F11 microparticles codified with rhodamine B.

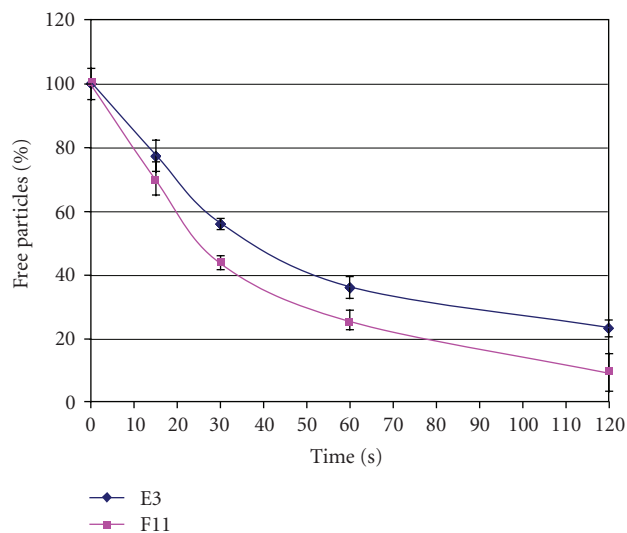


FIGURE 5: Change in free particles (%) in suspension as a function of magnetic separation time.

3.7.1. Analysis of Protein-Protein Interaction. To confirm the union, particles were incubated with a fluorescent-labeled antibody (fluorescein-labeled rabbit antimouse antibody),

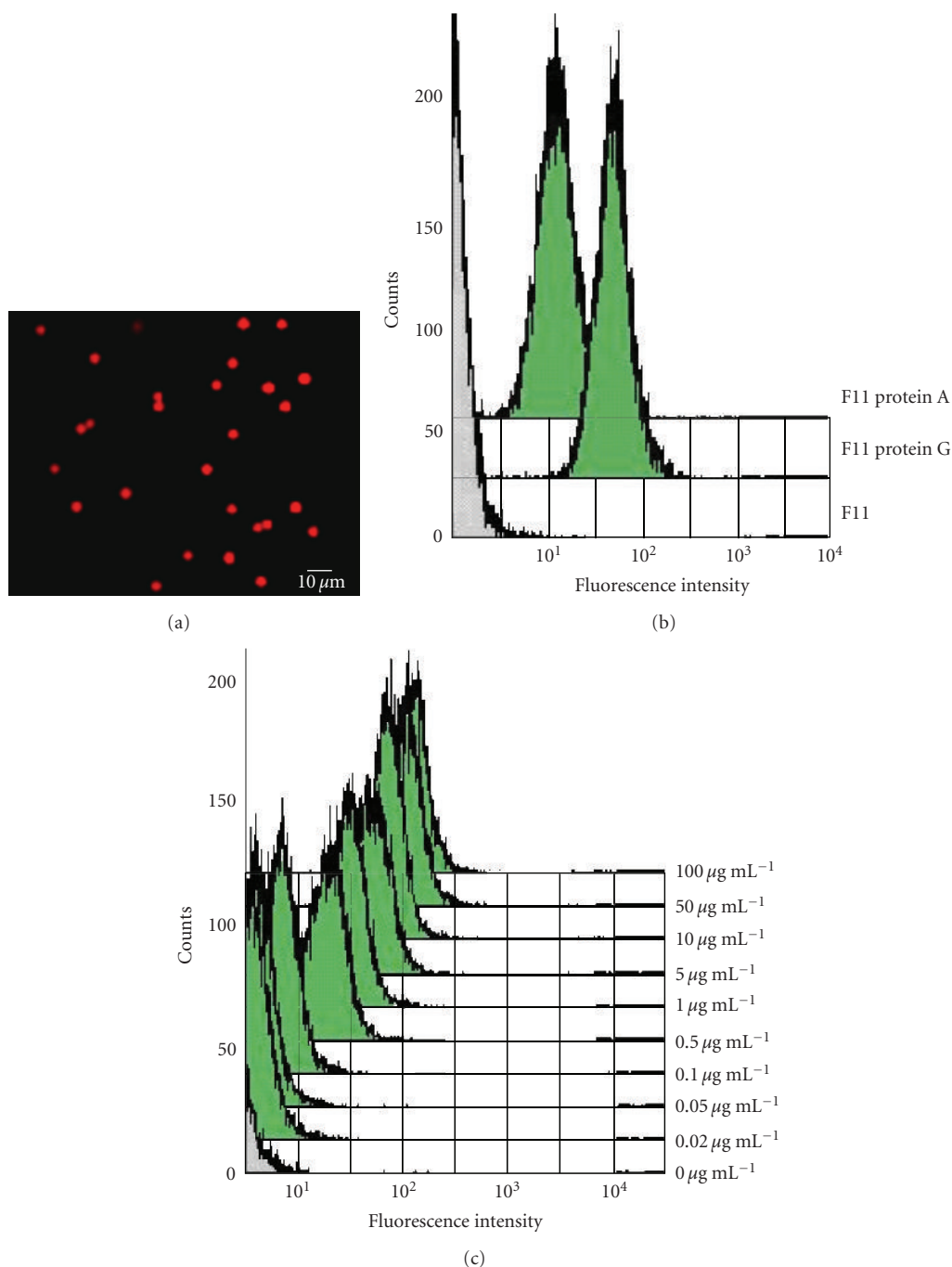


FIGURE 6: (a) Fluorescence microscope image of paramagnetic microparticles 5 μm in diameter codified with Rhodamine B (formulation F11) and fluorescence flow cytometry profiles for (b) naked E3 microparticles and coupled E3 microparticles with protein G or protein A after incubating with 0.1 mg/ml antibody solution and (c) protein G coupled E3 microparticles after incubation with increasing antibody concentration solutions.

measuring their fluorescence by flow cytometry (FACSCalibur, Becton Dickinson).

0.3 mg of microparticles conjugated to the analyte was incubated for 1 hour in 100 μL of a BSA 1% w/v solution in PBS buffer (pH 7.4). After that, samples were incubated with the fluorescent-labeled antibody in PBS buffer at several concentrations (0–100 $\mu\text{g/mL}$) for 1 hour, then washed three

times with Tween 20 0.02% (v/v), NaCl 2 M, in MES hydrate buffer 50 mM solution, pH 5.4 and then analyzed using flow cytometry.

After coupling protein A or protein G to F11 microparticles and incubating with a 0.1 mg/mL solution of fluorescent-labeled antibody, increased fluorescence was observed in comparison to that from particles not coupled with an

immunoglobulin binding protein (see Figure 6(b)). To confirm that the increased fluorescence was not due to the previously coupled protein, protein G-coupled F11 microparticles were incubated with different fluorescent antibody solutions. An increase in microparticle fluorescence was observed as the concentration of antibody increased (see Figure 6(c)) from 0.02 $\mu\text{g/mL}$ to 50 $\mu\text{g/mL}$, allowing a quantitative detection for the antibody in this interval of concentrations.

The same experiments were performed with E3 particles (data not shown), and the results were similar.

It is thus possible to conclude that the paramagnetic microparticles produced by FF technology are useful for immunoprecipitation assays.

4. Conclusions

A simple method has been described for the controllable production of functionalized paramagnetic polystyrene microparticles using a combination of flow focusing (FF) and the solvent extraction/evaporation technique. A stable magnetite suspension was produced using silicon oxide as stabilizing agent. Here, a two-phase fluid (magnetite suspension) was flow focused into a laminar capillary microjet to yield monodisperse drops by capillary breakup, showing no differences with a flow-focused single-phase liquid in terms of drop size prediction. This fact confirms the wide range of possible uses of FF, expanding the fluid natures that this technique can accommodate.

The process here reported is potentially a very helpful procedure for efficient microparticle engineering, yielding paramagnetic monodisperse microparticles with diameters of a few microns and a functional surface: a suitable tool for separation processes.

The production of encoded microparticles was also described. The functionality of dye-labelled beads was evaluated allowing conjugation of biomolecules such as proteins. Conjugated microparticles represent a valuable tool for the detection of analyte interactions, using flow cytometry as one of the most accurate and simple techniques for analysis.

To summarize, FF could be regarded as a suitable low-cost alternative for the mass production of high-quality micro-bead arrays and microparticles for separation processes. The dye-labeled microspheres produced have been validated for their useful properties in the analysis of biomolecules.

Notation

C:	Polymer concentration (% w/v)
Dg:	Drop diameter
Dj:	Jet diameter
Dp:	Particle diameter
D:	Diameter of the outlet orifice (μm)
D_0 :	Inner diameter of the capillary (μm)
D_{th} :	Theoretic particle diameter predicted by FF technology (μm)
D_{medium} :	Measured mean particle diameter (μm)

EA:	Ethyl acetate
EE:	Encapsulation efficiency
GSD:	Geometrical standard deviation (μm)
H:	Distance between the capillary and the outlet (μm)
ICP-MS:	Inductively coupled plasma mass spectroscopy
PMDS:	Poly(dimethylsiloxane)
PS:	Polystyrene
PSMiso:	Polystyrene isobutyl
PSMsec:	Polystyrene sec-butyl
PVA:	Poly(vinyl alcohol)
Qd:	Focused fluid flow rate (mL/h)
Qt:	Focusing fluid flow rate (mL/minute)
Q:	Amount of magnetite encapsulated
Q_i :	Initial magnetite amount
RhB:	Rhodamine B
SEM:	Scanning electron microscopy
SD:	Standard deviation (μm)
VC:	Variation coefficient.

Acknowledgments

This work was funded by the Spanish Ministerio de Ciencia y Tecnología (Project nos. DPI2002-04305-C02-02 and DPI2000-0392-P4-03), Consejería de Innovación de la Junta de Andalucía (Projects nos. 830446 and TEP-1190), and Corporación Tecnológica de Andalucía e Ingeniatrias Tecnológicas S.L. L. M.-Banderas, A. R.-Gil and R. G.-Prieto are grateful for financial support from the Spanish Ministerio de Ciencia y Tecnología, University of Sevilla-El Monte Foundation, and Consejería de Innovación de la Junta de Andalucía grants for researcher formation. The numerous suggestions of Dr. A. Cebolla are also gratefully acknowledged.

References

- [1] J. Ugelstad, K. H. Kaggerud, F. K. Hansen, and A. Berge, "Absorption of low molecular weight compounds in aqueous dispersions of polymer-oligomer particles. A two step swelling process of polymer particles giving an enormous increase in absorption capacity," *Makromolekulare Chemie*, vol. 180, no. 3, pp. 737–744, 1979.
- [2] D. Horák, F. Lednický, E. Petrovský, and A. Kapička, "Magnetic characteristics of ferrimagnetic microspheres prepared by dispersion polymerization," *Macromolecular Materials and Engineering*, vol. 289, no. 4, pp. 341–348, 2004.
- [3] J. Wang and S. P. Schwendeman, "Mechanisms of solvent evaporation encapsulation processes: prediction of solvent evaporation rate," *Journal of Pharmaceutical Sciences*, vol. 88, no. 10, pp. 1090–1099, 1998.
- [4] D. Tanyolac and A. R. Özduval, "Preparation of low-cost magnetic nitrocellulose microbeads," *Reactive and Functional Polymers*, vol. 45, no. 3, pp. 235–242, 2000.
- [5] S. Omi, A. Kanetaka, Y. Shimamori, A. Supsakulchai, M. Nagai, and G.-H. Ma, "Magnetite microcapsules prepared using a glass membrane and solvent removal," *Journal of Microencapsulation*, vol. 18, no. 6, pp. 749–765, 2001.

- [6] R. Wilson, D. G. Spiller, I. A. Prior, K. J. Veltkamp, and A. Hutchinson, "A simple method for preparing spectrally encoded magnetic beads for multiplexed detection," *ACS Nano*, vol. 1, no. 5, pp. 487–493, 2007.
- [7] H. Tokoro, T. Nakabayashi, S. Fujii, H. Zhao, and U. O. Häfeli, "Magnetic iron particles with high magnetization useful for immunoassay," *Journal of Magnetism and Magnetic Materials*, vol. 321, no. 10, pp. 1676–1678, 2009.
- [8] P. Tartaj, M. del Puerto Morales, S. Veintemillas-Verdaguer, T. González-Carreño, and C. J. Serna, "The preparation of magnetic nanoparticles for applications in biomedicine," *Journal of Physics D*, vol. 36, no. 13, pp. R182–R197, 2003.
- [9] M. A. M. Gijs, "Magnetic bead handling on-chip: new opportunities for analytical applications," *Microfluidics and Nanofluidics*, vol. 1, no. 1, pp. 22–40, 2004.
- [10] A. K. Gupta and M. Gupta, "Synthesis and surface engineering of iron oxide nanoparticles for biomedical applications," *Biomaterials*, vol. 26, no. 18, pp. 3995–4021, 2005.
- [11] S. Rudershausen, C. Grüttner, M. Frank, J. Teller, and F. Westphal, "Multifunctional superparamagnetic nanoparticles for life science applications," *European Cells and Materials*, vol. 3, supplement 2, pp. 81–83, 2002.
- [12] N. Wedemeyer, T. Pötter, S. Wetzlich, and W. Göhde, "Flow cytometric quantification of competitive reverse transcription-PCR products," *Clinical Chemistry*, vol. 48, no. 9, pp. 1398–1405, 2002.
- [13] S. P. Mulvaney, H. M. Mattoussi, and L. J. Whitman, "Incorporating fluorescent dyes and quantum dots into magnetic microbeads for immunoassays," *Biotechniques*, vol. 36, no. 4, pp. 602–609, 2004.
- [14] K. Kriz, F. Ibraimi, M. Lu, L.-O. Hansson, and D. Kriz, "Detection of C-reactive protein utilizing magnetic permeability detection based immunoassays," *Analytical Chemistry*, vol. 77, no. 18, pp. 5920–5924, 2005.
- [15] T. Banert and U. A. Peuker, "Synthesis of magnetic beads for bio-separation using the solution method," *Chemical Engineering Communications*, vol. 194, no. 6, pp. 707–719, 2007.
- [16] P. Wallemacq, J.-S. Goffinet, S. O'Morchoe et al., "Multi-site analytical evaluation of the abbott ARCHITECT Tacrolimus assay," *Therapeutic Drug Monitoring*, vol. 31, no. 2, pp. 198–204, 2009.
- [17] L. Martín-Banderas, M. Flores-Mosquera, A. M. Gañán-Calvo, et al., "Towards high-throughput production of uniformly encoded microparticles," *Advanced Materials*, vol. 18, no. 5, pp. 559–564, 2006.
- [18] A. M. Gañán-Calvo, L. Martín-Banderas, R. González-Prieto et al., "Straightforward production of encoded microbeads by Flow Focusing: potential applications for biomolecule detection," *International Journal of Pharmaceutics*, vol. 324, no. 1, pp. 19–26, 2006.
- [19] A. M. Gañán-Calvo, "Generation of steady liquid microthreads and micron-sized monodisperse sprays in gas streams," *Physical Review Letters*, vol. 80, no. 2, pp. 285–288, 1998.
- [20] R. Bocanegra, J. L. Sampedro, A. Gañán-Calvo, and M. Márquez, "Monodisperse structured multi-vesicle microencapsulation using flow-focusing and controlled disturbance," *Journal of Microencapsulation*, vol. 22, no. 7, pp. 745–759, 2005.
- [21] L. Martín-Banderas, M. Flores-Masquera, P. Riesco-Chueca et al., "Flow focusing: a versatile technology to produce size-controlled and specific-morphology microparticles," *Small*, vol. 1, no. 7, pp. 688–692, 2005.
- [22] M. A. Holgado, J. L. Arias, M. J. Cózar, J. Álvarez-Fuentes, A. M. Gañán-Calvo, and M. Fernández-Arévalo, "Synthesis of lidocaine-loaded PLGA microparticles by flow focusing. Effects on drug loading and release properties," *International Journal of Pharmaceutics*, vol. 358, no. 1–2, pp. 27–35, 2008.
- [23] M. A. Holgado, M. J. Cózar-Bernal, S. Salas, J. L. Arias, J. Álvarez-Fuentes, and M. Fernández-Arévalo, "Protein-loaded PLGA microparticles engineered by flow focusing: physico-chemical characterization and protein detection by reversed-phase HPLC," *International Journal of Pharmaceutics*, vol. 380, no. 1–2, pp. 147–154, 2009.
- [24] A. M. Gañán-Calvo and P. Riesco-Chueca, "Jetting-dripping transition of a liquid jet in a lower viscosity co-flowing immiscible liquid: the minimum flow rate in flow focusing," *Journal of Fluid Mechanics*, vol. 553, pp. 75–84, 2006.
- [25] A. M. Gañán-Calvo and J. M. Gordillo, "Perfectly monodisperse microbubbling by capillary flow focusing," *Physical Review Letters*, vol. 87, no. 27, Article ID 274501, 4 pages, 2001.
- [26] A. M. Gañán-Calvo, J. M. Fernández, A. Marquez Oliver, and M. Márquez, "Coarsening of monodisperse wet microfoams," *Applied Physics Letters*, vol. 84, no. 24, pp. 4989–4991, 2004.
- [27] S. Takeuchi, P. Garstecki, D. B. Weibel, and G. M. Whitesides, "An axisymmetric flow-focusing microfluidic device," *Advanced Materials*, vol. 17, no. 8, pp. 1067–1072, 2005.
- [28] C.-H. Chen, A. R. Abate, D. L. Eugene, E. M. Terentjev, and D. A. Weitz, "Microfluidic assembly of magnetic hydrogel particles with uniformly anisotropic structure," *Advanced Materials*, vol. 21, no. 31, pp. 3201–3204, 2009.
- [29] K. P. Yuet, D. K. Hwang, R. Haghighi, and P. S. Doyle, "Multi-functional superparamagnetic Janus particles," *Langmuir*, vol. 26, no. 6, pp. 4281–4287, 2010.
- [30] X. Gong, S. Peng, W. Wen, P. Sheng, and W. Li, "Design and fabrication of magnetically functionalized core/shell microspheres for smart drug delivery," *Advanced Functional Materials*, vol. 19, no. 2, pp. 292–297, 2009.
- [31] J. P. Nolan and F. Mandy, "Multiplexed and microparticle-based analyses: quantitative tools for the large-scale analysis of biological systems," *Cytometry A*, vol. 69, no. 5, pp. 318–325, 2006.
- [32] K. W. Bong, S. C. Chapin, and P. S. Doyle, "Magnetic barcoded hydrogel microparticles for multiplexed detection," *Langmuir*, vol. 26, no. 11, pp. 8008–8014, 2010.

Research Article

Biocompatible Metal-Oxide Nanoparticles: Nanotechnology Improvement of Conventional Prosthetic Acrylic Resins

**Laura S. Acosta-Torres,¹ Luz M. López-Marín,¹ R. Elvira Núñez-Anita,²
Genoveva Hernández-Padrón,¹ and Victor M. Castaño¹**

¹ Centro de Física Aplicada y Tecnología Avanzada, Universidad Nacional Autónoma de México, Boulevard Juriquilla 3001, Santiago de Querétaro, Querétaro 76230, Mexico

² Instituto de Neurobiología, Universidad Nacional Autónoma de México, Boulevard Juriquilla 3001, Santiago de Querétaro, Querétaro 76230, Mexico

Correspondence should be addressed to Victor M. Castaño, castano@fata.unam.mx

Received 28 April 2010; Revised 30 June 2010; Accepted 6 September 2010

Academic Editor: Libo Wu

Copyright © 2011 Laura S. Acosta-Torres et al. This is an open access article distributed under the Creative Commons Attribution License, which permits unrestricted use, distribution, and reproduction in any medium, provided the original work is properly cited.

Nowadays, most products for dental restoration are produced from acrylic resins based on heat-cured Poly(Methyl MethAcrylate) (PMMA). The addition of metal nanoparticles to organic materials is known to increase the surface hydrophobicity and to reduce adherence to biomolecules. This paper describes the use of nanostructured materials, TiO_2 and Fe_2O_3 , for simultaneously coloring and/or improving the antimicrobial properties of PMMA resins. Nanoparticles of metal oxides were included during suspension polymerization to produce hybrid metal oxides-alginate-containing PMMA. Metal oxide nanoparticles were characterized by dynamic light scattering, and X-ray diffraction. Physicochemical characterization of synthesized resins was assessed by a combination of spectroscopy, scanning electron microscopy, viscometry, porosity, and mechanical tests. Adherence of *Candida albicans* cells and cellular compatibility assays were performed to explore biocompatibility and microbial adhesion of standard and novel materials. Our results show that introduction of biocompatible metal nanoparticles is a suitable means for the improvement of conventional acrylic dental resins.

1. Introduction

To date, up to 95% dental prostheses are composed of Poly(Methyl MethAcrylate) (PMMA), due to its advantages, including its optical properties, biocompatibility, and aesthetics [1, 2]. However, important issues are still to be addressed in order to improve acrylic polymers properties for artificial dentures. For instance, microbial adhesion onto PMMA has been a long-standing drawback accompanying long-term PMMA wearers. In dentistry, adhesion and plaque formation onto PMMA-based resins is a common source of oral cavity infections and stomatitis [3]. These affections may continue a variety of human pathogens and have been commonly associated to the oral commensal *Candida albicans* [4], an opportunistic pathogen causing emergent disease within immune suppressed patients [5]. Microbial adhesion has also been a limiting factor for other PMMA

biomedical applications, such as ophthalmic prostheses, contact lenses and bone repair [6, 7]. Other weak points of PMMA materials include lack of strength and toxicity [8]. Therefore, the search for innovative solutions addressing these problems is of special interest in the development of acrylic materials-based implants.

Dental prostheses may include titanium oxide (TiO_2) as a coloring agent; hybrid materials ranging from yellowed-transparent to red colors may be obtained using TiO_2 into a given PMMA formulation. Interestingly, nanosized structured TiO_2 has proved to bear antimicrobial properties, due to TiO_2 -induced photocatalytic production of cytotoxic oxygen radicals [9]. In 1985, Matsunaga et al. reported for the first time the microbicidal effect of TiO_2 photocatalytic reaction [10]. TiO_2 exhibits strong oxidizing power under irradiation of UV light with water and oxygen environment around TiO_2 . Consequently, irradiated TiO_2 can decompose

and/or oxidize most of organic and/or inorganic compounds [11]. This phenomenon may increase the applicability of titania for use in the destruction of microorganisms, which consist primarily of organic-based compounds. In addition, its high chemical stability, low cost, and nontoxicity make TiO_2 ideal as an alternative material for improving antimicrobial properties. Up to now, antibacterial applications of TiO_2 have been employed in various environmental settings.

Various studies have shown that doping TiO_2 with metal or metal oxides, such as Fe^{3+} , strongly improve the photocatalytic activity, hence increasing their disinfection effect [10, 11]. In the present study, both TiO_2 and Fe_2O_3 nanoparticles have been integrated into alginate-containing PMMA resins designed as “pink” gingival substitute and artificial dental holders. Hybrid inorganic-PMMA materials were prepared by introducing TiO_2 and Fe_2O_3 nanoparticles during acrylate synthesis. A combination of physicochemical, microscopy, and biological analyses were used to characterize the novel nanoparticles-containing acrylic formulation.

2. Materials and Methods

2.1. Nanoparticles and Reagents. TiO_2 and Fe_2O_3 were kindly supplied by González Cano y Compañía (Mexico). Methyl Methacrylate, Peroxide Benzoyl and Toluene were purchased from Sigma (St. Louis, MO), and Sodium Alginate was obtained from Manufacturera Dental Continental (Mexico).

2.2. PMMA Synthesis. Standard PMMA was synthesized when Methyl MethAcrylate (MMA) monomer (200 g) was dispersed in 800 mL of deionized water in a five-neck glass reactor under nitrogen atmosphere at $70 \pm 1^\circ\text{C}$ and 1200 rpm under reflux. Then, the suspension was mixed with sodium alginate (2.5%) as suspension agent and peroxide benzoyl as initiator (1%). For the nanopigmented PMMA formulation, TiO_2 (0.0150 g) and Fe_2O_3 (0.009 g) were dissolved in water and incorporated with MMA to the reaction system. The resulting PMMA particles were carefully washed and dried at 60°C during 24 h. Specimens were prepared by mixing PMMA powder with MMA (3:1) and 1% initiator and packed into molds. Then, thermopolymerization was conducted in a water bath at $70 \pm 1^\circ\text{C}$ during 90 min followed by 30 min in boiling water. Specimens were trimmed with wet abrasive paper of grit 100 and 300 (Fandeli, Mexico), in order to obtain $65 \times 10 \times 2.5$ mm samples for flexural behavior analyses, $30 \times 10 \times 2.5$ mm for porosity test, 10×0.5 mm discs for water sorption and solubility tests, and 10×2 mm discs for toxicity assay and *Candida albicans* adhesion test. The upper and lower planes of discs for biological assays were untouched.

2.3. Dynamic Light Scattering. Prior to use, all the solvents used were filtrated with $0.2 \mu\text{m}$ filters to eliminate dust and the sample holder was cleaned with distilled water followed by acetone, to prevent contamination. For each sample, 2 mg of particles were suspended in 20 mL of solvent and filtrated. The samples were maintained in an ultrasonic bath for 10 min. The scattering cells (10-mL cylindrical vials) were

immersed in a large-diameter thermostated bath of index-matching liquid (transdecalin). Dynamic Light Scattering (DLS) measurements were performed in a B1-200SM instrument (Brookhaven Instruments Co., Holtsville, NY). The results were analyzed by using the Nonnegative Least Square (NNLS) and Contin methods.

2.4. X-Ray Diffraction (XRD). XRD was used to determine the phases present in the TiO_2 and Fe_2O_3 particles. Diffractograms were recorded on a MiniFlex, Rigaku Diffractometer. A 2θ diffraction angle per min ranging from 10° to 80° at 30 kV and 15 mA.

2.5. Spectroscopy. For the synthesized standard and nanopigmented PMMA, Fourier Transform Infra-Red (FTIR) spectroscopy was conducted in a Bruker Vector 33 Instrument, by the transmittance technique. Samples were prepared in KBr pellets with a weight content of around 1%. Briefly, both resin (~ 2 mg) and KBr (~ 150 mg) were ground together into an agate mortar with an agate pestle until the sample was well dispersed, and the mixture has the consistency of fine flour. Then, a translucent disk was prepared and FTIR spectra were obtained in the wavenumber region between 400 and 4000 cm^{-1} . Specimens were also analyzed by Raman Dispersive Spectroscopy in a Senterra apparatus (Bruker) equipped with $\lambda = 685 \text{ nm}$ laser and FT-Raman (Nicolet 910) with $\lambda = 1064 \text{ nm}$ in the laser, coupled with an Olympus microscope. The sample was directly deposited onto a holder with no further preparation.

2.6. Scanning Electronic Microscopy. SEM observations were carried out with a JSM-6060LV scanning microscope (JEOL, Peabody, MA). The samples were coated with gold by vacuum evaporation and examined at $\times 100$ magnifications.

2.7. Viscosimetry. Dilute PMMA solutions were made in toluene. The viscosities were measured using an Ubbelohde 1C capillary viscometer. The test was performed at 25°C and the viscosity average molecular weight (Mv) was calculated using the Mark-Houwink-Sakurada equation [12].

2.8. Flexural Behavior. Flexural strength (S) and flexural modulus (E) were measured in a tensile-compression cell (Mecmesin, Horsham, England), using a cross head of 0.5 kg/min. Specimens ($n = 10$) were loaded to failure in three-point bending. The parameters were calculated from the following [13]:

$$S = \frac{3PL}{2bh^2}, \quad E = \frac{FL^3}{4\delta bh^3}, \quad (1)$$

where P is the load at break, b and h are the width and the thickness of the specimen, respectively, L is the length between supports (10 mm), δ is the maximum deflection of the center of the beam, and F is the slope of the tangent to the initial straight-line portion of the load-deflection curve.

2.9. Porosity Test. Samples ($n = 10$) were initially weighted and placed in a silica gel desiccator. Every 24 h sample weight was recorded until constant weight was reached (± 0.0005 g). Internal porosity (V_{ip}) of each sample was calculated through the equation $W_a = (d_r - d_a)(V_{sp} - V_{ip})$, where W_a is the sample weight (g), d_r is the acrylic resin density (1.198 g/cm^3), d_a (0.00123 g/cm^3) is the local air density at 21°C and 585 mmHg , V_{sp} is volume of samples, and V_{ip} is the volume of internal porosity (cm^3) [14].

2.10. Water Sorption and Solubility Test. The discs ($n = 10$) were weighted (mg) and placed in a silica gel dessicator, every 24 h the discs were weighted until constant mass (m_1). Discs were placed in distilled water for 7 days at $37 \pm 1^\circ\text{C}$. After that, the discs were dried and weighted (m_2). The discs were placed in the dessicator again and weighted every 24 h until constant mass (m_3). Area (A) of each sample was calculated in cm^2 . Water sorption (W_s) and Solubility (Sl) were calculated as follows [15]: $W_s = (m_2 - m_1)/A$; $Sl = (m_1 - m_3)/A$.

2.11. Toxicity Assay. Specimens from standard and nanoparticles-pigmented PMMA resins were prepared and sterilized by exposure of both faces to ultraviolet irradiation during 5 min. Biocompatibility was assessed by an *in vitro* test performed in cultured cells in the presence of the new materials [8, 16, 17]. Briefly, NIH-3T3 mouse embryonic fibroblast-like cells were exposed to PMMA specimens, and proliferation was assessed measuring reductase enzymatic activity by transformation of 3-(4,5-dimethylthiazol-2-yl)-2,5-diphenyltetrazolium bromide (MTT) into a colored reduced form [18]. Cells were maintained in Dulbecco's Modified Eagle Medium (DMEM) (Gibco, Invitrogen, Carlsbad, CA) supplemented with 10% fetal bovine serum (Gibco) and 100 U/mL penicillin-streptomycin at 37°C in 5% CO_2 , 95% humidity. Cells were plated into 24-well sterile plates (Nunc-Thermo Fisher Scientific, Roskilde, Denmark) at a concentration of 10^4 cells per well and incubated in $500 \mu\text{L}$ culture medium for 24 h and 72 h. Then, the culture medium was renewed and specimens were carefully deposited in direct contact to NIH-3T3 cell monolayer. After incubation times, resins were removed, MTT assay was performed following the manufacturer instructions (Sigma, St. Louis, MO), and absorbance was measured in a microplate reader (Bio-Rad 680) at a wavelength of 655 nm . Cell cultures with medium only were used as controls. Each experiment was performed by triplicate.

2.12. Candida albicans Adhesion Test. *Candida albicans* strain 90026 (American Type Culture Collection, Manassas, VA) was cultured overnight in yeast broth (Sigma-Aldrich). Cells were harvested by centrifugation at $3,000 \text{ rpm}$ for 5 min, and pellet was adjusted to obtain a suspension with 0.15 optical density at 540 nm . Sterilized resin specimens were placed into 24-well sterile culture plates (Nunc) and $500 \mu\text{L}$ yeast suspension was added. After a 24-h incubation period at 37°C , nonadherent cells were removed from specimens by washing for 10 min under sonication, followed by 3 washings with distilled water for 1 min under shaking.

Adherent fungi were extracted by incubation with 1.0 mL benzalconium chloride for 15 min. Finally, a microbial cell viability assay based on luminescent ATP measurement (Bac Titer-Glo, Promega, Fitchburg, WI) was performed in order to determine the number of viable cells adhered to composite resins. Briefly, extract aliquots ($20 \mu\text{L}$ each) were mixed with $30 \mu\text{L}$ BacTiter Glo reagent in 1.5 mL -Eppendorf clear tubes and luminescence was recorded after 5 min in a 20/20 luminometer (Turner Biosystems, Promega) at wavelength of 590 nm emission. Relative luminescence intensity, in 10 sec-integration periods, was measured in three samples.

2.13. Statistical Analysis. One-way ANOVA and Tukey test ($P < .05$) were carried out for the following tests: elastic modulus, transverse strength, porosity, sorption water, solubility, cytotoxicity assay, and *Candida albicans* adhesion.

3. Results and Discussion

3.1. Characterization of Metal-Oxide Particles. As observed in Figure 1, metal oxide particles range from 150 to 350 nm in diameter, showing a normal size distribution. Average size of pigments was found to be 225.9 nm for TiO_2 and 299.7 nm for Fe_2O_3 particles. The pigments were also characterized by X-ray diffraction (XRD) in order to search whether specific crystal phases with antimicrobial properties are present in the powders. The XRD patterns of nanoparticles are shown in Figure 2. Diffractograms indicate crystalline structures for both nanomaterials. Rutile was found to be the major phase in the TiO_2 sample, although a certain amount of anatase morphology was also observed (Figure 2(a)). For their part, ferrite particles were found with the hematite crystalline structure (Figure 2(b)).

3.2. Production and Morphology of Standard and Nanopigmented Resins. Synthesis of PMMA was conducted by adding TiO_2 and Fe_2O_3 nanoparticles during the polymerization step, giving rise to pigmented resins. Standard formulations lacking nanoparticles were prepared and used as controls. SEM analyses showed that synthesis procedures reveal acrylic resins with homogeneous size distribution and morphology for both standard and hybrid materials. SEM micrographs showed the presence of regular spherical particles, with size distributions around $60 \mu\text{m}$ in diameter (Figure 3). The homogeneous distribution of particles suggests that sodium alginate is a suitable suspension agent promoting the formation of spherical PMMA particles, as it has been observed previously [12].

3.3. Spectroscopy. Standard and nanopigmented PMMA were analyzed by FTIR and Raman dispersive spectroscopy. As seen in Figure 4(a), the FTIR spectra show the main expected bands characterizing the vibrational spectrum of PMMA [19, 20], namely, the characteristic methylene C-H stretches bands at 2949 cm^{-1} and the ester carbonyl C=O stretching vibrations at 1722 cm^{-1} . The C-O deformation at 1166 cm^{-1} , the C-O-C vibration at 1141 cm^{-1} and CH_2 aromatic group at the band 1437 cm^{-1} . In Figure 4(b),

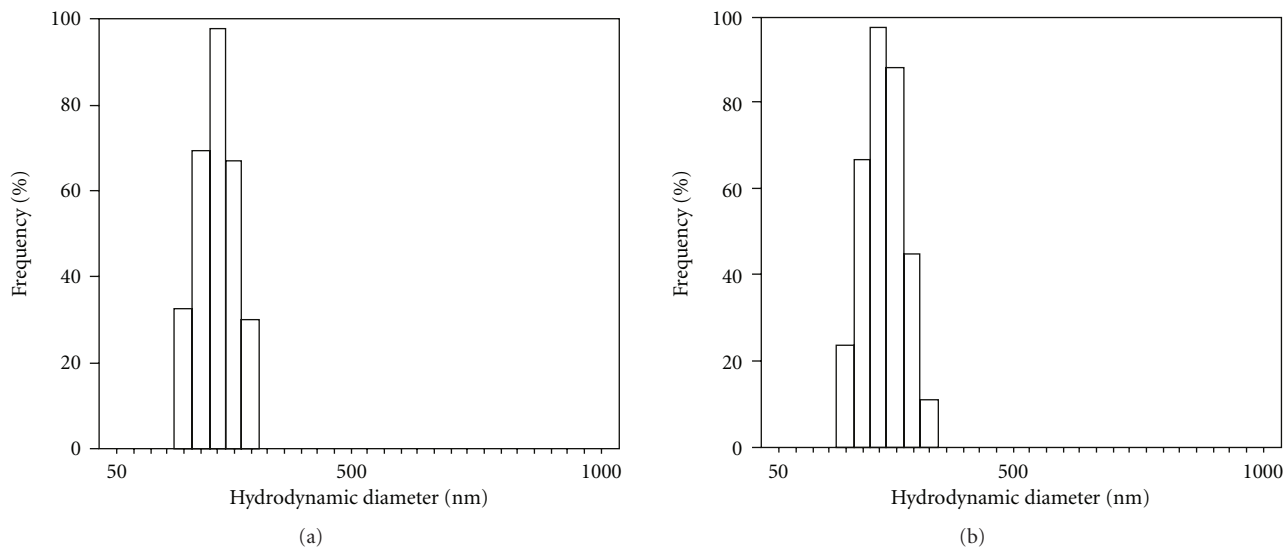


FIGURE 1: Characterization of metal oxide powders used for pigmented PMMA. Dynamic Light Scattering (DLS) was performed to determine the size distribution of TiO_2 (a) and Fe_2O_3 (b) nanoparticles.

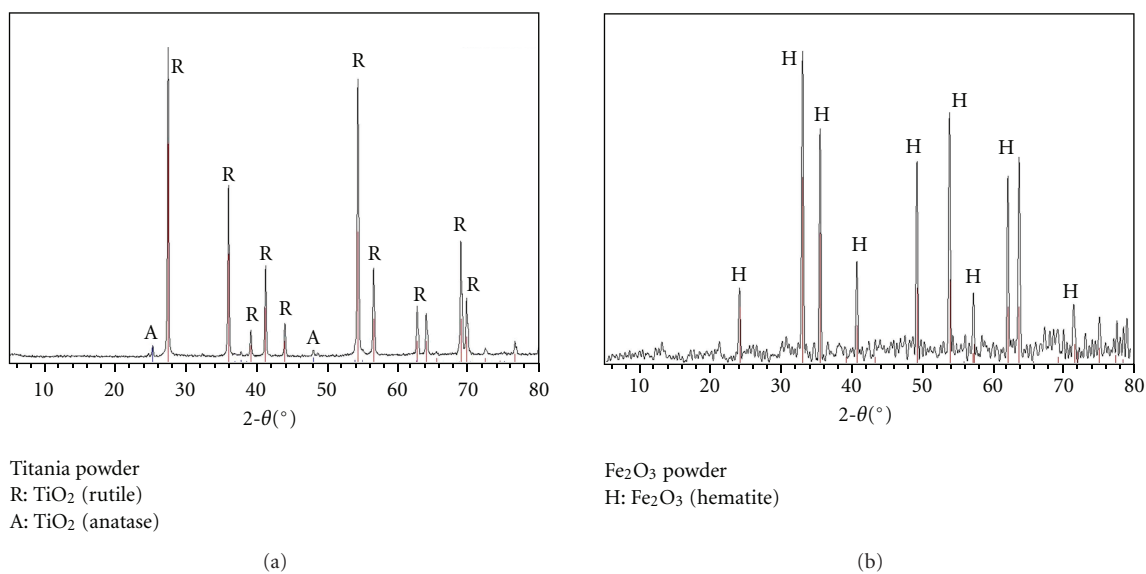


FIGURE 2: X-ray diffraction patterns of TiO_2 (a) and Fe_2O_3 (b) nanoparticles used in this study. Titania spectrum shows a predominant rutile crystalline structure whereas a hematite phase was found for ferrite.

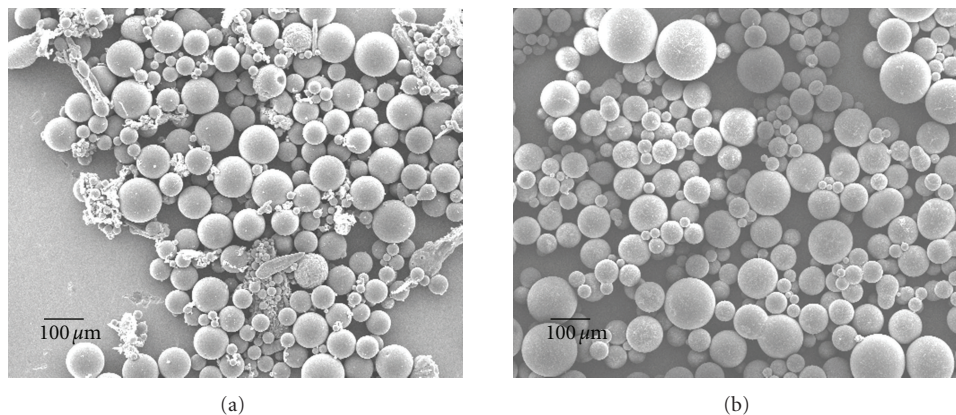


FIGURE 3: SEM micrograph of standard (a) and nanopigmented PMMA (b) at $\times 100$ magnification.

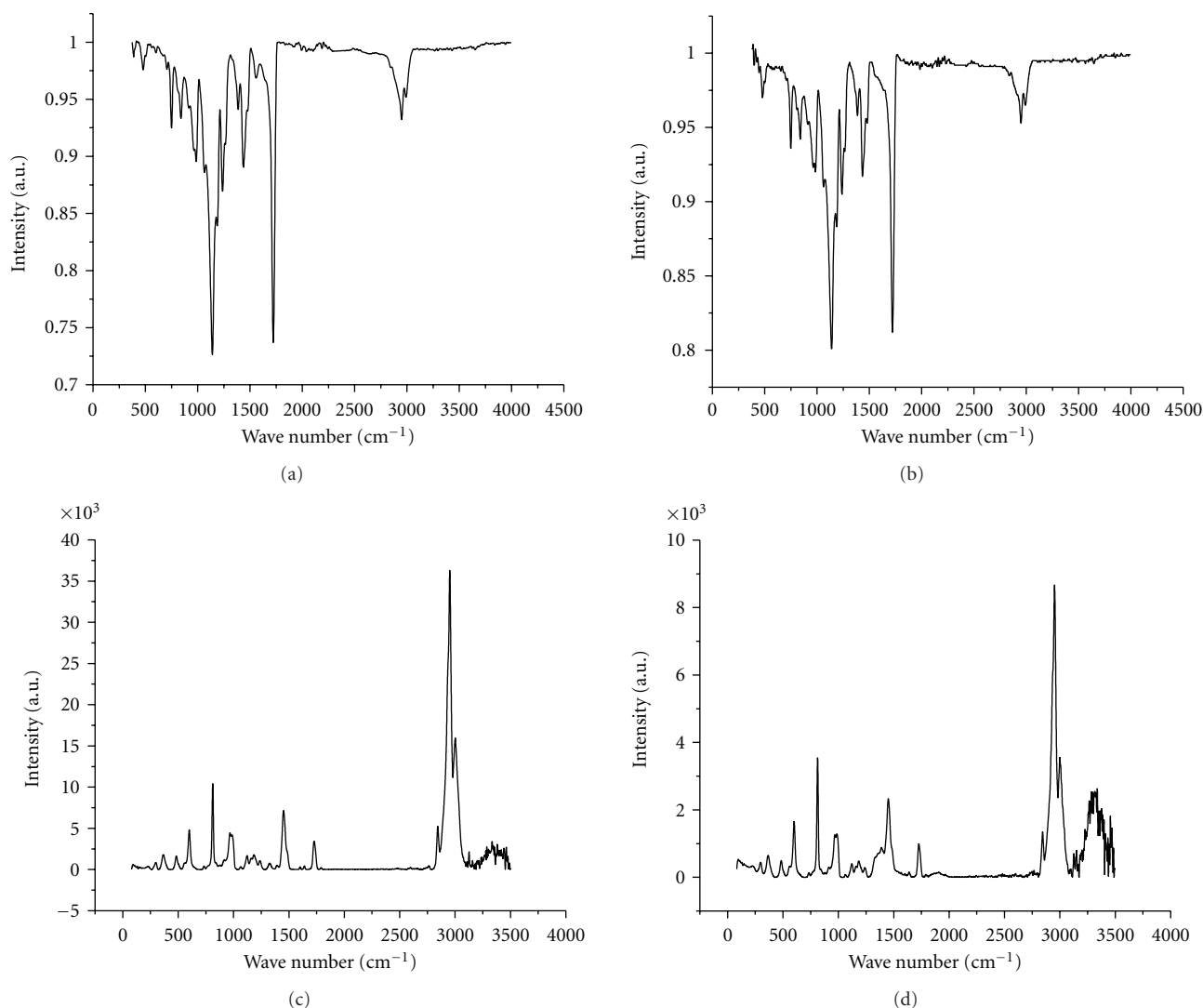


FIGURE 4: Spectroscopy analysis of PMMA resins. (a) FT-IR of standard PMMA. (b) FT-IR of nanopigmented PMMA. (c) and (d) Raman Dispersive spectra from synthesized PMMA resins without and with nanopigments, respectively. Intensity of peaks is in arbitrary units (a.u.).

the vibrational band observed between 2858 and 2958 cm⁻¹ refers to the stretching C–H from alkyl groups and the peak between 1722 cm⁻¹ are due to the stretching C=O and C–O from acetate group remaining from PMMA polymerization. The addition of the nanomaterials did not affect the structure of the original PMMA, but they have helped to substantially improve its properties [21].

A typical sequence of Raman spectra is depicted in Figures 4(c) and 4(d), for the samples: standard and pigmented PMMA, respectively. Bands at 1726, 994, and 812 cm⁻¹ correspond to the carbonyl group of the PMMA polymer [22]. The 601 and 385 cm⁻¹ bands correspond to the nanopigment materials.

3.4. Molecular Weight. The synthesized polymers were subjected to viscometry testing using toluene as solvent. Figure 5 shows the values obtained with the concentration and reduced viscosity of each polymer tested in order to obtain

the γ value of the graph equation. The γ value was replaced in the Mark-Howink-Sakurada equation to get the molecular weight (M_v) of each PMMA. The obtained values of the molecular weight distribution were 24 and 36×10^5 g/mol for the standard PMMA and nanopigmented PMMA, respectively, which probably attributable to the interaction of metal oxides with organic compounds during the synthesis of polymers.

3.5. Flexural Behavior and Porosity. Important physical properties of acrylic resins may be influenced by the presence of TiO₂ and Fe₂O₃ nanoparticles. In this work, the flexural modulus, flexural strength, and porosity of standard and nanopigmented polymer resins were determined [23, 24]. As observed in Table 1, flexural behavior was unchanged between standard and nanopigmented PMMA. There was no statistically significant difference in the elastic modulus values ($P > .05$). In contrast, the transverse strength and

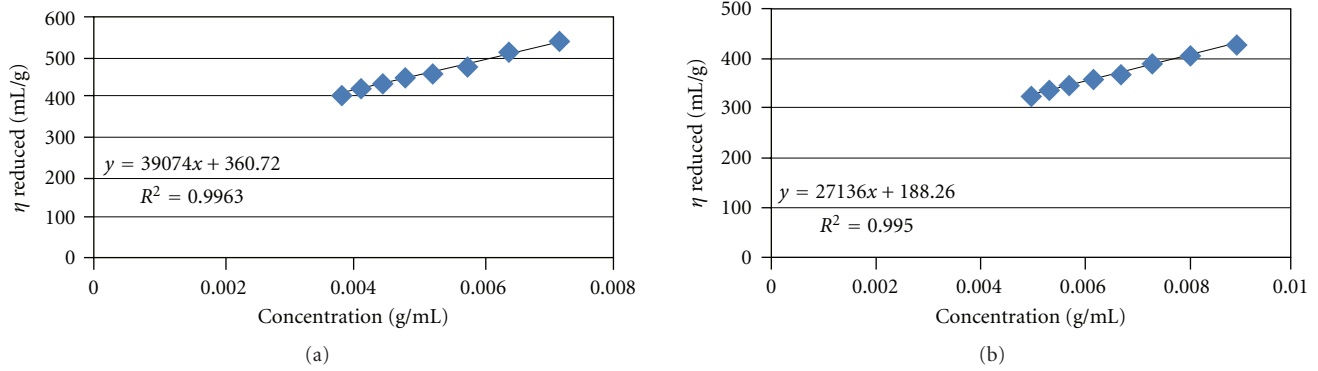


FIGURE 5: Determination of molecular weight distribution values for standard (a) and nanopigmented (b) PMMA, based on concentration and reduced viscosity analysis.

TABLE 1: Mechanical properties in synthesized standard and nanoparticles-containing PMMA resins.

	Flexural Modulus (GPa)	Flexural Strength (MPa)	Porosity (%)
Standard PMMA	2.5 ± 0.3	62.3 ± 4.9	10.5 ± 0.7
Nanopigmented PMMA	2.5 ± 1.4	77.6 ± 5.1	4.6 ± 0.4

TABLE 2: Mean values and standard deviation of water sorption and solubility tests from standard and nanopigmented PMMA.

	Water Sorption (mg/cm ²)	Solubility (mg/cm ²)
Standard PMMA	0.71 ± 0.5	0.041 ± 0.07
Nanopigmented PMMA	0.27 ± 0.2	0.035 ± 0.03

porosity values were found significantly different between standard and nanopigmented resins ($P < .05$). Flexural values are important in dental prosthetics because biting and mastication forces have a deforming effect during function, and any factor that increases the deformation of the base and changes the stress distribution may lead to denture fracture [2]. In contrast, a strong reduction of porosity was found with the introduction of nanosized metal oxide pigments. It has been reported that significant porosity can severely weaken acrylic resin prosthesis. Regarding hygiene, a denture must be nonporous in order to resist staining, calculus deposition, and adherent substances. A spongy denture tissue surface, full of nutritive substances, is an ideal incubator for species such as *Candida albicans*.

3.6. Water Sorption and Solubility Test. In a denture base material, water absorbed acts as a plasticizer and affects the dimensional stability, subjecting the material to internal stresses and possible crack formation [25, 26]. Water sorption of PMMA formulations was thus evaluated. Table 2 shows water sorption found in PMMA formulations. Nanopigmented PMMA presented lower sorption value than the standard PMMA. In solubility tests, both polymers

showed similar behavior. There was a statistically significant difference ($P < .05$) between groups in water sorption tests. When solubility of polymers was tested (Table 2), no differences were found between formulations, which showed low solubility. These results fulfill with the fact that polymer networks should be insoluble materials, so that chemical and physical processes with deleterious effects on the structure and function of dental polymers can be avoided [25].

3.7. Microbial Adhesion and Cellular Compatibility. Interactions between microbes and surface materials for prosthodontics may result in plaque formation and oral colonization by opportunistic pathogens. The first interactions leading to plaque formation is microbial adherence to surface materials. Herein we performed microbial tests to assess the attachment of *Candida albicans*, the most common oral-associated pathogen, onto standard and nanoparticles-containing PMMA. *C. albicans* was cultured under aerobic conditions to obtain a cell suspension and incubated with specimen disks. After removal of nonadherent fungi, a luminometric assay was performed to estimate adhesion on the new material. As shown in Table 3, PMMA containing nanoparticles showed a lowered *C. albicans* adhesion. Since the antifungal effect may be related to a wide spectrum of cellular toxicity, the activity of fibroblast-like cells cultured in the presence of standard and nanoparticles-containing materials was explored. An enzyme metabolic assay, reflecting viability of cultured cells, showed that nanoparticle-doped materials have a biocompatibility behavior similar to that of the control group, with no significant differences according to one-way ANOVA test (Figure 6). These results demonstrate that nanostructured metal coloring additives are a suitable means for producing nontoxic hybrid materials with antimicrobial properties for dentistry applications.

4. Conclusion

In this study, nanosized TiO_2 and Fe_2O_3 particles were employed during synthesis of PMMA. In recent years, metal oxide nanoparticles have been largely investigated for their activity as antimicrobial additives. In particular,

TABLE 3: Luminiscence assay results of adherent *Candida albicans* onto nonpigmented and nanoparticles-pigmented PMMA.

Acrylic resin	Luminiscence relative units (LRU)
Standard PMMA	25912 ± 12778
Nanopigmented PMMA	23447 ± 2161

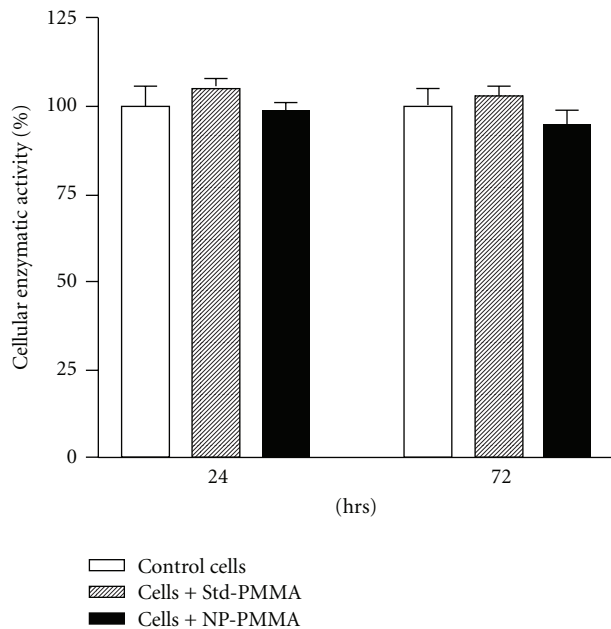


FIGURE 6: Biocompatibility of nonpigmented, standard PMMA (Std-PMMA) and $\text{TiO}_2/\text{Fe}_2\text{O}_3$ -containing PMMA (NP-PMMA) as assessed through a metabolic assay in NIH-3T3 fibroblast-like cell line cultures. Cells were exposed to PMMA formulations during 24 or 72 h. No significant differences were found between groups, according to one-way ANOVA test ($P < .05$).

TiO_2 is now considered a low-cost, clean photocatalyst with chemical stability and nontoxicity [27, 28] and has been used for a wide variety of environmental applications, including water treatment [9] and air purification [10, 29]. Herein we report that the introduction of nanosized metal oxide materials for preparing acrylic resins allows the production of polymer with both color and surface modifications. Interestingly, physical tests of nanopigmented and standard PMMA showed a lower porosity for $\text{TiO}_2/\text{Fe}_2\text{O}_3$ containing PMMA. This finding suggests that metal oxide nanoparticles are suitable additives for the improvement of PMMA formulations, since high porosities have been considered a critical drawback for PMMA in prosthodontics applications [30]. Moreover, the nanotechnology-assisted design allows a product with well controlled morphology, as assessed by SEM. Physicomechanical testing also showed that nanoparticles-containing PMMA behave as is specified by the International Standards for Denture Prosthetics [13, 15]. Since photocatalytic events induced by TiO_2 and ferrite nanoparticles may be a source of cellular toxicity, the hybrid pigmented PMMA material was analyzed for

biocompatibility, using the MTT assay, an *in vitro* cellular activity test widely used for dental materials [16, 17]. As shown in Figure 6, cells incubated for different periods with $\text{TiO}_2/\text{Fe}_2\text{O}_3$ containing PMMA indicated that the new formulation was devoid of toxicity. Antimicrobial properties in PMMA formulations were assessed by a luminometry assay of adherent *Candida albicans* viable cells. The results showed that using the nanoparticles-containing formulation, antimicrobial properties were increased in a slight manner only. Further research must thus include TiO_2 mainly composed by particles with anatase crystal structure, a morphology phase corresponding to the highest titania antimicrobial effects [11]. As it was shown by X-ray diffraction analyses, morphology of TiO_2 nanoparticles obtained for this study had a low anatase phase amount. Besides, the influence on PMMA properties of nanoparticles concentration remains an important issue to be addressed. In summary, this work points out a potential of metal oxide nanoparticles for the improvement of resin-based dental materials. Further research on the hybrid material is therefore encouraged for future prosthodontics developments.

Acknowledgments

The authors wish to thank Susana Vargas, Alicia del Real, and Carmen Vázquez for excellent technical assistance. Laura S. Acosta-Torres is recipient of a postdoctoral fellowship from DGAPA/UNAM.

References

- [1] M. Tanoğlu and Y. Ergün, "Porous nanocomposites prepared from layered clay and PMMA [poly(methyl methacrylate)]," *Composites Part A: Applied Science and Manufacturing*, vol. 38, no. 2, pp. 318–322, 2007.
- [2] O. Gurbuz, F. Unalan, and I. Dikbas, "Comparison of the transverse strength of six acrylic denture resins," *OHDMBSC*, vol. 9, pp. 21–24, 2010.
- [3] M. Yamauchi, K. Yamamoto, M. Wakabayashi, and J. Kawano, "In vitro adherence of microorganisms to denture base resin with different surface texture," *Dental Materials Journal*, vol. 9, no. 1, pp. 19–24, 1990.
- [4] S. Hahnel, M. Rosentritt, G. Handel, and R. Bürgers, "In vitro evaluation of artificial ageing on surface properties and early *Candida albicans* adhesion to prosthetic resins," *Journal of Materials Science: Materials in Medicine*, vol. 20, no. 1, pp. 249–255, 2009.
- [5] J. M. Saunus, A. Kazoullis, and C. S. Farah, "Cellular and molecular mechanisms of resistance to oral *Candida albicans* infections," *Frontiers in Bioscience*, vol. 13, pp. 5345–5358, 2008.
- [6] L. Kodjikian, C. Burillon, C. Roques et al., "Intraocular lenses, bacterial adhesion and endophthalmitis prevention: a review," *Bio-Medical Materials and Engineering*, vol. 14, no. 4, pp. 395–409, 2004.
- [7] M. Shi, J. D. Kretlow, A. Nguyen et al., "Antibiotic-releasing porous polymethylmethacrylate constructs for osseous space maintenance and infection control," *Biomaterials*, vol. 31, no. 14, pp. 4146–4156, 2010.

- [8] S. K. Kim, S. J. Heo, J. Y. Koak et al., "A biocompatibility study of a reinforced acrylic-based hybrid denture composite resin with polyhedraloligosilsesquioxane," *Journal of Oral Rehabilitation*, vol. 34, no. 5, pp. 389–395, 2007.
- [9] Q. Li, S. Mahendra, D. Y. Lyon et al., "Antimicrobial nanomaterials for water disinfection and microbial control: potential applications and implications," *Water Research*, vol. 42, no. 18, pp. 4591–4602, 2008.
- [10] L. Sikong, B. Kongreong, D. Kantachote, and W. Sutthisripok, "Photocatalytic activity and antibacterial behavior of Fe³⁺-doped TiO₂/SnO₂ nanoparticles," *Energy Research Journal*, vol. 1, pp. 120–125, 2010.
- [11] C. C. Trapalis, P. Keivanidis, G. Kordas et al., "TiO₂(Fe³⁺) nanostructured thin films with antibacterial properties," *Thin Solid Films*, vol. 433, no. 1–2, pp. 186–190, 2003.
- [12] L. S. Acosta-Torres, F. H. Barceló-Santana, C. A. Álvarez-Gayosso, and J. Reyes-Gasga, "Synthesis and characterization of poly(methyl methacrylate) polymerized by microwave energy or conventional water bath," *Journal of Applied Polymer Science*, vol. 109, no. 6, pp. 3953–3960, 2008.
- [13] ISO 1567, *Dentistry—Denture Base Polymers*, International Organization for Standardization, Geneva, Switzerland, 1999.
- [14] M. A. Compagnoni, D. B. Barbosa, R. F. de Souza, and A. C. Pero, "The effect of polymerization cycles on porosity of microwave-processed denture base resin," *Journal of Prosthetic Dentistry*, vol. 91, no. 3, pp. 281–285, 2004.
- [15] "Revised American Dental Association specification no. 12 for denture base polymers," *Journal of the American Dental Association*, vol. 90, no. 2, pp. 451–458, 1975.
- [16] E. Larraz, C. Elvira, M. Fernández et al., "Self-curing acrylic formulations with applications in intervertebral disk restoration: drug release and biological behaviour," *Journal of Tissue Engineering and Regenerative Medicine*, vol. 1, no. 2, pp. 120–127, 2007.
- [17] G. Meriç, J. E. Dahl, and I. E. Ruyter, "Cytotoxicity of silica-glass fiber reinforced composites," *Dental Materials*, vol. 24, no. 9, pp. 1201–1206, 2008.
- [18] T. Mosmann, "Rapid colorimetric assay for cellular growth and survival: application to proliferation and cytotoxicity assays," *Journal of Immunological Methods*, vol. 65, no. 1–2, pp. 55–63, 1983.
- [19] J. Jiang, "Ultrasonic-assisted synthesis of PMMA/Ni_{0.5}Zn_{0.5}Fe₂O₄ nanocomposite in mixed surfactant system," *European Polymer Journal*, vol. 43, no. 5, pp. 1724–1728, 2007.
- [20] L. H. Sperling, *Introduction to Physical Polymer Science*, John Wiley & Sons, New York, NY, USA, 4th edition, 2006.
- [21] J. I. Kroschwitz, *Polymer: Polymer Characterization and Analysis*, John Wiley & Sons, New York, NY, USA, 1990.
- [22] B. Schrader, *Infrared and Raman Spectroscopy: Methods and Applications*, VCH, 1995.
- [23] C. I. Vallo, G. A. Abraham, T. R. Cuadrado, and J. San Román, "Influence of cross-linked PMMA beads on the mechanical behavior of self-curing acrylic cements," *Journal of Biomedical Materials Research B*, vol. 70, no. 2, pp. 407–416, 2004.
- [24] S. Yannikakis, A. Zissis, G. Polyzois, and A. Andreopoulos, "Evaluation of porosity in microwave-processed acrylic resin using a photographic method," *Journal of Prosthetic Dentistry*, vol. 87, no. 6, pp. 613–619, 2002.
- [25] S. H. Tuna, F. Keyf, H. O. Gumus, and C. Uzun, "The evaluation of water sorption/solubility of various acrylic resins," *European Journal of Dentistry*, vol. 2, pp. 191–197, 2008.
- [26] L. D. F. R. Garcia, L. D. M. R. Roselino, F. M. Mundim, F. D. C. P. Pires-de-Souza, and S. Consani, "Influence of artificial accelerated aging on dimensional stability of acrylic resins submitted to different storage protocols," *Journal of Prosthodontics*, vol. 19, no. 6, pp. 432–437, 2010.
- [27] M. R. Hoffmann, S. T. Martin, W. Choi, and D. W. Bahnemann, "Environmental applications of semiconductor photocatalysis," *Chemical Reviews*, vol. 95, no. 1, pp. 69–96, 1995.
- [28] A. Fujishima, T. N. Rao, and D. A. Tryk, "Titanium dioxide photocatalysis," *Journal of Photochemistry and Photobiology C: Photochemistry Reviews*, vol. 1, no. 1, pp. 1–21, 2000.
- [29] T. Nonami, H. Hase, and K. Funakoshi, "Apatite-coated titanium dioxide photocatalyst for air purification," *Catalysis Today*, vol. 96, no. 3, pp. 113–118, 2004.
- [30] A. C. Pero, D. B. Barbosa, J. Marra et al., "Influence of microwave polymerization method and thickness on porosity of acrylic resin," *Journal of Prosthodontics*, vol. 17, no. 2, pp. 125–129, 2008.

Research Article

Water-Soluble Chitosan Nanoparticles Inhibit Hypercholesterolemia Induced by Feeding a High-Fat Diet in Male Sprague-Dawley Rats

Yi Tao, Hongliang Zhang, Bing Gao, Jiao Guo, Yinming Hu, and Zhengquan Su

Key Unit of Modulating Liver to Treat Hyperlipemia SATCM and Lipid Metabolism Laboratory of 3rd Level SATCM, Guangdong Pharmaceutical University, Guangzhou 510006, China

Correspondence should be addressed to Zhengquan Su, suzhq@scnu.edu.cn

Received 27 May 2010; Revised 7 July 2010; Accepted 10 July 2010

Academic Editor: Libo Wu

Copyright © 2011 Yi Tao et al. This is an open access article distributed under the Creative Commons Attribution License, which permits unrestricted use, distribution, and reproduction in any medium, provided the original work is properly cited.

Chitosan, a deacetylated product of chitin, has been demonstrated to lower cholesterol in humans and animals. However, chitosan is not fully soluble in water which would influence absorption in the human intestine. In addition, water-soluble chitosan (WSC) has higher reactivity compared to chitosan. The present study was designed to clarify the effects of WSC and water-soluble chitosan nanoparticles (WSC-NPs) on hypercholesterolemia induced by feeding a high-fat diet in male Sprague-Dawley rats. WSC-NPs were prepared by the ionic gelation method and the spray-drying technique. The nanoparticles were spherical in shape and had a smooth surface. The mean size of WSC-NPs was 650 nm varying from 500 to 800 nm. Results showed that WSC-NPs reduced the blood lipids and plasma viscosity significantly and increased the serum superoxide dismutase (SOD) activities significantly. This paper is the first report of the lipid-lowering effects of WSC-NPs suggesting that the WSC-NPs could be used for the treatment of hypercholesterolemia.

1. Introduction

Dyslipidemia, including hypercholesterolemia, hypertriglyceridemia, or their combination, is a major risk factor for cardiovascular disease. Generally, dyslipidemia is characterized by increased fasting concentrations of total cholesterol (TC), triglycerides (TG), and low-density lipoprotein cholesterol (LDL-C), in conjunction with decreased concentrations of high-density lipoprotein cholesterol (HDL-C) [1]. At present, these lipid imbalances are most routinely treated with pharmacological therapy. However, many cholesterol-lowering agents, especially statins, are associated with severe side effects [2]. In light of this, there has been great interest in the influence of dietary fibers, such as chitosan, on cholesterol absorption in the intestine.

Chitosan is a natural cationic polysaccharide consisting of (1-4)-2-amino-2-deoxy-D-glucopyranosyl units. It breaks down slowly to harmless products (amino sugars), which are completely absorbed by the human body [3]. Due to its nontoxicity and high biocompatibility, chitosan has been

formulated as dietary supplements, as carrier for oral peptide and protein drug delivery, as targeted drug delivery, and in the pharmaceutical and biomedical fields [4-6]. Due to the existence of amino groups, chitosan possesses positive charge, so it can bind negatively charged substrates such as lipids and bile acids. Chitosan also interfere with emulsification of neutral lipids by binding them with hydrophobic bonds [7]. Several studies have shown that chitosan has cholesterol-lowering properties both in animals and humans [8, 9].

However, chitosan has high viscosity and is not fully soluble in water, but it is in acidic solutions. Such properties of chitosan would decrease its absorption in the human intestine because most animal intestines, especially the human gastrointestinal tract, do not possess enzymes such as chitinase and chitosanase [10]. WSC has lower viscosity and is soluble in water. Subsequently, it seems to be readily absorbed in vivo. And, WSC has been reported to have the health benefits such as immunity regulation, antitumor, liver protection, blood lipids lowering, and antidiabetic

and antioxidant properties [11, 12]. In particular, previous studies revealed that the WSC was effective at lipid lowering compared to chitosan [13].

Furthermore, nanoparticles show some specific characteristics such as an increase of stability of therapeutic agents, controlled- and sustained-release properties, and the deeply penetration into tissues through fine capillaries [14]. We have prepared the WSC-NPs as a carrier to load the protein drug by the ionic gelation method [15]. And, WSC-NPs have the better solubility for the big total surface area and lower viscosity than WSC. Therefore, this study examined the effects of WSC and WSC-NPs on hypercholesterolemia induced by feeding a high-fat diet in rats.

2. Materials and Methods

2.1. Chemicals. WSC was purchased from Shandong Aokang Biotech Ltd (Shandong, China). The viscosity was more than 200 cps, and deacetylation value was 85%. Total cholesterol (TC), Triacylglycerol (TG), high-density lipoprotein cholesterol (HDL-C), and low-density lipoprotein cholesterol (LDL-C) kits were obtained from BioSino Bio-technology and Science Inc (Beijing, China). Superoxide dismutase (SOD) kits were purchased from Nanjing Jiancheng Bioengineering Institute (Wenzhou, China). Unless otherwise stated, all laboratory reagents were of analytical grade.

2.2. Animals and High-Fat Emulsions. Male Sprague-Dawley rats weighing 200 ± 20 g were purchased from Guangzhou University of Chinese Medicine Laboratory Animal Center (Guangzhou, China). All animal protocols were approved by the institutional animal care and use committee of Guangdong Pharmaceutical University (Guangzhou, China). They were housed in an isolator caging system in an air-conditioned animal room at $23 \pm 1^\circ\text{C}$. Rats were allowed free access to food and water.

Briefly, the high-fat emulsions were prepared as follows. 10.0 g cholesterol and 1.0 g propylthiouracil powder were dissolved into 20.0 g lard oil at 80°C and stirred for 10 min to ensure complete dissolution as the oil phase. The primary emulsions were prepared by diluting 5 mL emulsifier (Tween-80) and 20 mL sodium deoxycholate solution (2.0%) into the oil phase with a high-speed blender. Then, the distilled water was added to the primary emulsions to form the high-fat emulsions (100 mL) with stirring.

2.3. Preparation and Characterization of Water-Soluble Chitosan Nanoparticles. In this study, WSC-NPs were formed as a result of complex electrostatic interactions between the positively charged copolymers and negatively charged triphosphate (TPP) under mild conditions. Briefly, WSC (0.1% w/v) and TPP (0.1% w/v) were dissolved in purified water. For preparation of WSC-NPs, the WSC solution (500 mL) was stirred (800 rpm) at room temperature (25°C). Then, 0.1% TPP solution (100 mL) was added to the system while stirring was continued to complete nanoparticles formation. The rate of adding TPP was 0.75 mL/min. The nanosuspension was then spray dried using the Lab Spray

Dryer L-117 (Laiheng Scientific Co. Ltd, Beijing, China) with a standard nozzle (0.5 mm). The atomizing air flow rate was 10–15 L/min, and the flow rate was 600 mL/h. The inlet temperature was controlled at 160°C . The outlet temperature was determined by the inlet temperature and relative factors such as air and liquid feed flow rates and varied between 80 – 85°C . The stability of WSC-NPs is affected by various environmental conditions during long-term storage. Studies were carried out to evaluate the stability of the WSC-NPs for 5 months at room temperature.

The FTIRs were taken with KBr pellets on Perkin-Elmer Spectrum one FTIR (Shimadzu, FT-IR 8700, Japan). The particle size and size distributions of the nanoparticles were performed by particle sizer (Zetasizer 3000 HAS, Malvern Instruments Ltd., Worcs, UK). The morphology of the nanoparticles was examined under scanning electron microscopy (SEM) using a Hitachi S3700N (Hitachi Ltd, Japan) microscope at 10 kV.

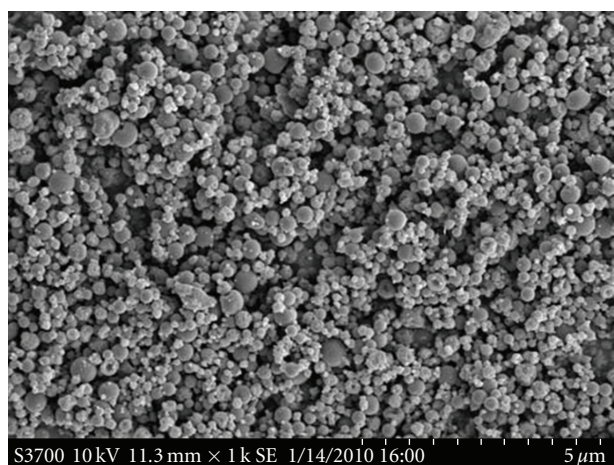
2.4. Experimental Procedure. The rats were fed *ad libitum* with a commercial diet for 5 days and were then assigned to 5 groups ($n = 8$) as follows: (a) normal diet fed rats (NF), (b) high-fat emulsions fed rats (HF), (c) high-fat emulsions and 450 mg/kg/d WSC fed rats (WSC), (d) high-fat emulsions and 450 mg/kg/d WSC-NPs fed rats (H-WSC-NP), and (e) high-fat emulsions and 225 mg/kg/d WSC-NPs fed rats (L-WSC-NP). The NF group received an equivalent amount of distilled water; the HF group, received high-fat emulsions daily by oral intubation until the study ended. The other groups were administered the high-fat emulsions by oral intubation for 2 weeks to establish the hyperlipidemic condition, and then the WSC and WSC-NPs samples were administered orally to the WSC and WSC-NPs groups for 4 weeks. All groups were fed the corresponding diets in which the composition conformed to GB14924.3 (Guangdong Laboratory Animal Center, Guangzhou, China) as the basal diets during the whole experiment. Each rat was weighed once a week.

At the end of the experimental period, blood samples were withdrawn from the orbital venous plexus using a capillary tube under ether anesthesia after an overnight fast.

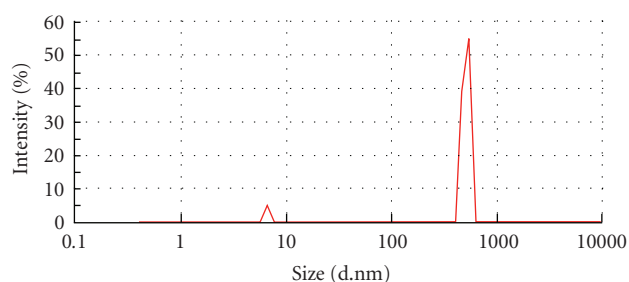
2.5. Serum Lipids and SOD. Blood was clotted at room temperature and centrifuged in a centrifuge at 3000 rpm for 15 min. Serum was separated, and TC, TG, HDL-C, and LDL-C were measured with commercial assay kits using the Automated Biochemistry Analyzer AMS-18 (Beijing Option Science and Technology Development Co. Ltd, Beijing, China).

The serum SOD contents were analyzed with commercially available analytical kit by the SPECORD S600 UV-Vis Spectrophotometer (Analytic Jena AG, Germany).

2.6. Plasma Viscosity. Blood samples were taken from the ocular vein using a heparinized capillary tube and centrifuged at 3000 rpm for 5 min in the Eppendorf Centrifuge 5810R (Eppendorf Co, Germany) to obtain the plasma. The plasma viscosity was measured by the Automatic Blood



(a)



(b)

FIGURE 1: SEM (magnification of 1000x) microphotographs of WSC-NPs (a) and particle size distribution of WSC-NPs (b).

Rheometer LBY-N6B (Beijing Precil Instrument Co. Ltd, Beijing, China).

2.7. Statistical Analysis. All data were expressed as means \pm SE. Differences between the groups were determined by one-way analysis of variance, using a statistical analysis software program (SPSS for windows, version Rel, 16.0, Spss Inc, Chicago, IL); the Student-Newman-Keuls Multiple-Range Test comparisons at P value of $<.05$ were made to determine significant differences among means.

3. Results and Discussions

3.1. Characterizations and Stability of WSC-NPs. The microphotographs and particle size of the WSC-NPs are shown in Figure 1. All nanoparticles were found to be nearly spherical in shape, and the external surfaces appeared smooth (Figure 1(a)). The mean particles size of WSC-NPs was 650 nm varying from 500 to 800 nm (Figure 1(b)). FTIR spectra of WSC-NPs and WSC matrix show that the tripolyphosphoric groups of TPP are linked with the ammonium group of WSC; the inter- and intramolecular actions are enhanced in WSC-NPs [15].

The stability studies show that there were no detectable changes in color, odor, taste, or pH and no visible microbial growth in the WSC-NPs.

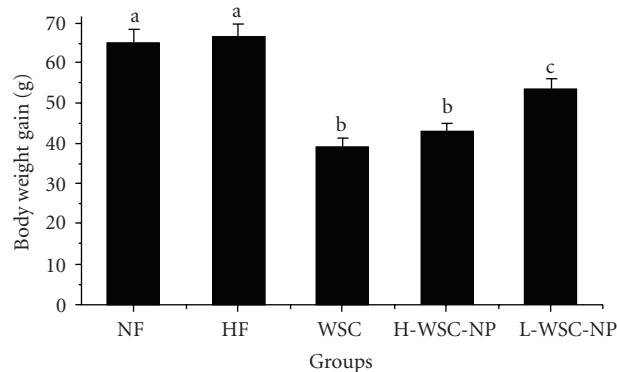


FIGURE 2: Effects on body weight gain in rats fed high-fat diets. Results are expressed as means \pm SE of eight rats. Values marked by the different letters are significantly different ($P < .05$).

3.2. Effects on Body Weight in Rats Fed High-Fat Diets.

A significantly lower weight gain was observed in all the treatment groups compared with the rats that consumed the normal diet and the high-fat diet (Figure 2), and H-WSC-NP, WSC produced lower counts compared with L-WSC-NP. However, weight gains were not significant between the H-WSC-NP and WSC groups.

Previously, WSC was shown to reduce body weight gain of rats that was caused by a high-fat diet [16]. In our study, the rats in the WSC group showed similar responses. Compared with the NF group, body weight gains of rats fed the WSC and H-WSC-NP were significantly lower than those fed the L-WSC-NP. This indicated that WSC could be used as weight-loss agent for healthy and obese humans, but further study is needed to clarify the antiobesity action and mechanisms of WSC-NPs.

3.3. Effects on Serum TC, TG, HDL-C, LDL-C, and SOD in Rats Fed High-Fat Diets.

The hyperlipidemic model showing that the serum concentrations of TC, TG, HDL-C, and LDL-C increased, was established in the HF group after 2 weeks (Table 1). Compared with the HF group, the TC and TG levels in H-WSC-NP and L-WSC-NP groups were significantly decreased, showing that the effect of WSC-NPs treatment was even more powerful than the treatment of WSC group. The serum LDL-C levels in the treatment groups were significantly decreased compared with the HF group, and no significant difference was observed among the treatment groups. There were no significant difference of HDL-C levels among all the groups (Table 1). The serum SOD was increased significantly in the H-WSC-NP and L-WSC-NP groups compared with the NF and HF groups, but increased slightly in the WSC group (Table 2).

The low levels of HDL-C and the high levels of LDL-C indicated an imbalance between cholesterol transport from the liver to the extrahepatic tissues and back to the liver [17]. Moreover, dyslipidemia is characterized by increased fasting concentrations of total cholesterol (TC), triglycerides (TG), and LDL cholesterol (LDL-C), in conjunction with decreased concentrations of HDL cholesterol (HDL-C). WSC and

TABLE 1: Effects on serum TC, TG, HDL-C, and LDL-C in rats fed high-fat diets.

Group	TC (mmol/L)	TG (mmol/L)	HDL (mmol/L)	LDL (mmol/L)
NF	1.59 ± 0.21 ^a	0.99 ± 0.20 ^d	0.70 ± 0.07 ^f	1.03 ± 0.18 ^h
HF	2.45 ± 0.28 ^b	1.46 ± 0.23 ^e	1.19 ± 0.14 ^g	1.33 ± 0.19 ⁱ
WSC	1.52 ± 0.78 ^a	1.33 ± 0.37 ^e	0.62 ± 0.17 ^f	0.78 ± 0.25 ^j
H-WSC-NP	0.46 ± 0.69 ^c	1.02 ± 0.33 ^d	0.67 ± 0.26 ^f	0.67 ± 0.32 ^j
L-WSC-NP	0.33 ± 0.24 ^c	0.82 ± 0.50 ^d	0.91 ± 0.33 ^{fg}	0.92 ± 0.26 ^j

Values are expressed as means ± SE ($n = 8$). Values marked by different letters within the same row are significantly different ($P < .05$).

TABLE 2: Effects on serum SOD in rats fed high-fat diets.

Group	Serum SOD (U/mL)
NF	83.43 ± 9.78 ^a
HF	87.18 ± 14.01 ^a
WSC	92.35 ± 6.32 ^b
H-WSC-NP	107.23 ± 16.25 ^c
L-WSC-NP	98.08 ± 12.68 ^b

Values are expressed as means ± SE ($n = 8$). Values marked by the different letters within the same row are significantly different ($P < .05$).

TABLE 3: Effects on plasma Viscosity in rats fed high-fat diets.

Group	Plasma viscosity (mPa.S)
NF	1.47 ± 0.25 ^a
HF	1.84 ± 0.40 ^b
WSC	1.68 ± 0.18 ^b
H-WSC-NP	0.86 ± 0.18 ^c
L-WSC-NP	1.13 ± 0.50 ^c

Values are expressed as means ± SE ($n = 8$). Values marked by different letters within the same row are significantly different ($P < .05$).

WSC-NPs significantly lowered TC, TG, and LDL-C levels in the plasma, which was consistent with previous reports [18]. Plasma concentration of HDL is inversely correlated with the risk of coronary heart disease, but low HDL-C poses no risk in the absence of elevated LDL cholesterol or TC. The levels of plasma HDL-C should be increased in the WSC-NP group; however, plasma concentration of HDL is influenced by several factors, including gender, race, and diet. Furthermore, WSC-NPs exhibited better cholesterol-binding capacity than WSC. This is consistent with the previous report that chitosan with finer particle size could effectively lower the plasma and liver lipid level in rats [19].

Excessive superoxide radicals may induce lots of senile diseases such as atherosclerosis. Any elevation in the level of the SOD was accompanied by a decrease in superoxide radicals [20, 21]. In the experiment, the serum SOD was elevated significantly by feeding the H-WSC-NP and L-WSC-NP compared with NF and HF groups, and WSC could not increase the serum SOD significantly. Therefore, it seems likely that WSC-NPs may improve the hypercholesterolemia induced by the high-fat diet through reducing serum TC, TG, and LDL-C, and elevating the SOD activity.

3.4. Effects on Plasma Viscosity in Rats Fed High-Fat Diets. As shown in Table 3, by experimental design, the average plasma viscosity of rats in the HF group increases significantly compared with the average level for rats in the NF group. In the three treatment groups, plasma viscosity showed a decreasing trend. When compared with the HF group, significant differences were seen for the H-WSC-NP and L-WSC-NP groups.

Plasma viscosity played an important role in the perfusion of the microvasculature and was a major determinant of endothelial shear stress [22]. Plasma viscosity was used as a marker for different diseases in humans such as coronary artery disease atherosclerosis [23]. The rats' plasma viscosity was increased significantly by feeding the high-fat emulsions, and the WSC-NPs and WSC reduced this increase effectively. Although the plasma viscosity tended to decrease in the WSC group, the differences were not statistically significant compared with HF group. The results suggested that the mechanisms of WSC to improve TC, TG, LDL, and SOD may differ with plasma viscosity. Furthermore, the WSC-NPs exhibited a better effect than the WSC, showing that WSC-NPs may serve as a useful agent for preventing hypercholesterolemia.

4. Conclusions

In conclusion, the data generated by this study demonstrated that WSC-NPs not only lower serum lipids levels and plasma viscosity but also increased serum SOD activities. Moreover, the hypercholesterolemia is affected by WSC-NPs even more than the WSC. Hence, the data obtained from this study could facilitate the further development of dietary intervention to hypercholesterolemia. Further studies are needed to clarify the mechanisms of the WSC-NPs to inhibit hypercholesterolemia induced by feeding a high-fat diet in male Sprague-Dawley rats.

To date, all rats appear healthy and remain active after oral administration of the WSC and WSC-NPs. Therefore, WSC and WSC-NPs are safe dietary fibers to inhibit hypercholesterolemia.

Abbreviations

WSC:	Water-soluble chitosan
WSC-NP:	Water-soluble chitosan nanoparticle
SOD:	Superoxide dismutase
TC:	Total cholesterol
TG:	Triglycerides
HDL-C:	High-density lipoprotein cholesterol
LDL-C:	Low-density lipoprotein cholesterol
TPP:	Triphosphosphate
SEM:	Scanning electron microscopy
FTIR:	Fourier transform infrared spectroscopy
NF:	Normal diet fed rats
HF:	High-fat emulsions fed rats
H-WSC-NP:	High-fat emulsions and 450 mg/kg/d WSC-NPs fed rats
L-WSC-NP:	High-fat emulsions and 225 mg/kg/d WSC-NPs fed rats

Acknowledgments

This paper was financially supported by Science and Technology Planning Project of Guangdong Province, China (no. 2009B020313006) and Science and Technology Planning Project of Zhongshan, China (no. 2009H017), and Foundation for University Key Teacher of Guangdong Pharmaceutical University, China.

References

- [1] K. A. Varady and P. J. H. Jones, "Combination diet and exercise interventions for the treatment of dyslipidemia: an effective preliminary strategy to lower cholesterol levels?" *Journal of Nutrition*, vol. 135, no. 8, pp. 1829–1835, 2005.
- [2] Y. Luo, G. Chen, B. Li et al., "Dietary intervention with AHP, a functional formula diet, improves both serum and hepatic lipids profile in dyslipidemia mice," *Journal of Food Science*, vol. 74, no. 6, pp. H189–H195, 2009.
- [3] E. S. Ostanina, V. P. Varlamov, and G. I. Iakovlev, "Inhibition of lipase activity by low-molecular-weight chitosan," *Prikladnaia biokhimiia i mikrobiologiia*, vol. 44, no. 1, pp. 38–43, 2008.
- [4] C. L. Bartels and S. J. Miller, "Dietary supplements marketed for weight loss," *Nutrition in Clinical Practice*, vol. 18, no. 2, pp. 156–169, 2003.
- [5] M. R. Rekha and C. P. Sharma, "Synthesis and evaluation of lauryl succinyl chitosan particles towards oral insulin delivery and absorption," *Journal of Controlled Release*, vol. 135, no. 2, pp. 144–151, 2009.
- [6] N. Bhattarai, H. R. Ramay, J. Gunn, F. A. Matsen, and M. Zhang, "PEG-grafted chitosan as an injectable thermosensitive hydrogel for sustained protein release," *Journal of Controlled Release*, vol. 103, no. 3, pp. 609–624, 2005.
- [7] G. Y. Park, S. Mun, Y. Park et al., "Influence of encapsulation of emulsified lipids with chitosan on their in vivo digestibility," *Food Chemistry*, vol. 104, no. 2, pp. 761–767, 2007.
- [8] J. Zhang, J. Liu, L. Li, and W. Xia, "Dietary chitosan improves hypercholesterolemia in rats fed high-fat diets," *Nutrition Research*, vol. 28, no. 6, pp. 383–390, 2008.
- [9] S. F. Ausar, M. Morcillo, A. E. León et al., "Improvement of HDL- and LDL-cholesterol levels in diabetic subjects by feeding bread containing chitosan," *Journal of Medicinal Food*, vol. 6, no. 4, pp. 397–399, 2003.
- [10] T. Fukamizo and R. Brzezinski, "Chitosanase from *Streptomyces* sp. strain N174: a comparative review of its structure and function," *Biochemistry and Cell Biology*, vol. 75, no. 6, pp. 687–696, 1997.
- [11] H. Yin, Y. Du, and J. Zhang, "Low molecular weight and oligomeric chitosans and their bioactivities," *Current Topics in Medicinal Chemistry*, vol. 9, no. 16, pp. 1546–1559, 2009.
- [12] Y. Maeda and Y. Kimura, "Antitumor effects of various low-molecular-weight chitosans are due to increased natural killer activity of intestinal intraepithelial lymphocytes in sarcoma 180-bearing mice," *Journal of Nutrition*, vol. 134, no. 4, pp. 945–950, 2004.
- [13] M. Sumiyoshi and Y. Kimura, "Low molecular weight chitosan inhibits obesity induced by feeding a high-fat diet long-term in mice," *Journal of Pharmacy and Pharmacology*, vol. 58, no. 2, pp. 201–207, 2006.
- [14] H. Hoyer, W. Schlocker, M. Greindl, T. Ostermann, and A. Bernkop-Schnurch, "Preparation and evaluation of thiomers nanoparticles via high pressure homogenization," *Journal of Microencapsulation*, vol. 27, no. 6, pp. 487–495, 2010.
- [15] H. L. Zhang, S. H. Wu, Y. Tao, L. Q. Zang, and Z. Q. Su, "Preparation and characterization of water-soluble chitosan nanoparticles as protein delivery system," *Journal of Nanomaterials*, vol. 2010, Article ID 898910, 5 pages, 2010.
- [16] H. G. Choi, J. K. Kim, D. H. Kwak et al., "Effects of high molecular weight water-soluble chitosan on in vitro fertilization and ovulation in mice fed a high-fat diet," *Archives of Pharmacological Research*, vol. 25, no. 2, pp. 178–183, 2002.
- [17] S. Hossain, A. Rahman, Y. Kabir, A. A. Shams, F. Afros, and M. Hashimoto, "Effects of shrimp (*Macrobrachium rosenbergii*)-derived chitosan on plasma lipid profile and liver lipid peroxide levels in normo- and hypercholesterolaemic rats," *Clinical and Experimental Pharmacology and Physiology*, vol. 34, no. 3, pp. 170–176, 2007.
- [18] D. J. Ormrod, C. C. Holmes, and T. E. Miller, "Dietary chitosan inhibits hypercholesterolaemia and atherogenesis in the apolipoprotein E-deficient mouse model of atherosclerosis," *Atherosclerosis*, vol. 138, no. 2, pp. 329–334, 1998.
- [19] M. Sugano and Y. Fujisaki, "Effect of the type of diet on the distribution of 3-hydroxy-3-methylglutaryl coenzyme A (HMG-CoA) reductase in rat small intestine," *Experientia*, vol. 36, no. 12, pp. 1399–1400, 1980.
- [20] F. Kimura, G. Hasegawa, H. Obayashi et al., "Serum extracellular superoxide dismutase in patients with type 2 diabetes: relationship to the development of micro- and macrovascular complications," *Diabetes Care*, vol. 26, no. 4, pp. 1246–1250, 2003.
- [21] R. A. DiSilvestro, "Influence of copper intake and inflammation on rat serum superoxide dismutase activity levels," *Journal of Nutrition*, vol. 118, no. 4, pp. 474–479, 1988.
- [22] U. Windberger, A. Bartholovitsch, R. Plasenzetti, K. J. Korak, and G. Heinze, "Whole blood viscosity, plasma viscosity and erythrocyte aggregation in nine mammalian species: reference values and comparison of data," *Experimental Physiology*, vol. 88, no. 3, pp. 431–440, 2003.
- [23] F. G. R. Fowkes, J. P. Pell, P. T. Donnan et al., "Sex differences in susceptibility to etiologic factors for peripheral atherosclerosis: importance of plasma fibrinogen and blood viscosity," *Arteriosclerosis and Thrombosis*, vol. 14, no. 6, pp. 862–868, 1994.

Research Article

Preparation and Characterization of Zein and Zein-Chitosan Microspheres with Great Prospective of Application in Controlled Drug Release

Vinícius Müller, Juliana Francis Piai, André Ricardo Fajardo, Silvia Luciana Fávaro, Adley Forti Rubira, and Edvani Curti Muniz

Grupo de Materiais Poliméricos e Compósitos (GMPC), Departamento de Química, Universidade Estadual de Maringá (UEM), Avenue Colombo, 5790, Maringá, 87020-900, Paraná, Brazil

Correspondence should be addressed to Edvani Curti Muniz, ecmuniz@uem.br

Received 2 June 2010; Revised 26 July 2010; Accepted 6 September 2010

Academic Editor: Libo Wu

Copyright © 2011 Vinícius Müller et al. This is an open access article distributed under the Creative Commons Attribution License, which permits unrestricted use, distribution, and reproduction in any medium, provided the original work is properly cited.

Biomaterials applied as carriers for controlled drug delivery offer many advantages over the conventional systems. Among them, the increase of treatment effectiveness and also a significant reduction of toxicity, due to their biodegradability property, are some special features. In this work, microspheres based on the protein Zein (ZN) and ZN associated to the natural polymer Chitosan (CHI) were prepared and characterized. The microspheres of ZN and ZN/CHI were characterized by FT-IR spectroscopy and thermal analysis, and the morphology was analyzed by SEM images. The results confirmed the incorporation of CHI within the ZN-based microspheres. The morphological analysis showed that the CHI added increased the microspheres porosity when compared to the ZN microspheres. The chemical and physical characterization and the morphological analysis allow inferring that ZN/CHI microspheres are good candidates to act as a carrier for controlled drug release.

1. Introduction

Carriers for drug delivery based on polymeric systems have been widely used not only for providing slow and gradual release of active components but also for targeting to specific organs of the body where the medicines may heal inflammation, tumor, and other diseases [1, 2]. One of most important concerns on drug administration is the need of maintenance of its characteristics during the delivery up to the target without changes in its molecular structure which could alter the drug-action capability [3]. The drug-loading on a polymer matrix, which one could act as an efficient carrier, is an interesting mean to ensure the preservation of drug molecular stability [4]. Polymer matrixes obtained from colloidal systems are good examples often employed for such purpose [5]. Among them, liposome, micelles, emulsions, and particles with micro, or nanodimensions can be mentioned [2].

The employment of natural polymers on obtaining colloidal systems enables the achievement of materials with

many interesting features (low toxicity, biocompatibility, and biodegradability), thus allowing their use as carriers. Several works have been published related to the use of natural polymers such as collagen, cellulose, zein, alginate, and chitosan in those systems [6–8]. Zein (ZN), a protein that belongs to the prolamine class, is the major protein from corn [9, 10]. Due to its ability for acting as a water barrier, ZN has been widely used as a coating for candies, nuts, fruits as well as food packaging [9]. There are also studies concerning medical application of ZN such as carriers for drug release at specific sites in the human body [11]. Although ZN is a water-insoluble protein it remains soluble in aqueous solutions containing at least 70% alcohol [12]. On the other hand, ZN has the ability to form films, suitable for coating, in the presence of water through intermolecular interactions which are responsible for joining the molecules together [9]. This property is also important for studies of edible films and coatings, both in the food industry, as well as gastroresistant film in the pharmaceutical and biomedical research.

Chitosan (CHI) [or poly(β -(1-4)-2-amine-2-deoxy-D-glucopyranose)] is a natural polysaccharide obtained from partial or total deacetylation of the biopolymer chitin, which is the major constituent of the invertebrates exoskeleton [13]. CHI shows well-known physical and biological features [14, 15]. It has been widely used in biomedical and pharmaceutical applications, such as carriers for controlled drugs and DNA release, in the manufacture of contact lenses, artificial membranes and skin, and periodontal and orthopedic applications [16–18].

The association of zein (ZN) with chitosan (CHI), forming microparticles, was investigated in this paper aiming the application of such biomaterial as carrier for controlled drug release.

2. Materials and Methods

2.1. Materials. Chitosan (CHI) (Golden Shell Biochemical Co., China), with deacetylation degree equal to 15% and M_V equal to $90 \times 10^3 \text{ g mol}^{-1}$, was determined according to Mao et al. [19]; Corn zein protein was supplied in powder form by Química Brasil Ltda. (CAS number 9010-66-6), with a M_W of $22 \times 10^3 \text{ g mol}^{-1}$; Hydrochloric Acid (Nuclear, Brazil); Acetic Acid (F. Maia, Brazil); Ethanol (TEDIA, Brazil); and Sodium hydroxide (Nuclear, Brazil).

2.2. Preparation of Microspheres. The microspheres based only on ZN were prepared by the solubilization of 2.0 g of ZN in 100 mL of ethanol-water (rate 4:1 ethanol/water) under magnetic stirring. The ZN alcoholic solution was transferred to a flask coupled to a high-speed laboratory mixer (Quimis, model Extratur). After this, the solution was vigorously mixed (12,000 rpm) for 15 min, and 100 mL of distilled water was slowly dropped to the system during the stirring (rate flow: 4 mL min^{-1}). The water addition changes the ratio ethanol-water to 2:3 v/v, inducing the loss of solubility of ZN and allowing the formation of microspheres droplets. So, the insoluble microspheres were collected through filtration under vacuum, after that were frozen under liquid N_2 and then lyophilized during 24 h. The preparation of ZN/CHI microspheres followed the same procedures described above unless by the addition of CHI solution instead of distilled water. The 1.0 wt/v-% CHI solution was prepared in 0.2 mol L^{-1} acetic acid solution at 65°C under magnetic stirring. After the lyophilizing step, the ZN/CHI microspheres were washed with 0.2 mol L^{-1} HCl solution to remove the free CHI. So, these microspheres were dried again under reduced pressure at room temperature. The two types of microspheres (ZN and ZN/CHI) were characterized by scanning electronic microscopy (SEM) images, Fourier transform infrared (FTIR) spectroscopy, differential scanning calorimetric (DSC), thermogravimetric analysis (TGA), and differentiate weight loss (DTG) analysis.

2.3. SEM Images. The morphologies of ZN and ZN/CHI microspheres were investigated by SEM images (Shimadzu, model SS 550). The microspheres surfaces were sputter-coated with a thin layer of gold for allowing the SEM

visualization. The images were taken by applying an electron accelerating voltage of 8 kV. The microspheres average diameters were calculated by means of the software Size Meter®, version 1.1, with differentiation threshold set according to the image scale.

2.4. FTIR Spectroscopy. The lyophilized ZN particles or the after-dried ZN/CHI particles were mixed with KBr to form thin discs that were characterized by FTIR (Shimadzu Scientific Instruments, Model 8300, Japan), operating in the region from 4000 to 400 cm^{-1} , resolution of 4 cm^{-1} . Also, for control FTIR, spectrum of CHI was obtained in the same conditions.

2.5. DSC Analyses. DSC analyses were performed on a calorimeter (Netzsch, model STA 409 PG/4/G Luxx, USA) operating in the following conditions: heating rate of $10^\circ\text{C min}^{-1}$, nitrogen atmosphere with flow rate of 20 mL min^{-1} , and temperature range from 22 to 400°C . For all analyses it was obtained firstly the respective baselines.

2.6. TGA Analyses. TGA analyses were carried out on a thermogravimetric analyzer (Netzsch, model STA 409 PG/4/G Luxx, USA) at a heating rate of $10^\circ\text{C min}^{-1}$ under nitrogen atmosphere with flow rate of 20 mL min^{-1} in a temperature range from 22 to 400°C .

3. Results and Discussion

Figure 1 shows the SEM images obtained from particles of ZN (Figures 1(a)–1(b)) and of ZN/CHI (Figures 1(c)–1(d)). The SEM images show that the particles are microspheres; indeed, however the size distribution is widely scattered. The average diameter of microspheres was calculated, in each case, from the simple average of 50 microspheres diameters randomly chosen, using the software Size Meter®. The calculated values were equal to $1.23 \pm 0.47 \mu\text{m}$ for the ZN microspheres and $4.30 \pm 1.93 \mu\text{m}$ for the ZN/CHI ones. From these values, it was possible verifying that the CHI incorporation into ZN microspheres increases in 3.5-fold the average diameter compared to neat ZN particles. This is totally expected considering the fact that CHI chains are larger than ZN chains (c.a. 4 times higher); therefore, the incorporation of CHI chains should promote an increase in mobility of polymer chains inside the particles reflecting in an increase of the size of ZN/CHI microspheres, which agrees with the calculated values. Another fact that might contribute to the average size of ZN/CHI particles to be higher than ZN particles is the higher miscibility of CHI chains in the parent solution in which the particles were obtained. Thus, the presence of CHI should affect not only the size but also the porosity of particles as can be observed in the micrographs on Figure 1.

According to the SEM images of Figure 1, it can be inferred also that both types of microparticles have the predominance of spherical shape. However, it could be observed that the ZN microspheres have smoother surfaces while ZN/CHI microspheres have irregular surfaces with spongy

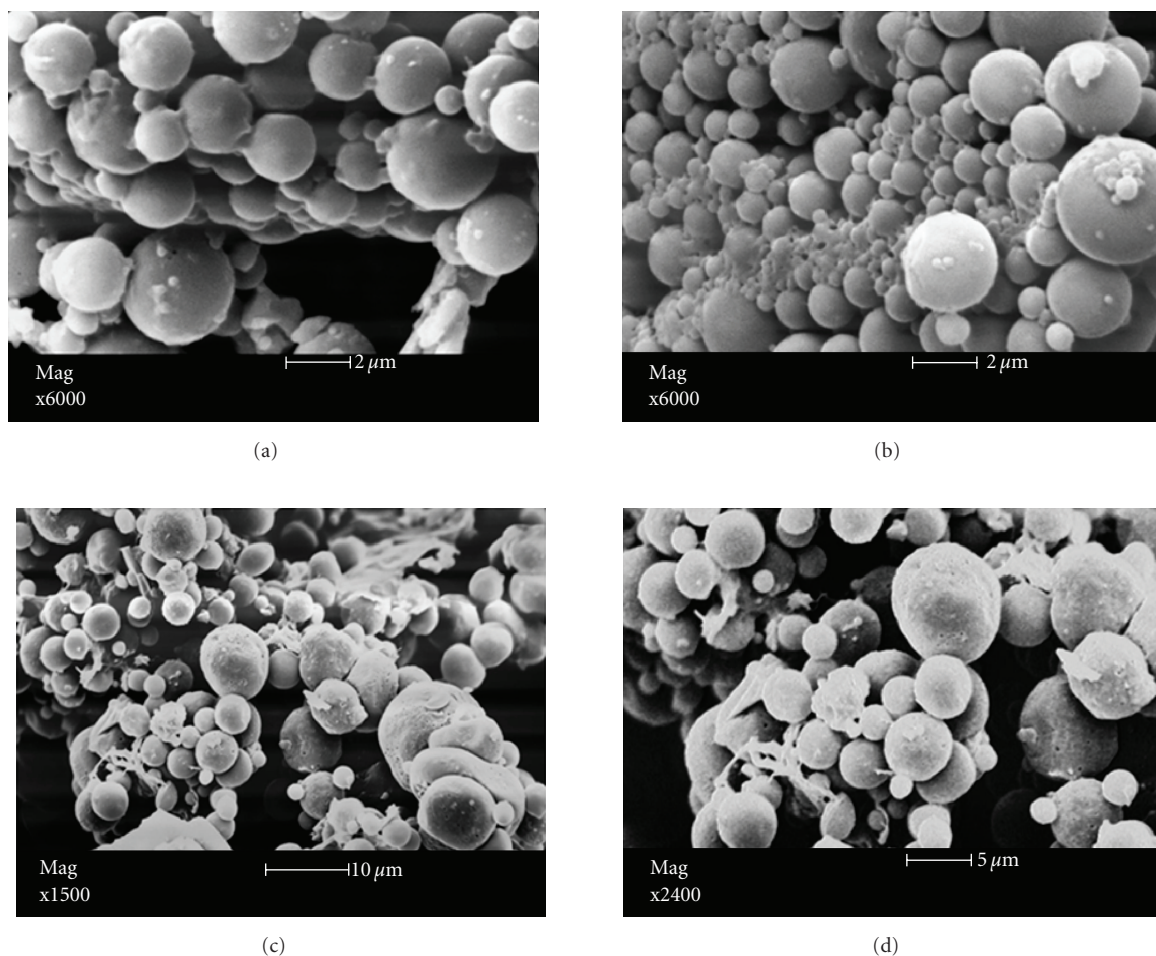


FIGURE 1: SEM images of ZN (a-b) and ZN/CHI (c-d) microspheres.

characteristics. This clear difference was interpreted having in the mind the fact that the two types of microparticles were prepared under different conditions. The microspheres constituted only by ZN were formed by the addition of distilled water in the ethanol-water solution, precipitating when the ethanol concentration lowered below the threshold value of 70%–30% (v/v) ethanol-water. Since the ZN/CHI microspheres were prepared by slow addition of aqueous CHI (0.2 mol L^{-1} acetic acid) solution into alcoholic solution of ZN, with vigorous mixing, the two procedures are quite different. In this sense, the precipitation of microspheres occurred due to the fact that zein became insoluble in alcoholic medium of less than 70% (ZN particles) and CHI became insoluble in this condition and/or in medium with $\text{pH} > 5$ (CHI/ZN particles) [20].

Another synthesis factor that may have influenced the surfaces of microspheres particles is the difference in the forming solutions viscosity. Comparing the alcoholic solution of ZN with the solution obtained after the CHI addition, there is an increase in its viscosity. The alcoholic ZN solution exhibits a low intrinsic viscosity ($[\eta]$) at 25°C equal to 19.85 mL g^{-1} . The addition of CHI solution, which exhibits higher $[\eta]$ (equal to 950.10 mL g^{-1}), into the system, may

have contributed to increasing the $[\eta]$ of ZN solution ($[\eta]$ equal to 308.50 mL g^{-1}). Thus, despite the vigorous mixing, the smooth surface observed on microspheres constituted by neat ZN was not achieved in ZN/CHI microspheres. Moreover, the higher surface roughness of ZN/CHI microspheres could contribute to increasing the drug adsorption on the microspheres and improving the encapsulation and releasing rates compared to neat ZN particles.

3.1. FTIR Spectroscopy. The ZN and ZN/CHI microspheres and pure CHI (powder) were characterized by FTIR spectroscopy technique (Figure 2). The FTIR spectrum of CHI (Figure 2(c)) exhibited a broad intense band at 3437 cm^{-1} assigned to O–H vibrational stretching. Close to this wavelength, a N–H vibrational stretching is also commonly verified, but due to widening of OH band it was hindered. The band at 1633 cm^{-1} was assigned to C=O from amide groups and to $-\text{NH}_2$ deformation [21], and the intense band at 1082 cm^{-1} was assigned to the C–O vibrational stretching, characteristics of primary alcoholic groups on CHI structure. Figure 2(a) shows the FTIR spectrum for ZN microspheres, where a clear OH band at 3387 cm^{-1} , two intense bands at 1656 and 1545 cm^{-1} , assigned to the amide

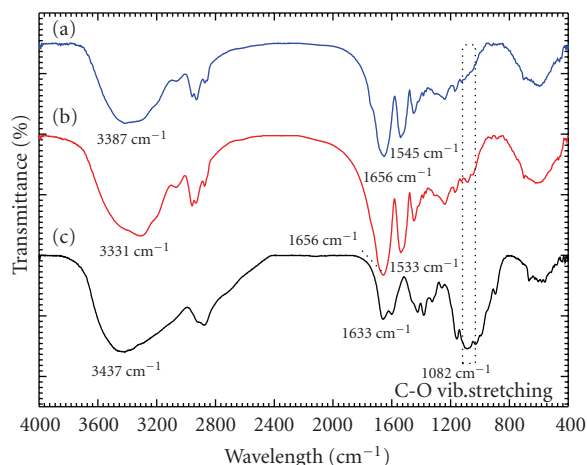


FIGURE 2: FTIR spectra of (a) ZN microspheres, (b) ZN/CHI microspheres, and (c) pure CHI.

bands, are observed. In one of amide band the predominance of C=O vibrational stretching occurs, and for the other amide band the C–N stretching predominates [22]. The FTIR spectrum from ZN/CHI microspheres (Figure 2(b)) presents a similar profile as compared to FTIR from ZN microspheres.

However, the band observed at 1545 cm^{-1} in the ZN microsphere FTIR spectrum, which can be assigned to N–H bond, was shifted to 1533 cm^{-1} in the ZN/CHI microsphere FTIR spectrum. This fact may indicate a possible interaction among the ZN and CHI chains, probably through hydrogen bonding among the amino groups present on both CHI and ZN chains. Furthermore, the formation of ZN/CHI microspheres was also confirmed by the arising of a band at 1082 cm^{-1} in their spectrum of low intensity, which was not observed in the ZN microsphere spectrum, confirming the presence of CHI.

Different from work by Torres-Giner et al. [23], in which a common solvent for both compounds to form ZN/CHI blends was used; in this work, a nonsolvent for both components was used for precipitating the microspheres. Thus, simultaneous precipitation of ZN and CHI during the microspheres formation was expected and confirmed by FTIR spectroscopy. The almost complete precipitation should occur due to the interaction among the ZN protein and CHI chains by hydrogen bonding. Some other works addresses the interaction of the polysaccharide chitosan with proteins (i.e. gelatin, collagen, etc.) through hydrogen bonds [24, 25]. The hydrogen bonds are formed due to the interaction among the amino groups present in the protein (ZN) structure and the amino groups on the CHI chains. By adding water to the system, which acts as nonsolvent for the ZN, the precipitation of microspheres occurs by decreasing the relative amount of alcohol and increasing the pH. So, microspheres are formed and are composed mainly by ZN with CHI incorporated into their structures.

3.2. Thermal Analyses. The thermal profiles of ZN and ZN/CHI microspheres were evaluated by DSC, TGA, and DTG analysis. Figure 3 shows the DSC curves of neat CHI,

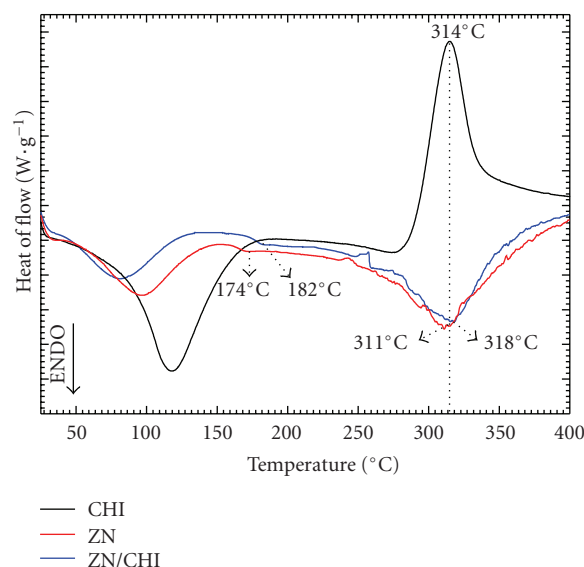


FIGURE 3: DSC curves of pure CHI, ZN and ZN/CHI microspheres.

ZN, and ZN/CHI microspheres. All the DSC curves show endothermic peaks in the range of temperature of 50 to 150°C . The presence of such peaks was attributed to the loss of volatile components or the possibility of chain relaxation [26]. Furthermore, in this temperature range is also verified the breakdown of hydrogen bonds which are present in zein structure and other molecular associations [27]. The DSC curve of pure CHI exhibits a strong exothermic peak at 307°C , which is attributed to the degradation of that polysaccharide [28].

Proteins have some features associated to their different tridimensional structure, such as the denaturation process. Some works show that the temperature of unfolding protein can be evaluated through thermal analysis [29, 30]. Mothe et al. [30] attributed the presence of an endothermic peak in proteins thermograms to the destabilization of their physical interactions, as hydrogen bonding, electrostatic interaction, and dipole-dipole interaction, thus causing the loss of three dimensional protein structures. DSC curves of ZN and ZN/CHI microspheres exhibited endothermic peaks at 311° and 318°C , which can be interpreted as the protein unfolding [31].

It was also verified through DSC curve, close to 174°C , an alteration on the linear profile of ZN curve. Such alteration was associated to the ZN glass transition temperature (T_g), and above this temperature the protein chains of ZN undergo to a flexible stage. This inference is supported by other studies that also determined the T_g of ZN in a temperature range of $160\text{--}180^{\circ}\text{C}$ [31, 32]. Moreover, the T_g for the ZN/CHI microspheres was observed at temperature higher than that observed for the pure ZN microspheres. The T_g of ZN/CHI microspheres increased c.a. 8°C from that without CHI. Thus, it can be evidenced that the incorporation of the polysaccharide CHI within the ZN microspheres makes the CHI/ZN structure get some flexibility in just a higher temperature. This fact was explained by the interaction among

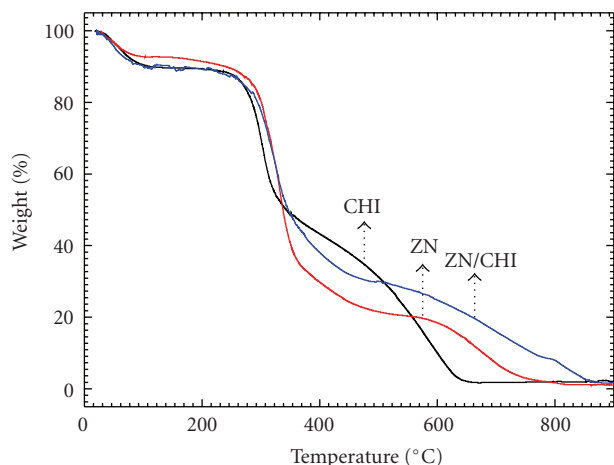


FIGURE 4: TGA curves of pure CHI, ZN, and ZN/CHI microspheres.

the ZN and CHI chains after the microsphere formation, as observed through the FTIR spectra (see Figure 1).

Figure 4 shows the TGA curves of CHI powder and microspheres of ZN and ZN/CHI. The decrease of about 10% on mass between 50° and 150°C was due to the vaporization of water and volatile components from the material.

In the same temperature range, the decrease of mass observed for ZN is lower than that for CHI or ZN/CHI. This happens due to the lower hydrophilicity of ZN, while the pure CHI and ZN/CHI microspheres exhibit higher hydrophilicity. Thus, the amount of water volatilized is greater for these latter two. From 200 to 400°C, the TGA curves for CHI, ZN, and ZN/CHI presented significant mass loss being in this event more intense for ZN, followed by ZN/CHI and CHI. The mass loss in this range (200–400°C) for ZN particles is about 60% while for the ZN/CHI the decrease is 50%. The DTG curve (first derivative of TGA curves versus temperature), presented in Figure 5, provides information of thermal stability of ZN and ZN/CHI particles compared to CHI.

The incorporation of CHI on ZN allows the formation of material pursuing thermal stability similar to ZN. This was inferred after analysis of DTG curves (Figure 5).

Furthermore, as observed by analysis of DSC curves, the incorporation of CHI shifted the T_g of microspheres to a larger value when compared with T_g exhibited by neat ZN microspheres. Also, the incorporation CHI on ZN particles promoted an increase at the temperature of the unfolding of zein. Note that for the pure ZN microspheres the unfolding temperature was observed to occur at 328°C whereas for the ZN/CHI microspheres this temperature appears at 332°C. These results reinforce the hypothesis that the incorporation of CHI into ZN-based microspheres allows advantages and amplifying some of their properties, for instance, the thermal stability.

4. Conclusions

In this work, microspheres based on the protein zein (ZN) and on ZN having the polysaccharide chitosan (CHI)

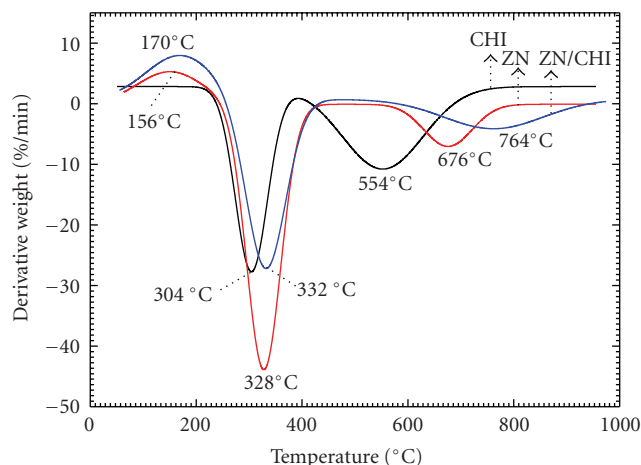


FIGURE 5: DTG curves of pure CHI, ZN and ZN/CHI microspheres.

incorporated were prepared through the technique of precipitation by the addition of a nonsolvent under high stirring. SEM images allowed observing that both types of obtained microspheres presented spherical shape. Detailed analyses of SEM showed that surface of ZN particles is smooth while the surface of ZN/CHI particles is rougher. This difference on the microspheres surfaces could be an advantage to their application as carrier to drug delivery. The microspheres average diameter was calculated through the use of specific software. The average diameter was equal to $1.23 \pm 0.47 \mu\text{m}$ for the ZN microspheres and $4.30 \pm 1.93 \mu\text{m}$ for the ZN/CHI ones. Analysis of FTIR spectroscopy, allowed inferring that the incorporation of the CHI into ZN microspheres effectively occurred. Thermal profile of the two types of microspheres was evaluated through DSC and TGA. Comparing the results, it was verified that the ZN/CHI microspheres presented similar thermal profile to that of the ZN microspheres. Furthermore, the CHI incorporation provided an increase in the T_g of ZN microspheres inducing increasing the temperature at which ZN chains get flexibility. So, in despite of both types of materials prepared, this work exhibited interesting features; such materials might be applied in studies to obtain viable carriers for controlled drug release. As discussed previously, the CHI incorporation provides ZN/CHI microspheres with some advantages over neat ZN microspheres.

Acknowledgments

Vinícius Müller thanks Prati, Donaduzzi, and Co. Ltd. (Toledo, Paraná, Brazil) for the undergraduation fellowship. Juliana Francis Piai, André Ricardo Fajardo, and Silvia Luciana Fávaro thanks CNPq and Capes for the doctorate fellowships. Edvani Curti Muniz and Adley Forti Rubira thanks CNPq for the financial support (Grant no. 309005/2009-4).

References

- [1] J. C. Middleton and A. J. Tipton, "Synthetic biodegradable polymers as orthopedic devices," *Biomaterials*, vol. 21, no. 23, pp. 2335–2346, 2000.

- [2] E. C. M. Cabral, R. L. Zollner, and M. H. Santana, "Preparation, characterization and *in vivo* assays of liposomes and microspheres (PLGA) useful for desensitization therapy in allergy," *First Brazilian Winter School on Nanobiotechnology-Rede Nanobiotec*, pp. 171–172, 2002.
- [3] Y. Kawashima, "Panoparticulate systems for improved drug delivery," *Advanced Drug Delivery Reviews*, vol. 47, no. 1, pp. 1–2, 2001.
- [4] Y. Gerelli, M. T. Di Bari, A. Deriu et al., "Structure and organization of phospholipid/polysaccharide nanoparticles," *Journal of Physics: Condensed Matter*, vol. 20, no. 10, Article ID 104211, 8 pages, 2008.
- [5] K. M. Lima, C. L. Silva, and J. M. Rodrigues-Júnior, "Microesferas biodegradáveis," *Biotecnologia Ciência & Desenvolvimento*, vol. 2, pp. 10–13, 2000.
- [6] A. Nascimento, M. C. M. Laranjeira, V. T. Fávere, and A. Josué, "Impregnation and release of aspirin from Chitosan/poly(acrylic acid) graft copolymer microspheres," *Journal of Microencapsulation: Micro and Nano Carriers*, vol. 18, no. 5, pp. 679–684, 2001.
- [7] S. H. Lim, I.-C. Liao, and K. W. Leong, "Nonviral gene delivery from nonwoven fibrous scaffolds fabricated by interfacial complexation of polyelectrolytes," *Molecular Therapy*, vol. 13, no. 6, pp. 1163–1172, 2006.
- [8] M. Kumar, X. Kong, A. K. Behera, G. R. Hellermann, R. F. Lockey, and S. S. Mohapatra, "Chitosan IFN- γ -pDNA nanoparticle (CIN) therapy for allergic asthma," *Genetic Vaccines and Therapy*, vol. 1, article 3, 2003.
- [9] R. Shukla and M. Cheryan, "Zein: the industrial protein from corn," *Industrial Crops and Products*, vol. 13, no. 3, pp. 171–192, 2001.
- [10] H. Bernstein, E. Morrel, E. Mathlowitz, K. Schwaller, and R. Thomas, "Protein microspheres and methods of using them," US patent no. 5679377, 1997.
- [11] P. Picklesimer, "Nanotechnologist plans to build things with bricklike corn molecules," *University of Illinois at Urbana-Champaign*, vol. 24, no. 17, 2005.
- [12] J. W. Lawton, "Zein: a history of processing and use," *Cereal Chemistry*, vol. 79, no. 1, pp. 1–18, 2002.
- [13] M. N. V. R. Kumar, "A review of chitin and Chitosan applications," *Reactive and Functional Polymers*, vol. 46, no. 1, pp. 1–27, 2000.
- [14] M. F. A. Goosen, *Applications of Chitin and Chitosan*, Technomic Publishing Company, Lancaster, Pa, USA, 1997.
- [15] S. P. Campana Filho and J. Desbrières, "Chitin, Chitosan and derivatives," in *Natural Polymers and Agrofibers Composites*, E. Frollini, A. Leão, and L. H. C. Mattoso, Eds., chapter 3, EMBRAPA Instrumentação Agropecuária, São Paulo, Brazil, 2000.
- [16] M. N. V. R. Kumar, R. A. A. Muzzarelli, C. Muzzarelli, H. Sashiwa, and A. J. Domb, "Chitosan chemistry and pharmaceutical perspectives," *Chemical Reviews*, vol. 104, no. 12, pp. 6017–6084, 2004.
- [17] S.-T. Lee, F.-L. Mi, Y.-J. Shen, and S.-S. Shyu, "Equilibrium and kinetic studies of copper(II) ion uptake by Chitosan-tripolyphosphate chelating resin," *Polymer*, vol. 42, no. 5, pp. 1879–1892, 2001.
- [18] I. Genta, P. Perugini, B. Conti, and F. Pavanetto, "A multiple emulsion method to entrap a lipophilic compound into Chitosan microspheres," *International Journal of Pharmaceutics*, vol. 152, no. 2, pp. 237–246, 1997.
- [19] S. Mao, X. Shuai, F. Unger, M. Simon, D. Bi, and T. Kissel, "The depolymerization of Chitosan: effects on physicochemical and biological properties," *International Journal of Pharmaceutics*, vol. 281, no. 1–2, pp. 45–54, 2004.
- [20] B. C. Janegitz, B. C. Lourenção, K. O. Lupetti, and O. Fatibello-Filho, "Desenvolvimento de um método empregando quitosana para remoção de íons metálicos de águas residuárias," *Química Nova*, vol. 30, no. 4, pp. 879–884, 2007.
- [21] C. Rosca, M. I. Popa, G. Lisa, and G. C. Chitanu, "Interaction of Chitosan with natural or synthetic anionic polyelectrolytes. 1. The Chitosan-carboxymethylcellulose complex," *Carbohydrate Polymers*, vol. 62, no. 1, pp. 35–41, 2005.
- [22] D. J. Sessa, A. Mohamed, and J. A. Byars, "Chemistry and physical properties of melt-processed and solution-cross-linked corn Zein," *Journal of Agricultural and Food Chemistry*, vol. 56, no. 16, pp. 7067–7075, 2008.
- [23] S. Torres-Giner, M. J. Ocio, and J. M. Lagaron, "Novel antimicrobial ultrathin structures of Zein/Chitosan blends obtained by electrospinning," *Carbohydrate Polymers*, vol. 77, no. 2, pp. 261–266, 2009.
- [24] Y. Chang, L. Xiao, and Q. Tang, "Preparation and characterization of a novel thermosensitive hydrogel based on Chitosan and gelatin blends," *Journal of Applied Polymer Science*, vol. 113, no. 1, pp. 400–407, 2009.
- [25] M. H. Uriarte-Montoya, J. L. Arias-Moscote, M. Plascencia-Jatomea et al., "Jumbo squid (*Dosidicus gigas*) mantle collagen: extraction, characterization, and potential application in the preparation of Chitosan-collagen biofilms," *Bioresource Technology*, vol. 101, no. 11, pp. 4212–4219, 2010.
- [26] L. S. Guinesi and E. T. G. Cavaleiro, "The use of DSC curves to determine the acetylation degree of chitin/Chitosan samples," *Thermochimica Acta*, vol. 444, no. 2, pp. 128–133, 2006.
- [27] M. Tillekeratne and A. J. Easteal, "Modification of Zein films by incorporation of poly(ethylene glycol)s," *Polymer International*, vol. 49, no. 1, pp. 127–134, 2000.
- [28] A. R. Fajardo, J. F. Piai, A. F. Rubira, and E. C. Muniz, "Time- and pH-dependent self-rearrangement of a swollen polymer network based on polyelectrolytes complexes of chitosan/chondroitin sulfate," *Carbohydrate Polymers*, vol. 80, no. 3, pp. 934–943, 2010.
- [29] P. Relkin, "Differential scanning calorimetry: a useful tool for studying protein denaturation," *Thermochimica Acta*, vol. 246, no. 2, pp. 371–386, 1994.
- [30] C. G. Mothe, A. Damico, and M. G. S. Machado, "Estudo termoanalítico, CLAE e fracionamento físico e químico do subproduto industrial do milho," *Ciência e Tecnologia de Alimentos*, vol. 25, pp. 1–7, 2005.
- [31] I. Doğan Atik, B. Özen, and F. TihmInIloğlu, "Water vapour barrier performance of corn-zein coated polypropylene (PP) packaging films," *Journal of Thermal Analysis and Calorimetry*, vol. 94, no. 3, pp. 687–693, 2008.
- [32] F. X. B. Santosa and G. W. Padua, "Thermal behavior of Zein sheets plasticized with oleic acid," *Cereal Chemistry*, vol. 77, no. 4, pp. 459–462, 2000.

Research Article

Dynamic Probing of Nanoparticle Stability *In Vivo*: A Liposomal Model Assessed Using *In Situ* Microdialysis and Optical Imaging

Chien-Chung Jeng,^{1,2} Shih-Hsun Cheng,^{2,3} Ja-an Annie Ho,⁴ Sam Hong-Yi Huang,² Jerry C. Chang,² Pi-Ju Tsai,⁵ Chung-Shi Yang,⁵ and Leu-Wei Lo²

¹ Department of Physics, National Chung Hsing University, Taichung 420, Taiwan

² Division of Medical Engineering Research, National Health Research Institutes, Zhunan, Miaoli 350, Taiwan

³ Institute of NanoEngineering and MicroSystems, National Tsing Hua University, Hsinchu 300, Taiwan

⁴ Department of Chemistry, National Tsing Hua University, Hsinchu 300, Taiwan

⁵ Center for Nanomedicine Research, National Health Research Institutes, Zhunan, Miaoli 350, Taiwan

Correspondence should be addressed to Leu-Wei Lo, lwlo@nhri.org.tw

Received 7 June 2010; Revised 10 August 2010; Accepted 6 September 2010

Academic Editor: Libo Wu

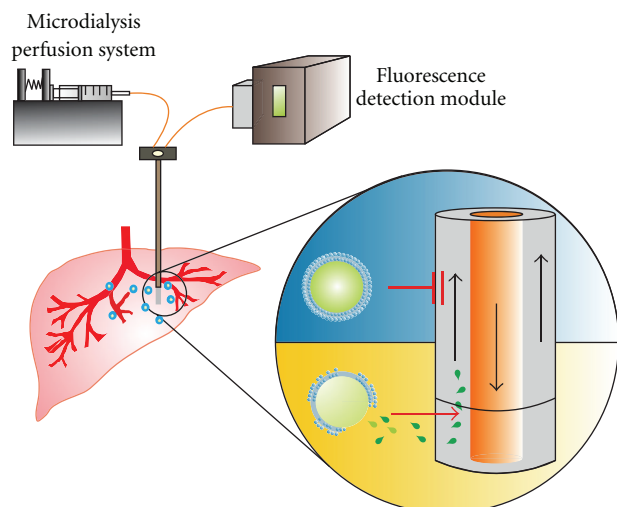
Copyright © 2011 Chien-Chung Jeng et al. This is an open access article distributed under the Creative Commons Attribution License, which permits unrestricted use, distribution, and reproduction in any medium, provided the original work is properly cited.

Nanoparticle-mediated drug delivery and controlled release has been a vigorous research area in contemporary nanomedicine. The *in vivo* stability of nanoparticle delivered on site is a prerequisite for the design of drug-controlled release by any means. In this study, the first methodology comprised of microdialysis and optical imaging to assess the liposome stability *in vivo* is reported. Macroscopically, we demonstrated the DPPG liposomes with negative surface charge fast accumulated in the rat liver upon their i.v. administration using optical imaging. Microscopically, the concurrent analysis of fluorescent molecules leaching from the liposomes, *in situ* sampled using microdialysis probe, provides the dynamic information of stability of DPPG liposomes *locus in quo*. The current combination of *in situ* microdialysis and optical imaging possesses a great potential for use as a platform technology to evaluate the nanoparticle stability and the bioavailability of drug payload released on targeted site *in vivo*.

1. Introduction

Nanoparticle-mediated drug delivery has been emerging as a vigorous research area. The nanoformulation of chemotherapeutics can improve the pharmacokinetics; the controlled release of drug can be further exploited with either inherent pathophysiological conditions like acidic pH in tumor, or external physical means such as photoirradiation and alternating magnetic fields [1–4]. The high stability of nanoparticle delivered on-site is a critical prerequisite for the design of drug controlled release by any means. The otherwise spontaneous release of drug will result in unwanted side effects and collateral tissue damages, to compromise the advantages of using nanoparticles as carriers. Thus, to define a methodology that can dynamically monitor the stability of targeted nanoparticles and bioavailability of drug payload *locus in quo* is important in validation of the activatable drug release strategy.

Nanomedicine approaches to drug delivery center on developing nanoscale particles to improve the bioavailability of a drug. The biodistribution of nanoparticles including blood circulation, immunosystem interaction, clearance, and metabolism are synergically determined by many factors such as size, shape, surface chemistry, and charge. Among nanoparticles, liposomes have played an important role in formulation for potential drugs to improve their therapeutic index. Due to their biocompatibility and biodegradability, liposomes are by far the most studied colloidal particles applied in medicine, particularly in antitumor therapy. The use of liposomes as drug carriers requires the liposomal preparations with various clearance rates and biodistribution patterns to better fit the specifics of each particular application. Liposome charge and liposome coating with different polymers, such as PEG, are among the parameters known to strongly affect biological properties of liposomes [5]. During the delivery process, after extravasation into



SCHEME 1: The microdialysis probe with total diameter of $360\ \mu\text{m}$ and molecular size cutoff at $100\ \text{kDa}$ was *in situ* implanted for simultaneous measurements of fluorescence intensity of extracellular fluid. If the liposomes are ruptured, the encapsulated CF molecules will be leaching out and collected by microdialysis probe. Thus, the stability of liposomes on site in liver can be dynamically assessed by the change of fluorescence intensity in microdialysates.

tumor tissue, liposomes remain within tumor stroma as a drug-loaded depot and eventually are subject to enzymatic degradation and/or phagocytic attack, leading to release of drug for subsequent diffusion to tumor cells. Therefore, the temporal profiles of biodistribution and stability of nanoformulated contrast agent/drug carrier *in vivo* are critical in determining the imaging/therapeutic efficacy and the necessity for advanced design of activatable controlled release.

There are a number of imaging modalities that have been reported to trace the biodistribution of nanoparticles *in vivo*, including positron emission tomography (PET) [6], magnetic resonance imaging (MRI) [7, 8], and optical image system [9]. However, these techniques, though noninvasive, are not sensitive enough to reflect the dynamic changes of nanoparticle stability incurred by variations of pathophysiological microenvironments or activations of external means for drug-controlled release. The indiscernibility of image signals contributed from the contrast agent of intact nanoparticles and that leaching from the disintegrated nanoparticles can seriously impede the interpretation of nanoparticle biodistribution. Current maneuvers to validate the nanoparticle biodistribution measured using imaging modalities are to acquire *ex vivo* tissue dissections for inductively coupled plasma-mass spectroscopy (ICP-MS) measurement and/or TEM imaging with energy dispersed X-ray spectroscopy (EDX) for element analysis [10, 11]. By verifying the physical residence of nanoparticles in tissues that colocalized with the imaging contrast, it can assure an appropriate interpretation of nanoparticle biodistribution using the aforementioned non-invasive imaging modalities. Nevertheless, these processes are time consuming

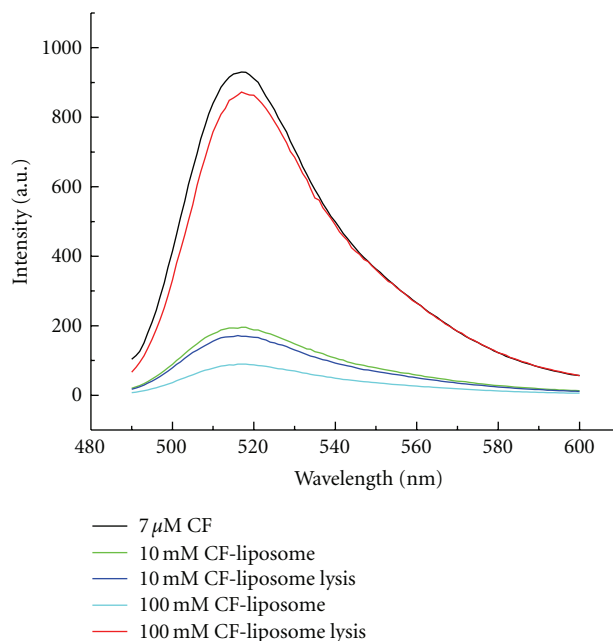


FIGURE 1: The dequenching effects of fluorescence liposomes were measured upon lysis by nonionic surfactant Triton X-100. A prominent quenching of fluorescence intensity was observed as the concentration of liposome-encapsulated CF increased from $10\ \text{mM}$ to $100\ \text{mM}$.

and difficult to acquire dynamic profiles of nanoparticle biodistribution and stability *locus in quo*.

Alternatively, to assess the stability of nanoparticle in response to local variations of microenvironments as residing in tissue, we exploited an *in vivo* microdialysis system. Such a technique used for intracerebral sampling, for example, can provide continuous monitoring of levels of compounds of a single animal and has been widely used for pharmacological and physiological studies to assay endogenous neurotransmitters or exogenous compounds [12, 13]. In the previous report [14], we applied fluorescent polystyrene nanospheres ($20\ \text{nm}$) to study the blood-brain barrier (BBB) permeability and used microdialysis probe which was implanted in the cerebral cortex of an anesthetized rat to *in situ* monitor the extravasation of administered fluorescent nanospheres into the brain across the blood-brain barrier. As illustrated in Scheme 1, since the microdialysis probe contains membrane with a specific molecular weight cutoff, it possesses a selective permeability for molecules with different sizes at locus of tissue, in the close vicinity of where the probe is positioned. If the contrast agent- or drug-encapsulating nanoparticles on site can maintain their morphological stability, their size will be too large to be selectively collected through the microdialysis membrane. On the contrary, the contrast agents or drug molecules leaching from the disintegrated nanoparticles, due to their small size, can easily diffuse through the probe membrane and be collected in microdialysates for further analysis. Thus, the microdialysis system has the potential of usage as a platform for dynamic monitoring of the nanoparticle stability *in vivo*, *locus in quo*.

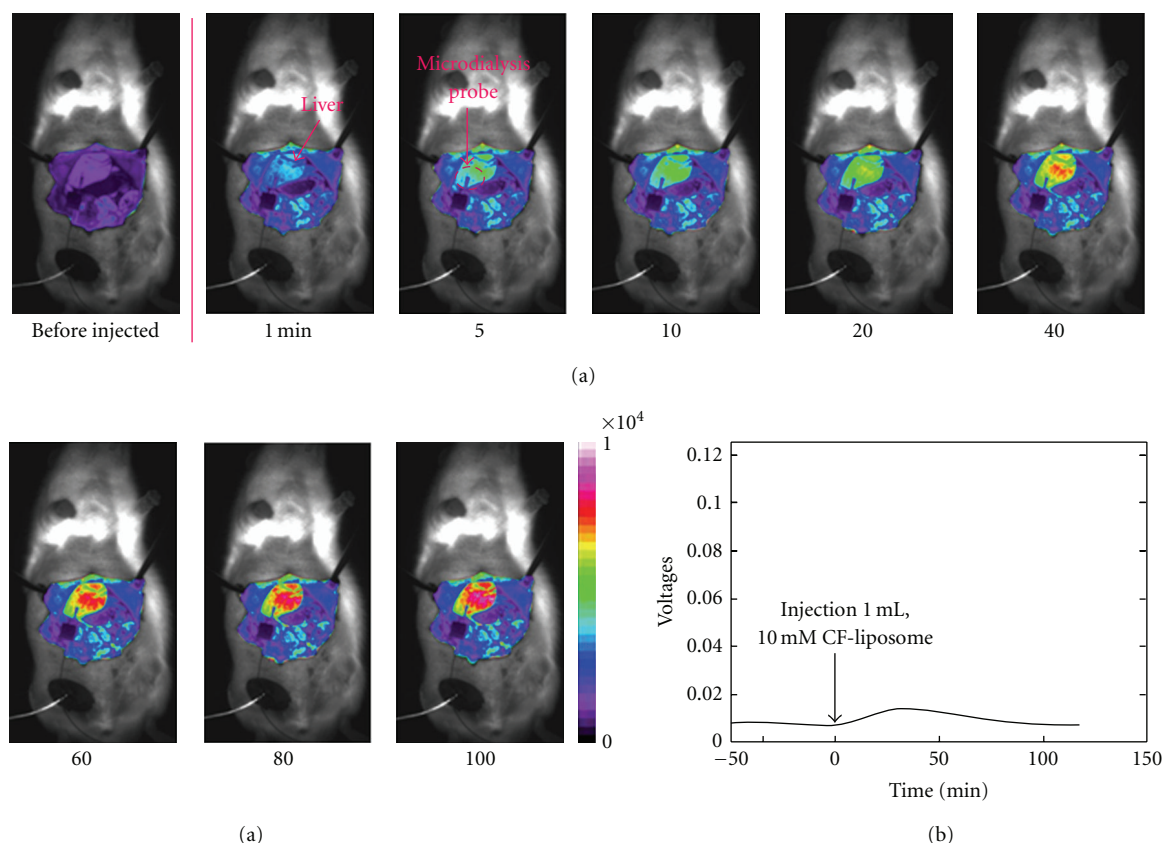


FIGURE 2: (a) The time-lapse optical images showed that liposome containing 10 mM CF, with the size of 200–240 nm, fast accumulated in rat liver as soon as 5 min after i.v. administration. The fluorescence intensity observed from liver gradually increased and reached its plateau in 100 min. To evaluate the stability of these on-site DPPG-liposomes in liver, the microdialysis probe with the molecular size cutoff at 100 kDa was implanted *in situ* to simultaneously analyze the fluorescence signals of extracellular fluid in liver, as indicated with a red-dotted circle. (b) The profile of fluorescence intensity in microdialysate showed no significant variation throughout the concurrent optical imaging course after the i.v. injection of CF-encapsulating liposomes.

In the present study, we synthesized carboxyfluorescein (CF)-encapsulating liposomes with different surface charges as models of drug carrier. An analytical method was implemented that combined the optical image system as well as *in vivo* microdialysis sampling technique to simultaneously monitor the biodistribution of liposomes *in vivo* and to assess their on-site stability at the extracellular space of liver tissue, where the liposomes accumulated the most after the intravenous (i.v.) administration. The current instrument configuration comprised of the optical image system and the microdialysis platform can provide dynamic observations of nanoparticle stability *in vivo*, from the macroscopic to microscopic scales.

2. Experimental Section

2.1. Preparation of Referenced CF-Encapsulating Liposomes (Dipalmitoylphosphatidyl Choline-Liposome: DPPC-Liposome). Liposomes were prepared using the film hydration method [14]. The lipid mixture consisted of a 10 : 10 : 1 molar ratio of DPPC, cholesterol, and DPPG. The total lipid mixture was dissolved in 4 mL of a solvent mixture

consisting of chloroform and methanol (8 : 2), followed by a 1-min sonication at 45°C. The organic solvent was then removed under vacuum on a rotary evaporator, leaving a milky white, gel-like suspension of proliposomes. It was followed by addition of 1 milliliter of CF solution (10 mM or 100 mM) to the lipid mixture. After sonication for 3 more min, the liposome preparation was ready to pass through a 0.2- μ m polycarbonate filter 20 times for the production of a homogeneous suspension of uniform size. Any unencapsulated dye or trace organic solvent was removed from the liposome preparation by gel filtration on Sephadex G-50 column at room temperature, followed by dialysis (MWCO, 12–14 kDa) against 0.01 M potassium phosphate buffer (pH 7.0) at 4°C in the dark.

2.2. Preparation of Relatively Cationic CF-Encapsulating Liposomes (Dipalmitoylphosphatidyl Ethanolamine-Liposome: DPPE-Liposome). The procedure was similar to that for DPPC liposome, except the lipid mixture used for DPPE liposome consisted of a 10 : 10 : 3 molar ratio of DPPC, cholesterol and DPPE.

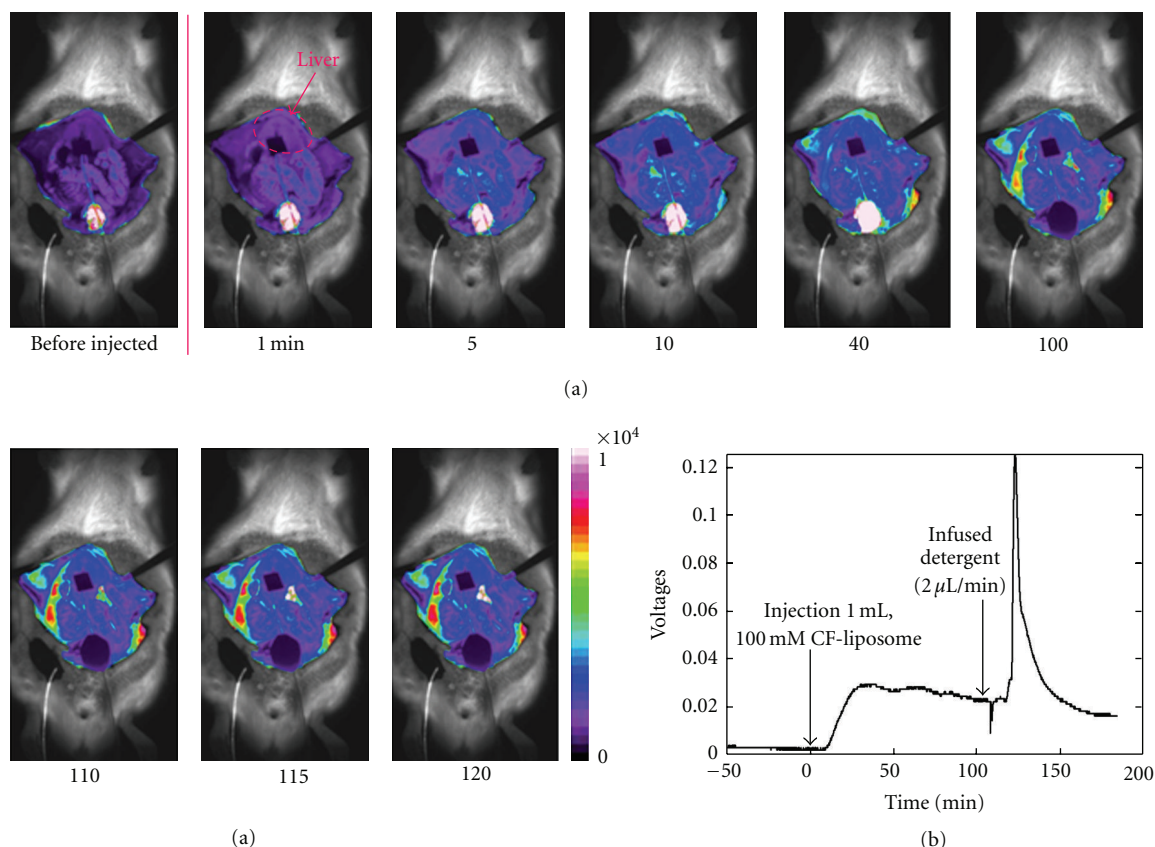


FIGURE 3: (a) The time-lapse optical imaging of liposome containing higher CF concentration at 100 mM illustrated no augmentation of fluorescence intensity in liver throughout the imaging course; the consistent self-quenching of fluorescence implicated the liposomes on site in liver remained their intact liposomal integrity. (B) At later phase of imaging course, the lysis buffer of Triton X-100 was locally infused at $2 \mu\text{L}/\text{min}$ via microdialysis probe. It caused the rupture of liposomal lipid integrity, resulting in an immediate increase of CF fluorescence intensity measured in the microdialysate.

2.3. Preparation of Relatively Anionic CF-Encapsulating Liposomes (Dipalmitoylphosphatidyl Glycerol-Liposome: DPPG-Liposome). The procedure was similar to that for DPPC liposome, except the lipid mixture used for DPPG liposome consisted of a 10 : 10 : 3 molar ratio of DPPC, cholesterol, and DPPG.

2.4. The HepG2 Cell Line Experiments. Human hepatoma cells (HepG2) were maintained in Dulbecco's modified Eagle's medium (DMEM) (Gibco; Carlsbad, CA) with 10% fetal bovine serum (Hyclone; Logan, Utah). Cells were seeded onto glass bottom dishes (35 mm OD \times 10 mm High, glass area: 22 mm dia., and glass thickness: 0.17 mm) (WillCo Wells BV; Amsterdam, Netherlands) at density of 1×10^5 cells/dish, and cultured overnight in culture medium. Cell nucleus were labeled by 10 mM Hoechst33342 (Molecular probe, Carlsbad, CA) for 5 min and rinsed twice with PBS buffer. DPPC liposome or DPPE liposome, encapsulating 100 mM carboxyfluorescein, were added to cells at concentration 5×10^5 liposome/ml in serum-free medium and cells were incubated for different time periods from 1 h to 4 h. Unfused liposome were removed by washing twice with PBS and replaced with DMEM medium without

phenol red. Live cells were observed with Leica AS MDW system (Leica Microsystems; Wetzlar, Germany) at high magnification (63X). Carboxyfluorescein was imaged using 490 nm excitation wavelengths and 530/30 nm BP emission filter. Hoechst 33342 was excited by 380 nm and its emission was collected by 465/20 nm BP emission filter.

2.5. In Vivo Microdialysis System. The microdialysis system was perfused with 50 mM phosphate buffer solution (pH 7.4) at a flow rate of $2 \mu\text{L}/\text{min}$. Microdialysis probes, made of polyethylene sulfonate with a molecular weight cutoff at 100,000, were purchased from CMA (Carnegie Medicine Association, Solna, Sweden). The microdialysates were allowed to flow through a polyimide-coated fused-silica capillary (360- μm o.d., 250- μm i.d.). A 2-cm segment of the capillary was stripped of the polyimide coating to serve as the detection window and placed inside a fluorescence detector (Argos 250 FL detector, Flux Instruments, Basel, Switzerland). Polyethylene catheters were inserted into the liver of the rats.

2.6. Optical Imaging System. The light from a 100 W mercury lamp (color temperature is 5700 K) was passed with

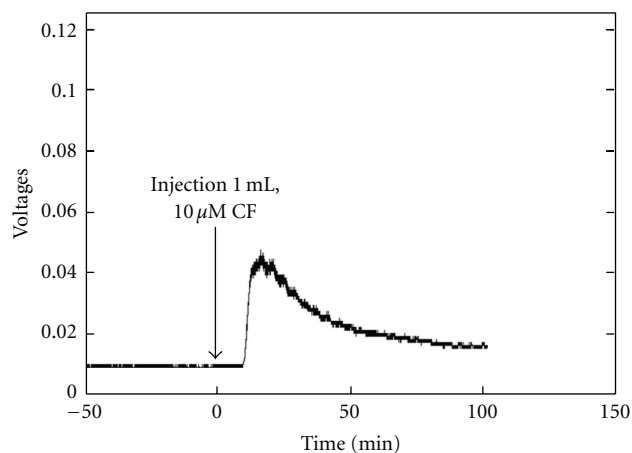


FIGURE 4: 10 μM free CF molecules were i.v. administered to validate the CF sensing of *in situ* microdialysis probe. The microdialysate of hepatic interstitial fluid demonstrated an increase of CF fluorescence intensity following the i.v. injection.

TABLE 1: Characteristics of fluorescent DPPG-liposome.

	10 mM CF-liposome	100 mM CF-liposome
Diameter	202.33 nm ^a	250.3 nm ^a
Volume of liposome	4.34×10^{-12} b	8.21×10^{-12} b
Number of Liposome	1.44×10^{13} c	8.95×10^{12} c
Dye molecule/liposome	23132	448557
Concentration of CF	10 mM	100 mM

^aThe particle size is average.

^bThe unit is μL .

^cThe unit is No. per mL.

an interference filter (model 545AF75, Omega) to induce fluorescence. The imaging sensor of the *in vivo* imaging system was a charge-coupled device (CCD) camera (model DW436, Andor, Northern Ireland) cooled down to -90°C . An interference filter (model FF495 Ex 02–25, Smerok, USA) covered the 50 mm f/1.2 lens (Nikon) to block the exciting light. The body temperature of the rats was maintained at 37°C with a heating pad.

3. Results and Discussion

3.1. Properties of Fluorescent Liposomes. We synthesized DPPG-liposomes containing 10 mM and 100 mM of CF, respectively, by using the film hydration method (shown in Experimental Section). The characteristics of liposomes were described in Table 1. The hydrodynamic diameters of liposome are around 200–250 nm and the calculated average volume of a single liposome is about $4.3\text{--}8.2 \times 10^{-12} \mu\text{L}$.

The average diameters of the liposomes were measured using the Coulter LS particle analyzer (Coulter Corp.,

Miami, FL). The spectral analysis displayed the maximal absorption and fluorescence emission of CF-encapsulated liposomes at 495 nm and 520 nm, respectively, which resembled those of CF solution (Figure 1).

Since the biodistributions of liposome and of other nanoparticles were reported to greatly depend on the surface charge [15–17], the zeta potentials of DPPG- and DPPE-liposomes were measured and listed in Table 2. As described in Experimental Section, to vary the molar ratios of DPPG and DPPE to DPPC and cholesterol in lipid mixtures, the constructed liposomes can possess different surface charges. The DPPG-liposomes containing 10 mM and 100 mM CF exhibited negative zeta surface potentials of -43.30 mV and -38.16 mV at pH 7.4, respectively. In contrast, the DPPE-liposomes encapsulating 10 mM and 100 mM displayed the relatively positive surface potentials of -10.99 mV and -15.00 mV at pH 7.4, respectively (Table 2).

3.2. Dequenching of Fluorescent Liposomes upon Lysis by Nonionic Surfactant. The 100 mM fluorescent CF encapsulated within DPPG liposomes with the sizes around 200 nm indicated apparent self-quenching of fluorescence, due to its relatively high concentration confined within a relatively small volume (Figure 1). The quenching effect could be evaluated by disintegrating liposomes with the nonionic surfactant, Triton X-100, to compare the fluorescence intensity before and after lysis. The lysis buffer containing surfactant Triton X-100 of 0.1% in PBS buffer (pH 7.4) was added and mixed gently to 3 mL of the liposome solution for 10 minutes at room temperature. As demonstrated in Figure 1, the liposome-encapsulated CF at 10 mM showed comparable levels of fluorescence intensity before and after lysis, while the 100 mM specimens indicating ninefold increase of that after the liposomes being lyzed. Thus, this dramatic change of fluorescence intensity before and after liposome disintegration could be further applied to sense the stability of liposomal structure as delivered on site in tissue. On the other hand, for tracking biodistribution of liposome *in vivo*, the 10 mM specimen was selected, due to its traceable, bright fluorescence intensity.

3.3. In Vivo Biodistribution versus In Situ Stability of Fluorescence Liposomes. The biodistribution of CF-encapsulating DPPG liposome was monitored dynamically by homemade small animal optical imaging system, and its on-site stability was simultaneously assessed using *in situ* microdialysis probe. Prior to imaging, male Sprague Dawley rats (weight ca. 250 g) were placed on Teklad 2916 diets for 5 days and fasted for 12 h, to minimize rodent chow autofluorescence within the GI-tract and anesthetized with urethane (1.5 g/kg) i.p. injection. DPPG-liposomes containing 10 mM and 100 mM CF, at a dosage of 16 mg/kg, were injected i.v. via the tail vein of animals, respectively. The time-lapse optical images showed that liposome containing 10 mM CF, with the size of 200–240 nm, fast accumulated in rat liver as soon as 5 min after i.v. administration (Figure 2(a)). The fluorescence intensity observed from liver gradually increased and reached its plateau in 100 min. To evaluate

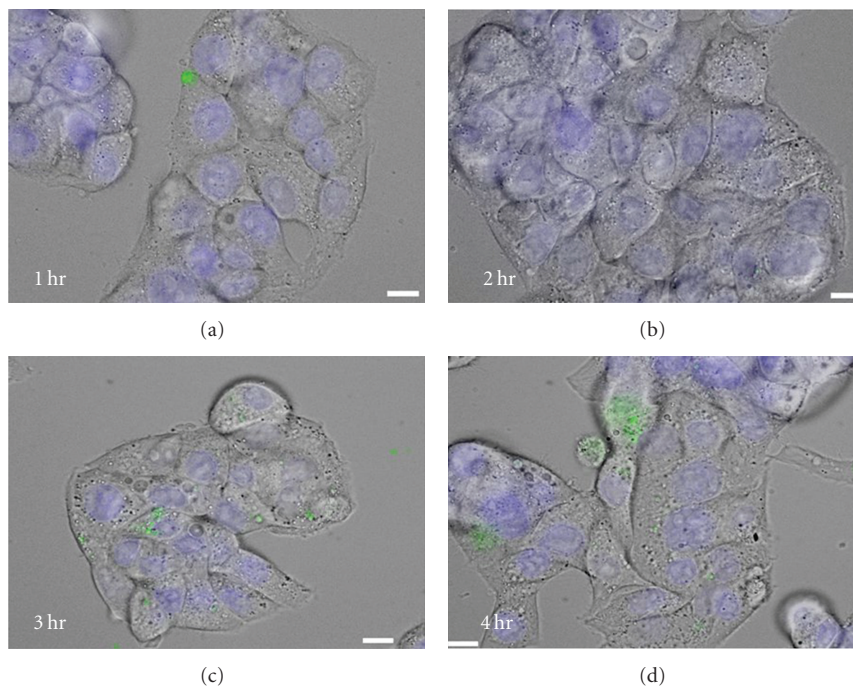


FIGURE 5: The HepG2 cells treated with DPPG liposomes containing 100 mM CF (surface charge ca. -40 mV) showed no CF fluorescence in the cytoplasm, implicating that no cell uptake of liposomes took place during the 4h imaging course. The scale bar is $10\text{ }\mu\text{m}$.

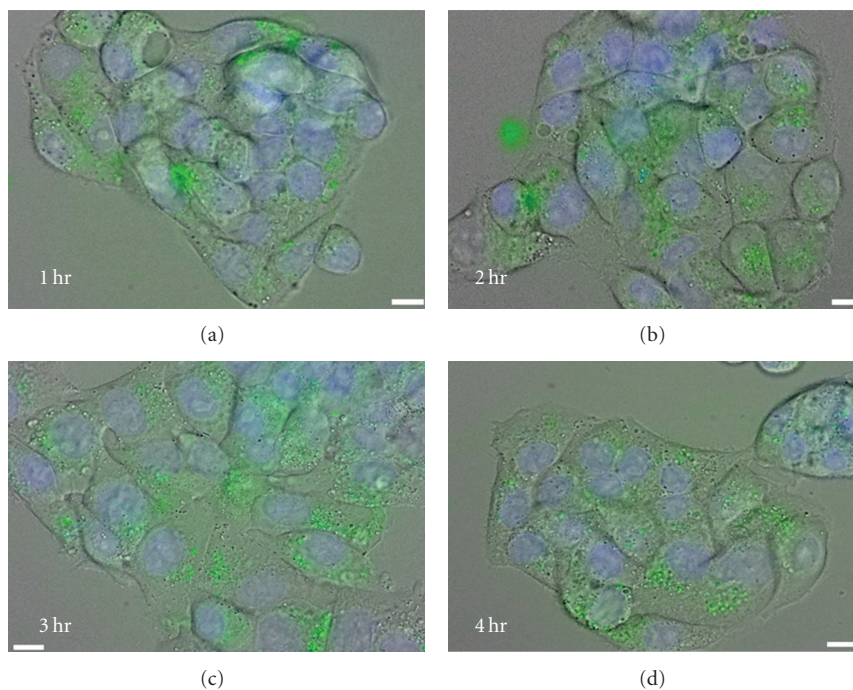


FIGURE 6: The HepG2 cells treated with DPPE-liposomes containing 100 mM CF (surface charge ca. -10 mV) showed pronounced increase of CF fluorescence in the cytoplasm, implicating that avid cell uptake of liposomes took place after the treatment. The scale bar is $10\text{ }\mu\text{m}$.

TABLE 2: The zeta potentials of fluorescent DPPG- and DPPE-liposomes.

	DPPG-liposome (10 mM CF)	DPPG-liposome (100 mM CF)	DPPE-liposome (10 mM CF)	DPPE-liposome (100 mM CF)
Zeta potential (mV)	-43.30	-38.16	-10.99	-15.00

the stability of these on-site DPPG liposomes in liver, the microdialysis probe with the molecular size cutoff at 100 kDa was implanted *in situ* to simultaneously analyze the fluorescence signals of extracellular fluid in liver (Shceme 1). As depicted in Figure 2(b), the profile of fluorescence intensity in microdialysates showed no significant variation throughout the concurrent optical imaging course after the i.v. injection of CF-encapsulating liposomes. It implicated that liposomes in liver were able to maintain their structural stability, preventing the encapsulated CF from leaching into the extracellular fluid and being sampled by the microdialysis probe. On the other hand, since the liposomes were not disintegrated, with the intact size of 200 nm, they were simply too large to permeate through the membrane of microdialysis probe.

For DPPG liposomes containing high concentration of 100 mM CF, due to the self-quenching phenomenon, there was no observable increase of fluorescence signal in liver of anesthetized rat during the optical imaging course, following the i.v. administration (Figure 3(a)). If the liposomes with 100 mM CF disintegrate on site, it would result in CF molecules permeating into the interstitial space of liver, consequently to compromise the self-quenching of fluorescence. Therefore, the dark time-lapse images of liver could be accounted for the macroscopic evidence that implicating the integrity of liposomes was remained intact at their loci of liver. To microscopic probing of the stability of liposomes encapsulating 100 mM CF, the positioned microdialysis in liver also revealed no increase of CF fluorescence in microdialysates over the 100-min concomitant optical imaging session (Figure 3(b)). The upshift of fluorescence baseline (from less than 0.01 to ca. 0.03 V) upon the i.v. injection of liposomes was due to the high concentration of encapsulated CF molecules. At the equilibrium, with 100 mM liposome-encapsulated CF, the concentration of free CF molecule in the prepared ready-to-use solution was much higher than that with 10 mM liposome-encapsulated CF. Consequently, it incurred the increase of baseline following the injection of liposome solution, as delineated in Figure 3(b). At later phase of imaging course, the lysis buffer of Triton X-100 was locally infused at 2 μ l/min via microdialysis probe. It caused the rupture of liposomal lipid integrity, resulting in an immediate increase of CF fluorescence intensity measured in the microdialysate (Figure 3(b)).

Since the lysis buffer diffused to the tissue only in the vicinity of microdialysis probe, its effective volume on tissue was very small; only those liposomes situated around the tip of microdialysis probe were subject to the lysis. Thus, this increase of fluorescence intensity, resulted from the leaching CF, could only be sensed by the microdialysis *in situ*, but not by the optical imaging measurement. As such, to deliver Triton-X for liposome disintegration was not an efficient means of controlled release, albeit it provided indirect evidence to substantiate the intact of liposomal structure *in situ* of liver. The release of CF molecules during the Triton-X lysis was a process of concentration-dependent diffusion, therefore, to probe the integrity of liposome via this means was better to use liposomes encapsulating 100 mM, rather than 10 mM.

To further validate the CF sensing of *in situ* microdialysis probe, 10 μ M free CF molecules were i.v. administered. As shown in Figure 4, with this CF concentration before the plasma dilution—less than a thousandth of that previously used with the liposome encapsulation, a prominent fluorescence signal was still able to be measured via the microdialysis sampling of extracellular fluid in liver. It implicated that the *in situ* microdialysis was suitable for monitoring of the drug controlled release in tissue *locus in quo*. In summary, all the evidence, from macroscopic optical imaging to microscopic microdialysis measurement, indicates that, following i.v. administration, the DPPG-liposomes would fast accumulate in the liver and reside in the extracellular space with the high stability of morphological integrity over the period of 2 h.

3.4. The Hepatoma Cell Uptakes of Liposomes versus Different Surface Charges. There are a number of reports demonstrating that the biodistribution of nanoparticles is surface charge-dependent [15–17]. In general, the nanoparticles with greater surface charge tend to be more avid for cell uptake via process like endocytosis. In the current study, the DPPG-liposomes, with the surface zeta potential of ca. -40 mV, were demonstrated to reside in the extracellular space of liver tissue. How the surface charge of liposomes leads the propensity of their interactions with cells was investigated with the *in vitro* model of human hepatoma cell line (HepG2). The HepG2 cells (1×10^5 cell number) were seeded onto a glass bottom dish and cultured overnight in culture medium. The cell nuclei were labeled by 10 mM Hoechst 33342 for 5 min and then rinsed twice with PBS buffer. Afterwards, the DPPG-liposomes (ca. -40 mV) or DPPE-liposomes (ca. -10 mV), both encapsulating 100 mM carboxyfluorescein, were respectively added to HepG2 cells at concentration of 5×10^5 liposome/ml in serum-free medium, incubated for various time periods, from 1 h to 4 h. If the treated liposomes are engulfed into cells, the encapsulating 100 mM CF can be released from the disrupted liposomal structure via two possible pathways: direct lipid-cell membrane fusion or cell endocytosis. In the latter pathway, the lipase in endosomes is responsible to digest the liposome to release the CF molecules [5]. Both cases will result in the increase of intracellular fluorescence intensity, due to the compromise of CF fluorescence self-quenching by its dilution in cytoplasm. In our study, the time-lapse fluorescence microscopy illustrated that, with the DPPG-liposomes, no CF fluorescence was observed in the cytoplasm of HepG2 cells, implicating no cell uptake of liposomes occurred in 4 h (Figure 5). However, with the DPPE-liposomes possessing relatively positive surface charge as compared to the DPPG liposomes, the pronounced intracellular fluorescence intensity was observed throughout the 4 h imaging course (Figure 6). These results of liposome-cell interaction are consistent to that for other reported nanoparticles [15–17] and are supportive to the *in vivo* observation of extracellular residence of DPPG liposomes in liver.

4. Conclusions

In this study, we successfully implement the first methodology comprised of microdialysis and optical imaging to dynamically assess the stability of liposome *in vivo*. Macroscopically, with the time-lapse optical imaging, we demonstrated that the DPPG-liposomes with surface charge around -40 mV would accumulate in the liver of anesthetized rat upon their i.v. administration in 5 min. Microscopically, the concurrent analysis of fluorescent molecules in extracellular fluid of liver tissue, *in situ*-sampled using microdialysis probe, provided the dynamic information of stability of DPPG-liposomes *locus in quo*. From macroscopic to microscopic results, all the evidence implicated that the DPPG-liposomes could reside in the extracellular space of liver, with stable and intact morphological integrity, over a period of 2 h at least. The microdialysis probing the lipid integrity of liposome, by analyzing the increase of fluorescence intensity in microdialysates that attributed to the leaching of CF molecules, provides itself as a platform technology used for evaluation of nanoparticle stability (not only for liposome) and the bioavailability of drug payload released on targeted site *in vivo*. As such, the current combination of *in situ* microdialysis and optical imaging possesses a great potential to be used vigorously in the research of nanoparticle-mediated drug targeted delivery and controlled release.

Acknowledgments

This study was conducted with the support of the NHRI Intramural Research Grants MED-098-PP-04 and NM-098-PP-01 from National Health Research Institutes of Taiwan and of the Grant NSC 098-2221-E-400-001 from the National Science Council of Taiwan.

References

- [1] K. K. Coti, M. E. Belowich, M. Liong et al., "Mechanised nanoparticles for drug delivery," *Nanoscale*, vol. 1, no. 1, pp. 16–39, 2009.
- [2] J. Lu, E. Choi, F. Tamanoi, and J. I. Zink, "Light-activated nanoimpeller-controlled drug release in cancer cells," *Small*, vol. 4, no. 4, pp. 421–426, 2008.
- [3] T. D. Nguyen, K. C.-F. Leung, M. Liong, Y. Liu, J. F. Stoddart, and J. I. Zink, "Versatile supramolecular nanovalves reconfigured for light activation," *Advanced Functional Materials*, vol. 17, no. 13, pp. 2101–2110, 2007.
- [4] L.-A. Tai, P.-J. Tsai, Y.-C. Wang, Y.-J. Wang, L.-W. Lo, and C.-S. Yang, "Thermosensitive liposomes entrapping iron oxide nanoparticles for controllable drug release," *Nanotechnology*, vol. 20, no. 13, Article ID 135101, 2009.
- [5] T. Ishida, H. Harashima, and H. Kiwada, "Liposome clearance," *Bioscience Reports*, vol. 22, no. 2, pp. 197–224, 2002.
- [6] S.-J. Kim, D. J. Doudet, A. R. Studenov et al., "Quantitative micro positron emission tomography (PET) imaging for the *in vivo* determination of pancreatic islet graft survival," *Nature Medicine*, vol. 12, no. 12, pp. 1423–1428, 2006.
- [7] M.-S. Martina, J.-P. Fortin, C. Ménager et al., "Generation of superparamagnetic liposomes revealed as highly efficient MRI contrast agents for *in vivo* imaging," *Journal of the American Chemical Society*, vol. 127, no. 30, pp. 10676–10685, 2005.
- [8] E. M. Shapiro, S. Skrtic, K. Sharer, J. M. Hill, C. E. Dunbar, and A. P. Koretsky, "MRI detection of single particles for cellular imaging," *Proceedings of the National Academy of Sciences of the United States of America*, vol. 101, no. 30, pp. 10901–10906, 2004.
- [9] Q. L. M. de Chermont, C. Chanéac, J. Seguin et al., "Nanoprobes with near-infrared persistent luminescence for *in vivo* imaging," *Proceedings of the National Academy of Sciences of the United States of America*, vol. 104, no. 22, pp. 9266–9271, 2007.
- [10] K. Kametani and T. Nagata, "Quantitative elemental analysis on aluminum accumulation by HVTEM-EDX in liver tissues of mice orally administered with aluminum chloride," *Medical Molecular Morphology*, vol. 39, no. 2, pp. 97–105, 2006.
- [11] A. Patri, T. Umbreit, J. Zheng et al., "Energy dispersive X-ray analysis of titanium dioxide nanoparticle distribution after intravenous and subcutaneous injection in mice," *Journal of Applied Toxicology*, vol. 29, no. 8, pp. 662–672, 2009.
- [12] U. Ungerstedt, "Measurement of neurotransmitter release by intracranial dialysis," in *Measurement of Neurotransmitter Release In Vivo*, C. A. Marsden, Ed., pp. 210–245, John Wiley & Sons, New York, NY, USA, 1984.
- [13] E. C. M. de Lange, M. Danhof, C. Zurcher, A. G. de Boer, and D. D. Breimer, "Repeated microdialysis perfusions: periprobe tissue reactions and BBB permeability," *Brain Research*, vol. 702, no. 1-2, pp. 261–265, 1995.
- [14] C.-S. Yang, C.-H. Chang, P.-J. Tsai, W.-Y. Chen, F.-G. Tseng, and L.-W. Lo, "Nanoparticle-based *in vivo* investigation on blood-brain barrier permeability following ischemia and reperfusion," *Analytical Chemistry*, vol. 76, no. 15, pp. 4465–4471, 2004.
- [15] T. S. Levchenko, R. Rammohan, A. N. Lukyanov, K. R. Whiteman, and V. P. Torchilin, "Liposome clearance in mice: the effect of a separate and combined presence of surface charge and polymer coating," *International Journal of Pharmaceutics*, vol. 240, no. 1-2, pp. 95–102, 2002.
- [16] F. Alexis, E. Pridgen, L. K. Molnar, and O. C. Farokhzad, "Factors affecting the clearance and biodistribution of polymeric nanoparticles," *Molecular Pharmaceutics*, vol. 5, no. 4, pp. 505–515, 2008.
- [17] J. S. Souris, C. -H. Lee, S. -H. Cheng et al., "Surface charge-mediated rapid hepatobiliary excretion of mesoporous silica nanoparticles," *Biomaterials*, vol. 31, no. 21, pp. 5564–5574, 2010.